# Control and energy management of MMC-based multi-terminal HVDC grids

Kosei Shinoda

## To cite this version:

Kosei Shinoda. Control and energy management of MMC-based multi-terminal HVDC grids. Electric power. Ecole Centrale de Lille, 2017. English. NNT : 2017ECLI0017 . tel-03934547

**HAL Id: tel-03934547**
**https://theses.hal.science/tel-03934547v1**

Submitted on 11 Jan 2023

A. *N° d'ordre : 331*

**CENTRALE LILLE**

# THESE

Présentée en vue
d'obtenir le grade de

## DOCTEUR

En

**Spécialité : Génie Électrique**

Par

## SHINODA Kosei

**DOCTORAT DELIVRE PAR CENTRALE LILLE**

Titre de la thèse :

# Contrôle et Opération des Réseaux HVDC Multi-Terminaux à base de Convertisseurs MMC

# Control and Energy Management of MMC-based Multi-Terminal HVDC Grids

Soutenue le 21 Novembre 2017 devant le jury d'examen :

| | |
|---|---|
| **Président** | *Seddik BACHA, Professor, Université Grenoble Alpes* |
| **Rapporteur** | *Mike BARNES, Professor, University of Manchester* |
| **Rapporteur** | *Kai STRUNZ, Professor, Technische Universität Berlin* |
| **Examinateur** | *Maryam SAEEDIFARD, Assistant Professor, Georgia Institute of Technology* |
| **Invité** | *Pierre RAULT, Research Engineer, RTE* |
| **Directeur de thèse** | *Xavier GUILLAUD, Professor, Centrale Lille* |
| **Encadrant** | *Abdelkrim BENCHAIB, R&D Manager, Supergrid Institute, GE Grid Solution* |
| **Encadrant** | *Jing Dai, Assistant Professor, CentraleSupélec* |

Thèse préparée dans le Laboratoire L2EP

Ecole Doctorale SPI 072 (Lille I, Lille III, Artois, ULCO, UVHC, EC Lille)

# Abstract

High Voltage Direct Current (HVDC) technology has appeared in practical applications along with remarkable advances in power electronics. With the recent deployment of the cross-border HVDC link project between France and Spain and the offshore wind farm projects in the North Sea using the Modular Multilevel Converter (MMC), considerable attention has been drawn to this converter as the most suitable technology for high power and high voltage applications today.

The scope of this thesis includes control of the MMC alone, an HVDC transmission link, and a Multi-Terminal DC (MTDC) grid composed of several MMC stations.

First, our studies focus on the internally stored energy, an important additional degree of freedom brought by the complex topology of the MMC which is not available for conventional Voltage Source Converters (VSCs). In order to draw out the utmost of this additional degree of freedom, an in-depth analysis on the limits of this internally stored energy is carried out. Its admissible range which ensures the maximum allowable voltage of the converter components and the minimum amount of the energy necessary to maintain its proper operation is mathematically formulated and confirmed by using a small-scale MMC prototype.

The aforementioned additional degree of freedom of the MMC can provide a completely new solution to the mitigation of the DC voltage fluctuations in HVDC transmission systems. From the analysis on the DC voltage dynamics and its interaction with the MMC, the possibility of using this feature of the MMC is explored, which results in a novel control strategy for the MMC, named Virtual Capacitor Control. Under the proposed control, the MMC behaves as if there were a physical capacitor whose size is adjustable and can be even bigger than the physical capacitor embedded in the converter. It is able to increase the equivalent capacitance of an HVDC system to mitigate the variations of the DC voltage without any adverse effects on the AC system; thus, it can greatly broaden the operability of HVDC systems.

Finally, the scope is extended to a MMC-based MTDC grid. One of the crucial challenges for such system is to cope with a sudden loss of a converter station which may lead to a great variation of the system voltage. For that purpose, the voltage droop method is commonly used to adjust the converter power according to the DC voltage deviation in order to maintain the energy balance of the system. The influence of the droop parameters on the MTDC grid is analyzed from both static and dynamic aspects, and it is shown that the desired control action may not be exerted when the available headrooms of the converter stations are insufficient. We thus propose a novel voltage droop control structure which permits to provide different actions depending on the sign of DC voltage deviation caused by the disturbance to the system as well as an algorithm that determines the droop parameters taking into account the operating point and the available headroom of each station.

# Acknowledgment

This thesis would not have been possible without the help, encouragement, and support of countless people who, in one way or another, contributed to this achievement. I thank all of them, and I present to them all my gratitude.

First and foremost, I would like to offer my sincerest gratitude to my thesis director, Prof. Xavier Guillaud, for his unwavering guidance and patient support throughout this Ph.D. study. I greatly appreciate the faith he has had in me to carry out this work and his help that steered me in the right direction whenever needed. I feel privileged to do my Ph.D. work under his direction, and I am indebted to him more than words can express.

I gratefully acknowledge my co-supervisors, Abdelkrim BENCHAIB and Jing DAI, for their immense contributions to accomplish this Ph.D. work. I would like to thank Abdelkrim for his valuable advice from his industrial expertise, but also for being my moral support during this long period. His warm encouragement has been invaluable for completing this work. I owe a lot of gratitude to him for always being there for me. My sincere thanks also go to Jing for his dedicated involvement and continuous support. I greatly benefited his assistance and insightful remarks as well as fruitful discussions with him. It was a great pleasure working with him.

For my dissertation, I would also like to acknowledge my gratitude to the rest of my jury members. I am grateful to Prof. Mike BARNES and Prof. Kai STRUNZ, who managed their busy schedules to find a time to review this manuscript and provided me with bountiful compliments. I am also grateful to Prof. Maryam SAEEDIFARD and Dr. Pierre RAULT for their insightful comments on the dissertation and encouragement. My sincere thanks go to Prof. Seddik BACHA, who led me to aspire to this endeavor, for presiding the jury committee and for his extensive professional and personal guidance during the last four years. It is my great honor to have those eminent researchers in my jury committee.

I would like to offer my special thanks to Bruno LUSCAN, the director of Programme 1 of SuperGrid Institute, who believed in us and supported us with strong leadership

from the very beginning. I'm extending my thanks to the sub-program directors, Serge POULLAIN, Alberto BERTINATO and Sébastien SILVANT for their valuable advices and discussions.

I have been blessed with friendly and cheerful fellow doctoral students: Ahmed, William, Dieynaba, Swann, and Janailson. I am grateful to them for stimulating discussions, mutual encouragement, and friendship. Also, I thank the future doctors: Miguel, Juan-Carlos, Amjad, Guilherme, Raga and Nicolas, for providing me inspirations in many ways. I wish them successful achievements. I want to thank all present and past members of SuperGrid, Programme 1, that I have had the pleasure to work with. Eric, Sellé, Boussaad, Leo, Teihotua, Frédéric, Philippe, and all the internship students, deserve my special thanks.

I want to extend my thanks to the members of L2EP: Julian, Shabab, Moez, Frédéric and François for their warm welcome and fruitful discussions during my stay in Lille.

I owe a very important debt of gratitude to Hubert de la GRANDIERE, the Chief Executive Officer of SuperGrid Institute, for providing me this opportunity to undertake my research in such an extraordinary human and scientific environment.

I warmly thank and appreciate my grandparents, mother, father, for their unconditional support and heartfelt encouragements.

Last but not least, I shall never forget to thank my loving wife, Miu, who accompanied me to France and supported my pursuit with patience. Without your encouragements, this accomplishment could not have been possible.

Kosei SHINODA
February, 2018

# Résumé de la thèse en français

## Contexte

En réponse à l'augmentation de la consommation globale d'énergie et aux préoccupations environnementales, les décideurs politiques recherchent aujourd'hui des alternatives aux ressources d'énergie fossile qui sont limitées et polluantes. Les ressources en énergie renouvelable abondamment disponibles, telles que le vent, l'énergie solaire, la biomasse, la géothermie, etc., sont considérées comme des alternatives prometteuses, et elles devraient remplacer les centrales électriques à base de fossiles classiques dans la flotte de génération dans les décennies à venir. Néanmoins, le fait d'accommoder les ressources renouvelables géographiquement dispersées, qui sont probablement situées à des endroits éloignés défavorables à l'intégration des réseaux électrique, et le traitement de leur nature intermittente ont déjà imposé un stress importante aux systèmes de transmission d'énergie existants. D'autres part, l'augmentation significative des capacités d'interconnexion entre des pays voisins devrait permettre non seulement pallier l'intermittence des énergies renouvelables, mais aussi d'améliorer la sécurité et la fiabilité de l'alimentation électrique.

Un renforcement fondamental du système de transmission par des moyens efficaces et flexibles est attendu. La transmission courant continu haute tension (HVDC) est considérée comme un bon candidat. La limite de distance du transport de l'énergie électrique via des câbles souterrains ou sous-marins, qui est approximativement de 50 km avec la technologie traditionnelle basée sur courant alternatif (AC), n'existe pas avec HVDC. De plus, l'absence de l'effet de peau et le dispositif de compensation de puissance réactive rendent le HVDC économiquement attrayante pour transport d'électrique à longue distance. En conséquence, de nombreux projets ont été lancés ces dernières décennies.

La transmission courant continu haute tension (HVDC) est considérée comme un bon candidat. La limite de distance du transport de l'énergie électrique via des câbles souterrains ou sous-marins, qui est approximativement de 50 km avec AC haute tension, n'existe pas avec HVDC. De plus, l'absence de l'effet de peau et le dispositif de compensation de puissance réactive rendent le HVDC économiquement attrayante pour transport d'électrique à longue distance. En conséquence, de nombreux projets ont été lancés ces dernières décennies.

La transmission HVDC est devenue une solution techniquement et économiquement attrayante grâce au progrès remarquable de la technologie convertisseur, représentée par les convertisseurs multiniveaux modulaires (MMCs). En raison de ses divers avantages par rapport aux topologies de convertisseurs conventionnels, le MMC est considéré comme la technologie standard et utilisé dans plusieurs projets récents.

Avec le nombre croissant d'applications HVDC, est né le concept de connexion de plusieurs stations HVDC pour former un réseau multi-terminal à courant continu (MTDC). Le réseau MTDC fait l'objet d'études intensives pour la connexion de parcs éoliens offshores. La production d'énergie éolienne dépend fortement des conditions météorologiques. Cela implique que les infrastructures coûteuses HVDC ne sont probablement pas utilisées à leur pleine capacité tout le temps, surtout aux moments de production faible des parcs éoliennes. Si plusieurs parcs éoliens offshores sont connectés à de multiples réseaux onshores via un réseau MTDC, le taux d'utilisation des infrastructures HVDC peut être considérablement augmenté car le réseau MTDC peut servir toujours de chemins d'interconnexion supplémentaire entre les réseaux onshores lors de la faible génération d'énergie éolienne. De plus, un réseau MTDC maillé permet de continuer la transmission même si certaines lignes sont hors service, ce qui peut améliorer la disponibilité et la fiabilité du système.

Si le nombre de points de connexion augmente, ces réseaux MTDC peuvent évoluer vers une nouvelle infrastructure où le MTDC est superposé sur le réseau AC déjà existant, connue sous le nom de "Supergrid". En Europe, Supergrid est considéré comme une solution attrayante pour accueillir des ressources renouvelables. On s'attend à ce que cela augmente la flexibilité de la transmission de puissance et la fiabilité de l'alimentation en servant de réseau transmission supplémentaire superposé sur la système de transmission existant. Cependant, l'intégration de plusieurs convertisseurs, qui peuvent être développés par différents fabricants avec leurs propres topologies, paramètres et algorithmes de commande, pour former un tel réseau MTDC et fonctionner ensemble d'une manière coordonnée, pourra engendrer un certain nombre de défis.

L'objectif de cette thèse est de développer une stratégie de commande des réseaux MTDC basés sur MMC qui apporte encore plus de stabilité, de sécurité et d'efficacité. Afin de profiter pleinement du réseau MTDC basé sur MMC, ce travail porte sur la commande du système sous différentes perspectives. Pour distinguer ce travail des autres, notre attention est portée sur le comportement de l'énergie dans le système.

Les travaux de cette thèse débutent par la modélisation de convertisseurs MMC. Notre attention se focalise sur les dynamiques de l'énergie stockée à l'intérieur du convertisseur, ce qui différentie le comportement de ce convertisseur et sa structure de commande des technologies classiques. Ensuite, on étude l'interactions entre les caractéristiques distinctives du MMC et de la dynamique du système DC. Par rapport aux systèmes à courant alternatif, les systèmes DC sont moins extensivement étudiés. Une analogie entre les systèmes DC et le système AC en termes d'énergie nous permet de mieux comprendre le comportement dynamique des systèmes HVDC et de révéler son problème critique. Nous proposons une nouvelle solution qui valorise l'énergie interne du MMC pour supporter les systèmes DC. Enfin, la portée est étendue au réseau MTDC. Dans un tel system, plusieurs stations de convertisseur avec des spécifications différentes doivent fonctionner de manière coopérative. Nous proposons donc une nouvelle structure de commande de la tension, ainsi qu'un algorithme qui nous permet de mieux tenir en compte la capacité disponible de chaque station et de respecter les contraintes du système.

## Modélisation et Commande de l'Energie de MMC

La commande de MMC comprend deux niveaux distincts. D'une part, le bas niveau porte sur la commande des commutateurs et vise à l'équilibrage des tensions des sous-modules. D'autre part, le haut niveau donne les consignes au bas niveau pour réguler les courants, les puissances et l'énergie interne du système. Tout d'abord, la dynamique du courant interne du MMC est étudiée, et son modèle analytique est présenté. Les contrôleurs internes qui gèrent les courants alternatif et continu sont ensuite développés en inversant la relation de causalité entre les tensions du bras du convertisseur et les courants à réguler. L'un des défis de commande de MMC est de réguler l'énergie dans le convertisseur distribuée parmi les six bras. Par un changement adéquat des variables, ces six variables d'état ont été transformées en six autres variables: l'énergie totale stockée à l'intérieur du MMC et cinq variables restantes qui représentent la distribution de l'énergie entre les bras. À partir du modèle énergétique développé, les deux types de contrôleurs d'énergie totale interne du MMC ont été développés: l'un régule l'énergie échangée avec le réseau DC, et l'autre l'énergie échangée avec le réseau AC. Leurs différences ont été démontrées par des simulations. Il a été démontré que le MMC possède une caractéristique inhérente – la commandabilité de l'énergie interne - qui permet d'agir comme un stockage d'énergie qui échange de l'énergie avec l'un des réseaux associés sans affecter l'autre.

# Analyse des Contraintes sur l'Energie Interne du MMC

Afin de tirer le meilleur parti du degré de liberté apporté par l'énergie interne du MMC, une analyse approfondie de ses limitations est fournie. La limite supérieure de l'énergie est définie comme l'énergie maximale admissible qui ne dépasse pas la tension maximale admissible des sous-modules (SMs), et la limite inférieure signifie l'exigence minimale de l'énergie nécessaire pour assurer le bon fonctionnement du MMC sans sur-modulation.

Les pulsations d'énergie internes, qui apparaissent comme les ondulations de tension dans les bras, sont d'abord analysées. Ensuite, les limites d'énergie supérieures et inférieures sont formulées mathématiquement qui dépendent du point de fonctionnement du convertisseur, et elles sont validées par des résultats expérimentaux d'une modélisation MMC à petite échelle. En outre, une analyse de sensibilité de l'influence du transfert de puissance active et réactive, de la tension de réseau AC et DC et de la taille du condensateur SM sur les limites d'énergie supérieure et inférieure a été fournie.

# Virtual Capacitor Control

La dynamique générale des systèmes DC est décrite par analogie avec les systèmes AC. Il est révélé que la tension continue est extrêmement volatile par rapport à la fréquence des systèmes AC en raison de l'énergie considérablement réduite stockée dans le système DC. Pour remédier à ce problème, une nouvelle stratégie de commande, nommée Commande Capacité Virtuelle, est proposée. Elle permet au MMC de se comporter comme s'il existait un condensateur physique dont la taille est réglable. Ceci est réalisé par le calcul de consigne d'énergie en conjonction avec la variation de la tension continue. En modifiant simplement le coefficient de la capacité virtuelle, le degré de contribution de l'énergie interne peut être ajusté. Ainsi est-il possible d'augmenter virtuellement la capacité équivalente du réseau pour atténuer les fluctuations de tension continue. Sa faisabilité est démontrée et validée par des simulations d'un modèle détaillé de HVDC sur le logiciel EMTP-RV.

Ce degré de liberté supplémentaire peut élargir considérablement l'opérabilité des systèmes à courant continu, ce qui permet de maintenir la tension continue dans une gamme prescrite sans engendrer un coût supplémentaire ou un impact négatif sur le réseau AC.

# Commande des Réseaux MTDC

La commande et l'opération des réseaux MTDC doivent assurer que la tension du réseau continu ne dépasse pas une limite maximale admissible. Comme la plupart des systèmes AC comprend une structure hiérarchique pour assurer l'alimentation électrique de haute qualité et résister à des perturbations éventuelles, la commande du réseau MTDC devrait avoir une structure hiérarchique similaire. Par analogie avec la structure de commande du système AC, la commande du système DC peut être structurée en cascade sous forme de réglage primaire, secondaire et tertiaire. L'un des défis majeurs pour le réglage primaire d'un tel système est de faire face à une perte soudaine d'une station de convertisseur qui peut entraîner une grande variation de la tension du système. La méthode de statisme de tension est couramment utilisée à cet effet. L'influence des paramètres de droop sur le comportement du système est analysée d'aspects statique et dynamique. Il est montré que l'action de commande souhaitée avec l'approche traditionnelle du statisme risque de ne pas être réalisée lorsque la marge disponible de réserve du convertisseur est insuffisante. Nous proposons donc une nouvelle structure de commande de la tension qui permet de fournir différentes actions en fonction du signe de l'écart de tension DC causé par la perturbation, ainsi qu'un algorithme qui détermine les paramètres de statisme en tenant compte du point de fonctionnement et donc de la marge disponible de chaque station.

# Perspectives et Futurs Travaux

Les travaux de cette thèse ouvrent la voie à la commande du MMC et la gestion des réseaux MTDC. Les nouveaux degrés de liberté pour l'opération de system et les solutions proposées peuvent certainement étendre la flexibilité et l'opérabilité des réseaux MTDC. Cependant, pour l'exploitation d'un tel système d'alimentation d'énergie qui exige une fiabilité et une qualité extrêmes, il sera judicieux d'améliorer la conception de commande du convertisseur. L'utilisation de la théorie de la commande avancée est une solution attrayante pour améliorer les performances du convertisseur. L'intégration de l'analyse sur les limites d'énergie dans les critères d'optimisation est une application intéressante. En autre, la maîtrise d'un défaut franc ou de conditions asymétriques dans le réseau AC est une condition importante pour la commande du convertisseur HVDC en pratique. La modélisation de MMC en séquences positives et négatives et l'élaboration de la conception du contrôleur pour empêcher la propagation de la perturbation au réseau DC doivent être résolues.

Enfin, l'analyse fournie sur les limites d'énergie concernait uniquement la topologie du sous-module à demi-pont. Le travail futur à cet égard englobe l'extension de l'étude fournie aux différentes topologies des sous-modules, telles que le pont complet, le double clamping, etc.

# Contents

# Nomenclature

| | |
|---|---|
| $i$ | Subscript for phase component $i \in \{a, b, c\}$ |
| $u$ | Superscript for upper arm |
| $l$ | Superscript for lower arm |
| $n$ | Number of inserted sub-modules in an arm |
| $N$ | Number of total sub-modules in an arm |
| $m_i^{u,l}$ | Upper or lower arm modulation index |
| $C_{sm}$ | Sub-modulel capacitance |
| $C_\Sigma$ | Total capacitance of an arm |
| $C_{mmc}$ | Sum of capacitance of all six arms |
| $C_{dc}$ | DC capacitance |
| $v_{Ci,j}^{u,l}$ | $j$th sub-module capacitor voltage in upper or lower arm of phase $i$ |
| $v_{C\Sigma i}^{u,l}$ | Available total voltage in an arm |
| $v_{mi}^{ac}$ | Modulated AC voltage |
| $v_{mi}^{dc}$ | Modulated DC voltage |
| $v_{mi}^{u,l}$ | Arm voltage |
| $i_i^{u,l}$ | Arm current |
| $i_i^{dc}$ | DC current in phase $i$ |
| $i_{dc}$ | DC current |
| $i_i^{ac}$ | AC grid current in phase $i$ |
| $i_i^{cir}$ | Circulating current in phase $i$ |
| $W_i^{u,l}$ | Total energy in each arm of phase $i$ |

| | |
|---|---|
| $W_{mmc}$ | Total energy in MMC |
| $p_i^{dc}$ | DC power of phase $i$ |
| $P_{dc}$ | DC power |
| $P_{dc}^*$ | DC power reference |
| $p_i^{ac}$ | AC power of phase $i$ |
| $P_{ac}$ | AC active power |
| $P_{ac}^*$ | AC active power reference |
| $Q_{ac}$ | AC reactive power |
| $Q_{ac}^*$ | AC reactive power reference |
| $P_n$ | Nominal Power |

# List of Figures

# List of Tables

# Chapter 1

# General Introduction

## 1.1 Trends in Power Transmission Systems

Electricity is vital to modern life. Lighting, pumping, cooling, etc, all those bare essentials are almost invariably powered by electricity due to its extraordinary versatility. Furthermore, the application of the electric power is almost limitless as it includes communications, computations, and locomotives as we see them forming the highly advanced modern society today. The relative importance of electricity has been increased in accordance with industrialization and the need for comforts throughout history. As shown in Fig. 1.1, the world global electricity consumption is rising driven by the exponential economic growth and electrification in non-OECD countries[1] [1]. There is no doubt that this upward trend will continue in the upcoming future.

In response to the continuous rise of the overall energy consumption and growing concern on sustainable development, many countries have revisited their national energy policies towards decarbonation of the energy sector: for example, China's 13th Renewable Energy Development Five Year Plan pledges a 15 % share of non-fossil energy by 2020 [16] and Australia's Renewable Energy Target of 33000 GWh large-scale renewable energy installation will account for about 23.5 % of its consumption by 2020 [17].

In Europe, the European Council has adopted in 2008 the first climate and energy package which sets out the compulsory targets of attaining 20 % share of renewable energy for final energy consumption, 20 % greenhouse gas emissions reductions (compared to the 1990 level) and a 20 % improvement in energy efficiency by 2020 [18]. By reflecting the

---

[1] The Organization for Economic Cooperation and Development (OECD) is a forum of 35 countries including most of economically developed countries. See [15] for the list of OECD member countries.

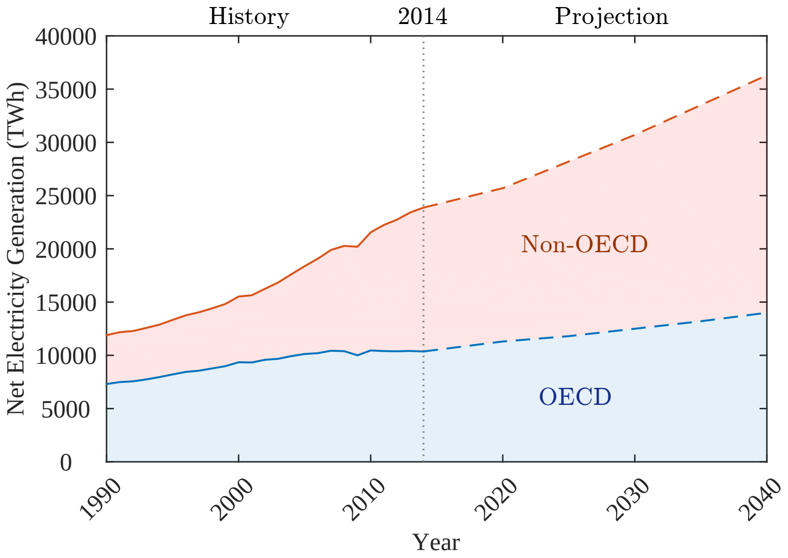

Note: This graph is made by the author from the information open to the public as of June 2017.

Figure 1.1: OECD and non-OECD net electricity generation, 1990-2040 [1][2][3].

current developments, a new policy framework for the period between 2020 and 2030 was agreed in 2014 [19]. The European Union and its member states are firmly on course to meet those targets [20], and now they are increasing the solidarity to achieve the more ambitious long-term goals of 80 $\sim$ 95 % abatement of greenhouse gas emissions by 2050 [21].

Promoted by those initiatives, renewable energy has grown at an astonishing speed in Europe. It accounted for 77 % of the newly introduced generation capacity from 2007 to 2015 [22]. Nevertheless, there still remain many issues which obstruct a further increase of renewable energy. Today's European power systems were mostly developed before the deregulation of the energy sector where the large vertically integrated utilities dominated the entire energy supply chain from generation, transmission, distribution to retailing. The transmission systems were historically developed in the way preferred by the utilities. Reflecting their long-term forecasts of the electric consumption growth, investment was made from the perspective of the whole energy supply chain. The generation plants were mostly built near high electricity consumption areas or the locations where resources are easily accessible. Then the transmission grids were developed to link the consumption areas and the utility-owned power plants. In upcoming decades, much of the fossil-fuel based power plants in generation fleets are foreseen to be replaced by the renewables which are not involved in the original planning of the transmission grid design [23]. Since they are most likely located differently and often far from the center of electricity consumption, unanticipated directions and amounts of power flow can impose stress on the transmission grid. Moreover, the inherent volatility of the renewable energy sources disrupts the traditional way of power system operation which is based on approximately

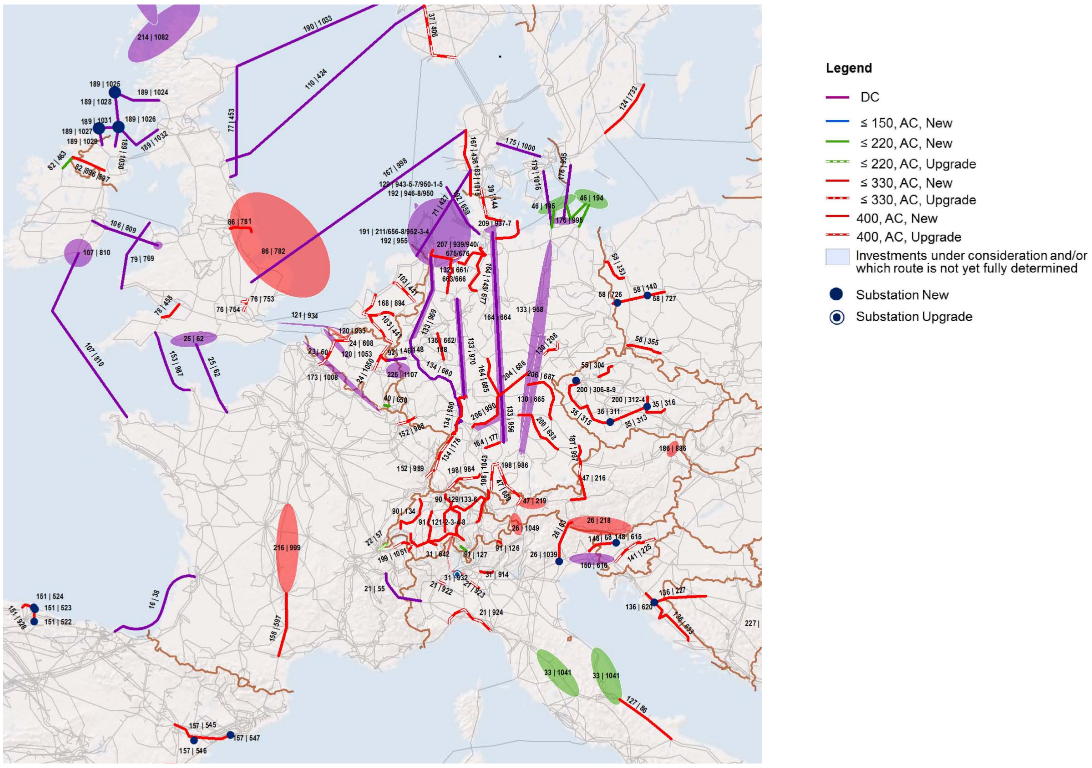

Figure 1.2: Pan-European significance investments – long-term horizon (beyond 2019) [4].

predictable demand and fully controllable generators. As a consequence, those renewable energy resources drive the existing electric power transmission systems close to their physical limits.

The need for enhancing the existing transmission systems is more pronounced than ever. The European Network of Transmission System Operators for Electricity (ENTSO-E) explored the community-wide Ten-Year Network Development Plan (TYNDP) to provide viable future scenarios of power system development for a long planning horizon [24]. This reported the needs for the significant investment to reinforce the existing transmission grid infrastructure (see Fig. 1.2). Developments of transmission corridors that bridge the regions with high-potential renewable resources (hydro in Scandinavia, wind in the North Sea and the Atlantic Ocean, solar in the Mediterranean region, etc.) to the densely populated areas all across the European continent are at stake. Moreover, in line with the Energy Union package targeting 15 % of interconnection capacity by 2030 [25], significant increase of interconnection capacities with neighboring countries are expected not only to avoid spillage of the renewable energies but also to improve security and reliability of the power supply by handling their high variation.

## 1.2 Incentives for HVDC Transmission

The first electric power system was a DC system pioneered by Thomas Alva Edison in the late 1880's. The subsequent power systems were constructed continuously afterwards until Nikola Tesla advocated AC technology. Due to a number of advantages, such as the ease of stepping up and down voltage levels to reduce the transmission losses in distant power transmission, the facility to interrupt fault currents, the widespread use of induction motor, AC systems prevailed in this battle, the so-called *war of current*, and eventually became the standard for bulk power transmission across the world, while DC ebbed away from the main stream of electric power systems.

However, since the late 20th century, DC transmission regained worldwide attention driven by the dramatic change in the outlook of the energy sector and remarkable advancement in power electronics technology [26]. Much attention is focused on its advantages over AC as it possesses necessary features to cope with the high penetration of renewable energy.

Wind energy is considered as a keystone in the policy of the European countries to reach their renewable energy integration targets. Due to the social acceptability regarding the visual, noise, and vibration impacts which restrict the potential sites for the onshore wind farms, offshore wind energy is considered as the attractive resources in Europe and promised to increase in the next decades [27]. WindEurope (former European Wind Energy Association (EWEA)) reported in [28] that the potential wind energy resource in Europe is substantial and can even meet all the electricity demand in Europe. However, integration of the abundant offshore wind energy poses new technical challenges. Offshore wind farms are most probably located far away from the electric coupling point of the onshore grid. The longer the distance of the power transfer in HVAC transmission system, the larger the generation of the reactive power by the submarine cables which occupies the total power capacity [29][30]. This makes offshore wind energy virtually inaccessible by the conventional HVAC technology beyond 100 km. HVDC transmission is recognized as a solution to this problem because such limitation does no longer exist.

Investment for long distance transmission is often discussed with the concept of the so-called "break-even distance" [31]. Fig. 1.3 shows a graphic representation of the relative costs of HVDC and HVAC systems over distance. The DC cost curve is not as steep as the AC cost curve because of lower losses (no skin effect, no proximity effect) and absence of reactive power compensation devices. The typical break-even distance amounts to less than 50 km for cable transmission [32]. Hence, for such long-distance power transmission, HVDC technology appears as a better economic solution over conventionally used HVAC transmission [33].

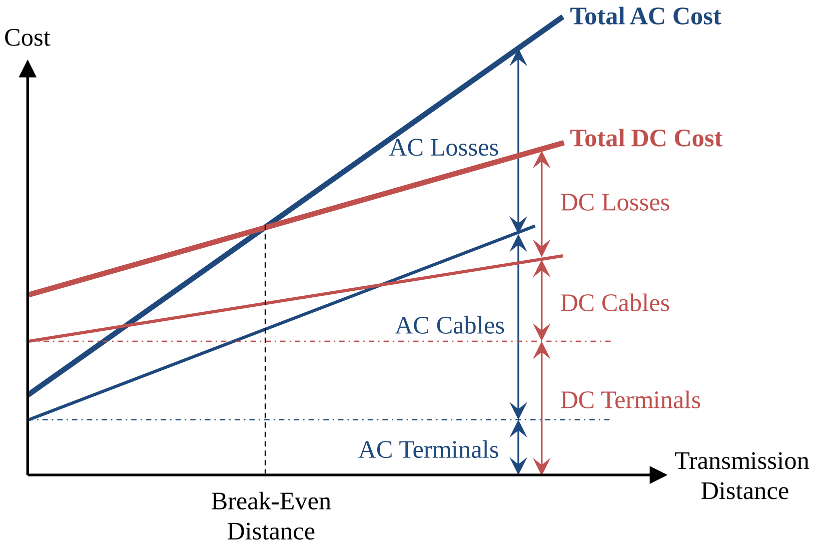

Figure 1.3: AC versus DC transmission [5].

In order to accommodate the large amount of renewable energy, enhancing the existing HVAC grids is an issue. Upgrading of the existing grids is possible by strengthening the existing paths or developing other paths. For the former case, increasing the voltage rating is a common solution. However, this is only possible if the existing infrastructure were designed taking into account such an upgrade. For the latter solution, building new overhead HVAC lines is extremely difficult in Europe because of the limited available space and public opposition which can significantly increase the construction period [34]. A feasible solution to overcome the shortage of the transmission capacity is to convert existing AC lines to DC lines [35]. In its simplest form, the transmission capacity for the same line-to-ground voltage can be increased by a factor of $\sqrt{2}$. According to [36][37], converting parallel three-phase AC circuits into three bi-pole HVDC networks can increase by 2 to 3 times the power capacity using the existing infrastructure asset.

Overlaying HVDC system onto the existing AC grid forms AC/DC hybrid grid. It can offer another benefit to the power system in terms of stability. With the latest technology of self-commutated Voltage Source Converters (VSCs), an HVDC transmission system can be much more flexible. Its independent controllability of active and reactive power allows efficient support of the voltage stability of the AC system in steady state and also during transients. Moreover, it is an useful way to control the power flow of the system. The recent deployment of the new France-Spain HVDC interconnection called INELFE (INterconexión ELéctrica Francia-España) link is expected to greatly improve the power exchange in congested areas, contribute to the security of the power supply and accomplish better integration of the electricity markets of those countries [38].

Another application of HVDC can be found in interconnection of two different synchronous systems, such as the France-United Kingdom submarine cable interconnection [39]. Due to the asynchronous nature of its connection, HVDC serves as firewall when encountering a disturbance on the one side, which is not possible by AC links [40].

## 1.3 Evolution in Power Electronics

HVDC technology has made remarkable progress along with the notable technological innovations of converters. Fig. 1.4 briefly introduces important milestones of the development of HVDC technology. The world's first commercial application of HVDC transmission was the Gotland HVDC link built in 1954 [41]. The AC/DC conversion system was based on mercury-arc valves and had a power rating of 20 MW with ±100 kV [42]. It was followed by a number of large HVDC projects around the world. In less than two decades, the advent of the solid-state semiconductor valves took over from the mercury-arc valves. In 1967, as a world pioneering project, one of the mercury-arc valve based converters in the Gotland transmission system was replaced by a thyristor valve [43]. Its higher reliability, smaller size and lower environmental risk over mercury-arc converter made the thyristor based converter a commercially attractive option, and eventually it made mercury-arc converter virtually extinct [44]. Both mercury-arc and thyristor based converters are categorized as *Line-Commutated Current Source Converters* (CSC or LCC). The name comes from its fundamental property that the commutation within the converter is driven by the AC grid line voltage and that the associated inductance on the DC side acts as an energy source that provides constant current. Such systems have inherent restrictions for their application, such as the requirement of being connected to a relatively strong AC system. Nevertheless, owing to the advancement of thyristor technology in terms of current rating, cost and reliability, CSC has become a mature technology and is widely used primarily for large-power HVDC transmission over very long distances all over the world [45][46].

The emergence of the Insulated-Gate Bipolar Transistor (IGBT) in the late 20th century made another converter type the so-called *Self-Commutated Voltage Source Converter* (VSC) attractive for HVDC transmission. Its first commercial application was again in Gotland [47]. The operation principle of VSC is quite distinct from that of CSC. Instead of the inductance, a VSC has a capacitor which appears as a constant voltage source on a DC side. By commutating the IGBTs at a very fast rate, the VSC can feed a quasi-sinusoidal voltage with significantly lower harmonics compared to the CSC technology. The VSC no longer needs to be connected to a strong AC grid, and it can even be connected to an AC system with no local generation [48]. In addition, the VSC provides significant control flexibility that has effectively overcome some existing defects of CSC.

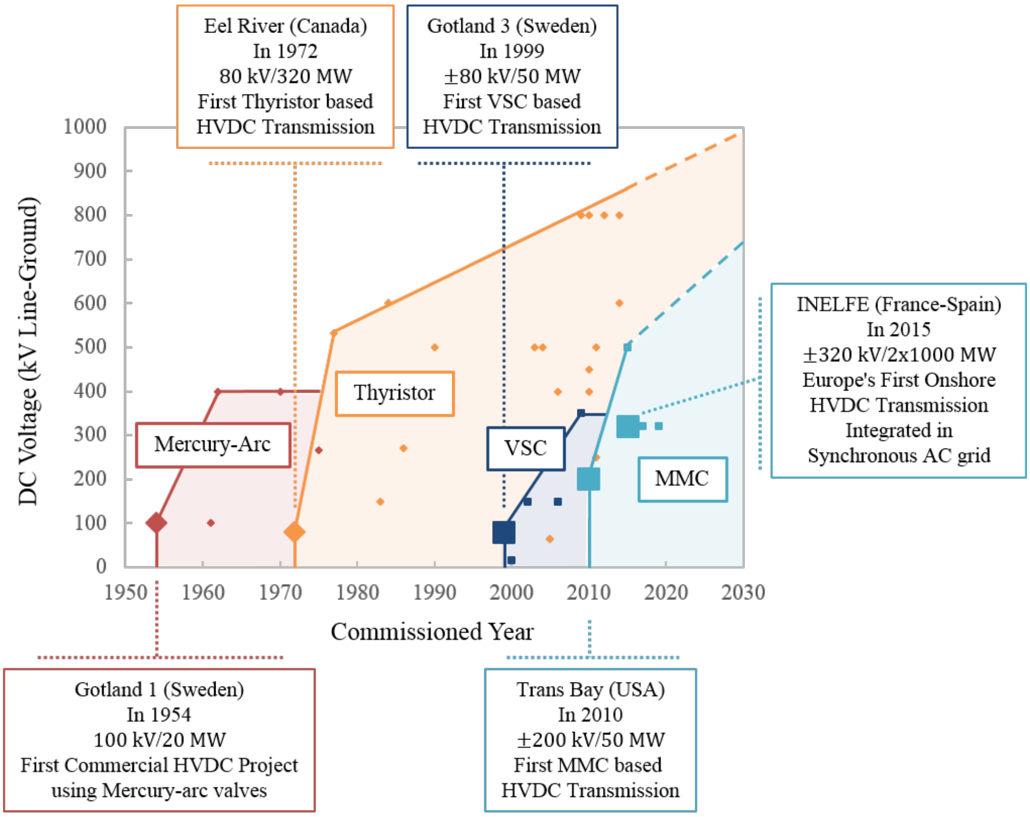

Note: This figure is made by the author from the information open to the public as of June 2017.
However, some differences or unintentional omissions could be possible.

Figure 1.4: Important milestones of the development of HVDC technology.

The recent development in the field of VSC technology focuses on the state-of-the-art topology called the *Modular Multilevel Converter* (MMC) invented by Prof. Marquardt [49]. It was an important milestone of the history of HVDC technology. Its innovative design offers many technical and economical advantages. Thanks to its modular structure, the MMC enjoys significantly higher reliability, wider range of applications, better power quality and efficiency over the classical two-level VSC topology [50]. The topology of the MMC also brings the great advantage of scalability. Higher voltage ratings can be easily achieved by increasing the number of stacked sub-modules, which makes it suitable for HVDC applications [51]. In addition, as less harmonics are produced by the MMC, the installation of large filters is no longer needed; therefore, the overall footprint of the station becomes significantly smaller which makes it suitable for an offshore wind farm station. For those reasons, the MMC is considered as the most promising converter topology that will play an essential role in the future electric power systems. However, for all its desirable features, there are some open problems. Due to its complex circuit topology and the large number of control variables, the complexity of its control system significantly increases, which entails difficulties in the control design. Thus, further understanding of its complex topology and development of elaborated control system are expected.

## 1.4 Multi-Terminal DC Grid as Supergrid

HVDC transmission is considered as the most promising and technically feasible solution for the fundamental upgrade of the existing AC transmission system in many cases. In line with the growing number of HVDC applications, the concept of connecting several HVDC stations to form a Multi-Terminal DC (MTDC) grid arose and gained great attention of power system engineers and researchers today. The MTDC grid has been intensively studied for the connection of offshore wind farms [52][53], and it is expected to be a solution to improve economic efficiency and provide more flexibility for collecting wind energy [27]. Wind power generation highly depends on the weather conditions. This implies that expensive HVDC infrastructures are probably not utilized at their full capacity all the time. In contrast, if several offshore wind farms are connected to multiple onshore grids via an MTDC grid, the utilization rate of the HVDC infrastructures can be significantly increased because the MTDC grid can serve as additional interconnection paths during low wind power generation [54]. Moreover, the MTDC grid enables transmission even if a certain line is out of service, which can improve the availability and reliability of the system [55].

If the number of connection points increases, such MTDC grids may evolve into a new bulk power overlay grid, which is known as a “Supergrid” [56]. In Europe, the Supergrid is considered as an attractive solution to accommodate geographically spread renewable energy sources while acquiring further reliability and flexibility [32]. Such a new overlay grid can serve as an additional transmission structure to alleviate the congestion of existing HVAC grids while further integrating electricity markets and increasing the security of the power supply [57]. However, there are a number of remaining challenges to be tackled for the realization of the supergrid. In the following, the major challenges are elaborated [58]:

- Control: For secure operation of the DC system, the DC voltage must be maintained within a certain range just like the frequency in an AC system. Thus, the converter control must deal with any power disturbance that causes rise or fall of the DC voltage. The ability to handle disturbances depends on the converter topology, control algorithm and parameters. Even though many studies have already been taken, further exploration is required.
- Interactions with the AC systems: When a converter outage occurs in the DC system, the remaining converter stations must compensate for the deficit of power by abruptly changing their power injections or withdrawals. From the AC systems, this can be seen as a series of contingencies and may trigger a cascading failure. Therefore, special caution must be taken in development of the converter control.

- Protection: When a short-circuit fault occurs in the DC system, the stored energy in the DC system is discharged, and this generates extremely high fault currents. Such fault current can severely damage the semiconductor devices in the converters. Thus, immediate interruption of the fault current and isolation of the fault point are essential.

The development of the Supergrid is foreseen to be gradual, first by interconnecting several existing HVDC systems, and then by incorporating new converter stations [59]. So far, all the HVDC projects have been developed individually to meet the specifications required by TSOs. Their solutions may significantly vary depending on the manufacturers. For the development of the Supergrid, multiple converter stations based on different technologies and control algorithms must work in a cooperative manner. Although there have been several initiatives toward standardization [60][61], there is still no consensus.

## 1.5 Motivation and Outline of the Thesis

The motivation of this thesis reflects two main paradigms: the breakthrough innovation of the MMC and the growing interest in the MTDC grid. The aim of this thesis is to develop a control strategy of MMC-based MTDC grids which brings further stability, security, and efficiency. In order to take full advantage of the MMC-based MTDC grid, this work deals with the control of the system from different perspectives: from the converter level to the grid level. The primary focus is on the control of the MMC itself, especially on what can be brought by its unique topology characterized by distributed energy storage. It is then followed by an analysis on the interaction between the MMC and DC system. The critical parameter that characterizes the DC system dynamics is identified, and the way to improve the dynamic behavior by using the unique characteristic of the MMC is proposed. Finally, the MTDC grid operation and the coordination of the system regulation is investigated.

This thesis is organized as follows:

Chapter 2 first reviews the recent developments of HVDC technology focusing on the two converter technologies, CSC and VSC, outlining their operation principles and technical features. Their advantages and disadvantages are itemized to highlight the technical challenges. Thereafter, a detailed description of the MMC topology and its distinct characteristics are introduced.

Chapter 3 presents the fundamental equations which describe the current dynamics of the MMC. The internal dynamics such as the evolution and distribution of the energy stored inside the MMC is analyzed, and the different control strategies to regulate the internally stored energy are developed.

Chapter 4 provides a thorough analysis on the limitations imposed on the internal energy stored in the MMC. The principal aim of this chapter is to establish the analytic formulas which enable the user to straightforwardly calculate those energy limits based on the operating point. Since the capacitor voltage ripples have a great impact on the energy limits, their behavior is first analyzed, and the analytic expressions which allow precise estimation of the behavior of the voltage ripples are derived. Based on them, the upper and lower limits of the internally stored energy are mathematically formulated. Afterwards, the derived analytic formulas are confirmed by experiments on a small-scale MMC mock-up.

Chapter 5 investigates the way of using the additional degree of freedom of the MMC — the internally stored energy. Firstly, a crucial requirement for the DC systems is identified by establishing the analogy between DC systems and well-known AC systems. It is revealed that, without explicit control, the DC voltage tends to be inherently much more volatile against power disturbances than the frequency of conventional AC systems. In order to solve this problem, this chapter proposes a novel control method, named Virtual Capacitor Control, which enables the utilization of this additional degree of freedom to attenuate voltage fluctuations of DC systems.

Chapter 6 first introduces a general overview of the MTDC grid operation and its control hierarchy. The behavior of a droop-controlled MTDC grid against a sudden disturbance is investigated, and the restrictions in the droop parameters selection are identified. Virtual capacitor control is applied to the MTDC grid, and the advantages brought by this control are demonstrated. Thereafter, the particular issues of the conventional droop approach are investigated. It is revealed that the desired control action may not be taken when the available headroom of the converter station is insufficient. We thus propose a novel voltage droop control structure which permits different actions depending on the sign of DC voltage deviation caused by the disturbance to the system. A method to effectively allocate the reserve capacity taking into account the operating point and the available headroom of each station is developed and discussed.

Chapter 7 draws the major conclusions of the thesis and addresses the direction of the future work.

## 1.6 Main Contributions of the Thesis

The main contributions of this thesis are summarized below:

- Development of a generic energetic model of the MMC
    - A generic energetic model of the three-phase MMC is developed focusing on the dynamics of the energy stored in the six converter arms. Through the mathematical manipulations, the internal dynamics of the MMC are modeled with a tripartite focus: total stored energy, vertical and horizontal dispersion of the energy. This offers a clear insight into the locations, quantities and dynamics of the energy stored in the MMC.
- Development of total energy controllers
    - Two types of controllers to regulate the total energy stored in the MMC are developed: one regulates the energy by power exchange with the AC grid, and the other with the DC grid. Each control can be performed without having any effects on the other side of the grid. By simulations, the inherent ability of the MMC to act as an buffer energy storage is demonstrated.
- Development of the arm energy balancing controllers
    - The controllers for the regulation of the dispersion of the energy between and within the phase legs are developed.
- Derivation of the analytical expressions of the limits imposed on the energy stored in MMC
    - The maximum and minimum allowable levels of the internally stored energy that ensure the security and functionality of the MMC are analyzed and formulated as functions of the operating power and associated grid conditions. The derived formulas are confirmed by experiments on a small-scale MMC mock-up.
- Virtual Capacitor Control
    - A novel control method for the MMC that enables utilization of the energy storage capability of the MMC to mitigate the DC voltage fluctuations by enhancing the equivalent capacitance of the HVDC system is proposed.
    - A methodology to determine the size of the virtual capacitor required to limit the DC voltage variation within a desired level is proposed.

- Sensitivity analysis on the primary voltage control parameter in MTDC grid
  - The influence of the droop parameters on the static and dynamic behavior of the MTDC grid is analyzed.
- Identification of the limitations on the conventional droop approach
  - It is revealed by means of a comprehensive analysis, that the conventional droop approach cannot ensure securing the voltage within the desired range when the available headrooms of the converter stations are insufficient.
- Proposition of the Variable Voltage Droop Control
  - A novel methodology of primary voltage control that enables efficient allocation of the reserve capacity to the individual stations, according to their available headroom capacities, is proposed.

## 1.7 List of Publications

## Patents

1. K. Shinoda, A. Benchaib, X. Guillaud, and J. Dai, “Virtual capacitance,” WO Patent 2017021642, August 3, 2015.
2. K. Shinoda, A. Benchaib, X. Guillaud, and J. Dai, “Module for controlling the internal energy of a converter”, WO Patent 2018007741, July 5 2016.
3. K. Shinoda, A. Benchaib, X. Guillaud, and J. Dai, “Convertisseur muni d’un module de gestion de l’énergie en partie alternative,” WO Patent Application, July 7, 2017.
4. K. Shinoda, A. Benchaib, X. Guillaud, and J. Dai, “Centralized MTDC grid controller with variable droop selection algorithm”, Patent Application, 2017.
5. A. Bertinato, B. Luscan, A. Benchaib, K. Shinoda, S. Poullain, “Procédé de control d’un réseau haute tension courant continu en cas de défaillance”, WO Patent Application, July 11, 2017

# Journal

1. K. Shinoda, X. Guillaud, S. Bacha, A. Benchaib, B. Francois, "Modelling of a VSC-based multi-terminal HVDC network for dynamic stability analysis", *COMPEL - The international journal for computation and mathematics in electrical and electronic engineering*, Vol. 36 Issue: 1, pp.240-257, 2016.
2. K. Shinoda, A. Benchaib, J. Dai and X. Guillaud, "Virtual Capacitor Control: Mitigation of DC Voltage Fluctuations in MMC-Based HVdc Systems," in *IEEE Transactions on Power Delivery*, vol. 33, no. 1, pp. 455-465, Feb. 2018.

# Conference

1. K. Shinoda, A. Benchaib, J. Dai and X. Guillaud, "Energy control of modular multilevel converter with a novel analytic filter," in *18th European Conference on Power Electronics and Applications (EPE'16 ECCE Europe)*, Karlsruhe, 2016, pp. 1-10.
2. K. Shinoda, J. Freytes, A. Benchaib, J. Dai, H. Saad, and X. Guillaud, “Energy Difference Controllers for MMC without DC Current Perturbation,” in *the 2nd International Conference on HVDC (HVDC2016)*, Shanghai, 2016, pp. 717–722.
3. K. Shinoda, A. Benchaib, J. Dai and X. Guillaud, "DC voltage control of MMC-based HVDC grid with Virtual Capacitor Control," in *19th European Conference on Power Electronics and Applications (EPE'17 ECCE Europe)*, Warsaw, 2017, pp. 1-10.
4. K. Shinoda, A. Benchaib, J. Dai and X. Guillaud, "Analysis of the Lower Limit of Allowable Energy in Modular Multilevel Converters," in *20th European Conference on Power Electronics and Applications (EPE'18 ECCE Europe)*, Riga, 2018, submitted.
5. K. Shinoda, A. Benchaib, J. Dai, and X. Guillaud, “Virtual capacitor for DC grid stability enhancement”, in *Cigré Session*, 2018, accepted.

# Chapter 2

# State of the Art of HVDC Technology

## 2.1 Chapter Introduction

HVDC technology has become a technically and economically attractive option thanks to the remarkable advancement of the power electronics converter technology. The converter technologies used in modern HVDC transmission systems can be classified into two main configurations. The one is the Line-Commutated Current Source Converter (CSC or LCC), which is nowadays a mature technology and widely used for large-power HVDC transmission over very long distance. The other is the IGBT-based Self-Commutated Voltage Source Converter (VSC). Despite the numerous advantages that the VSC technology can offer, its application to HVDC transmission has been limited due to several technical obstacles including its high switching losses and the low blocking voltage capability of IGBTs. The recent development of the Modular Multilevel Converter (MMC) topology greatly extended the application range of the VSC, and it receives growing attention as the most preferable converter topology for future DC grids.

This chapter first reviews the recent development of both CSC and VSC technologies by outlining their operation principles and technical features. Their advantages and disadvantages are highlighted to emphasize the technical challenges to be solved. Thereafter, a detailed description of the MMC topology and its distinct characteristics are introduced. Then the recent research on the modeling approaches and its general control design are discussed.

## 2.2 HVDC Transmission System Configuration

The basic configuration of the HVDC transmission system can be distinguished by their circuit arrangement [62]. A suitable configuration can be selected according to the nature of the project and the location of the converter stations [26]. Fig. 2.1 shows the schematic view of common HVDC system configurations [34]. The following paragraphs describe their features and relative advantages and drawbacks.

**Asymmetric Monopolar Scheme** The asymmetric monopolar scheme with earth return, shown in Fig. 2.1a, is the simplest configuration for long-distance power transmission. The two converters are connected by only one HVDC conductor, i.e. a cable or a line, and the other pole of each station is connected to an earth electrode. The current flows through the conductor and the ground/sea earth return path. Such system is advantageous in respect of the cost, particularly for HVDC cable transmission, because the cost of the HVDC cable often takes a large portion of the overall cost of the project. However, in many cases, the environmental constrains prohibit continuous earth current. When the use of the earth electrodes is not allowed, a dedicated low voltage conductor is installed as shown in Fig. 2.1b.

**Symmetric Monopolar Scheme** The symmetric monopolar scheme, shown in Fig. 2.1c, is an alternative monopole scheme. It consists of two HVDC conductors with the opposite voltage polarity. The earth reference can be provided by a high impedance reactor on the AC side and capacitor's mid-point for the DC side. Thus, no current flow through earth during normal operation. However, it has a higher cost because two fully insulated conductors are needed.

**Bipolar Scheme** The bipolar configuration is a combination of two asymmetric monopole schemes. The mid-point of the two cascaded converter is linked either by electrodes (Fig. 2.1d ) or a dedicated metallic return (Fig. 2.1e). The advantages of the bipolar scheme is the reduced cost and losses due to the shared common return path. Under normal operation, both poles are controlled to transfer equal power. The DC voltages are equal but of opposite polarity so that the magnitude of the DC currents are identical. Therefore, the current flows through the earth or the metallic return is canceled by the two currents in opposite direction. Another advantage is redundancy. When one of the poles is suffering from a fault or is shut down for maintenance, the remaining pole with the return path configures an asymmetric monopole scheme. Thus, it can continue to transfer power at half of the overall transmission capacity or more by using overloading capabilities.

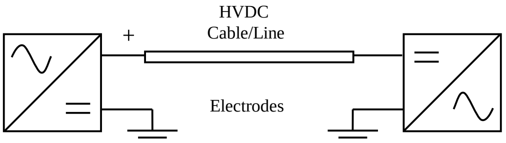

(a) Asymmetric monopolar scheme with earth return

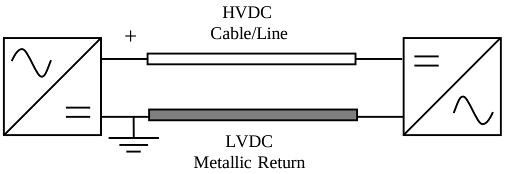

(b) Asymmetric monopolar scheme with metallic return

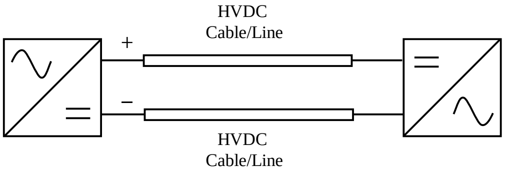

(c) Symmetric monopolar scheme

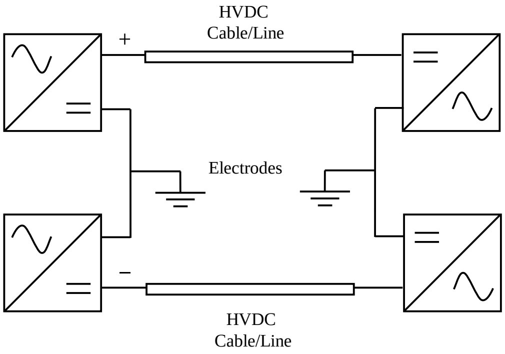

(d) Bipolar scheme with earth return

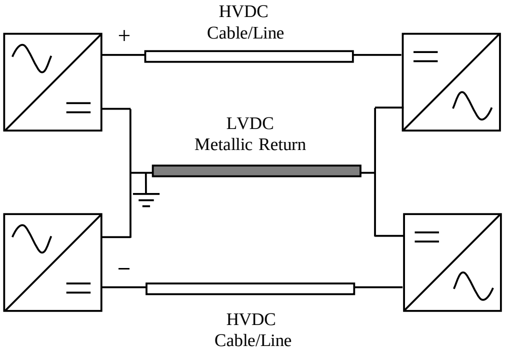

(e) Bipolar scheme with metallic return

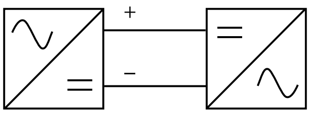

(f) Back-to-back

Figure 2.1: HVDC system configurations.

**Back-to-Back** A schematic view of back-to-back configuration is shown in Fig. 2.1f. In the back-to-back scheme, the two converter stations are located close to each other, often at the same site. This scheme is used to interconnect two AC systems which may have different frequencies .

## 2.3 HVDC Converter Technologies

In this section, the principles of the aforementioned two main converter technologies, the CSC and the VSC, and their primary components are introduced. Their application fields as well as the requirement of peripheral equipment reflect their operation principles. Those are identified and compared to clarify their main advantages and disadvantages.

### 2.3.1 Line-Commutated Current Source Converter

One of the first large HVDC systems based on thyristor valves was a 320 MW back-to-back interconnection built in 1972 [63]. From then down to present, the CSC technology has been extensively used all around the world, and is considered a trusted means of HVDC transmission [64][65].

#### 2.3.1.1 Components of CSC

The thyristor is the key element of CSC. It is a truly bi-stable semiconductor switching device with three-terminals ($A$: Anode, $K$: Cathode, and $G$: Gate) [66]. Its circuit symbol and $IV$ characteristic are shown in Fig. 2.2a and 2.2b. A thyristor consists of four layers alternately doped by $n$-type or $p$-type material, i.e. $p$-$n$-$p$-$n$. The thyristor can block voltage in both the forward and the reverse directions by the reverse-biased $p$-$n$ junctions existing across the device. When the device is forward-biased, it can be triggered into its conduction state by applying a short current pulse to the gate terminal. Once the device conducts, it will remain latched and behaves like a diode, irrespective of the gate voltage. The device will turn off only when the forward current decreases to a threshold level (Holding current: $I_H$) or the forward voltage potential is removed [67].

Because the thyristors can control a large power with a relatively small size, they are found in a wide range of applications. Modern thyristors are available up to a blocking voltage of 8.5 kV and DC current capacity of 5 kA [68]. For HVDC applications, the required voltage level is achieved by a series connection of a sufficient number of thyristors

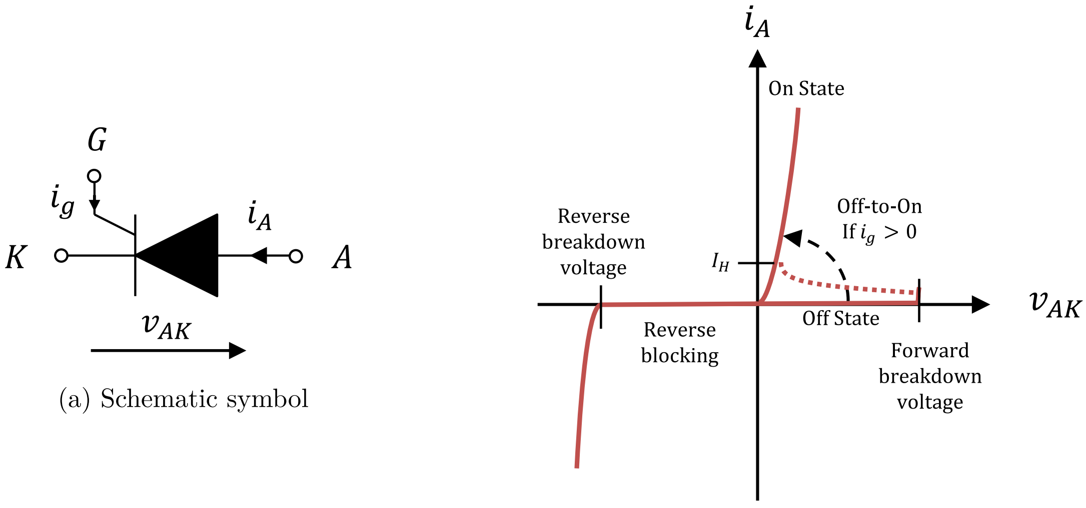

(a) Schematic symbol

(b) $IV$ characteristic

Figure 2.2: Thyristor.

[69]. For this kind of application, the Light-Triggered Thyristor (LTT), which uses light pulse for gate control of the device instead of the electric pulse, offers several advantages. The gating light pulse is transmitted through the optic fiber cables with a shorter gate delay and a very small amount of energy ($\sim$ 40 mW) [5]. Moreover, electrical insulation between the main circuit and the gate control circuit allows better tolerance of noise and higher reliability of operation in high voltage environment.

Fig. 2.3 depicts the general components of a CSC station. Its core element is the full-wave 6-valve circuit shown in Fig. 2.4a. This topology is also universally known as the Graetz bridge. The thyristors are switched on by the gate trigger pulse sent at the appropriate instance in each cycle [70]. The angle between the time at which the valve becomes forward biased and the firing time is referred to as the firing angle $\alpha$. The firing angle changes neither the duration of the periodic current conduction nor its amplitude, but the phase displacement of the current wave. Since $\alpha$ can only be positive, the AC current is always delayed from the AC voltage; that is, the converter inherently consumes reactive power. If the commutation process does not complete before the thyristor becomes reversely biased, this valve will continue to conduct for subsequent cycles and create a short circuit on the DC side. This is referred to as commutation failure and is a common problem of the CSC, particularly for inverter mode. A commutation failure usually occurs due to a fault on the AC side or a sudden increase of DC current. A voltage drop of 0.10 to 0.14 p.u. on the AC side terminal is enough to cause a commutation failure [71]. Once a commutation failure happens, the DC voltage goes to nearly zero and a large current flows into the failed converter. Therefore, the entire system needs to trip, and the power transmission comes to halt for certain duration.

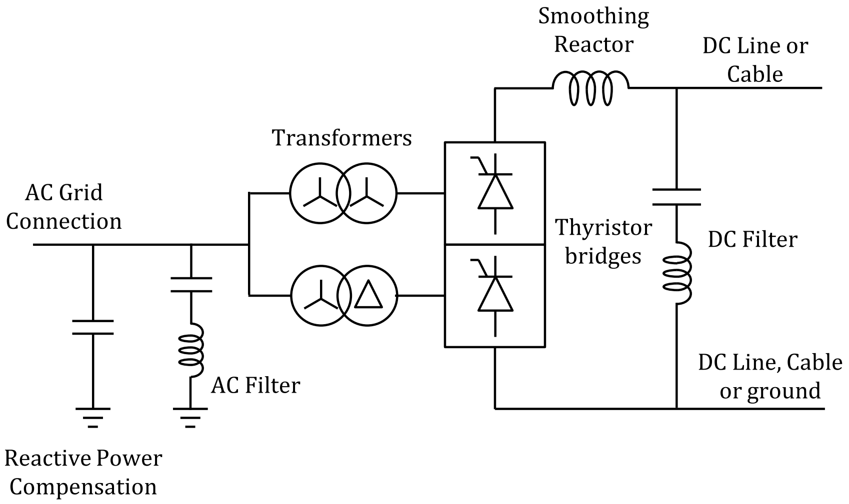

Figure 2.3: CSC converter station [6].

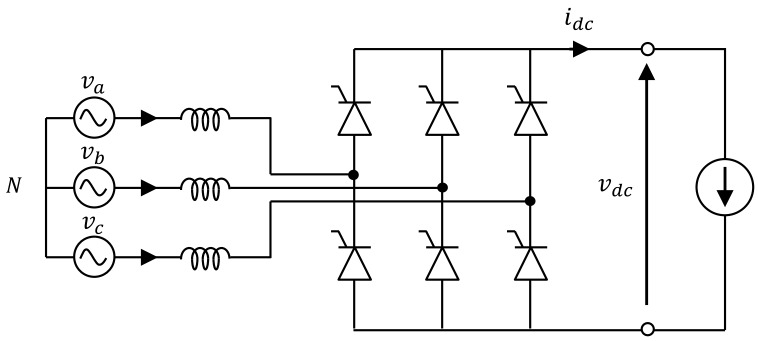

(a) Graetz bridge

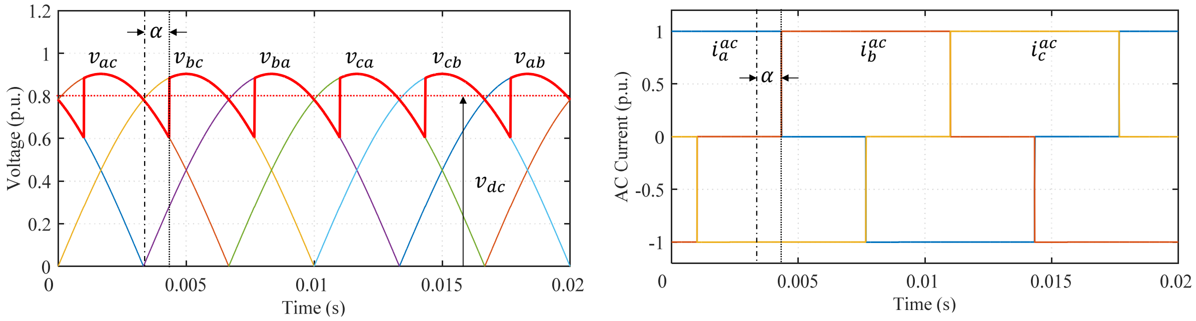

(b) DC voltage waveform

(c) AC current waveform

Figure 2.4: LCC Converter.

To obtain a higher DC voltage, several thyristor bridges can be connected in series. In practice, the 12-pulse arrangement, in which two Graetz bridges are connected in series, is commonly used [72]. On the AC side, the converters are fed from a Y-Y and a Y-$\Delta$ transformers or a single Y-Y-$\Delta$ transformer. Thanks to the 30° phase shift between the bridges, the 5th and 7th harmonics in the AC current are effectively eliminated[1]. On the DC side, the 6th and 18th harmonics on the DC voltage ripple are reduced[2].

In a CSC station, the following components are implemented to ensure its proper operation.

- Harmonic Filters: Due to the blocky shape of the AC current, CSC requires large harmonic filters. Those filters are tuned to provide sufficiently low impedance for the relevant harmonic components.
- Shunt Capacitors: CSC can only operate with the lagging AC current; hence it inherently appears as a reactive load. The absorption of reactive power can be around 50 % of the transferred active power [70]. Thus, shunt capacitors are placed on the AC side of the converter to provide reactive power and to maintain the AC bus voltage within an acceptable range. The shunt capacitors are installed by means of switchable capacitor banks or often integrated into the AC side harmonic filter. For weak AC systems, Static Var Compensators (SVCs), or a STATCOM can be the alternative means for the reactive power compensation. Those harmonic filters and reactive power compensation take up a large space of the station footprint.
- DC Reactor: The smoothing DC reactor plays an important role to reduce DC harmonic currents by acting as a series impedance. This smoothing reactor can also prevent commutation failure in converters and restrain short-circuit currents.

#### 2.3.1.2 Operation principle of CSC-HVDC transmission system

In a CSC-HVDC transmission system, the reactance on the DC side acts as the energy storage element maintaining the current constant. Due to the fundamental property of the thyristor, the valve can conduct only in one direction. Therefore, in the transmission system, the converters on both sides are arranged in opposite directions. The reversal of power direction is accomplished only by changing the polarity of the DC voltage while maintaining the current direction. In general, the rectifier station maintains the constant

---

[1] In general, a CSC with a pulse number of $p$ generates AC current harmonics order of $pk \pm 1$ where $k$ is a positive integer.

[2] On the DC side, $p$-pulse bridge generates multiples of $p$th harmonics.

current while the inverter station regulates the DC voltage. The DC voltage can be controlled by means of the ignition angle [70].

For the operation of CSCs, reasonably strong AC voltage is required to perform thyristor commutation. However, in typical applications of HVDC transmission where power is supplied from a large AC network to a remote area such as a small island load, a stiff AC voltage vector may not be guaranteed. The problems that occur in the operation of the CSC with a week AC grid[3] (e.g. $SCR < 2$) include voltage instability, harmonic resonance and possible commutation failure [73].

### 2.3.2 Self-Commutated Voltage Source Converter

The emergence of Self-Commutated Voltage Source Converters (VSCs) has greatly expanded the application field of HVDC transmission in power systems. Due to the different functionality of the elementary components, the operational principle of the VSC differs from that of the CSC. The VSC can not only overcome the existing limitations of the CSC but also provide greater control flexibility making it especially attractive for certain applications.

#### 2.3.2.1 Components of VSC

The IGBT is the key element of the VSC. The IGBT is also categorized as a bi-stable four layered semiconductor switching device. An equivalent circuit of an IGBT cell can be constructed by combining a power MOSFET for the input driver and a bipolar junction transistor for the output. Thus, it has both the advantage of the high input impedance of the MOSFET and the output conduction characteristic of the bipolar transistor, making it suitable for high voltage applications [67]. Fig. 2.5 shows the device symbol of the IGBT and its $VI$ characteristic. Like the MOSFET, the IGBT is a gate voltage controlled device. When a positive voltage to the emitter potential is applied on the gate terminal, the device turns into the on-state and conducts current. However, whereas the thyristor can only turn on the device and requires voltage reversal and zero current to turn off, the IGBT has self-extinguishing current capability meaning that it can be turned off by reducing the gate voltage to zero. The IGBTs are favored for high voltage applications (>1000 V) and a switching frequency lower than 20 kHz [74]. Unlike the MOSFET, the IGBT is inherently designed to conduct in the forward direction. Due to its asymmetrical structure, a very low on-state voltage drop and high forward blocking voltage are achieved at the expense of reduced reverse blocking capability [75].

---

[3] Short Circuit Ratio (SCR) is a measure that indicates the relative strength of AC systems.

The nominal current rating of the device depends on the power dissipation and temperature rise. To realize a high power IGBT device, there are several packaging technologies, such as the PressPack design or wire-bond type [76]. They are basically constructed by connecting multiple cells in parallel to achieve higher current rating while maintaining better thermal performance. The available high voltage IGBT module's characteristics are summarized in Table 2.1.

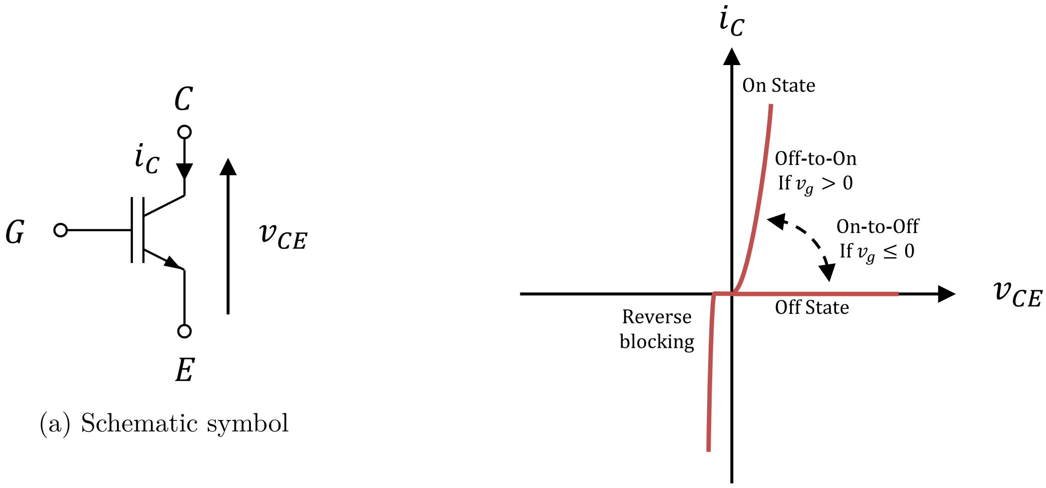

(a) Schematic symbol

(b) *IV* characteristic

Figure 2.5: IGBT.

Table 2.1: IGBT device ratings for high voltage application [10][11].

| Device | Manufacturer | Voltage rating | Nominal current | On-state voltage |
|---|---|---|---|---|
| FZ1500R33HL3 | Infineon | 3.3 kV | 1500.0 A | 2.4 V |
| FZ1200R45HL3 | Infineon | 4.5 kV | 1200.0 A | 2.35 V |
| FZ750R65KE3 | Infineon | 6.5 kV | 750.0 A | 3.0 V |
| 5SNA 1500E330305 | ABB | 3.3 kV | 1500.0 A | 2.5 V |
| 5SNA 1200G450350 | ABB | 4.5 kV | 1200.0 A | 2.6 V |
| 5SNA 1200G450350 | ABB | 6.5 kV | 750.0 A | 2.9 V |

Fig. 2.6 depicts the general components of a VSC converter station. The designation *Voltage Source Converter* is named after the existence of the capacitor connected across the DC terminal which behaves as a voltage source.

Fig. 2.7a shows a schematic view of the simplest VSC converter referred to as a 2-level VSC. The self-commutating capability of the IGBT allows the VSC to output two discrete voltage levels at the AC terminal by commutating the positive and negative potentials of the DC voltage source. By controlling the gate signal sequentially, a high frequency square wave voltage is perceived at the AC terminal. Since the IGBT has only

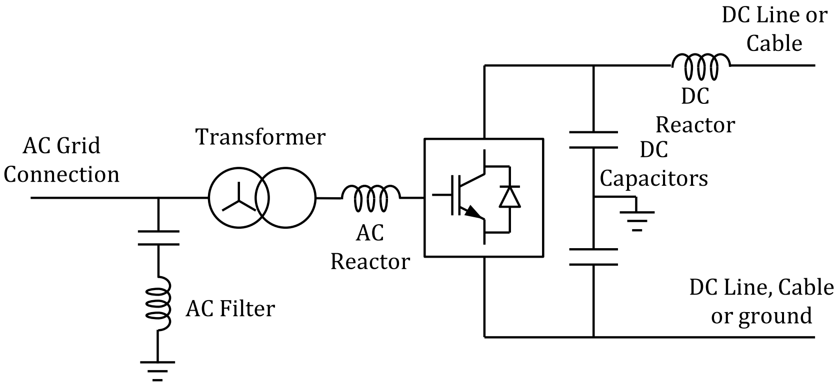

Figure 2.6: VSC converter station [6].

the forward voltage blocking capability, a freewheeling diode in anti-parallel across the IGBT is needed to provide a current path to flow in reverse direction and protect the IGBT against reverse voltage [77].

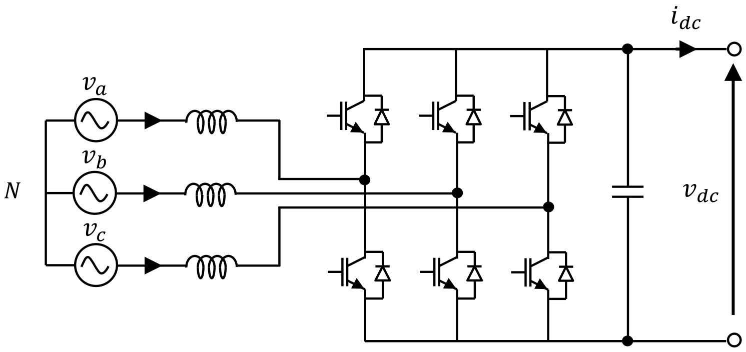

(a) 2-level VSC converter

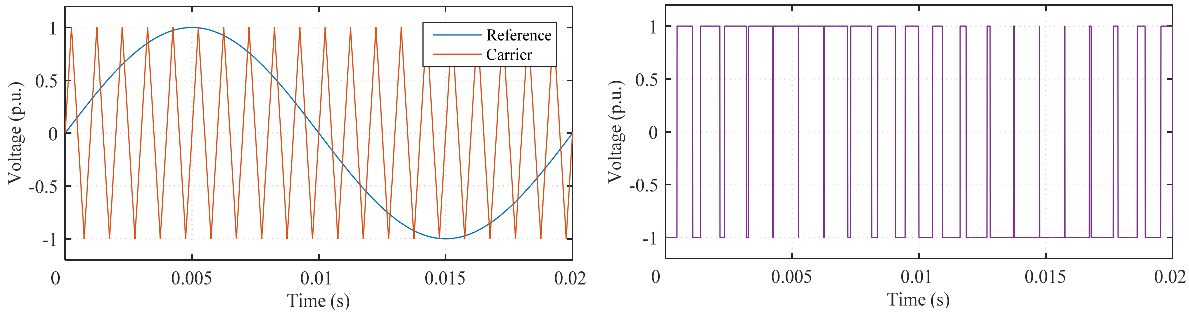

(b) Voltage reference and carrier wave (c) AC voltage output of 2-level VSC with PWM

Figure 2.7: VSC Converter.

The Pulse Width Modulation (PWM) is widely used to modulate VSCs. With PWM, the gate signal is determined by comparing the required AC voltage reference signal and the carrier wave. Commonly a triangular wave signal is used. The generated gate signal can be a square wave with continuous changes in its pulse duration with respect to the required AC voltage as seen in Fig. 2.7b and 2.7c. In this way, the lower harmonics which are seen in CSCs are nearly eliminated. High frequency harmonics filters must be installed on the AC side of the converter. In general, they have a much smaller footprint compared to the harmonic filter needed for CSCs. As a consequence, the overall footprint is much smaller than that of a CSC station of the same rating [73]. To achieve good voltage quality, the VSC valves are typically switched at around 1 to 2 kHz [78]. Such a high switching frequency yields relatively high switching losses.

VSC operation results in harmonic current injection to the DC circuit. The DC capacitor not only provides the DC voltage necessary to operate the VSC, but also plays an important role for harmonic filtering. The harmonic currents cause fluctuation of the voltage across the DC capacitor, which is known as the voltage ripple. The larger the capacitance of the capacitor is, the smaller the voltage ripple becomes. Thus, choosing an appropriate size of the capacitor is important to keep this voltage ripple within a tolerable range [78].

#### 2.3.2.2 Operation principle of VSC-HVDC transmission system

To understand the principle of VSC operation, Fig. 2.8 illustrates a simple circuit diagram of a VSC connected to an AC grid. In the figure, $V_m$ represents the controlled AC voltage at the VSC terminal, and $V_{ac}$ is the AC grid voltage. $X$ represents the equivalent inductance between the VSC and the AC grid which may include the inductance of transformer, harmonic filter, and so on. Here, the resistance is neglected for the sake of simplicity. Taking the $V_{ac}$ as the voltage angle reference, the phasor diagram of the converter output and the voltage drop across the inductance is obtained as shown in Fig. 2.9. The active and reactive powers are thus defined by the well-known following equations:

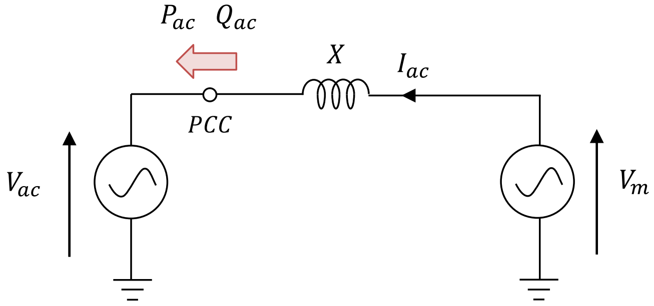

Figure 2.8: Simplified circuit diagram of a VSC connected to AC grid.

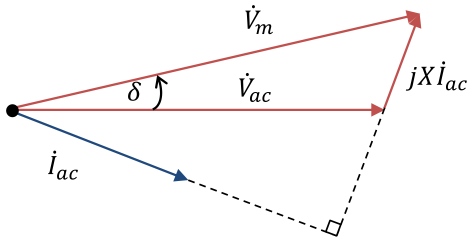

Figure 2.9: Phasor diagram of corresponding circuit.

$$P_{ac} = \frac{V_{ac}V_m \sin\delta}{X} \tag{2.1}$$

$$Q_{ac} = \frac{V_m \cos\delta - V_{ac}}{X} V_{ac} \tag{2.2}$$

where $\delta$ is the angle difference. If $\delta$ is small enough, the equations above can be rewritten as:

$$P_{ac} = \frac{V_{ac}V_m\delta}{X} \tag{2.3}$$

$$Q_{ac} = \frac{(V_m - V_{ac})\, V_{ac}}{X}. \tag{2.4}$$

As can be seen from (2.3) and (2.4), the active power is determined mainly by $\delta$, and the reactive power depends on the voltage difference between $V_m$ and $V_{ac}$. When the VSC voltage leads the AC grid voltage, the VSC injects active power to the AC grid; that is, the VSC operates as an inverter, and the power is withdrawn from the DC grid. The corresponding DC current flows from the other end of the DC grid towards the VSC. If the VSC voltage lags behind that of the AC grid, the VSC withdraws active power from the AC grid, and the same power is injected to the DC grid. Similarly, if the amplitude of the VSC voltage is higher than that of the AC grid, the VSC injects reactive power to the AC grid; hence, it acts as a shunt capacitor. Conversely, if the amplitude of the VSC is smaller, the VSC consumes reactive power as a shunt inductor.

The VSC can generate an AC voltage waveform with desired magnitude and phase angle. Although it is subjected to the constraints imposed by the DC grid voltage and its power rating, the VSC can control the active and reactive powers independently and even simultaneously. In other words, the VSC can be operated within all four quadrants of PQ plane.

In a VSC-HVDC transmission, reversal of power direction is possible without changing the DC voltage polarity. The direction of the current can be changed smoothly through zero while maintaining the DC voltage constant. Since the DC cables are always exposed to the same voltage polarity, excluded cross-linked polyethylene (XLPE) cables can be used. Compared to the classic cables such as mass impregnated (MI) or oil-filled (OF) cables, XLPE has a higher operating temperature, higher mechanical strength and lower environmental risk [77]. Moreover, XLPE cables systems offer easier installation for both land and submarine applications [79].

### 2.3.3 Comparison between VSC and CSC

The VSC technology offers a number of benefits thanks to its high controllability. This subsection provides a summary of the advantages and disadvantages of the VSC technology over CSC.

The major advantages of VSC transmission over CSC are summarized below:

- The VSC can inject or absorb reactive power irrespective of the active power direction. Very fast reactive power control is possible by an appropriate control, which can bring significant benefits to AC grid voltage stability [78].
- The self-commutating ability enables several switching operations during a power frequency cycle. With the PWM at sufficiently high switching frequency, the lower harmonics are eliminated and voltage distortion is significantly reduced.
- Whereas CSC is normally able to operate only with a strong AC grid, the VSC can function with very weak networks.
- There is no need for large reactive power compensation and large low harmonics filters which dictate the large portion of the CSC station site. Thus, the overall footprint of the site is significantly reduced [73].
- The VSC can operate with very small or no current whereas CSC cannot operate at a DC current below a certain threshold.
- In a VSC-HVDC system, the operating voltage polarity is unchanged and independent of the direction of the power flow. This allows the use of the XLPE cables which have a higher temperature, higher mechanical strength and lower environmental risk compared to the classic cables [33].
- In case of total or partial shutdown of the AC system, the VSC-HVDC system can provide active and reactive power dynamically as an ideal standby system to re-energize and stabilize AC system during the restoration process [80].

Although the VSC technology provides many technical advantages, it has not been able to completely replace the contemporary CSC scheme mainly due to the following issues [81]:

- Due to the high switching frequency to reduce harmonics, the VSC inherently has higher switching losses. The typical value of power loss of a 2-level VSC is 1.7 % [73], which is significantly higher than that of the modern CSC (0.7 % [69]). This certainly reduces the economic merit of the VSC-HVDC transmission.
- In general, thyristors have much higher blocking voltage and current ratings compared to IGBTs. Therefore, to achieve higher power rating, the VSC needs more switching devices than the CSC. For high voltage application, IGBTs must be stacked in series, which requires precise control and simultaneous switching of all the stacked IGBT cells to disperse the voltage stress.

To overcome those obstacles, advanced converter topology and switching control techniques have been awaited.

## 2.4 Modular Multilevel Converter (MMC)

The 2-level VSC technology has greatly broadened the application range of HVDC transmission in power systems. However, its high switching losses, voltage stress on the switching device, and high frequency harmonic distortion were still bottlenecks for its high voltage application. To overcome those issues, multilevel VSC converter topologies prevailed in the mid 1990's [7]. Fig. 2.10 illustrates the conceptional scheme of the multilevel converter with different number of levels. The multilevel converter is characterized by having more than two possible voltage levels. The fundamental advantages of the multilevel converter are the reduced harmonic distortion, improved power quality and reduced voltage stress on the semiconductor device [82]. The multilevel converter topology, namely the *Cascaded Full-bridge Inverter*[4] and *Neutral-Point-Clamped Converter* [83], gained great attention and rapidly increased their industrial applications [84]. However, although the technical merits of these multilevel converter topologies are well understood, their applications are limited to Medium Voltage (MV) because of the very high control complexity and quadratic increase of the losses with the voltage level [85].

### 2.4.1 MMC as Multilevel VSC

In 2001, Professor Marquardt from the Universität der Bundeswehr München proposed a new concept of multilevel converter, named the Modular Multilevel Converter (MMC)

---

[4] This technology is also known as H-bridge Inverter because of the appearance of its power module topology. However, in order to avoid misunderstandings with the Half-bridge module, the term Full-bridge is used.

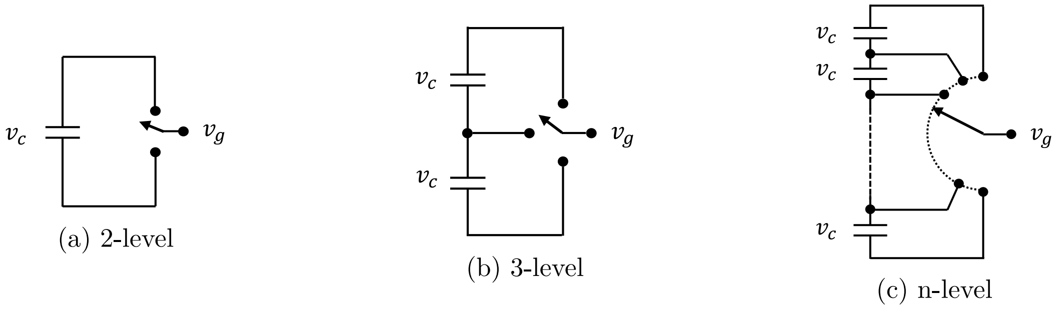

(a) 2-level

(b) 3-level

(c) n-level

Figure 2.10: Concept of multilevel converter [7].

[49]. The emergence of the MMC is an important milestone in the history of HVDC technology. The MMC topology inherits all the advantages of the conventional VSCs such as the flexible power control in four quadrants PQ plane. Furthermore, it overcomes technical obstacles that conventional VSCs have confronted and offers many interesting features.

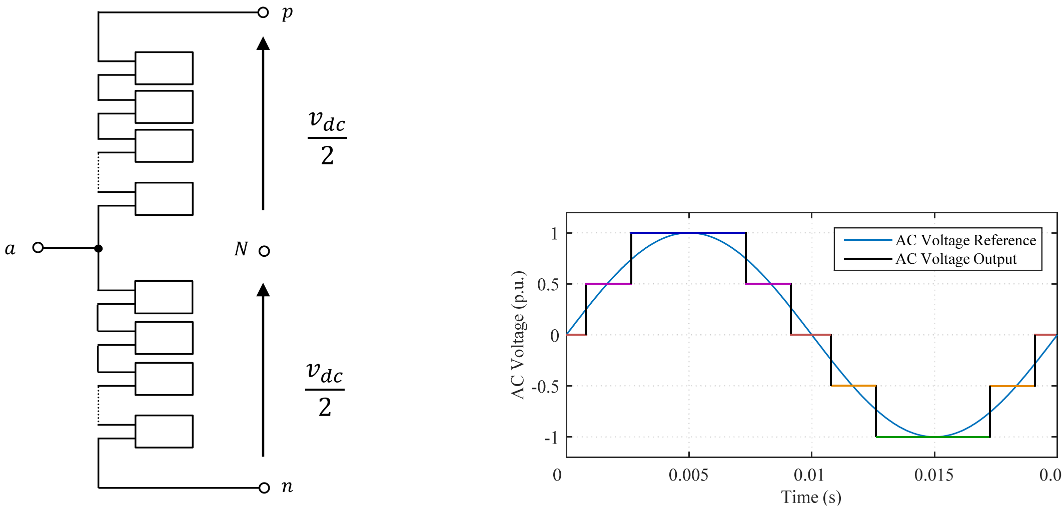

(a) Single-phase MMC topology [49].

(b) Example of AC voltage output waveform of five level MMC.

Figure 2.11: Modular multilevel converter (single-phase).

Fig. 2.11a shows the structure of the MMC proposed for the first time. An MMC consists of a set of identically designed power modules, which are commonly referred to as sub-modules (SMs). There are several SM topologies proposed in literature (see Subsection 2.4.2), but they have in common that each SM has switching devices and a floating DC capacitor acting as a switchable voltage source. By acting on the control signal of these SMs, the voltage of the capacitor can be either inserted or bypassed. Such modular architecture provides great reliability and maintainability. A failure of a SM can be easily handled, and the converter can continue its operation by using the remaining SMs without experiencing any interruption [86]. In terms of structure, a single-phase MMC is divided into an upper and a lower valve, which are referred to as arms. Its

AC output terminal is placed at the middle of the converter branch, and the two other terminals are connected to the positive and negative poles of the DC grid.

The following provides a brief description of its operation principle using a five-level MMC as an example. The AC output voltage level depends on the number of the SMs per arm. With $N$ SMs per arm, $N+1$ level AC voltage output can be obtained. Fig. 2.12 shows five example states of the MMC, each corresponding to a different AC output voltage[5]. The MMC operates using the SMs as voltage sources to synthesize both the DC and AC voltages. The DC voltage is given by the sum of all the SM voltages inserted between the positive and negative DC poles while the AC voltage is synthesized by varying the proportion of the number of the on-state SMs in the respective arms. In Fig. 2.12a, only the SMs in the upper arm are inserted. Therefore, the potential of the AC output terminal is equal to that of the negative pole of the DC bus, i.e. $v_m^{ac} = -v_{dc}/2$. By incrementing the number of the SMs inserted in the lower arm and decrementing that of the upper arm, the AC output terminal potential increases step by step until the case shown in Fig. 2.12e. In this way, the MMC is able to generate a staircase AC voltage output as shown in 2.11b where each voltage step corresponds to that shown in Fig. 2.12. When the number of the SMs is sufficiently large, the MMC can generate a nearly ideal sinusoidal voltage waveform at the AC terminal. This results in significantly smaller harmonic distortion compared to the conventional 2-level VSC [87].

Another important advantage of this topology is the scalability. A higher DC voltage rating can be achieved by simply increasing the number of SMs [88]. Since the voltage across the semiconductor switches is restricted to the SM's capacitor voltage, the voltage stress on the switching devices is drastically reduced. Thus, the MMC is free from the problem of voltage sharing among the series connected semiconductor devices which the conventional VSC converter confronted. Concerning the IGBT switching losses, with MMC, the SMs switch on and off only when the change of the state is requested, whereas conventional VSCs need to switch all the series-connected semiconductors at once. Thus, the switching losses of the MMC is much less significant than that of the conventional VSC technology.

Fig. 2.13 illustrates a general configuration of a three-phase MMC which is customarily used for HVDC applications. From the perspective of the DC grid, the MMC appears as three single-phase MMCs connected in parallel. Each phase generates a desired DC voltage independently. A small difference between those voltages generates balancing currents which circulate from one phase leg to another [89]. In practice, the arm inductors are integrated to attenuate the circulating current to an acceptable level [90]. Those arm inductors are also used to limit the rise of short-circuit current in case of a DC fault.

---

[5] The MMC state shown in Fig. 2.12 are not the unique solution to obtain the desired voltage levels, but we will treat in Subsection 2.5.1 the issue of choosing the SM to be inserted.

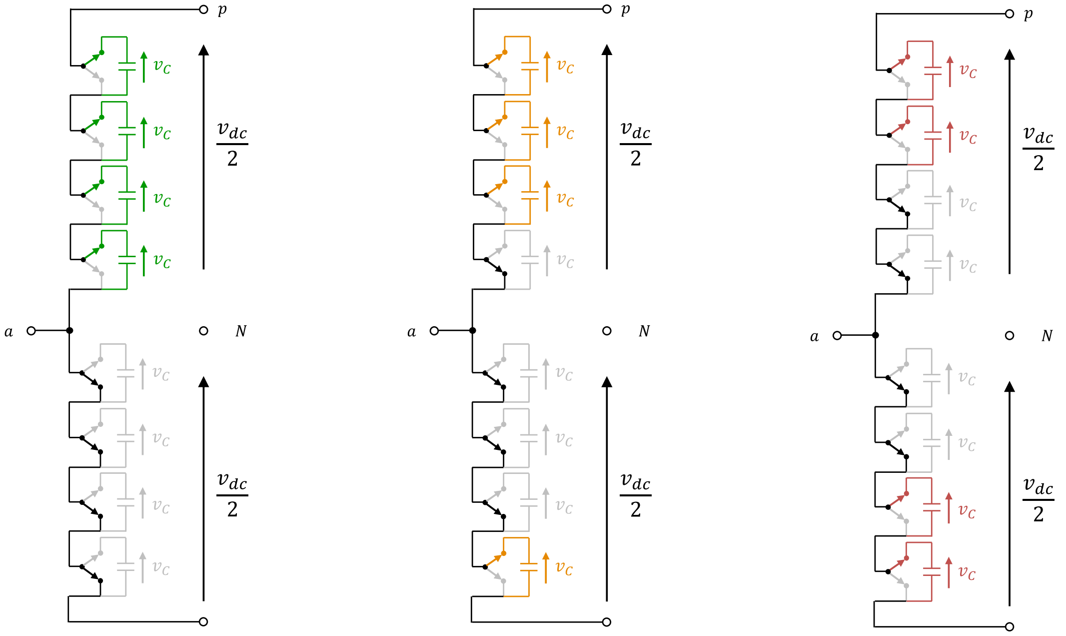

(a) $v_m^{ac} = -\frac{v_{dc}}{2}$ (b) $v_m^{ac} = -\frac{v_{dc}}{4}$ (c) $v_m^{ac} = 0$

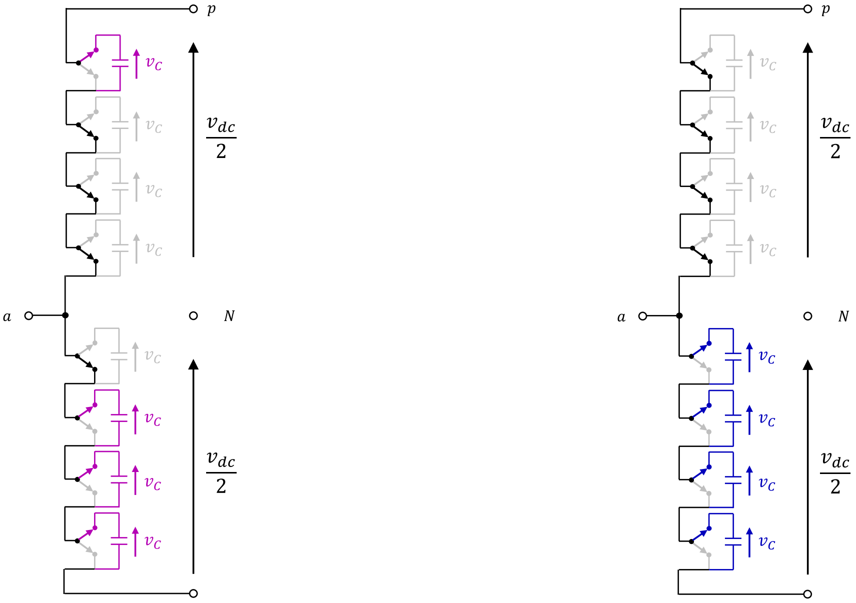

(d) $v_m^{ac} = \frac{v_{dc}}{4}$ (e) $v_m^{ac} = \frac{v_{dc}}{2}$

Figure 2.12: Conceptional picture of operation principle of MMC with four SMs per arm.

For practical application of the MMC in an HVDC transmission system, the number of SMs needed to achieve the required voltage rating becomes quite large. For example, in the INELFE link [38], which consists of two monopolar MMC-based HVDC links with the rated DC voltage of ±320 kV, each MMC arm is composed of over 400 SMs [51].

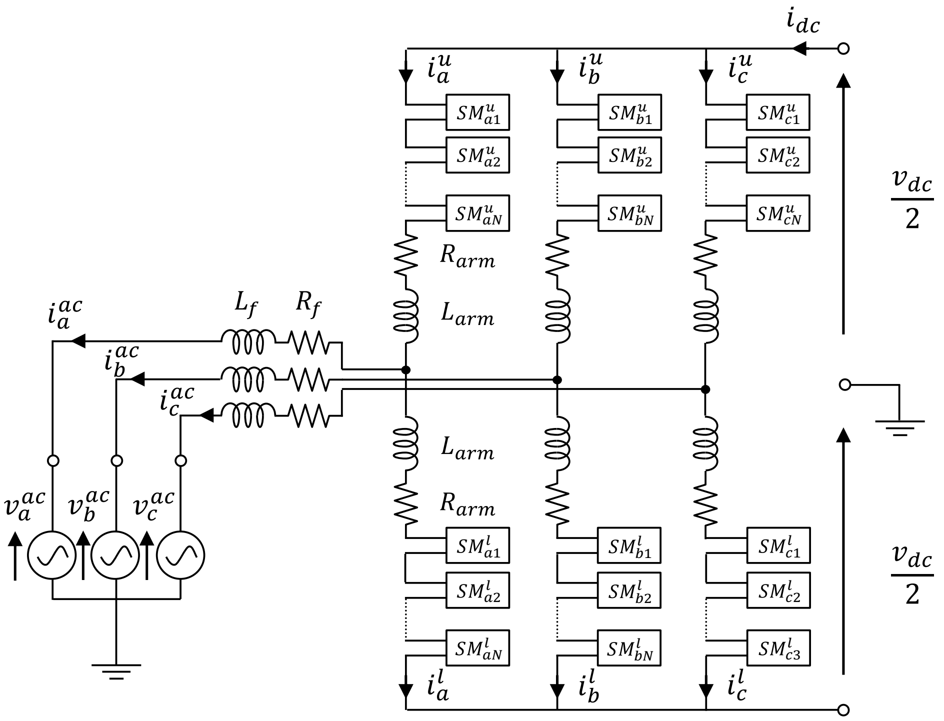

Figure 2.13: Three-phase MMC Topology.

### 2.4.2 MMC Sub-Modules

In the MMC, the SMs are the principal elements that execute the control actions commanded by the converter controller. Several internal structures of the SMs can be applied for the MMC. The following paragraphs provides an overview of the major SM topologies and the control states of the most common SM.

#### 2.4.2.1 Sub-module topologies

There are several SM's topologies commercially available or proposed in literature. The suitable one can be selected according to the losses, the module size, or its relevant characteristic.

(a) Half-bridge (b) Full-bridge

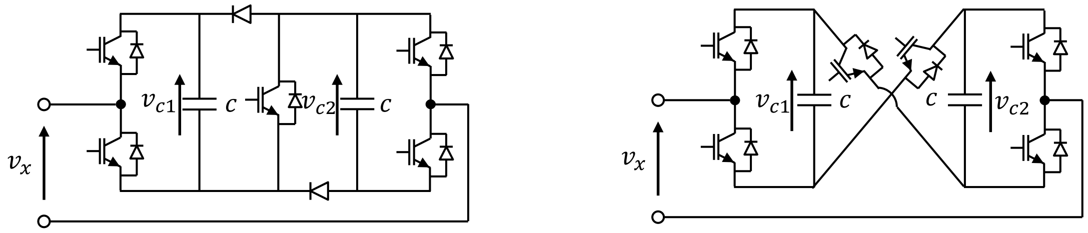

(c) Clamp double (d) Cross-connected half-bridge

Figure 2.14: Sub-module topologies.

**Half-bridge** The most common SM's topology is the half-bridge topology shown in Fig. 2.14a. It consists of only two IGBT switches with anti-parallel diodes and a DC capacitor. The terminal voltage $v_x$ of each sub-module can be either zero or $v_c$; thus, a converter arm equipped with the half-bridge SMs can apply only one voltage polarity. In case of short-circuit fault on DC side, all IGBTs must be blocked to stop feeding fault current, and either a breaker on the AC or DC side must be tripped [91].

**Full-bridge** In the full-bridge topology shown in Fig.2.14b, the terminal voltage can take either a positive or negative value, i.e $\pm v_c$, or zero. Thus, it has the ability to reduce the DC current to zero by imposing the appropriate polarity of the terminal voltage. This fault clearing ability is advantageous especially in case of connection to a weak AC grid because the converter can continue to provide reactive power support as a STATCOM without interruptions [92]. However, compared to the half-bridge topology, the full-bridge SM has twice the number of series connected switches in the normal current path; hence, it features higher losses as well as a higher cost compared to the half-bridge [93].

**Clamp-Double** The clamp-double SM topology, proposed in [87], is shown in Fig. 2.14c. In normal operation, it is equivalent to two series-connected half-bridge SMs. The losses are slightly increased due to the additional switch in the middle. During the fault, it is turned off resulting in energy absorption by the parallel capacitors [94].

**Cross-Connected Half-bridge** The cross-connected half-bridge topology shown in 2.14d consists of two half-bridge cells connected back to back in a crossed fashion [95]. During the fault, the two capacitors can absorb and block the short-circuit current. This topology can generate a full reverse voltage equivalent as the full-bridge topology while having a more compact module size and smaller losses.

Table 2.2: Comparison of features of various SM topologies [12][13][14].

| SM circuit | Voltage level | DC fault handling | Losses |
|---|---|---|---|
| Half-bridge | 0, $v_c$ | No | Low |
| Full-bridge | 0, $\pm v_c$ | Yes | High |
| Clamp-double | $-v_{c1,2}$, 0, $v_{c1,2}$, $v_{c1}+v_{c2}$ | Yes | Medium |
| Cross-connected | 0, $\pm v_{c1,2}$, $\pm(v_{c1}+v_{c2})$ | Yes | Medium |

Table 2.2 provides a comparison of various SMs. For long HVDC transmission with overhead lines, those with fault clearing capability are preferable choices because the system may suffer from frequent disturbance caused by lightning [96]. However, since the number of devices through the current path is closely related to the losses, an MMC based on clamp-double or full-bridge SMs has around 35 and 70 % higher losses compared to the half-bridge topology, respectively [97]. Moreover, those alternative topologies need a significantly larger number of extra semiconductor devices. Thus, they are only used when the requirement of fault clearing ability outweighs the increased capital cost and power losses. Therefore, only the half-bridge topology is considered in this thesis.

#### 2.4.2.2 State and current path of half-bridge sub-module

A half-bridge sub-module topology can take three different conduction states illustrated in Fig. 2.15 [50].

**On-State** When $S1$ is turned on and $S2$ is off, the voltage of the capacitor is applied at the SM's terminal irrespective of the current direction, that is, the SM's voltage is inserted in the converter arm. Depending the direction of the current, the capacitor is charged through the diode $D1$ or discharged through $S1$.

**Off-State** In off-state, $S1$ is turned off and $S2$ is turned on. In this condition, zero voltage appears at the output terminal. The current flows through either $S2$ or $D2$ depending on the direction; thus, the SM is bypassed. Thereby, the capacitor voltage remains unchanged.

**Blocked State** The condition in which both switches are turned off is called the blocked state. The capacitor may be charged when the current flows from DC pole to AC grid. In contrast, when the current flows toward the DC side, the diode $D2$ bypasses the capacitor. In case of a short circuit in DC grid, an excessive current flows toward the point of fault, and thus all the IGBTs turn into blocked state.

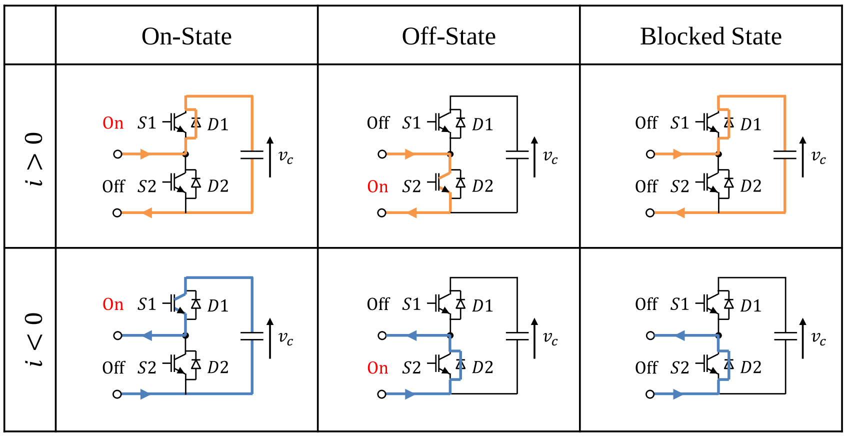

Figure 2.15: Current paths of half-bridge SM.

### 2.4.3 Modeling Approaches of MMC

Electromagnetic-transient (EMT) simulation software is a tool to analyze the power system dynamics. It allows the user to investigate converter behavior during normal or contingency state. It is also useful for development and testing of the converter control design as well as for control parameter tuning. However, the large number of the IGBTs and the cell capacitors in the MMC introduces a great challenge for their implementation in the EMT program. In general, an EMT simulation is based on nodal analysis formulation in which all the network components are given in an admittance matrix [98]. To properly replicate the switching operation of an MMC, the admittance matrix must be altered at every time an IGBT changes its switching state [99], which makes employment of the EMT simulation of an MMC-based system practically impossible [100]. To solve this issue, several modeling approaches of the MMC are proposed [101][102][103][104]. Depending on the degree of simplification, the type of the dynamic phenomena to be obtained by simulations may differ. Therefore, it is important to choose an adequate model according to the type of study and the required level of accuracy. Most of the available MMC models are well documented in [105]. This section briefly introduces the typical MMC models existing in literature. Fig. 2.16 shows the conceptualized diagram of model evolution in terms of complexity in decreasing order. They are first classified by whether the number of the explicit state variables is kept as the real system order or not. Then they are further divided according to the simplification approach.

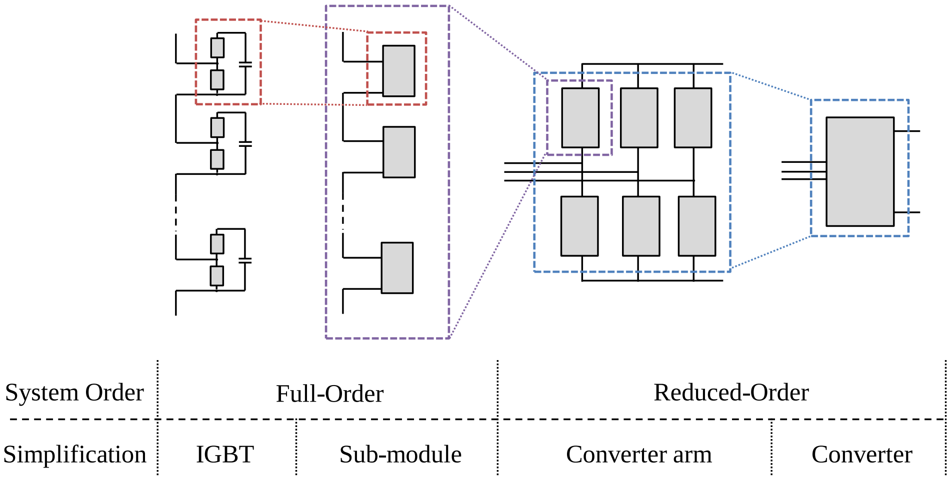

Figure 2.16: MMC model evolution [8].

#### 2.4.3.1 Full-Order Detailed Model

A physical IGBT circuit model presented in [106] is shown in Fig. 2.17 a). In this model, the operating characteristics is kept as close to the real IGBT as possible. However, it is too complex to model the entire converter. The approximated semiconductor model was presented in [51]. This model, shown in Fig. 2.17 b), includes an ideal switch and two diodes, whose *VI* curves are adjusted to replicate the non-linear behavior. This model enables to accurately represent the conduction event and current distribution. It also allows the user to readily implement different SM topologies. However, the introduction of the large number of switches and nonlinear components imposes heavy computational burden.

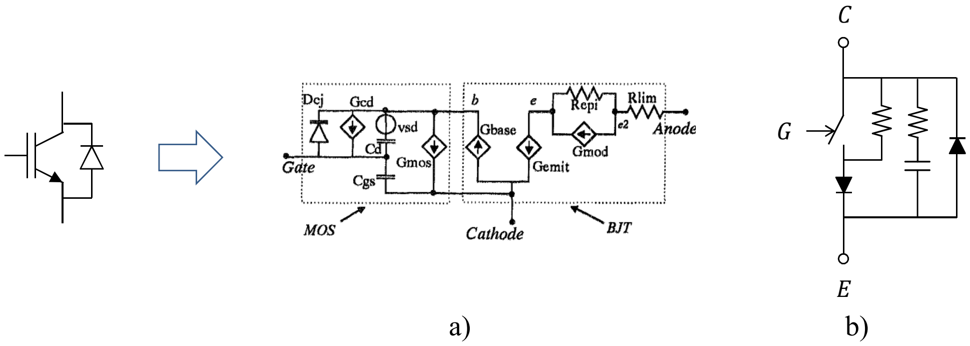

a) b)

Figure 2.17: Examples of IGBT modelling approach.

In order to reduce the computational requirement, further simplification is needed. The traditional approach used for VSC modeling is to represent the IGBT with the anti-parallel diode by a resistor which has two-state resistances: $R_{ON}$ (ON-state $\approx m\Omega$) and $R_{OFF}$ (OFF-state $\approx M\Omega$) [107]. In this way, the SM is represented by the two resistors $R_1$ and $R_2$, which are controlled by the gate signal and the current direction, as shown in Fig. 2.18.

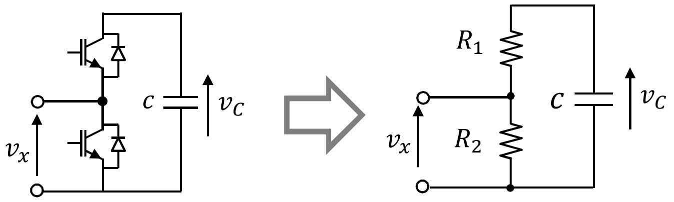

Figure 2.18: Representation of IGBTs in full-order detailed model of MMC.

Using those models enables to replicate the phenomena of the system with good accuracy. However, it necessitates implementing thousands of elements to perform simulations which requires very high computational effort. Therefore, such simulations should be used for testing different SM topologies or as an accurate reference for verifying a further simplified model [108].

#### 2.4.3.2 Full-Order Equivalent Model

In order to reduce computation time, a simplification approach on the SM is proposed in [100]. Using the trapezoidal integration rule, the SM is represented by a Thévenin or Norton equivalent circuit as shown in Fig. 2.19.

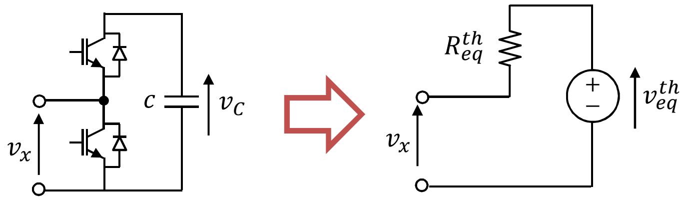

Figure 2.19: Representation of SM in full-order equivalent model of MMC.

When the chain connection of the SMs in an arm is considered, it turns out to be a series connected Thévenin equivalent circuits; thus, all the SMs in a arm can be aggregated into a single Thévenin voltage source and a corresponding resistance. In this way, the order of the nodal admittance matrix is drastically reduced. The equivalent Thévenin voltage source is determined by the individual firing pulses and separately recorded SM's capacitor voltage history, so that the state of individual SMs can be replicated. Therefore, this model is suitable for designing low level control which will be described in the following section.

#### 2.4.3.3 Reduced-Order Arm Average Model

In this model, the IGBTs are not explicitly represented, but only the general behavior of the MMC arm [8]. Let us first assume that the voltages of all the SM's capacitors

$v_{C1...N}$ are identical and that the capacitance of the SMs are sized identically. Then, the sum of all the capacitor voltages in each arm, $v_{C\Sigma}$, is expressed by:

$$\frac{v_{C\Sigma}}{N} = v_{C1} = v_{C2} = \ldots = v_{CN} \tag{2.5}$$

where $N$ represents the total number of SMs in an arm. Under such assumptions, the voltage inserted in the arm $v_m$ is given by:

$$v_m = \frac{n}{N} v_{C\Sigma} \tag{2.6}$$

where $n$ is the number of on-state SMs. Since the current flows through the arm is common for all the active SMs, the evolution of $v_{C\Sigma}$ is derived from the current flows through the arm and the switching state of the SMs:

$$\begin{aligned} C\frac{dv_{C\Sigma}}{dt} &= C\frac{dv_{C1}}{dt} + C\frac{dv_{C2}}{dt} + \ldots + C\frac{dv_{CN}}{dt} \\ &= n\,i \end{aligned} \tag{2.7}$$

Dividing both side of (2.7) by $N$ yields:

$$\frac{C}{N}\frac{dv_{C\Sigma}}{dt} = \frac{n}{N}\,i. \tag{2.8}$$

Equations (2.6) and (2.8) imply that, if the number of the SMs is sufficiently large, the general behavior of all the SMs in the arm can be represented by an ideal DC/DC chopper controlled by the continuous duty cycle $m = n/N$, as shown in Fig. 2.20 [109].

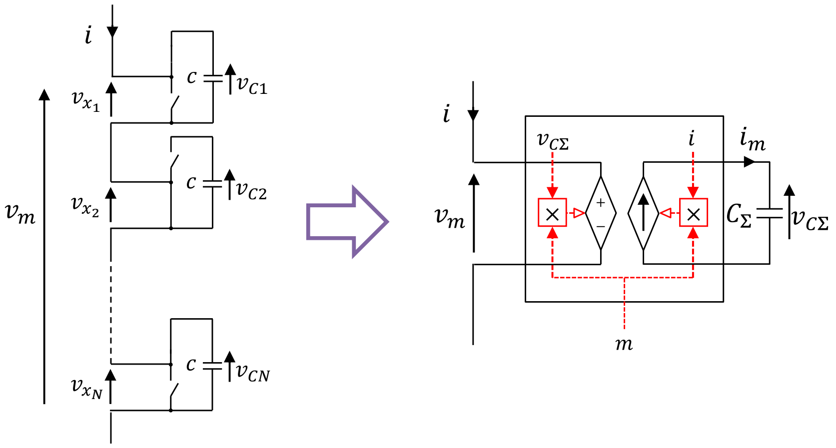

Figure 2.20: Representation of converter arm in reduced-order arm average model of MMC.

The DC/DC chopper is associated with the equivalent capacitor expressed by:

$$C_\Sigma = \frac{C}{N}. \tag{2.9}$$

In this model, all the SM capacitors in an arm are collapsed into a single capacitor; thus, they are no longer distinguishable. However, the energy charging or discharging of each MMC arm is still taken into account. Understandably, the reduction of the number of the state variables in the MMC model drastically contributes to the reduction of computation time [8].

#### 2.4.3.4 Reduced-Order Converter Average Model

In this type of model, the whole converter is simplified concerning only the positive sequence dynamics at the fundamental AC system frequency [110]. Such model is intended for the use in large-scale power system simulations under the phasor approximation [111]. There are several attempts to apply the classical phasor modeling technique for 2-level or 3-level VSCs on the MMC [112][51][113]. However, those approaches tend to neglect the important topological differences between the MMC and the conventional VSCs. In particular, there is a significant difference in terms of the location of the energy storage between them. In literature, the energy stored inside the MMC is often integrated to the DC bus [8][104]. This makes the distribution of the energy among the MMC and the DC grid indistinguishable.

An average MMC model based on a physical analysis, shown in Fig.2.21, is presented in [114]. This model is based on the assumption that the energy in the MMC is evenly distributed among all the converter arms by the local control. Although the distribution of the energy storage among the converter arms are no longer distinguished, this model can well replicate the averaged dynamics of the total energy stored inside the MMC. Therefore, it can be used to study the interactions between the internal energy of the MMC and the connected AC or DC grid.

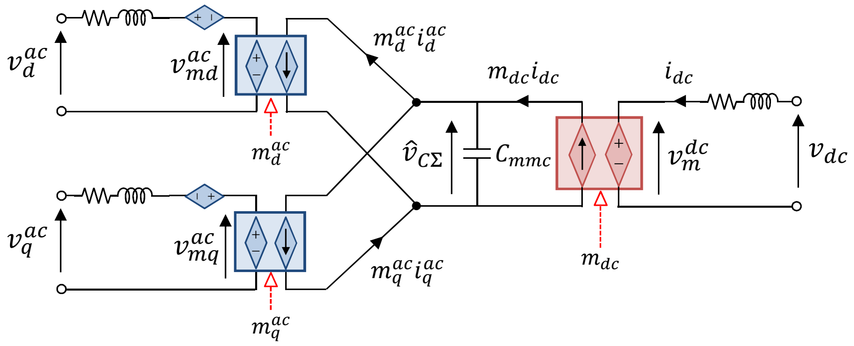

Figure 2.21: Reduced-order converter average model of MMC.

## 2.5 General Control Structure of MMC

In essence, the main objective of the HVDC transmission system is to transmit bulk power from one point to the other. The converter control plays the fundamental role to achieve the desired power flow. In addition, in order to provide stable operation of the system without compromising safety of equipments, additional controls may be required to regulate the DC and AC grid voltages and/or currents depending on the application. However, all the control actions are, in fact, achieved by the gate control of the hundreds of IGBTs. Therefore, it is natural to divide the overall control scheme according to the time scale of the intended dynamic phenomena. Here, the control of the MMC is divided into two main levels: one is called *Low Level Control*, and the other is *High Level Control*. The conceptual picture of the general control structure of the MMC is illustrated in Fig. 2.22. The arm voltage references $v_{mi}^{u,l*}$ are calculated by the high level control, and then converted to the gate signals by the low level control. The roles of those controls are described in the following.

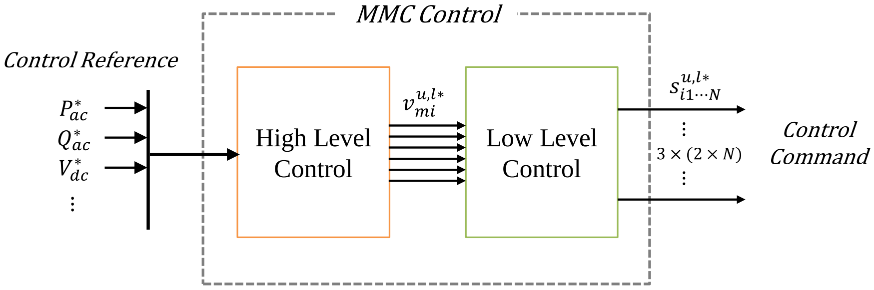

Figure 2.22: General control structure of MMC.

## 2.5.1 Low Level Control

The aim of the low level control is to synthesize the desired voltages in the upper and lower arms by selecting certain SMs to be inserted in each arm. Fig. 2.23 illustrates the general structure of the low level control. In its widely used scheme, the low level control is divided into three stages: *Modulation Index Calculation, Modulation,* and *SM selection.*

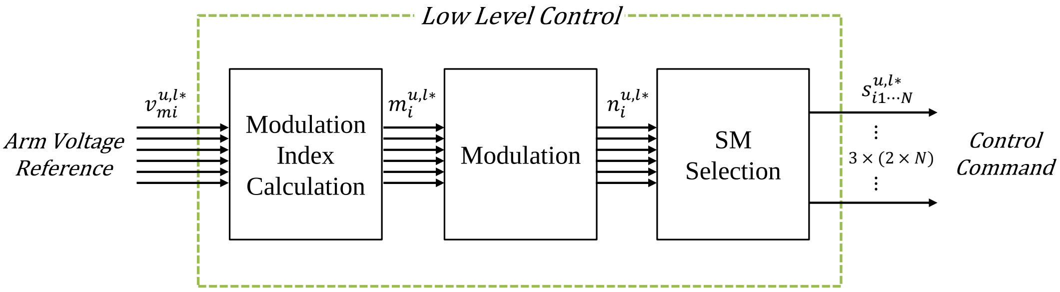

Figure 2.23: Structure of low level control.

### 2.5.1.1 Modulation Index Calculation

The low level control first generates the modulation indices according to the voltage reference provided by the high level control. The modulation index is a signal which is usually defined as the ratio of the output voltage magnitude to the voltage of the voltage source [78]. However, it is important to note that the implication of the modulation indices in the MMC control is not the same as in the conventional VSCs. Unlike the conventional VSC scheme where the DC link capacitor behaves as the voltage source, the MMC operates by using the SM capacitors as the voltage source. Therefore, careful attention must be paid on this stage. Various approaches for the modulation indices calculation can be found in literature [12][115][116]. In general, the modulation indices calculations are expressed by:

$$m_i^{u*} = \frac{v_{mi}^{u*}}{v_s}, \qquad m_i^{l*} = \frac{v_{mi}^{l*}}{v_s}. \tag{2.10}$$

The differences among the existing approaches are thus characterized by the choice of the denominator $v_s$. Each method has its advantages and disadvantages in terms of performance and implementation complexity. In the following, the major approaches are briefly introduced.

**Direct Modulation** This approach is widely seen in literature [111][117][118]. It adapts the method commonly used for the conventional VSCs [119]. The modulation indices are obtained by dividing the arm voltage reference by the DC grid voltage, i.e. $v_s = v_{dc}$. Since the actual output voltages of the MMC are generated by using the SM capacitor voltages, any dynamic or steady-state variations of the capacitor voltage result in degradation of the output voltage waveform. It is known that substantial harmonic components in the converter current can be generated under this approach [109].

**Closed-loop modulation** This approach is based on the actual capacitor voltages available in the converter arm [109]. For the upper arm of phase $i$, the denominator of (2.10) can be given by $v_s = v_{C\Sigma i}^u = \sum_{j=1}^{N} v_{cij}^u$ where $v_{cij}^u$ is the $j$th SM capacitor voltage. This approach reflects the actual voltage insertion process in the MMC. Thus, the voltage insertion can be achieved with good accuracy, and the unwanted harmonic currents can be eliminated. A potential drawback is the implementation complexity which involves the high speed communication necessary to transmit the measured voltages of thousands of SMs in real time. In addition, the measurement noises and delays associated with the SM monitoring may adversely affect the control system. This can be solved by dedicated techniques, such as using the observer based monitoring system proposed in [120].

**Open-loop modulation** An alternative approach is proposed in [121]. In this approach, the modulation indices are calculated based on the estimated arm capacitor voltages $\tilde{v}_{C\Sigma i}^{u,l}$ instead of the actual measurement. The estimations are obtained by solving the equations describing the steady-state behavior of the MMC. The major advantage is the avoidance of the massive amount of communications for the SM monitoring. However, this approach strongly depends on the accurate estimation of the SM capacitor voltage, and thus all the parameters must be precisely known. In addition, the accurate estimation may not be guaranteed during transients.

Based on the above, the closed-loop modulation index calculation is adapted to the control scheme of the MMC in this thesis.

#### 2.5.1.2 Modulation Techniques

Various modulation techniques are developed or adapted for the use in the MMCs. The multi-carrier PWM [117] and the space vector modulation [122] are both well-established modulation techniques and have been applied to the MMC [12][123]. However, they involve high switching frequency and thus introduce high losses. In order to avoid this, a Selective Harmonic Elimination (SHE) method is applied to the MMC in [124]. In this method, the switching patterns are pre-calculated offline to eliminate the low-order harmonics of the output voltage waveform. The SHE method allows very few commutations per cycle, and therefore can achieve better efficiency. On the negative side, the complexity increases as the number of the voltage levels increases. Therefore, in the case of HVDC applications with a large number of SMs, this method becomes impractical.

The modulation technique widely used for the MMC in HVDC application is called Nearest Level Control (NLC) [118][125]. The principle of the NLC is to find the number of the SMs to be switched on in the arm, denoted by $n_i^{u,l*}$, by using $round(x)$ function:

$$n_i^{u,l*} = round\left(N\, m_i^{u,l*}\right). \tag{2.11}$$

In this way, the function returns the nearest integer which corresponds to the number of the SMs to be inserted in the arm.

#### 2.5.1.3 Balancing Control Algorithm

The capacitor voltages of all the SMs must to be maintained withing a certain tolerance band. The SM capacitor may be charged, discharged or remain constant depending on its switching state and the current direction through the capacitor. Therefore, it is necessary to monitor the capacitor voltages and select appropriate SMs at each switching interval.

For this purpose, the so-called Balancing Control Algorithm (BCA) is implemented subsequently to the modulation step. While the NLC only determines the number of SMs to be activated, the BCA takes the role of selection of the individual SMs. There are many BCAs proposed in literature, and they are well documented in [126]. As concluded in [126], the variation of the capacitor voltages and the number of switching operations per cycle are a trade-off. Since every switching operation generates losses, high switching frequency is not preferred in terms of efficiency. Therefore, an appropriate algorithm should be chosen according to the converter specification, acceptable voltage ripple and efficiency requirement.

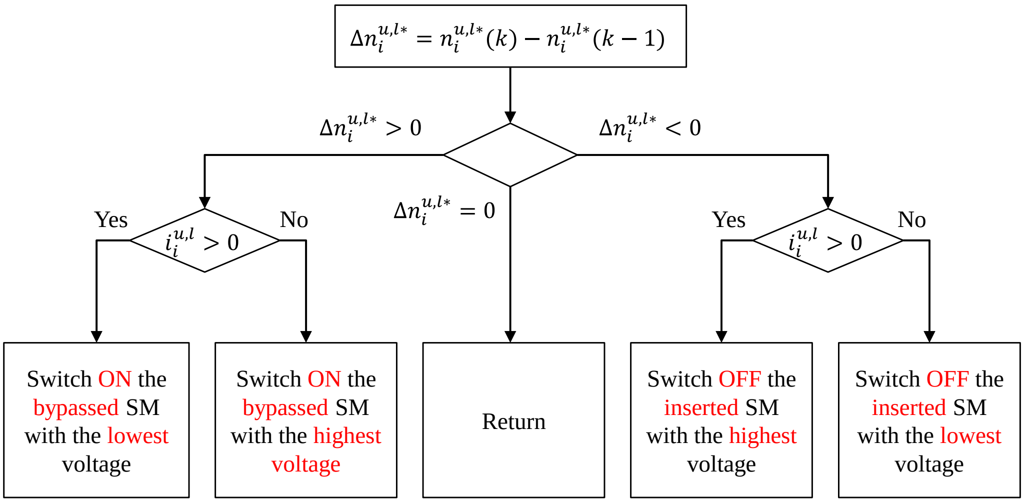

Figure 2.24: Reduced switching frequency BCA flowchart.

Since the detail of the BCA is not the scope of this thesis, only the basic one, called Reduced Switching Frequency algorithm [127], shown in Fig. 2.24, is briefly introduced here. This algorithm is based on the difference between the number of on-state SMs in previous time-point $n_i^{u,l*}(k-1)$ and the new requested number $n_i^{u,l*}(k)$. If an extra SM needs to be activated ($\Delta n_i^{u,l*} > 0$), depending on the current direction, one of the off-state SMs is switched on. In contrast, if one of the SMs needs to be switched off ($\Delta n_i^{u,l*} < 0$), one of those currently in on-state is switched off in accordance with the current direction. In such way, only one (or less if $\Delta n_i^{u,l*} = 0$) SM is switched at each BCA cycle. This results in significant reduction of the switching losses.

### 2.5.2 High Level Control

The high level control aims to provide the arm voltage references to the low level control. The structure of this control layer greatly depends on the application of the converter. For an HVDC application, this control layer must ensure the scheduled power transfer or maintain the DC grid voltage according to the converter control mode.

As the MMC is essentially a kind of VSC, many of the control schemes seen in literature adapted the well-established vector-oriented AC current control technique used for the classical VSCs [128][101]. However, an inconvenience was found in the so-called circulating current. The circulating currents are generated by the voltage inequality among the phase legs. They circulate within the converter in the form of second harmonics and cause large distortions of the capacitor voltages, high power losses and may even lead to instability [129]. These unique phenomenon for the MMC topology have been intensively investigated by researchers [89][111]. In order to control and effectively suppress them, a Circulating Current Suppressing Controller (CCSC) is proposed in [127]. This additional controller extracts the circulating current components and adds up supplemental signals on the voltage references to compensate for the mismatch between the phase leg voltages. Proportional Resonant (PR) control [130] and Repetitive control [131][132] are alternative solutions to eliminate the harmonics.

The root cause of the circulating current is, in fact, that those control schemes which adapt the conventional VSC controls do not fully take into account the topological difference between the MMC and classical VSCs. The complex topology of the MMC with its additional control variables turns out to be a Multi-Input-Multi-Output (MIMO) bilinear system [133]. Several efforts have been made to deal with the strong coupling between the state variables and to achieve desired control objectives [134][135]. Model Predictive Control (MPC) is a suitable and efficient method for handling nonlinear MIMO systems [136]. The applications of the MPC scheme to the MMC have been studied in [137][138][139]. Other control strategies based on nonlinear control theories have been discussed in [140][141].

Despite the numerous publications in this area, most of them tend to focus on the MMC alone rather than considering the MMC as a part of the overall system. This thesis aims to assess the global control of MMC-based DC systems consolidating the distinctive features of the MMC with the DC system dynamics and stability. For this purpose, the aforementioned nonlinear control strategies may not be preferred because they can hide the interaction between the MMC and the DC system and may hinder intuitive comprehension. Therefore, the cascaded control structure, seen in [142] and [143], is adapted in this thesis. The cascaded control structure offers straightforward comprehension of the overall control strategy avoiding misconceptions, and allows ready implementation of additional controllers according to the operation strategy. The high level control is decomposed into two stages as shown in Fig. 2.25: *Inner Control* is designed to achieve fast current control, and *Outer Control* provides current references to the inner control to achieve specific objectives according to the converter operating mode. More details on the high level control will be given in the next chapter.

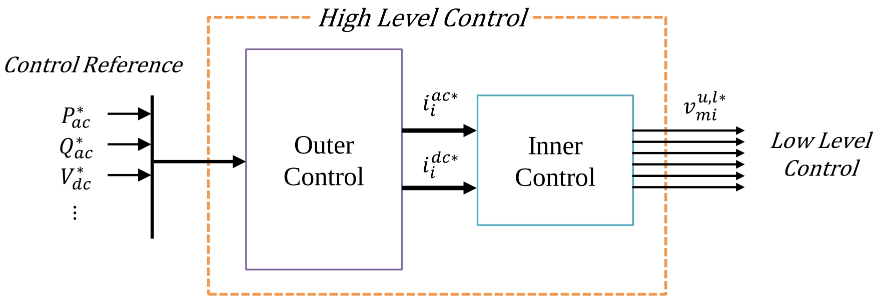

Figure 2.25: General structure of high level control.

## 2.6 Chapter Conclusion

This introductory chapter first reviewed the evolution of the HVDC technology. Along with the remarkable advancement of the power electronic devices, the structure and operational principle of the HVDC converters have changed drastically. Thyristor-based CSC has become a mature technology and has been extensively used to transmit bulk power over long distances. The advent of the IGBT made the VSC topology available for HVDC applications. The VSC technology provides significant advantages over the CSC scheme, such as better control flexibility and the possibility to operate with weak AC systems.

The recent evolution of VSC technology yielded the state-of-the-art topology called MMC. Its modular concept allows a range of voltage level requirements with superior power quality. The fundamentals of the MMC as well as its relevant characteristics were introduced. Its complex structure with distributed energy storage components differentiates the modeling approach and modulation technique as well as the operation principle from that of the classical VSCs. The overview of the recent developments on the MMC control techniques and the general control design strategy were introduced. The following chapter will provide a detailed description of the high level controller design of the MMC and demonstrate its distinct features.

# Chapter 3

# Modeling and Control of MMC

## 3.1 Chapter Introduction

The previous chapter introduced the evolution of the converter technology. HVDC converters are customarily classified into two types: namely, the line-commutated Current Source Converter (CSC) and the self-commutated Voltage Source Converter (VSC). VSCs offer significant advantages over CSCs in terms of control flexibility. However, their high switching losses and voltage stress on the switching device have been the major bottlenecks to expand their application range towards higher voltage and power ratings. The state-of-the-art VSC topology, the Modular Multilevel Converter (MMC) overcomes several obstacles which the classical VSCs confronted, and it is nowadays considered as the most promising converter technology for HVDC applications.

The complex topology of the MMC and its modular structure entail additional control requirements which naturally differentiate the overall controller structure from that of conventional VSCs. As introduced previously, the general controller structure of an MMC is divided into two stages: the Low Level Control and the High Level Control. The low level control aims to synthesize the desired arm voltages by varying the number of on-state sub-modules (SMs) in each arm. The high level control is placed on top of the low level control. It governs mainly the system variables such as power flow at the point of common coupling (PCC), AC and DC grid voltages, etc.

This chapter focuses on the basic controller design of the high level control. As discussed in the previous chapter, the cascaded control structure is adapted throughout this thesis. Fig. 3.1 shows the conceptional image of the global control structure of MMC. In cascaded control, a subordinate controller should have a faster response time than

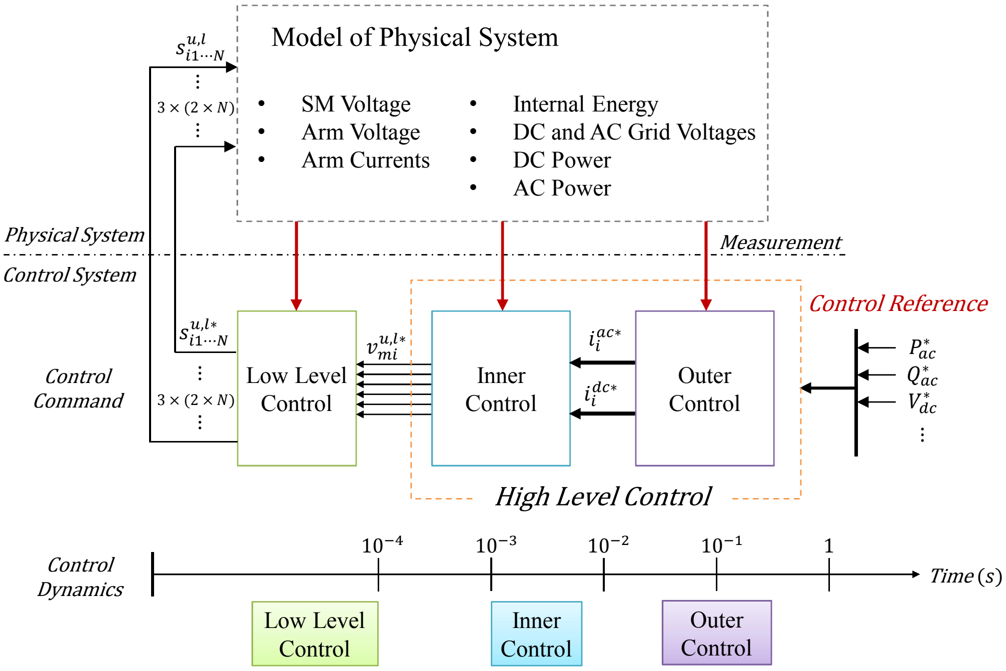

Figure 3.1: Global control structure of MMC with corresponding time constants.

the upper level controller to ensure sufficient time to correct the error before the upper controllers interact undesirably. From the point of view of the upper level controllers, if their response time is sufficiently slower than that of the subordinate controllers, the subordinate control dynamics can be neglected; thus, they can be considered as an unity gain. With this in mind, the high level controllers are developed in order of response time.

This chapter first recalls the fundamental equations which describe the current dynamics of the MMC. The inner control and its control laws are developed by inverting the analytic model of the MMC while keeping the causality relations between the control inputs and the dynamics of the currents to be controlled [144]. The outer control is also discussed in this chapter. The internal dynamics such as the evolution and distribution of the energy stored inside the MMC are analyzed, and the different control strategies to regulate the internally stored energy are discussed.

## 3.2 Dynamic Model of MMC

Fig. 3.2 shows the general configuration of a three-phase MMC. $L_f$ and $R_f$ represent the transformer inductance and resistance. $i_i^u$ and $i_i^l$ are the current through the upper and lower arms, respectively. Each converter arm is composed of $N$ SMs connected in series. The number of SMs must be sufficiently large to achieve the desired voltage rating in an HVDC application. This also allows the MMC to synthesize almost perfect sinusoidal arm voltages.

Since the aim of this chapter is to develop the high level control of the MMC, the dynamics of individual SMs are out of the scope of the concerned time scale. Thus, the reduced-order arm average model representation introduced in previous chapter is considered (see Section 2.4.3.3). Fig. 3.3 shows the reduced-order arm average model of the three-phase MMC. In this model, only the average behavior of each arm is considered, and the dynamics pertinent to the individual SMs are neglected, i.e. it is assumed that the SM voltages are perfectly balanced by an ideal Balancing Control Algorithm (BCA). The SM capacitors in one arm are aggregated into an equivalent capacitor $C_\Sigma = C/N$ whose voltage corresponds to the sum of all the SM capacitor voltages in the arm, denoted by $v_{C\Sigma i}^{u,l}$. In the MMC, the arm voltages are synthesized by using the voltages available in the SMs. The synthesized arm voltage $v_{mi}^u$ and $v_{mi}^l$ and the modulated current $i_{mi}^u$ and $i_{mi}^l$ are expressed by using the continuous modulation indices $m_i^{u,l}$:

$$\begin{aligned} v_{mi}^u &= m_i^u v_{C\Sigma i}^u && (3.1)\\ v_{mi}^l &= m_i^l v_{C\Sigma i}^l && (3.2) \end{aligned}$$

$$\begin{aligned} i_i^u &= \frac{i_{mi}^u}{m_i^u} && (3.3)\\ i_i^l &= \frac{i_{mi}^l}{m_i^l}, && (3.4) \end{aligned}$$

and the evolution of the total capacitor voltages are expressed by:

$$\frac{dv_{C\Sigma i}^u}{dt} = \frac{i_{mi}^u}{C_\Sigma} \qquad (3.5)$$

$$\frac{dv_{C\Sigma i}^l}{dt} = \frac{i_{mi}^l}{C_\Sigma}. \qquad (3.6)$$

In the following, the fundamental equations that describe the current dynamics of the MMC are given. By applying Kirchhoff's voltage law on phase $i$ of the MMC shown in Fig. 3.3, the following two equations are derived:

$$\begin{aligned} \frac{v_{dc}}{2} - v_{mi}^u - L_{arm}\frac{di_i^u}{dt} - R_{arm}i_i^u &= L_f\frac{di_i^u}{dt} - L_f\frac{di_i^l}{dt} + R_f i_i^u - R_f i_i^l + v_i^{ac} && (3.7)\\ -\frac{v_{dc}}{2} + v_{mi}^l + L_{arm}\frac{di_i^l}{dt} + R_{arm}i_i^l &= L_f\frac{di_i^u}{dt} - L_f\frac{di_i^l}{dt} + R_f i_i^u - R_f i_i^l + v_i^{ac}. && (3.8) \end{aligned}$$

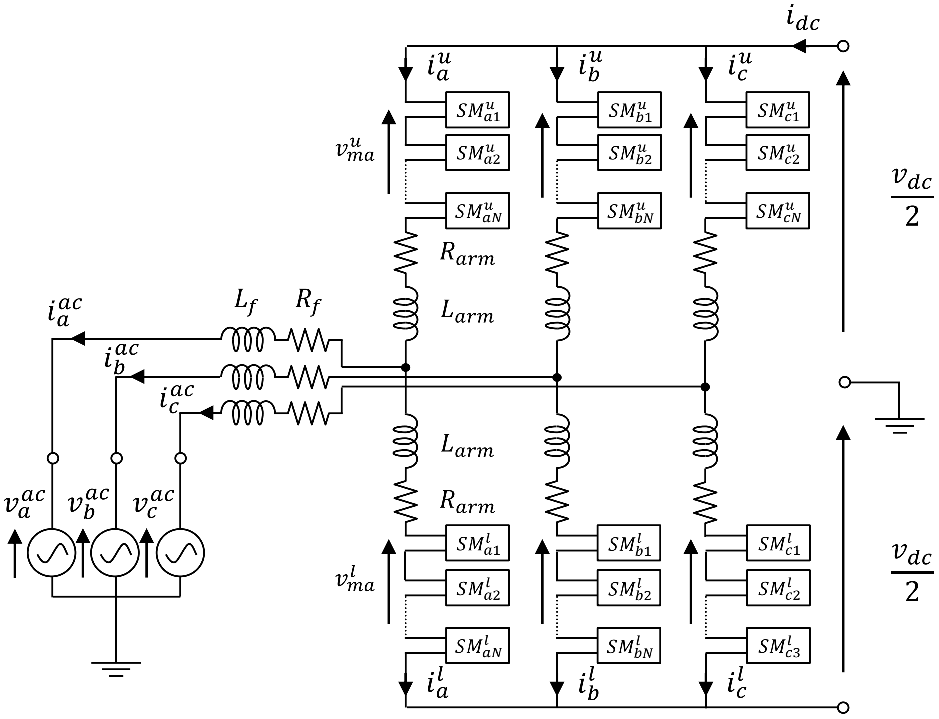

Figure 3.2: Three-phase MMC Topology.

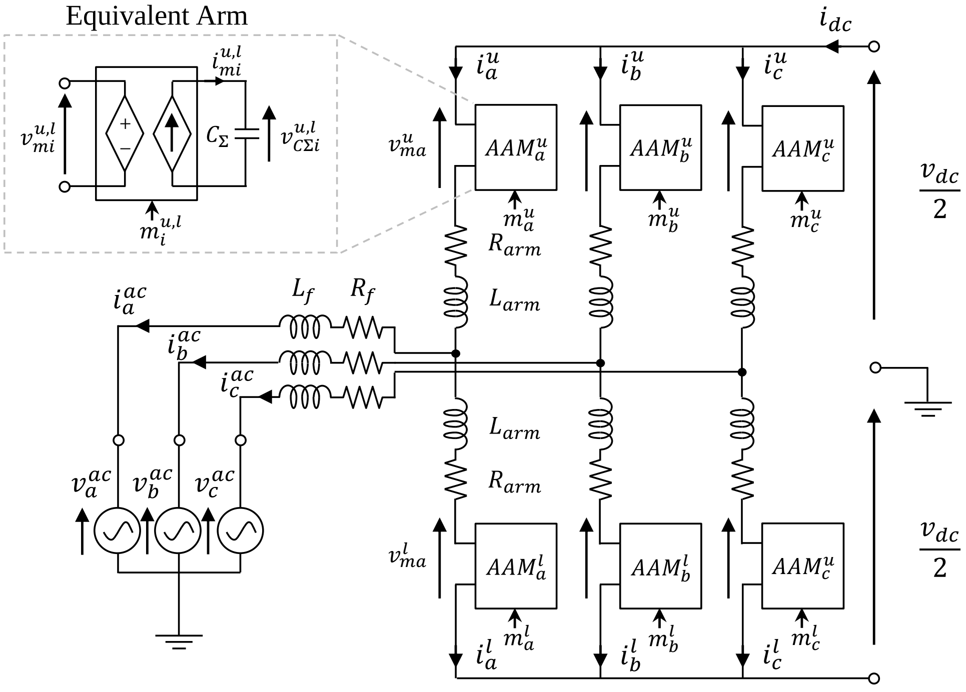

Figure 3.3: Reduced-order arm average model of the three-phase MMC.

Those equations can be rearranged in matrix form:

$$\begin{bmatrix} -L_{arm} - L_f & L_f \\ -L_f & L_{arm} + L_f \end{bmatrix} \begin{bmatrix} \dfrac{di_i^u}{dt} \\ \dfrac{di_i^l}{dt} \end{bmatrix} = \begin{bmatrix} R_{arm} + R_f & -R_f \\ R_f & -R_{arm} - R_f \end{bmatrix} \begin{bmatrix} i_i^u \\ i_i^l \end{bmatrix} + \begin{bmatrix} v_{mi}^u \\ -v_{mi}^l \end{bmatrix} + \begin{bmatrix} -\dfrac{v_{dc}}{2} + v_i^{ac} \\ \dfrac{v_{dc}}{2} + v_i^{ac} \end{bmatrix}. \tag{3.9}$$

As it can be noticed, there are coupling elements in the matrices, which makes the control of those arm currents complex and not straightforward. Thus, a mathematical manipulation is carried out.

On the one hand, the current $i_i^{ac}$ which goes into the AC grid can be defined as:

$$i_i^{ac} = i_i^u - i_i^l. \tag{3.10}$$

By summing (3.7) and (3.8), the following equation is obtained:

$$\frac{v_{mi}^l}{2} - \frac{v_{mi}^u}{2} - v_i^{ac} = \left(L_f + \frac{L_{arm}}{2}\right)\frac{di_i^{ac}}{dt} + \left(R_f + \frac{R_{arm}}{2}\right) i_i^{ac}. \tag{3.11}$$

By defining the equivalent AC voltage and the internal AC impedance as:

$$v_{mi}^{ac} = \frac{v_{mi}^l - v_{mi}^u}{2} \tag{3.12}$$

$$R_{eq,i}^{ac} = R_f + \frac{R_{arm}}{2}, \qquad L_{eq,i}^{ac} = L_f + \frac{L_{arm}}{2}, \tag{3.13}$$

(3.11) is rearranged as follows:

$$v_{mi}^{ac} - v_i^{ac} = L_{eq,i}^{ac}\frac{di_i^{ac}}{dt} + R_{eq,i}^{ac} i_i^{ac}. \tag{3.14}$$

The interpretation of (3.14) is shown in Fig. 3.4. From the AC grid stand point, the upper and lower arms appear to be the single AC voltage source $v_{mi}^{ac}$ and the equivalent resistance and inductance. The difference between $v_i^{ac}$ and $v_{mi}^{ac}$ is applied to the equivalent resistance and inductance which generates the grid current $i_{ac}$.

On the other hand, subtraction of (3.8) from (3.7) yields the equation below:

$$v_{dc} - v_{mi}^u - v_{mi}^l = L_{arm}\frac{d\left(i_i^u + i_i^l\right)}{dt} + R_{arm}\left(i_i^u + i_i^l\right). \tag{3.15}$$

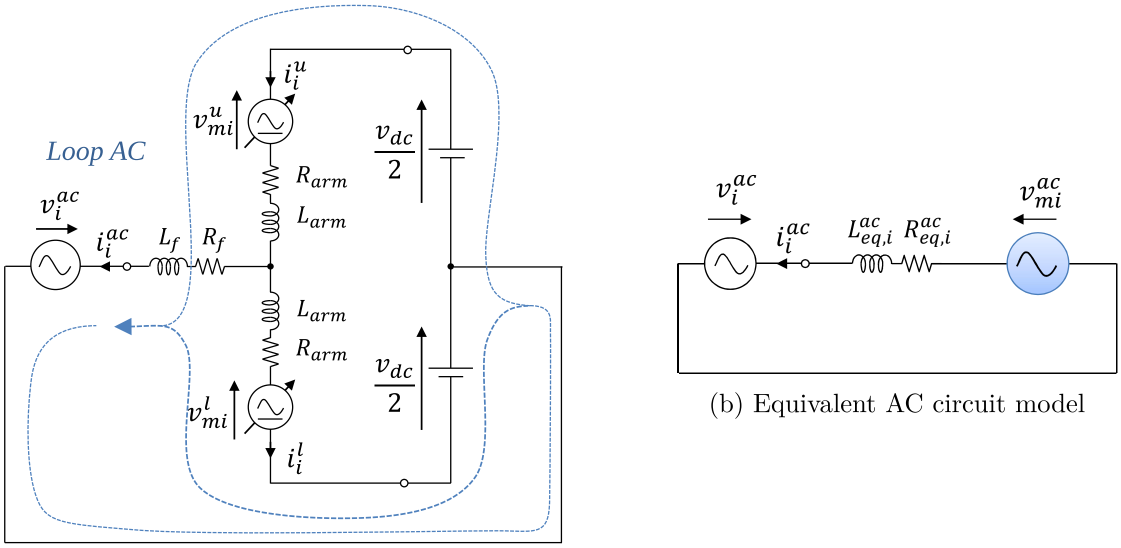

(b) Equivalent AC circuit model

(a) AC circuit path

Figure 3.4: AC circuit of MMC (shown only single phase).

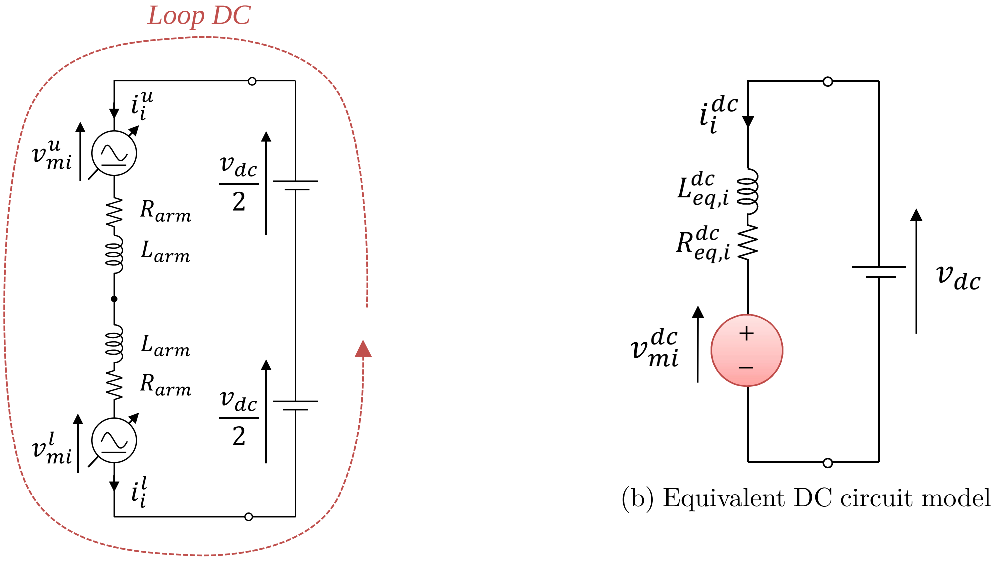

(b) Equivalent DC circuit model

(a) DC circuit path

Figure 3.5: DC circuit of MMC (shown only single phase).

From the DC grid, the upper and lower arms appear to be in a series connection. By introducing the DC current and voltage:

$$i_i^{dc} = \frac{i_i^u + i_i^l}{2} \tag{3.16}$$

$$v_{mi}^{dc} = v_{mi}^u + v_{mi}^l, \tag{3.17}$$

and defining the equivalent DC resistance and inductance as:

$$R_{eq,i}^{dc} = 2R_{arm}, \qquad L_{eq,i}^{dc} = 2L_{arm}, \tag{3.18}$$

(3.15) can be rearranged into:

$$v_{dc} - v_{mi}^{dc} = L_{eq,i}^{dc}\frac{di_i^{dc}}{dt} + R_{eq,i}^{dc} i_i^{dc}. \tag{3.19}$$

The equivalent DC circuit is shown in Fig. 3.5. The DC current $i_i^{dc}$ is generated by the voltage difference between $v_{dc}$ and the equivalent common mode DC voltage $v_{mi}^{dc}$ applied on the equivalent DC inductor and resistor.

Consequently, the coupled two equations, (3.7) and (3.8), are rewritten in matrix form:

$$\begin{bmatrix} L_{eq,i}^{ac} & 0 \\ 0 & L_{eq,i}^{dc} \end{bmatrix} \begin{bmatrix} \dfrac{di_i^{ac}}{dt} \\ \dfrac{di_i^{dc}}{dt} \end{bmatrix} = \begin{bmatrix} -R_{eq,i}^{ac} & 0 \\ 0 & -R_{eq,i}^{dc} \end{bmatrix} \begin{bmatrix} i_i^{ac} \\ i_i^{dc} \end{bmatrix} + \begin{bmatrix} v_{mi}^{ac} \\ -\,v_{mi}^{dc} \end{bmatrix} + \begin{bmatrix} -v_i^{ac} \\ v_{dc} \end{bmatrix}. \tag{3.20}$$

This clearly shows the decoupling between the AC and DC sub-systems. The two grid currents, $i_i^{ac}$ and $i_i^{dc}$, are governed by the independent dynamic equations in which $v_{mi}^{ac}$ and $v_{mi}^{dc}$ are regarded as control inputs, and the grid voltage $v_i^{ac}$ and $v_{dc}$ are exogenous inputs of the system.

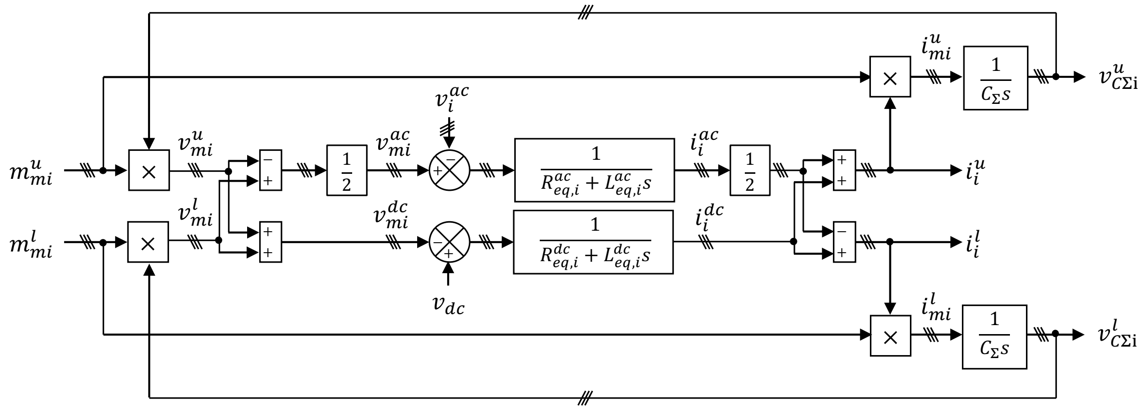

Figure 3.6: Block diagram representation of three-phase MMC model.

By combining (3.1) to (3.6) and the AC and DC current equations, (3.14) and (3.19), the block diagram representation of the three-phase MMC model is obtained as shown in

Fig. 3.6. Each phase of the MMC is characterized by 4 state variables; hence, a three-phase MMC has 11 state variables (six equivalent capacitor voltages, three DC currents, and two AC currents[1]) in total, and they all need to be controlled by the high level control layer for the secure operation of the MMC.

## 3.3 Inner Control of MMC

The *inner control*, also called *current control*, is the lowest control layer in the high level control. The inner control regulates both the AC and DC grid currents. Based on the analytical model obtained in the previous section, this section describes the detailed control structure of this layer.

### 3.3.1 Inner Control Design

In order to fully regulate both AC and DC currents, the inner control is developed by inverting the causality relations from the input $m_{mi}^{u,l}$ to the currents to be controlled. If we suppose that the low level control works properly and its dynamics is sufficiently faster than that of the inner control, the following assumption can be readily made:

$$m_{mi}^{u} \overset{hyp}{=} m_{mi}^{u*}, \qquad m_{mi}^{l} \overset{hyp}{=} m_{mi}^{l*}. \tag{3.21}$$

As discussed in Subsection 2.5.1.1, there are several modulation index calculation approaches existing in literature. The choice of the calculation approach greatly influences the overall design of the inner control. Therefore, the following focuses on the approach referred to as the closed-loop modulation index calculation (see Subsection 2.5.1.1 ), i.e. the modulation indices are generated by:

$$m_{i}^{u*} = \frac{v_{mi}^{u*}}{v_{C\Sigma i}^{u}}, \qquad m_{i}^{l*} = \frac{v_{mi}^{l*}}{v_{C\Sigma i}^{l}}. \tag{3.22}$$

Then, inversion of (3.12) and (3.17) yields:

$$\begin{bmatrix} v_{mi}^{u*} \\ v_{mi}^{l*} \end{bmatrix} = \begin{bmatrix} -1 & \frac{1}{2} \\ 1 & \frac{1}{2} \end{bmatrix} \begin{bmatrix} v_{mi}^{ac*} \\ v_{mi}^{dc*} \end{bmatrix}. \tag{3.23}$$

---

[1] Under balanced condition, only two phases can be explicitly controllable because $i_a^{ac} + i_b^{ac} + i_c^{ac} = 0$ must hold.

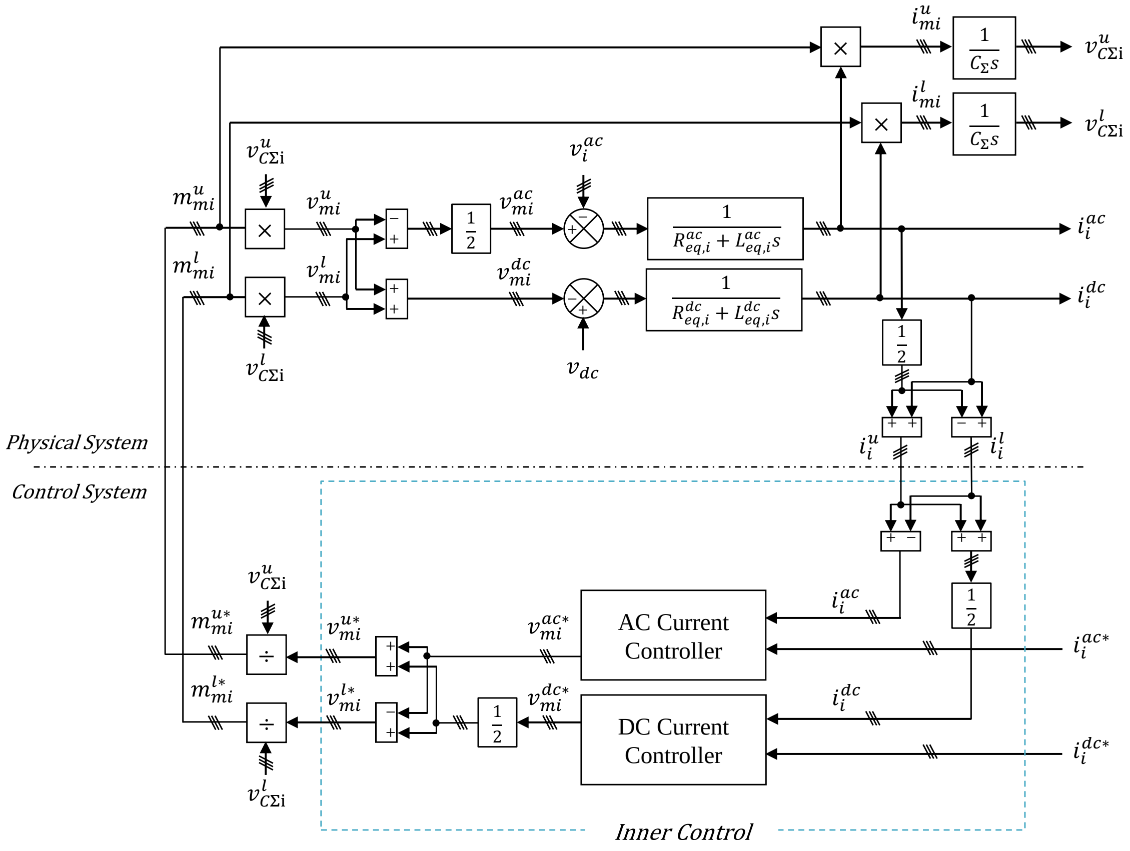

Figure 3.7: Block diagram of general inner control loop.

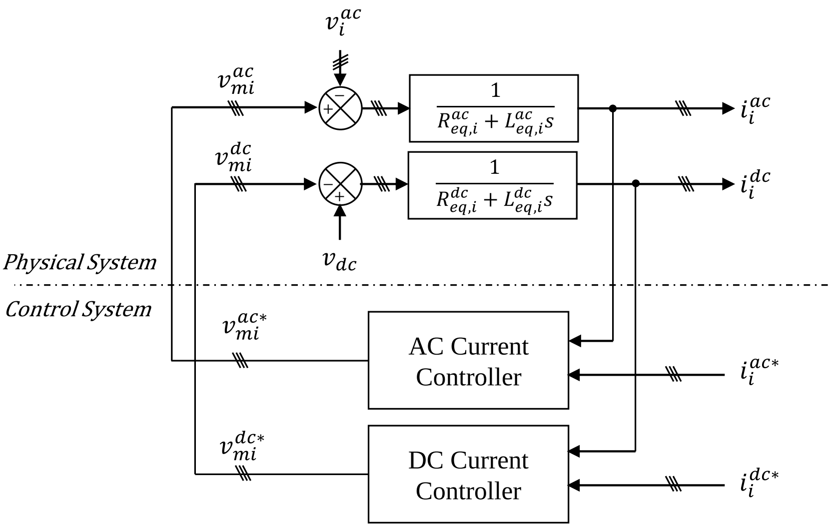

Figure 3.8: Block diagram of equivalent inner control loop.

Fig. 3.7 shows the general structure of the inner control loop, which can be simplified to the equivalent form depicted in Fig. 3.8. As seen, the control of the AC currents and the DC currents are now fully decoupled. Both currents can be independently controlled by the respective controllers. The following subsections describes the detailed structure of each controller.

#### 3.3.1.1 AC Current Controller

For the 3-phase MMC, as well as the classical VSC in general, the control of the AC current $i_i^{ac}$ is achieved in rotating frame by using Park transformation [145]. The Phase Lock Loop (PLL) ensures that the rotating frame is aligned in phase with the grid voltage angle. By applying the Park transformation to the AC circuit equation (3.14), the dynamic equations of the AC current in the $dq$ frame are obtained as:

$$\frac{di_d^{ac}}{dt} = \frac{1}{L_{eq}^{ac}}\left(v_{md}^{ac} - v_d^{ac} - R_{eq}^{ac} i_d^{ac} + \omega L_{eq}^{ac} i_q^{ac}\right) \tag{3.24}$$

$$\frac{di_q^{ac}}{dt} = \frac{1}{L_{eq}^{ac}}\left(v_{mq}^{ac} - v_q^{ac} - R_{eq}^{ac} i_q^{ac} - \omega L_{eq}^{ac} i_q^{ac}\right) \tag{3.25}$$

where $\omega$ is the AC grid angular frequency and $R_{eq}^{ac} = R_{eq,i}^{ac}$, $L_{eq}^{ac} = L_{eq,i}^{ac}$ . As it is observed in (3.24) and (3.25), they contain the coupled terms due to the product rule in the $dq$ complex frame. Fig. 3.9 shows the block diagram representation of the AC current dynamics in the $dq$ frame.

The AC current can be controlled by two controllers deriving the voltage references in the $dq$ frame, $v_{md}^{ac*}$ and $v_{mq}^{ac*}$. The AC current control laws are then obtained as:

$$v_{md}^{ac*} = v_d^{ac} + (i_d^{ac*} - i_d^{ac})C_i^{ac}(s) - \omega L_{eq}^{ac} i_q^{ac} \tag{3.26}$$

$$v_{mq}^{ac*} = v_q^{ac} + (i_q^{ac*} - i_q^{ac})C_i^{ac}(s) + \omega L_{eq}^{ac} i_d^{ac} \tag{3.27}$$

where the $C_i^{ac}(s)$ represents the controller in Laplace domain. The decoupling terms are introduced to compensate for the coupling terms [146]. This decoupled control structure allows independent control of $d$- and $q$-axis currents according to their respective references. The voltage reference in the $abc$ frame, $v_{mi}^{ac*}$, is calculated by means of the inverse Park transformation. The block diagram representation of the obtained AC current controller is shown in Fig. 3.10.

Let us consider a case where a simple Proportional Integral ($PI$) controller is used to correct the error. Then $C_i^{ac}(s)$ is expressed by the proportional gain $K_p^{i^{ac}}$ and the integral gain $K_i^{i^{ac}}$:

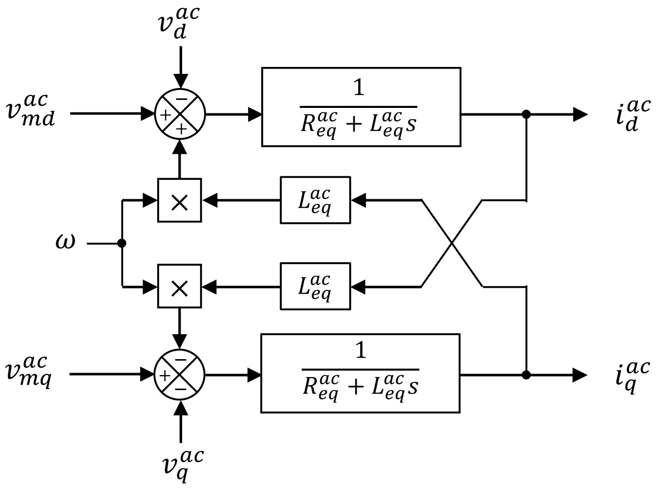

Figure 3.9: Block diagram representation of AC current dynamics in $dq$ frame.

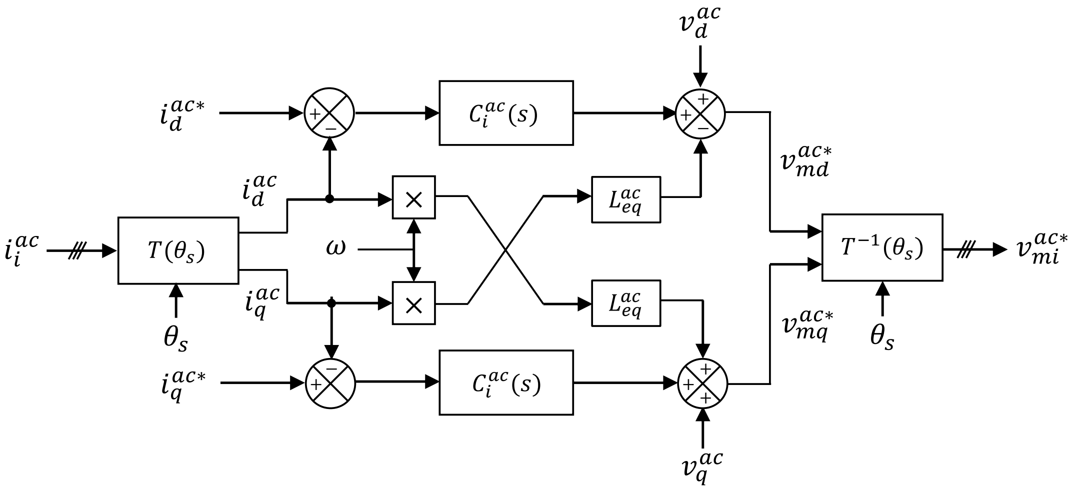

Figure 3.10: Block diagram representation of AC current controller.

$$C_i^{ac}(s) = K_p^{i^{ac}} + \frac{K_i^{i^{ac}}}{s}. \tag{3.28}$$

The gain parameters are tuned according to the closed loop transfer function. Combining (3.24) and (3.26), the closed loop transfer function is obtained:

$$\frac{i_d^{ac}}{i_d^{ac*}}(s) = \frac{1 + \dfrac{K_p^{i^{ac}}}{K_i^{i^{ac}}} s}{\dfrac{L_{eq}^{ac}}{K_i^{i^{ac}}} s^2 + \dfrac{K_p^{i^{ac}} + R_{eq}^{ac}}{K_i^{i^{ac}}} s + 1}. \tag{3.29}$$

It is known that the denominator of the transfer function largely dictates the dynamics of the closed loop system. The gain parameters are determined by using the pole placement method: the denominator of the transfer function is compared to the second-order characteristic equation whose dynamics are known:

$$T(s) = 1 + \frac{2\zeta}{\omega_n} s + \frac{1}{\omega_n} s^2 \tag{3.30}$$

where $\omega_n$ is the natural frequency and $\zeta$ is the damping ratio. To achieve the desired response time $t_r^{i^{ac}}$, the gain parameters

$$K_p^{i^{ac}} = 2\zeta\omega_n L_{eq}^{ac} - R_{eq}^{ac} \tag{3.31}$$

$$K_i^{i^{ac}} = \omega_n^2 L_{eq}^{ac} \tag{3.32}$$

with $\omega_n = 3/t_r^{i^{ac}}$ and $\zeta = 0.707$ are obtained.

#### 3.3.1.2 DC Current Controller

As previously discussed, the DC current dynamics are independent of the AC current dynamics. Thus, the DC currents are controlled by a separate controller. Similarly to the previously presented AC current control, the DC currents can also be controlled in the rotating frame [147]. However, for the sake of simplicity, a classical *abc* frame control is considered here.

The DC current control is deduced directly from (3.19). Similarly, the DC current control can be achieved through the three independent *PI* controllers. Denoting the controller by $C_i^{dc}(s)$, the control law for $i_i^{dc}$ is derived as:

$$v_{mi}^{dc*} = v_{dc} - \left(i_i^{dc*} - i_i^{dc}\right) C_i^{dc}(s), \tag{3.33}$$

and its block diagram representation is depicted in Fig. 3.11.

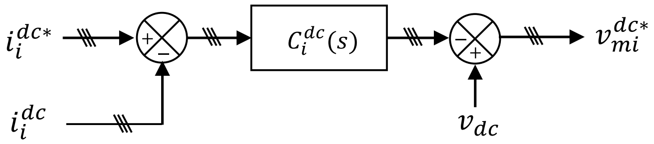

Figure 3.11: Block diagram representation of DC current controller for phase $i$.

The gain parameters of the *PI* controllers are tuned in the same way as the AC controller. From the closed-loop transfer function, the gain parameters are determined according to the desired response time

$$K_p^{i^{dc}} = 2\zeta\omega_n L_{eq,i}^{dc} - R_{eq,i}^{dc} \tag{3.34}$$

$$K_i^{i^{dc}} = \omega_n^2 L_{eq,i}^{dc}. \tag{3.35}$$

### 3.3.2 Global Diagram of Inner Control Loop

Combining the physical model with the developed controllers for the AC and DC currents, the complete inner control loop is obtained as illustrated in Fig. 3.12. The five state variables of the three phase MMC, i.e. two AC currents in the $dq$ frame and three DC phase currents, are now under control. With the aforementioned tuning technique of the controllers, their dynamic responses are confined within a desired time range. Even if a brutal change of the inputs is imposed, both AC and DC currents converge to the vicinity of the respective references within the assigned response time.

## 3.4 Outer Control of MMC

The outer control mainly deals with the controls of the system variables. All the control commands of the outer control come down to the control inputs of the inner control, i.e. $i_d^{ac*}$, $i_q^{ac*}$ and $i_i^{dc*}$. Since the MMC is a specific type of the VSC, operation in the four quadrants of the $PQ$ plane is possible. In addition to the active and reactive power on the AC side, the MMC can control the DC power independently. This is achieved by using the remaining control inputs of the inner controller $i_i^{dc*}$.

### 3.4.1 Power Control

The independent control of the AC currents in the synchronous frame greatly facilitates the control of the active and reactive power in a three-phase system. When the $d$-axis of

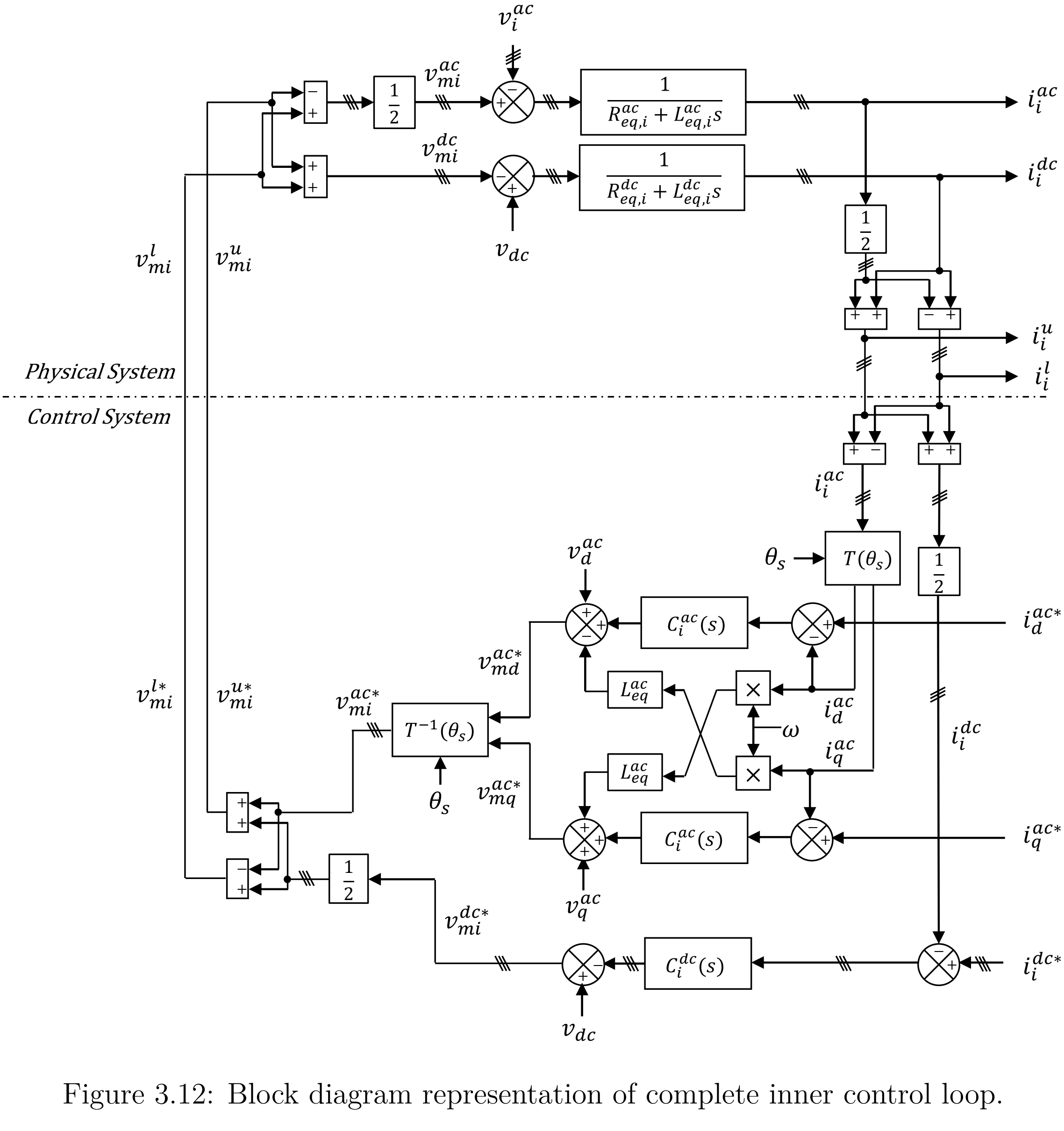

Figure 3.12: Block diagram representation of complete inner control loop.

the rotating frame is aligned to the grid voltage, the total three-phase AC power at the PCC is simply given by:

$$
\begin{aligned}
P_{ac} &= v_d^{ac} i_d^{ac} && (3.36)\\
Q_{ac} &= -v_d^{ac} i_q^{ac}. && (3.37)
\end{aligned}
$$

Therefore, the desired power transfer $P_{ac}^*$ and $Q_{ac}^*$ can be achieved by feeding the AC current references. A feed-back control for the power control is a possible choice if the converter is connected to a relatively weak AC grid [148]. However, since it imposes additional dynamics to the system and restricts the response time on the controllers on higher levels, the simple open-loop control [148] is used here. The current set-points are directly derived from the power references and the $d$-axis voltage as below:

$$
\begin{aligned}
i_d^{ac*} &= \frac{P_{ac}^*}{v_d^{ac}} && (3.38)\\
i_q^{ac*} &= -\frac{Q_{ac}^*}{v_d^{ac}}. && (3.39)
\end{aligned}
$$

As such, the AC active and reactive powers converge to their reference values within the response time of the inner controller. The AC power references can be defined by the system operator or locally adjusted by other controllers in upper hierarchy to support the associated AC grid voltage and frequency in case of contingency.

The MMC can control the DC power independent of the AC power. The desired DC power transfer $P_{dc}^*$ is achieved by deriving the appropriate common mode DC current references $i_i^{dc*}$. In normal operation, the DC current is equally distributed among all the three legs. Then, $i_i^{dc*}$ is derived by using the measured DC voltage $v_{dc}$:

$$
i_i^{dc*} = \frac{P_{dc}^*}{3v_{dc}}. \tag{3.40}
$$

### 3.4.2 Other Outer Controls

The outputs of the outer control, in other words the current references $i_d^{ac*}$, $i_q^{ac*}$ and $i_i^{dc*}$, can be generated by synthesis of several controllers in accordance with the operation mode of the converter. For the purpose of the AC frequency regulation, a supplemental active power can be provided by adjusting the $d$-frame current reference $i_d^{ac*}$ for the purpose of frequency regulation. The AC grid voltage can be supported by acting on $i_q^{ac*}$ to inject or absorb reactive power. For the DC side, the grid voltage is controlled by regulating the power injected or withdrawn from the DC grid; hence it can be achieved by controlling $i_i^{dc*}$. The AC grid control is out of the scope of this thesis and will not be discussed further. The latter is discussed in detail in Chapter 5.

Turning the attention to the internal dynamics of the MMC, one may notice that the six state variables out of eleven, i.e. the total capacitor voltages, are not controlled at this stage. For secure operation of the MMC, all the state variables need to be controlled explicitly; otherwise, some of them may take unacceptable values and lead to unstable operation. Therefore, several additional controllers are implemented. The following section describes their control design in great detail.

## 3.5 Energy Control

The total capacitor voltage in each arm needs to be controlled explicitly. It can be noticed from Fig. 3.2 that their dynamics are nonlinear. In order to regulate them by simple linear controllers, several change of variables are introduced and discussed in the following.

### 3.5.1 Energetic Model of MMC

The capacitors in the converter arms can be regarded as energy storage devices. Thus, the control objective here can be reworded as the management of the energy distributed among the six arms. The energy stored in the upper and the lower arm of phase $i$, denoted by $W_i^u$ and $W_i^l$, are expressed as:

$$W_i^u = \frac{1}{2}C_\Sigma \left(v_{C\Sigma i}^u\right)^2 \tag{3.41}$$

$$W_i^l = \frac{1}{2}C_\Sigma \left(v_{C\Sigma i}^l\right)^2 . \tag{3.42}$$

The stored energy varies along with the power exchanged in each arm. If no energy dissipation during the conversion is considered, the power exchanged at each arm is given by the product of the arm voltage and the arm current:

$$p_{mi}^u = v_{mi}^u i_i^u \tag{3.43}$$

$$p_{mi}^l = v_{mi}^l i_i^l . \tag{3.44}$$

By combining (3.43) and (3.44) with the previously defined variables (3.12) and (3.17) as well as (3.10) and (3.16), the following holds:

$$\frac{dW_i^u}{dt} = v_{mi}^u i_i^u = \left(\frac{v_{mi}^{dc}}{2} - v_{mi}^{ac}\right)\left(i_i^{dc} + \frac{i_i^{ac}}{2}\right) \tag{3.45}$$

$$\frac{dW_i^l}{dt} = v_{mi}^l i_i^l = \left(\frac{v_{mi}^{dc}}{2} + v_{mi}^{ac}\right)\left(i_i^{dc} - \frac{i_i^{ac}}{2}\right) . \tag{3.46}$$

As seen, there is a strong coupling between the upper and lower arm energy which makes their control complex. For the sake of simplicity, [109] proposed to consider two variables: the sum of the energy in the leg, $W_i^{\Sigma}$, and the difference between the upper and lower arm, $\Delta W_i^{\Delta}$, as defined below:

$$\begin{aligned} W_i^{\Sigma} &= W_i^u + W_i^l && (3.47)\\ \Delta W_i^{\Delta} &= W_i^u - W_i^l. && (3.48) \end{aligned}$$

The symbol $\Delta$ preceded $W_i^{\Delta}$ is added to the notation used in [109] to discriminate the essential meanings of $W_i^{\Sigma}$ and $\Delta W_i^{\Delta}$. The $W_i^{\Sigma}$ signifies the actual energy stored in each leg, whereas $\Delta W_i^{\Delta}$ represents a deviation of the energy which is ideally zero when the upper and lower arm energy are properly balanced. By using the above mentioned change of variables with (3.45) and (3.46), the dynamics of the internal energy in the MMC are expressed in much simpler forms:

$$\begin{aligned} \frac{dW_i^{\Sigma}}{dt} &= v_{mi}^{dc} i_i^{dc} - v_{mi}^{ac} i_i^{ac} && (3.49)\\ \frac{d\Delta W_i^{\Delta}}{dt} &= \frac{v_{mi}^{dc} i_i^{ac}}{2} - 2 v_{mi}^{ac} i_i^{dc}. && (3.50) \end{aligned}$$

On the one hand, the terms in the right side of (3.49) correspond to the instantaneous DC and AC power exchanged in each phase. This is intuitively understandable since, if the converter leg is considered as an energy storage, the mismatch between the power inflow and outflow leads to a deviation of the stored energy level. On the other hand, (3.50) is rather complex. It can be inferred by looking (3.50) with (3.45) and (3.46) that the upper and lower arms intrinsically exchange energy within the phase leg during the grid frequency cycle without changing the average values.

In (3.49) and (3.50), the link between the controllable current variables and those energy variables remains unclear. To derive more comprehensive expressions of the internal energy, further simplification and change of variables are introduced.

Since the energy dissipated in the MMC is relatively small, the following assumptions on the DC and AC voltages can be made:

$$v_{mi}^{dc} \overset{hyp}{=} v_{dc} \tag{3.51}$$

$$v_{mi}^{ac} \overset{hyp}{=} v_i^{ac}. \tag{3.52}$$

In view of the three-phase circuit configuration, the DC grid current $i_{dc}$ is given by:

$$i_{dc} = i_a^{dc} + i_d^{dc} + i_c^{dc}. \tag{3.53}$$

The DC grid current inflow or outflow directly contributes to the actual energy stored inside the MMC. However, there are some currents which may not flow out from the MMC but circulate among the converter legs. Those currents, customarily called circulating currents, can be defined as [149]:

$$\begin{aligned} i_a^{cir} &= i_a^{dc} - \frac{i_{dc}}{3} \\ i_b^{cir} &= i_b^{dc} - \frac{i_{dc}}{3} \\ i_c^{cir} &= -i_a^{cir} - i_b^{cir}. \end{aligned} \tag{3.54}$$

According to the definition above, the sum of the circulating currents is zero. Thus, they have no impact on the DC grid current or the actual energy stored inside the MMC.

The definition of the leg energy is rearranged in the following. The total energy stored in the MMC is given by the sum of $W_i^{\Sigma}$ for three phase legs:

$$W_{mmc} = W_a^{\Sigma} + W_b^{\Sigma} + W_c^{\Sigma}. \tag{3.55}$$

If each phase is designed identically, the overall energy stored inside the MMC should be equally distributed among the three phase legs in normal operation. Thus, it is reasonable to consider the energy deviation from the balanced condition. When the energy is evenly distributed among the legs, each leg should store one third of the total energy. Denoting the deviation of the leg energy from the balanced condition by $\Delta W_i^{\Sigma}$, it can be defined as:

$$\Delta W_a^{\Sigma} = W_a^{\Sigma} - \frac{W_{mmc}}{3} \tag{3.56}$$

$$\Delta W_b^{\Sigma} = W_b^{\Sigma} - \frac{W_{mmc}}{3} \tag{3.57}$$

$$\Delta W_c^{\Sigma} = W_c^{\Sigma} - \frac{W_{mmc}}{3} = -\Delta W_a^{\Sigma} - \Delta W_b^{\Sigma}. \tag{3.58}$$

Only the phases $a$ and $b$ need to be defined because the deviation of the third phase can be deduced from the others. Now the energy stored in the three legs are viewed from two aspects: the actual energy stored in the MMC $W_{mmc}$, and the two variables which are ideally zero when the energy is evenly distributed among the three legs.

From all the definitions and assumptions, (3.49) and (3.50) can be rewritten in a different form as follows:

$$\frac{dW_{mmc}}{dt} = v_{dc} i_{dc} - \sum_i v_i^{ac} i_i^{ac} \tag{3.59}$$

$$\begin{aligned} \frac{d\Delta W_i^{\Sigma}}{dt} &= v_{dc} i_i^{dc} - v_i^{ac} i_i^{ac} - \frac{1}{3}\left( v_{dc} i_{dc} - \sum_i v_i^{ac} i_i^{ac} \right) \\ &= \frac{1}{3} \sum_i v_i^{ac} i_i^{ac} - v_i^{ac} i_i^{ac} + v_{dc} i_i^{cir} \qquad i = a, b \end{aligned} \tag{3.60}$$

$$\begin{aligned} \frac{d\Delta W_i^{\Delta}}{dt} &= \frac{v_i^{dc} i_i^{ac}}{2} - 2 v_i^{ac} i_i^{dc} \\ &= \frac{v_i^{dc} i_i^{ac}}{2} - 2 v_i^{ac} \frac{i_{dc}}{3} - 2 v_i^{ac} i_i^{cir} \qquad i = a, b, c \end{aligned} \tag{3.61}$$

Equation (3.59) is straightforward; the total energy stored inside the MMC simply depends on the DC power inflow and the AC power outflow. The other two equations need further clarification. In (3.60), the first term of the right side corresponds to the average AC power delivered per phase. The second term is the instantaneous AC power output of the phase $i$, which is a time-varying sinusoidal at twice the grid frequency. In the time average over a grid frequency cycle, those two terms cancel each other in a balanced operation. In (3.61), the first two terms of the right side are the product of a DC and an AC component; thus, their time average over a grid frequency cycle should be zero. Therefore, it is rather reasonable to consider the time average of (3.60) and (3.61). Defining the time average value during a grid frequency cycle $T$ as:

$$\langle f(t)\rangle \overset{def}{=} \frac{1}{T}\int_0^T f(t)dt,$$

the average of (3.60) and (3.61) can be expressed as follows:

$$\left\langle \frac{d\Delta W_i^{\Sigma}}{dt} \right\rangle = \left\langle v_{dc} i_i^{cir} \right\rangle \qquad i \in a, b \tag{3.62}$$

$$\left\langle \frac{d\Delta W_i^{\Delta}}{dt} \right\rangle = \left\langle -2 v_i^{ac} i_i^{cir} \right\rangle \qquad i \in a, b, c. \tag{3.63}$$

Consequently, the six total capacitor voltages are transformed into another six different variables: $W_{mmc}$, $\left\langle \Delta W_a^{\Sigma} \right\rangle$, $\left\langle \Delta W_b^{\Sigma} \right\rangle$, $\left\langle \Delta W_a^{\Delta} \right\rangle$, $\left\langle \Delta W_b^{\Delta} \right\rangle$ and $\left\langle \Delta W_c^{\Delta} \right\rangle$, whose approximated dynamics are expressed by (3.59), (3.62) and (3.63). Fig. 3.13 shows the block diagram representation of the internal energy dynamics. The energy distributed among the MMC is gathered into one state variable whose variation depends on the actual power exchanged on both DC and AC sides of the MMC, whereas the remaining five states only depend on internal currents which circulate inside the MMC and have no impact on the DC and AC grids as well as on the total energy in the MMC.

### 3.5.2 Total Energy Control

As previously described, when the total energy stored in the MMC is of concern, the MMC can be considered as a buffer energy storage. In terms of power, (3.59) can be rewritten as:

$$\frac{dW_{mmc}}{dt} = P_{dc} - P_{ac} = P_w \tag{3.64}$$

where $P_w$ is defined as the mismatch between the DC and AC power. It is apparent from (3.64) that the internal energy level of the MMC changes when a mismatch between the DC power inflow and the AC power outflow is imposed. If this mismatch is not explicitly compensated, it can lead to an excessive or insufficient energy level. Therefore,

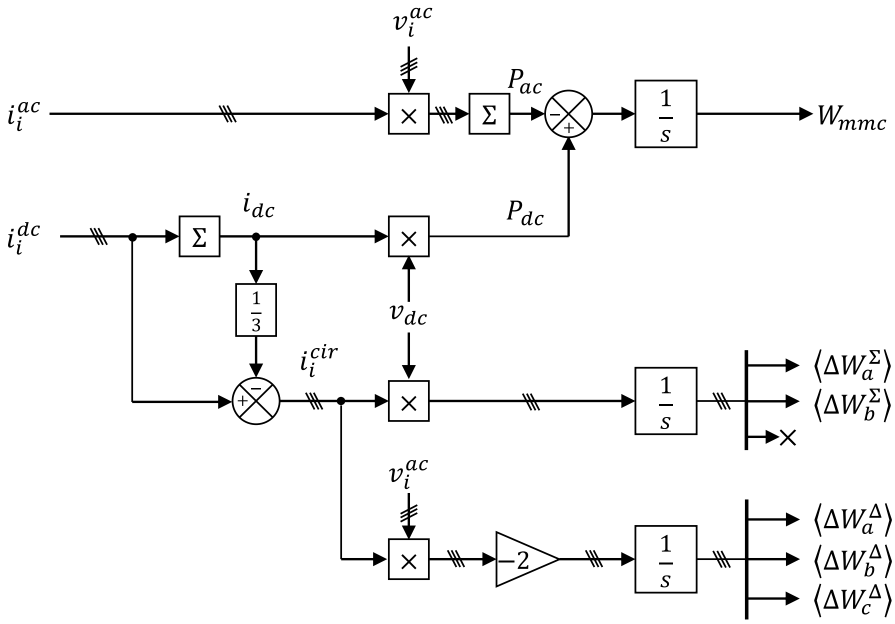

Figure 3.13: Block diagram representation of equivalent average energy model of MMC.

an additional controller which ensures adequate energy level is required. It is noteworthy to state that such controller is not required for the classical VSCs because the energy stored in the station capacitor on the DC side is imposed by the grid voltage. Whether this energy control is performed on the mismatch imposed by the DC side or AC side depends on the control design [150]. When the concerned time constant of the energy control is sufficiently apart from that of the inner control loop, the internal energy dynamics can be neglected. Then the energy controller can be designed by inverting the relevant part of (3.13).

#### 3.5.2.1 DC Side Energy Control

Suppose that the AC power follows a reference given by the operator.

$$P_{ac} \overset{hyp}{=} P_{ac}^* \tag{3.65}$$

An additional controller adjusts the DC power to regulate the desired energy level. Denoting the energy controller by $C_w(s)$, the control law of the total energy is expressed by:

$$\begin{aligned} P_{dc}^* &= P_{ac}^* + P_w^* & (3.66)\\ P_w^* &= \left(W_{mmc}^* - W_{mmc}\right) C_w(s) & (3.67)\end{aligned}$$

Fig. 3.14 shows the block diagram of the energy model of the MMC and the energy control loop.

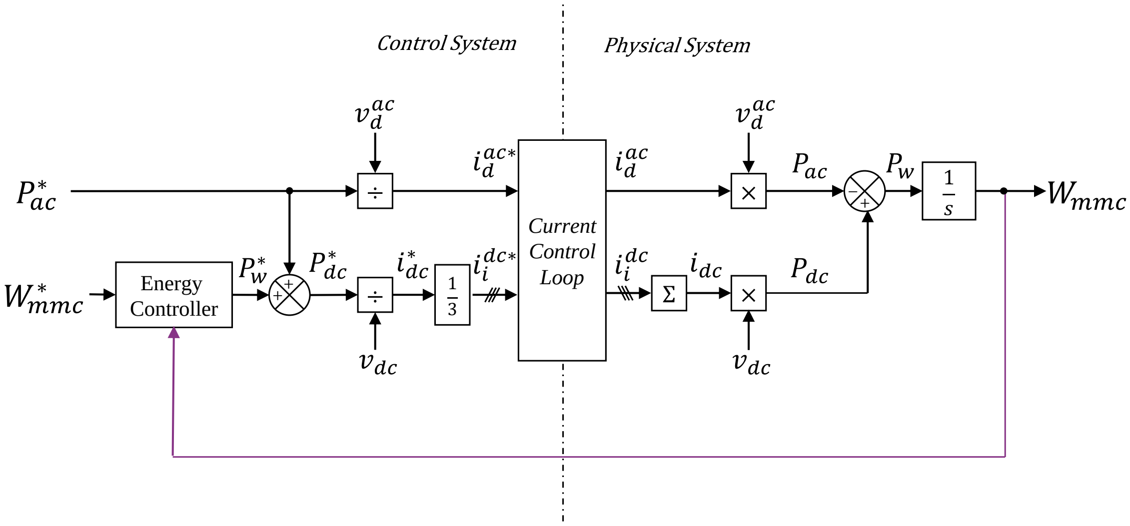

Figure 3.14: Schematic diagram of energy control loop in which the energy is controlled by DC power (only relevant parts are shown).

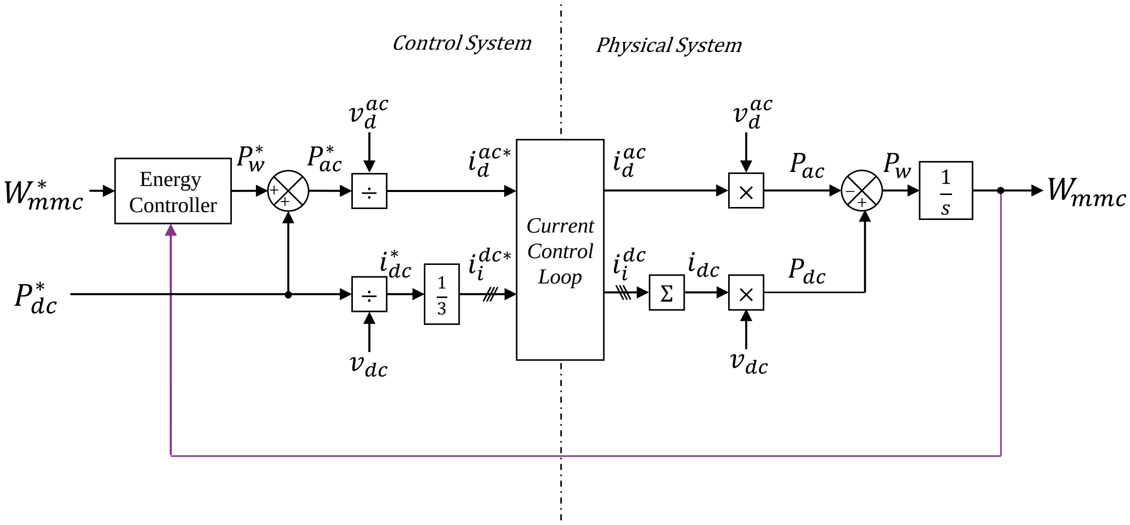

Figure 3.15: Schematic diagram of energy control loop in which the energy is controlled by AC power (only relevant parts are shown).

#### 3.5.2.2 AC Side Energy Control

In case that the total energy inside the MMC is regulated by the AC power exchange, the DC power can follow the desired reference without intervention of the energy controller, i.e.

$$P_{dc} \overset{hyp}{=} P_{dc}^{*}. \tag{3.68}$$

The energy controller adjusts the AC power; thus, the control law given in previous section becomes:

$$P_{ac}^{*} \quad = \quad P_{dc}^{*} - P_{w}^{*} \tag{3.69}$$

Fig. 3.15 shows the block diagram of the energy model of the MMC and the energy control loop in which the energy is regulated by the AC side.

#### 3.5.2.3 Comparison of Energy Control Strategies

In order to further understand the control of the total energy in the MMC, simple simulations are carried out. The MMC model is developed using the reduced-order arm average model (see Section 2.4.3.3), and the controllers explained until here are implemented. The MMC is connected to ideal voltage sources on both AC and DC sides. Several step changes of the energy reference are generated during the simulation (see Fig. 3.16 ), and the influence on the AC and DC power as well as the internal energy dynamics are observed for two energy control strategies: energy control by the DC and the AC side. To highlight the direction of power injection, the initial power flow is set zero for both cases.

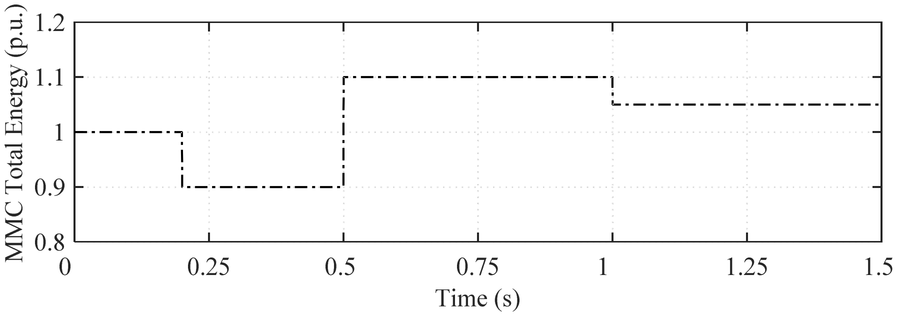

Figure 3.16: Energy reference $W_{mmc}^{*}$.

Fig. 3.17 shows the simulation results in case where the energy control is performed on the DC side. As seen in Fig. 3.17a, the variations of the power are observed only on the

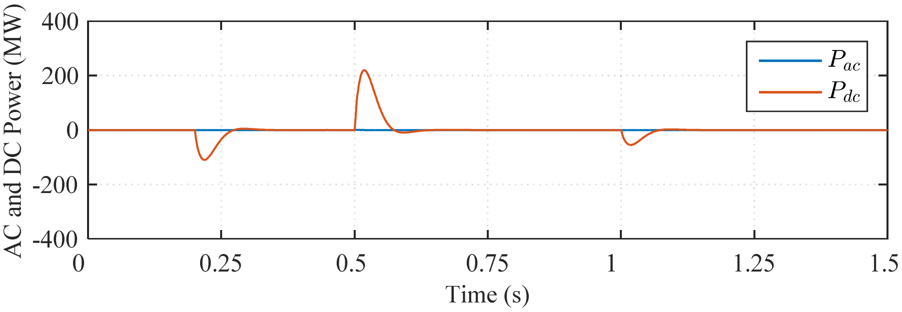

(a) AC and DC power

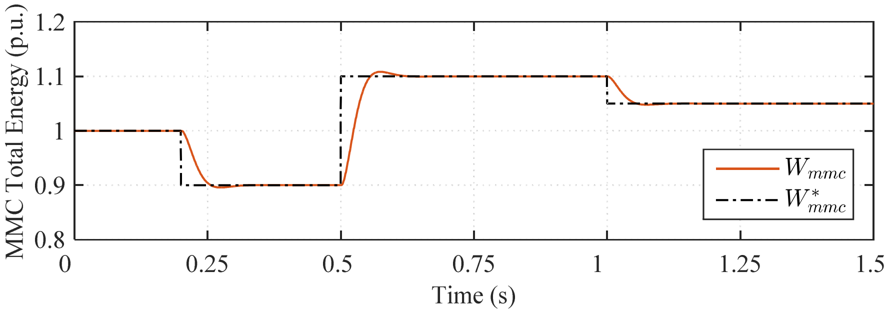

(b) Total energy

Figure 3.17: Simulation results: energy control by DC side.

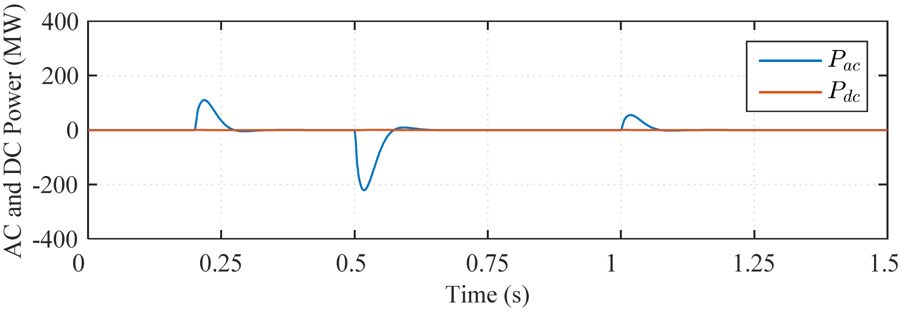

(a) AC and DC power.

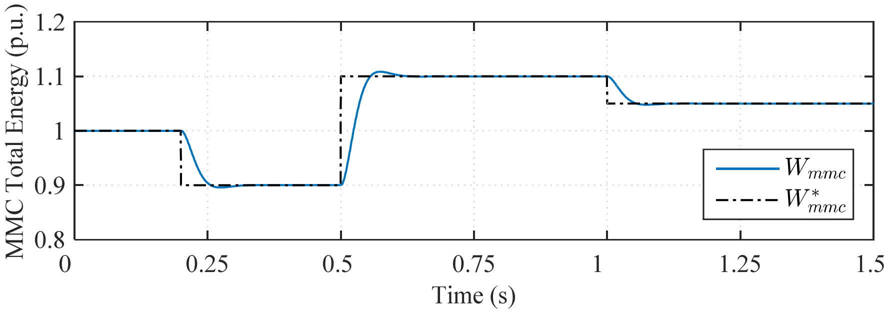

(b) Total energy.

Figure 3.18: Simulation results: Energy control by AC side.

DC power while the AC power is maintained at constant. Fig. 3.17b shows the internal energy dynamics. When the energy discharges (e.g. $t = 0.2$ s), the DC power is injected to the DC grid. The simulation results in which the energy is controlled on the AC side are depicted in Fig. 3.18. As seen in Fig. 3.18a, the power variations appear only in $P_{ac}$. The power supplied to or absorbed from the AC grid is realized by discharging or charging the internal energy (see Fig. 3.18b).

Viewed from another angle, the simulation results imply that the MMC can exchange energy with either the AC or DC grid by using the internal energy storage without effecting the other side of the grid. This unique feature of the MMC — the controllability of the internally stored energy — does not exist in the conventional VSCs. Therefore, it can be considered as an additional degree of freedom peculiar to the MMC. This new degree of freedom can possibly broaden the role of the converter in the HVDC system and be used to improve the associated grid dynamics; however, its potential had not been revealed yet.

### 3.5.3 Arm Energy Balancing Control

As stated before, the total energy stored in the MMC is an additional degree of freedom which enables to exchange additional power with either DC or AC grid without interfering the other side. By the simple closed-loop control, the charging or discharging of the internal energy can be optionally regulated. However, the aforementioned control does not take into account the distribution of the energy among the converter arms. Therefore, supplemental controllers are needed to ensure the appropriate distribution of the energy. Specifically, the controllers which regulate the remaining five state variables, i.e. $\left\langle \Delta W_a^{\Sigma} \right\rangle$, $\left\langle \Delta W_b^{\Sigma} \right\rangle$, $\left\langle \Delta W_a^{\Delta} \right\rangle$, $\left\langle \Delta W_b^{\Delta} \right\rangle$ and $\left\langle \Delta W_c^{\Delta} \right\rangle$, need to be implemented. In literature, the energy balancing issues are customarily split into two parts [143][133]:

1. Horizontal Energy Balancing: Horizontal energy balancing involves the control of the energy distribution among the phase legs. In case of divergence, an equal energy distribution can be achieved by controlling the energy transfer from a leg with higher energy level to lower ones.
2. Vertical Energy Balancing: Vertical energy balancing describes the energy distribution between the upper and the lower arms of each phase. A proper distribution of the energy in vertical direction can be achieved by exchanging the energy between the upper and lower arms within a phase.

According to the definitions of the five state variables introduced in Section 3.5.1, adequate horizontal energy balance can be interpreted as regulating $\left\langle \Delta W_a^{\Sigma} \right\rangle$ and $\left\langle \Delta W_b^{\Sigma} \right\rangle$ to zero (see (3.56) to (3.58)), whilst the vertical energy balancing can be ensured by maintaining $\left\langle \Delta W_a^{\Delta} \right\rangle$, $\left\langle \Delta W_b^{\Delta} \right\rangle$, and $\left\langle \Delta W_c^{\Delta} \right\rangle$ at zero (see (3.48)). Both energy balancing controls utilize the circulating currents not to interfere with the AC and DC grid currents. As expressed in (3.54), the circulating currents of only two out of three phases are usable to regulate the five state variables. Thus, some decomposition techniques must be needed. A possible solution is to decompose the circulating currents in terms of the frequency [109]. It may be noticed from (3.62) that the evolution of $\left\langle \Delta W_i^{\Sigma} \right\rangle$ depends on the non-oscillatory component of the circulating current. In contrast, (3.63) implies that $\left\langle \Delta W_i^{\Delta} \right\rangle$ is mainly affected by fundamental-frequency components. Thus, the circulating current is redefined as the superposition of the non-oscillatory component $i_{0\omega i}^{cir}$ and the fundamental-frequency component $i_{1\omega i}^{cir}$, i.e. $i_i^{cir} = i_{0\omega i}^{cir} + i_{1\omega i}^{cir}$. The horizontal energy balancing control is achieved by regulating the references of $i_{0\omega i}^{cir}$, and the vertical energy balancing control is achieved by regulating $i_{1\omega i}^{cir}$. The constraint of not interfering with the DC grid current, i.e. $\sum_{i \in a,b,c} i_i^{cir} = 0$, is ensured at each control unit. The following describes the detailed control structure for each energy balancing control.

### 3.5.3.1 Horizontal Energy Balancing Control

The horizontal energy balancing control is achieved by adequately deriving the non-oscillatory circulating current reference $i_{0\omega i}^{cir*}$ necessary to correct the error between the reference value and the present state of $\left\langle \Delta W_i^{\Sigma} \right\rangle$. For this purpose, the instantaneous signals $\Delta W_i^{\Sigma}$ must be filtered to extract the average values $\left\langle \Delta W_i^{\Sigma} \right\rangle$. As (3.60) indicates, the instantaneous signal of $\Delta W_i^{\Sigma}$ contains $2\omega$ frequency components due to the single phase AC active power pulsating at twice of the fundamental frequency. Effective elimination of those oscillatory components can be achieved by using the notch filter given by [151]:

$$F_{\omega_n}(s) = \frac{s^2 + \omega_n^2}{s^2 + 2\omega_n s + \omega_n^2}. \tag{3.70}$$

Denoting the filter tuned to eliminate $2\omega$ components by $F_{2\omega}(s)$, the extraction of the average value of $\Delta W_i^{\Sigma}$ can be written as:

$$\left\langle \Delta W_i^{\Sigma} \right\rangle = F_{2\omega}(s)\, \Delta W_i^{\Sigma}. \tag{3.71}$$

The horizontal energy balancing controller is then designed from (3.62). Denoting the *PI* controller by $C_{w\Sigma}(s)$, the control law of the horizontal energy balancing is expressed by:

$$i_{0\omega i}^{cir*} = \frac{1}{v_{dc}} \left( \left\langle \Delta W_i^{\Sigma *} \right\rangle - \left\langle \Delta W_i^{\Sigma} \right\rangle \right) C_{w\Sigma}(s) \qquad i = a, b \tag{3.72}$$

where $\left\langle \Delta W_i^{\Sigma *} \right\rangle$ is the reference signal which is normally set to zero. Then the reference for three phases, $\boldsymbol{i}_{0\omega}^{cir*} = \begin{bmatrix} i_{0\omega a}^{cir*} & i_{0\omega b}^{cir*} & i_{0\omega c}^{cir*} \end{bmatrix}^T$, is calculated ensuring the balance between the three phases:

$$\boldsymbol{i}_{0\omega}^{cir*} = \boldsymbol{M}_\Sigma \begin{bmatrix} i_{0\omega a}^{cir*} \\ i_{0\omega b}^{cir*} \end{bmatrix}, \tag{3.73}$$

where

$$\boldsymbol{M}_\Sigma = \begin{bmatrix} 1 & 0 \\ 0 & 1 \\ -1 & -1 \end{bmatrix}. \tag{3.74}$$

The detailed control structure is depicted in Fig. 3.19.

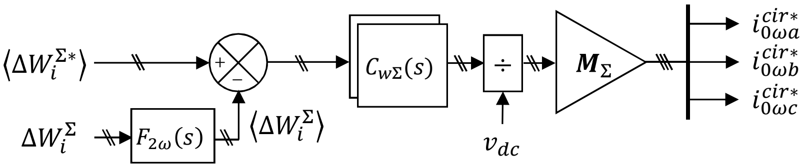

Figure 3.19: Block diagram representation of horizontal energy balancing controller.

#### 3.5.3.2 Vertical Energy Balancing Control

In a similar manner, the instantaneous signal of $\Delta W_i^{\Delta}$ must be filtered to extract the average, $\left\langle \Delta W_c^{\Delta} \right\rangle$. As noticed from (3.63), $\Delta W_i^{\Delta}$ consists of fundamental-frequency components in steady state. Therefore, by the notch filter $F_{1\omega}(s)$, the average value of $\Delta W_i^{\Delta}$ can be extracted:

$$\left\langle \Delta W_i^{\Delta} \right\rangle = F_{1\omega}(s)\, \Delta W_i^{\Delta}. \tag{3.75}$$

Denoting the *PI* controller by $C_{w\Delta}(s)$, the control law is developed from (3.63):

$$I_{1\omega i}^{cir*} = -\frac{1}{\sqrt{2}V_{ac}} \left( \left\langle \Delta W_i^{\Delta *} \right\rangle - \left\langle \Delta W_i^{\Delta} \right\rangle \right) C_{w\Delta}(s) \qquad i = a, b, c \tag{3.76}$$

where $V_{ac}$ is the rms value of the AC grid voltage. Then the calculated reference must be aligned with the AC voltage angle $\theta$ while ensuring the balance of the generated instantaneous references in the three phases. As described in detail in [152], it is possible to generate the balanced current references by introducing the coupling elements in the following way:

$$\boldsymbol{i}_{1\omega}^{cir*} = \boldsymbol{M}_\Delta \begin{bmatrix} I_{1\omega a}^{cir*} \\ I_{1\omega b}^{cir*} \\ I_{1\omega c}^{cir*} \end{bmatrix}, \tag{3.77}$$

where

$$\boldsymbol{M}_{\Delta} = \begin{bmatrix} \cos\theta & \frac{1}{\sqrt{3}}\cos\left(\theta + \frac{\pi}{2}\right) & \frac{1}{\sqrt{3}}\cos\left(\theta - \frac{\pi}{2}\right) \\ \frac{1}{\sqrt{3}}\cos\left(\theta - \frac{7\pi}{6}\right) & \cos\left(\theta - \frac{2\pi}{3}\right) & \frac{1}{\sqrt{3}}\cos\left(\theta - \frac{\pi}{6}\right) \\ \frac{1}{\sqrt{3}}\cos\left(\theta + \frac{7\pi}{6}\right) & \frac{1}{\sqrt{3}}\cos\left(\theta + \frac{\pi}{6}\right) & \cos\left(\theta - \frac{4\pi}{3}\right) \end{bmatrix}. \tag{3.78}$$

The diagonal elements make the reference values aligned to the AC voltage, while the off-diagonal elements ensure the balance in each column vector. The off-diagonal elements are shifted 90 degrees from the voltage angle of the corresponding phase, so they have minimum influence on the active power exchange between the upper and lower arms. The detailed control structure is depicted in Fig. 3.20.

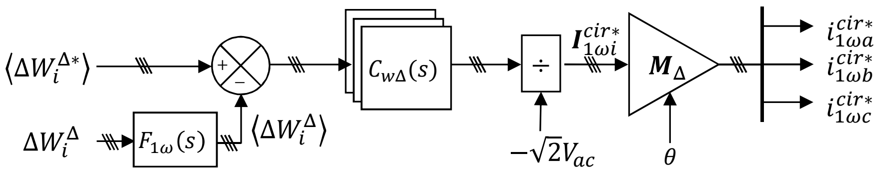

Figure 3.20: Block diagram representation of vertical energy balancing controller.

#### 3.5.3.3 Verification by Simulation

The horizontal and vertical energy balancing controllers are developed and implemented to the MMC used in the previous simulations. Fig. 3.21 shows the overview of the arm energy balancing control.

The set-point of the active power and the reference for the total energy are set at 500 MW and 1.0 p.u., respectively. The energy balancing controllers are initially deactivated. Then, at $t = 0.5$ s, the horizontal energy balancing controller is activated, and likewise the vertical energy balancing controller is activated at $t = 1.0$ s.

The obtained results are depicted in Fig. 3.22 and 3.23. As seen in Fig. 3.22a, the total energy stored in the MMC is maintained at a constant during the simulation. However, as observed in Fig. 3.22b, this energy may not be evenly distributed among the arms. Fig. 3.22c shows the horizontal energy balance. The time average values obtained by filtering the double fundamental frequency components are shown in dot-dash lines. When the horizontal energy balancing controller is activated at $t = 0.5$ s, the deviation of the

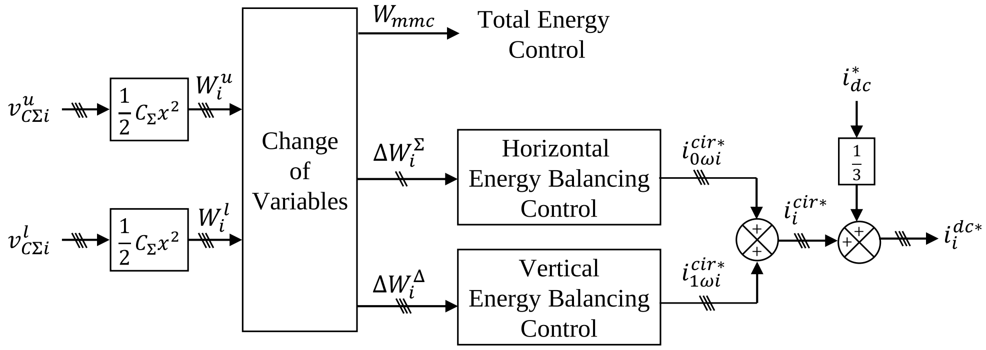

Figure 3.21: Overview of arm energy balancing control.

energy among the legs are reduced and converged to zero. Fig. 3.22d shows the vertical energy balance. The time average values are shown in dot-dash lines as well. Soon after the vertical energy balancing controller is activated, the vertical energy deviations are converged to zero, so that the energy in the upper and lower arms are balanced. As observed, there is no significant interaction between the horizontal and vertical energy balancing controls. Thus, their decoupling by the frequency decomposition technique is verified. When both horizontal and vertical energy deviations are eliminated, the energy distributed among the six arms converges to the same level (see Fig. 3.22b).

Fig. 3.23a shows the circulating currents. As expected, the non-oscillatory components are generated when the horizontal energy balancing controller is activated, whereas the fundamental-frequency components are generated by the vertical energy balancing controller. The AC and DC power as well as the AC/DC grid currents are shown in Fig. 3.23b, 3.23c, and 3.23d. No interaction with the energy balancing controllers is observed, and the AC and DC power are maintained at constant. From those simulation results, it is shown that the developed horizontal and vertical energy balancing controllers can effectively balance the energy among the converter arms without any interference with the actual energy exchanged between the AC/DC grids with the MMC.

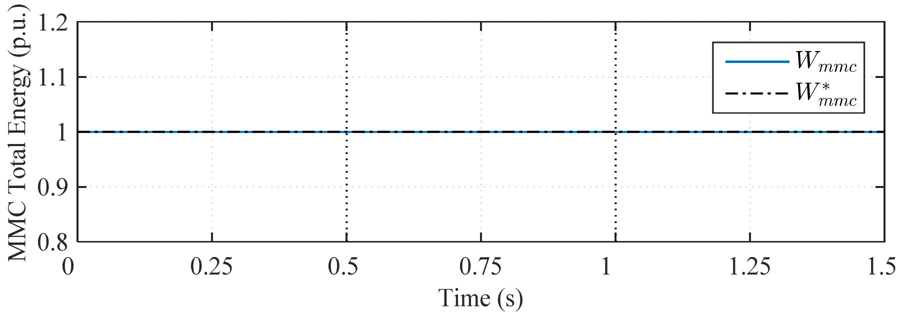

(a) Total energy

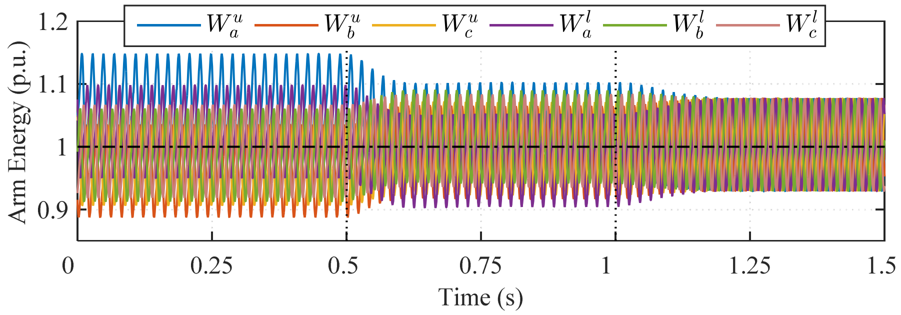

(b) Arm energy

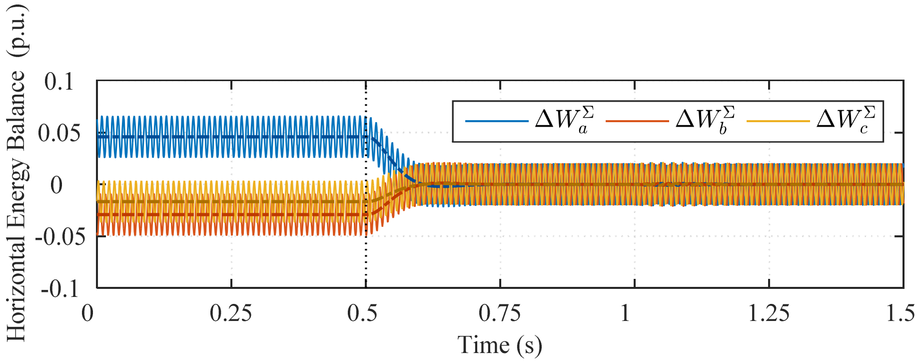

(c) Horizontal energy balance

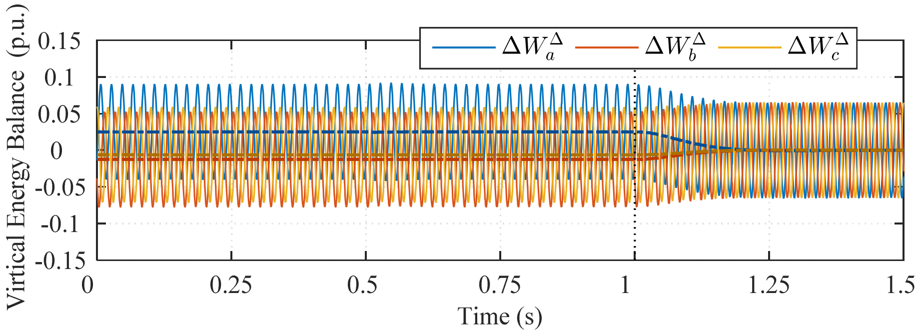

(d) Vertical energy balance

Figure 3.22: Simulation results: Arm energy balancing control (Energy).

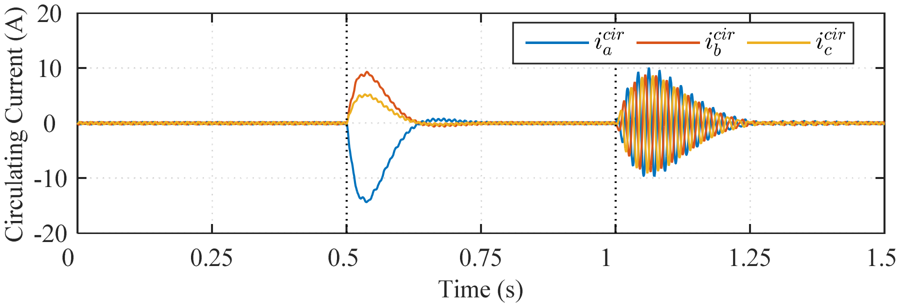

(a) Circulating current

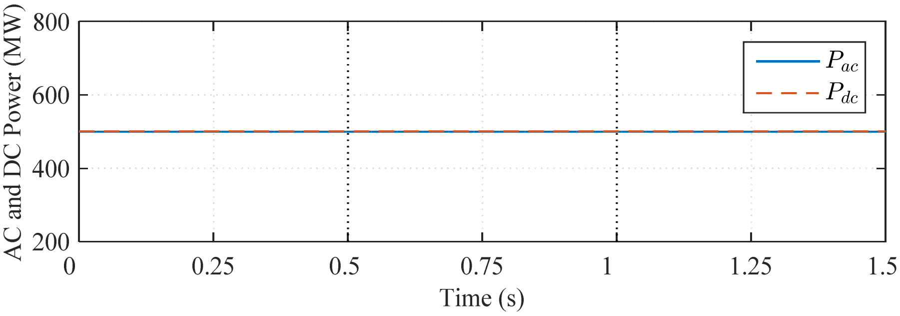

(b) AC and DC power

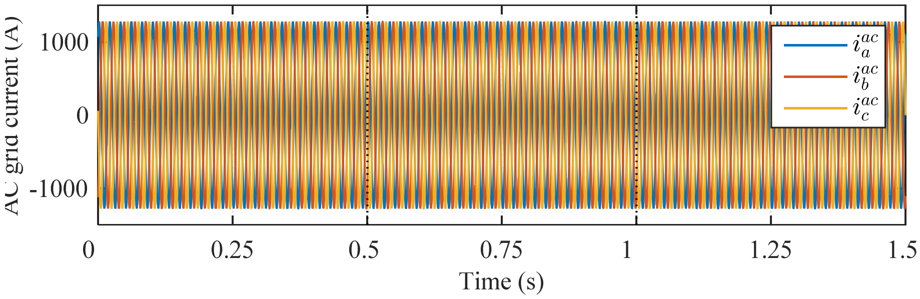

(c) AC grid current

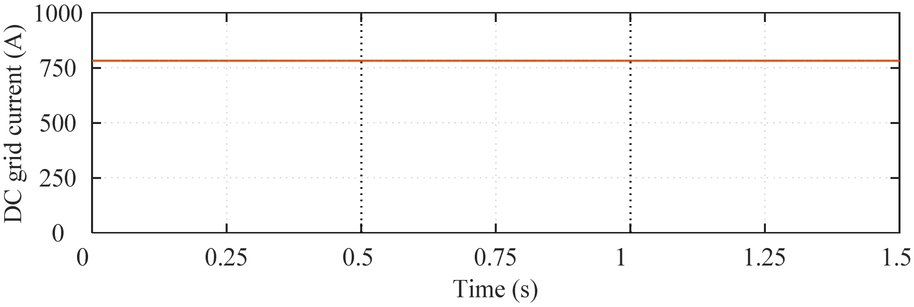

(d) DC grid current

Figure 3.23: Simulation results: Arm energy balancing control (Current & Power).

## 3.6 Chapter Conclusion

This chapter presented the basic design of the high level control of the MMC. Due to its unique topology and the modular structure, the MMC has a much larger number of the state variables to be controlled than classical VSCs. The controller considered in this chapter adapted the well-accepted cascaded control structure. The main advantage of such structure is that the complex system like MMC can be controlled by a set of relatively simple controllers.

The internal current dynamics of the MMC was first analyzed and modeled by leaving the gate control and switching states of the numerous power electronic devices out of account. The inner controller which governs the AC and DC currents was then developed by inverting the causality relation between the converter arm voltages and the currents to be controlled.

The outer controller was designed by regarding the dynamics sufficiently slower than the subordinate inner control loop. One of the challenges in this control level was to regulate the energy stored in the six converter arms. By an adequate change of variables, those six state variables were transformed into another set of six variables: the total energy stored inside the MMC and five other variables that represent the dispersion of the energy among the arms. From the developed energetic model, the two types of total energy controllers were developed, and their distinct differences were demonstrated by simulations. As the simulation results imply, the MMC can exchange energy with one of the associated grids by acting as an buffer energy storage without affecting the other grid. This inherent feature of the MMC — controllability of the internally stored energy — can be considered as an important additional degree of freedom which may be used to provide ancillary service to the associated grids. The following chapter will provide an in-depth analysis on this degree of freedom and a methodology to determine its feasible range to ensure proper operation of the MMC.

# Chapter 4

# Analysis of Energy Constraints on MMC

## 4.1 Chapter Introduction

The previous chapter demonstrated that the topology of the MMC enables independent control of the power exchange on the DC and AC sides. The mismatch between the DC power and the AC power induces a variation of the internally stored energy. In other words, the MMC can behave as an energy buffer capable of supplying or absorbing power exchanged with one side of converter without affecting the other side. This distinct feature of the MMC is an additional degree of freedom which does not exist in classical VSCs, and it may bring a great contribution to the stability of the associated grids.

Although this internal energy can be an attractive degree of freedom, its utilization is subject to certain limitations. In particular, it is conceivable that the internal energy cannot take any level. An excessive level of energy may lead to an abnormal voltage level of the capacitors in sub-modules (SMs) or even a failure of the components. On the contrary, a deficit of energy can potentially result in a deterioration of the proper function of the MMC. Therefore, the aforementioned degree of freedom can be effectively used only within a limited range.

In most of the earlier studies, this internally stored energy of the MMC was considered as a constant which is involuntarily determined by the SM capacitor size and the nominal DC voltage. Since the SM capacitor physically dominates the overall SM volume, minimizing its size has been one of the intensive research subjects of the MMC [88][153]. As will be discussed later, the SM capacitor voltage ripple is a driving factor for dimensioning of the MMC. The inventor of the MMC, Prof. Marquardt, provided an analysis of the peak-to-peak capacitor voltage ripple estimation in [154]. A numerical dimensioning approach to determine the minimum required size of the SM capacitor to satisfy the capacitor voltage specifications was proposed in [155]. A design criterion of the MMC from industrial perspective was demonstrated in [88]. A theoretical analysis on the minimum energy requirement provided in [156] revealed that the minimum energy requirement of the MMC is determined not only by the voltage constraints of the capacitor but also, to a greater extent, by the required power transfer capability. Although [156] describes the relation between the minimum energy requirement and the power transfer capability in a comprehensive manner, it involves a drawback in common with [88] or [155], which is that the proposed analytic expressions are solved by means of numerical calculations. Thus, those approaches may be useful for MMC dimensioning, i.e. in advance to the operation of the MMC, but not applicable during its actual operation where the associated grid conditions may not be precisely fixed at the nominal value. Furthermore, since those approaches focused on the dimensioning of the MMC, the relation between the present level of the internal energy and the permissible margins has never been clarified. In [157, 158, 159], extension of operational region by common mode DC current harmonics injection was discussed, which can reduce and shift the peak of the capacitor voltage ripple. Thus, by appropriate control, a better utilization of the capacitor voltage can be achieved. A similar approach that uses a Lagrange multiplier was proposed in [160]. What can be said in common about those approaches is that they are only possible at the expense of higher Joule losses and current rating of the SMs. Thus, they are not considered further in this thesis.

This chapter provides a thorough analysis on the limitations imposed on the internal energy stored in the MMC. The prime aim of this chapter is to derive the analytic formulas which enable to directly calculate those energy limits based on the operating point. Since the capacitor voltage ripples have a great impact on the energy limits, their behavior is first analyzed, and the analytic expressions which allow to precisely estimate the behavior of the voltage ripples are derived. Based on them, the upper and lower limits of the internally stored energy are mathematically formulated. Afterwards, the derived analytic formulas are confirmed by experiments on a small-scale MMC mock-up. Finally, the main points of this chapter are summarized in the conclusion.

## 4.2 Definition of Internal Energy Limits

First, the essential requirements to maintain the proper function of the MMC need to be specified. In order to facilitate the discussions, the topology of the MMC and the notation of some important variables are revisited. The most popular half-bridge SM topology is assumed. In practical operation, the voltages of the individual SM capacitors are balanced by means of a Balancing Control Algorithm (BCA) [126]. This allows considering only the average behavior of the converter arms which can be represented with great accuracy by the reduced-order arm average model shown in Fig. 4.1 (see Section 2.4.3.3 for more details on this model). The $N$ series-connected SMs are aggregated and represented by the total available voltage $v_{C\Sigma i}^{u,l}$ applied on the equivalent capacitor $C_\Sigma = C_{sm}/N$. The voltage applied on the arms $v_{mi}^{u,l}$ are determined by the continuous modulation index $m_i^{u,l}$.

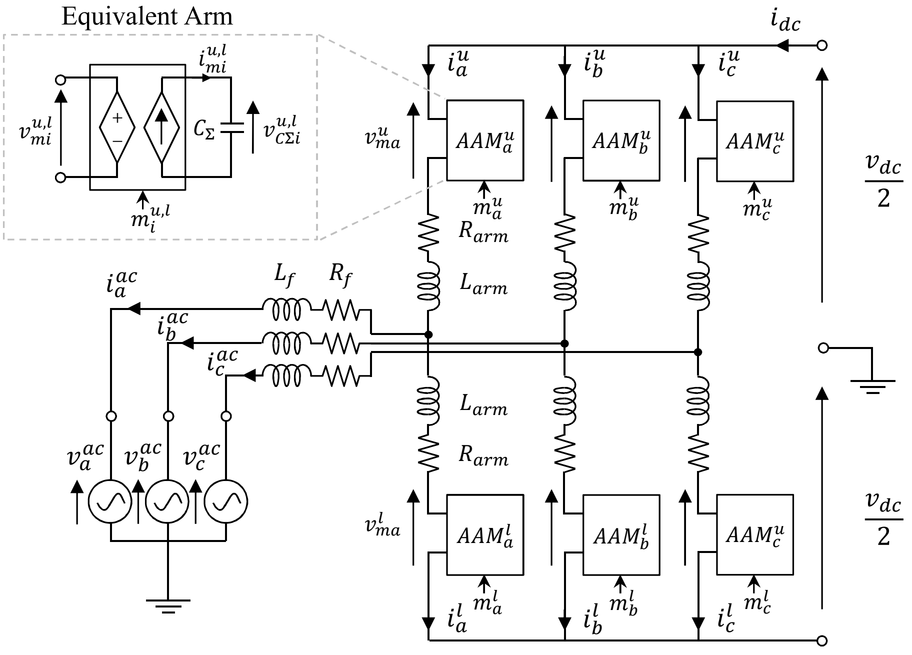

Figure 4.1: Reduced-order arm average model of three-phase MMC.

The equivalent capacitor in each arm can be regarded as an energy storage device:

$$W_i^u = \frac{1}{2} C_\Sigma \left(v_{C\Sigma i}^u\right)^2 \tag{4.1}$$

$$W_i^l = \frac{1}{2} C_\Sigma \left(v_{C\Sigma i}^l\right)^2 . \tag{4.2}$$

The total energy stored in the MMC is the sum of the energy in the six arms. Thus,

$$W_{mmc} = \sum_{i=a,b,c} W_i^u + \sum_{i=a,b,c} W_i^l . \tag{4.3}$$

The limits on the total energy is of the prime importance because its difference from the present level of the energy indicates the amounts of the energy which can be charged or discharged by the MMC. In fact, those limits are determined by the constraints imposed on the energy stored in each arm where the actual control actions are taken. As discussed in the previous chapter (see Section 3.5.3), the total energy in the MMC is evenly distributed among the six arms in steady state under an adequate arm energy balancing control. However, unlike the total energy which is normally constant in steady state, the energy in each arm contains intrinsic oscillations due to the instantaneous power exchange in each arm. That is to say, it is necessary to ensure that the total energy $W_{mmc}$ remains within the upper and lower limits, denoted by $W_{mmc}^{Lim+}$ and $W_{mmc}^{Lim-}$, as illustrated in Fig. 4.2, such that the energy in each arm will fulfill all the physical and control requirements even with those unavoidable intrinsic oscillations.

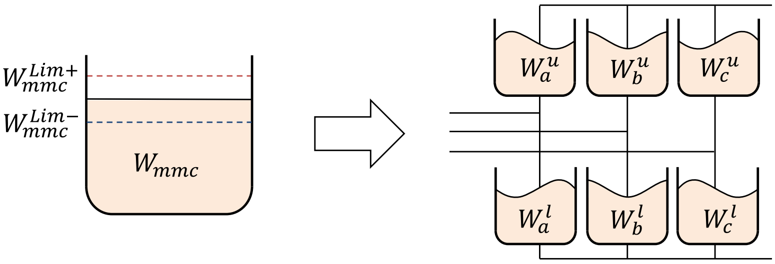

Figure 4.2: Conceptional image of energy location and constraints.

### 4.2.1 Constraint Related to Upper Energy Limit

The energy in the MMC is stored in the form of electrostatic energy in the SM capacitors. Thus, an increase of the total energy is equivalent to a rise in capacitor voltages. The maximum voltage that the capacitor can safely be exposed to is referred to as the rated voltage and is normally specified in the data sheets provided by the manufacturer [161]. Denoting the rated voltage of the SM capacitor by $V_C^{Max}$, any SM voltage $v_{Cij}^{u,l}$ must respect the following inequality at any moment $t$:

$$v_{Cij}^{u,l}(t) \leq V_C^{Max}. \tag{4.4}$$

When $N$ SMs comprise an arm and that no difference between the individual SM voltages are considered, the above mentioned expression can be rewritten as follows:

$$v_{C\Sigma i}^{u,l}(t) \leq V_{C\Sigma}^{Max}, \tag{4.5}$$

where $V_{C\Sigma}^{Max}$ is the maximum limit for the aggregated voltage in the arms which is equal to $V_{C\Sigma}^{Max} = N\, V_C^{Max}$. Perhaps it seems simple to respect the inequality above if the total capacitor voltage is constant. However, the instantaneous disparity in power exchanged in the arms gives rise to intrinsic voltage ripples in steady state.

Fig. 4.3 shows the typical shape of $v^{u}_{C\Sigma a}$ in nominal condition and that at the maximum limit of the total energy. An increase of the total energy causes a rise in the offset level of the capacitor voltages. Therefore, in order to ensure the proper operation of the MMC, the total energy must be maintained below the limit $W^{Lim+}_{mmc}$, so that the capacitor voltage will not violate the inequality above at its peak.

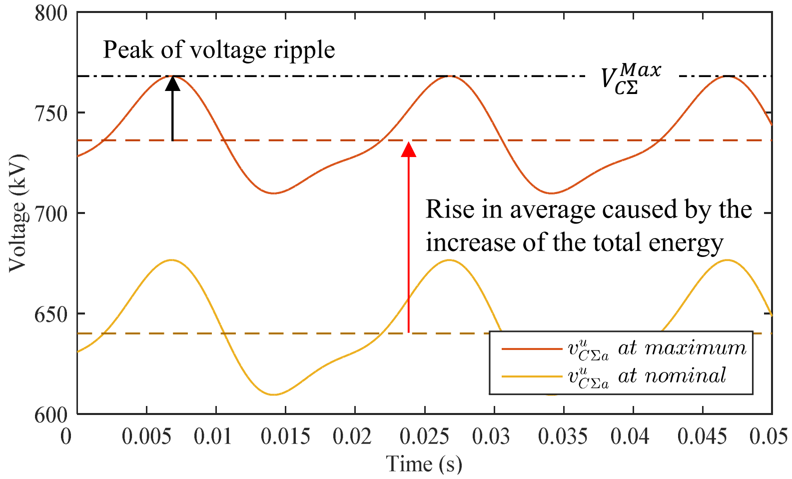

Figure 4.3: Conceptional image of constraint related to upper energy limit.

### 4.2.2 Constraint Related to Lower Energy Limit

In contrary to the previous constraint, the MMC must maintain a sufficient amount of energy to ensure its proper function. Let us suppose that the MMC controller commands to apply a certain voltage in an arm. In the MMC, the arm voltage is synthesized by using the SM capacitor voltages. Assuming that the number of the SMs in the arm is sufficiently large allows us to consider the continuous modulation indices $m^{u,l*}_{i}$ and the following relations which govern the synthesis of the arm voltage:

$$v^{u}_{mi}(t) = m^{u*}_{i}(t)\, v^{u}_{C\Sigma i}(t), \qquad v^{l}_{mi}(t) = m^{l*}_{i}(t)\, v^{l}_{C\Sigma i}(t). \tag{4.6}$$

The maximum voltage which can be realized in the arm is limited by the sum of the SM voltages; thus, $m^{u,l*}_{i} \leq 1$. Then, the following inequality must be respected:

$$v^{u}_{mi}(t) \leq v^{u}_{C\Sigma i}(t), \qquad v^{l}_{mi}(t) \leq v^{l}_{C\Sigma i}(t). \tag{4.7}$$

The inequalities above imply that a certain level of the capacitor voltage must be always secured; otherwise, the arm voltage required to deliver the desired power cannot be applied.

Fig. 4.4 shows the typical shape of $v^u_{C\Sigma a}$ and the arm voltage $v^u_{ma}$. A decrease in the total energy in the MMC appears as a decrease in the offset level of the capacitor voltages. In order to satisfy the inequality above, the total energy must be maintained above the limit $W^{Lim-}_{mmc}$, so that the total capacitor voltage will be always higher than the arm voltage to be synthesized. The desired arm voltage varies along with the power transfer and the associated grid conditions. Moreover, the shape of the capacitor voltage ripple changes according to the operating point of the converter. Therefore, a thorough analysis is required.

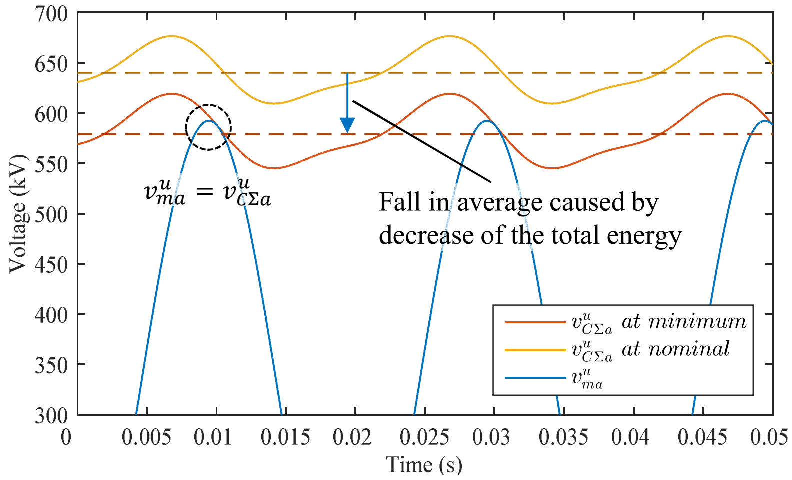

Figure 4.4: Conceptional image of constraint related to lower energy limit.

### 4.2.3 Workflow of Energy Limits Derivation

In Fig. 4.5, the workflow of the energy limits derivation which is described in the following is illustrated. We consider the DC/AC grid voltages ($V_{dc}$, $V_{ac}$, and $\omega$ ), AC active and reactive power ($P_{ac}$ and $Q_{ac}$) and the converter specifications as the input variables because they are definitely known in steady state. As mentioned earlier, the capacitor voltage ripples have a great influence on the energy limits. The analytic expressions that represent the steady-state behavior of the capacitor voltage ripples are the basis of the energy limits estimation. Based on the developed analytic expressions of the capacitor voltage ripple, the upper and the lower energy limits, $W^{Lim+}_{mmc}$ and $W^{Lim-}_{mmc}$, are analyzed separately with regard to the aforementioned constraints. In the end, both energy limits are formulated as functions of the aforementioned input parameters.

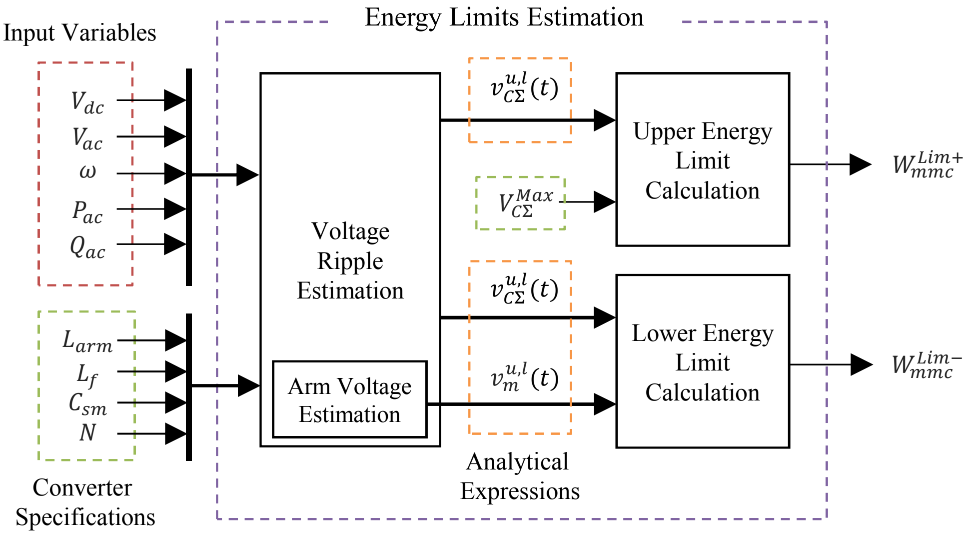

Figure 4.5: Workflow of energy limits estimation.

## 4.3 Analysis of Capacitor Voltage Ripples

The energy stored inside the MMC is restricted by the aforementioned constraints. The capacitor voltage ripples have a great influence on those constraints. In order to ensure the proper operation of the MMC, a thorough analysis on the capacitor voltage behavior is needed. This section provides a detailed analysis of the capacitor voltage ripple, and then the derived expressions are verified by simulations.

### 4.3.1 Steady-State Analysis of Arm Voltage and Current

For the sake of clarity, a symmetrical operation of the MMC is assumed. Therefore, the following analysis considers only one phase out of the three, and the index for the phase $i \in \{a, b, c\}$ in the subscript is omitted. However, the following analysis will be applicable for any other phase by only adjusting the phase shift.

In the MMC, the energy is stored in the form of electrostatic energy in the capacitors. Thus, the capacitor voltage ripple can be estimated from the steady-state behavior of the energy stored in the arm. The variation of the arm energy can be deduced from the power exchanged at the arm; hence, the product of the arm voltage and the current flows through the arms:

$$\begin{aligned} \frac{dW^{u}\left(t\right)}{dt} &= i^{u}\left(t\right)v_{m}^{u}\left(t\right) && (4.8)\\ \frac{dW^{l}\left(t\right)}{dt} &= i^{l}\left(t\right)v_{m}^{l}\left(t\right), && (4.9) \end{aligned}$$

where the arm voltages and currents are expressed by the synthesis of the AC and DC components (See Section 3.2):

$$\begin{aligned} v_{m}^{u}\left(t\right) &= \frac{v_{m}^{dc}\left(t\right)}{2} - v_{m}^{ac}\left(t\right) && (4.10)\\ v_{m}^{l}\left(t\right) &= \frac{v_{m}^{dc}\left(t\right)}{2} + v_{m}^{ac}\left(t\right) && (4.11)\\ i^{u}\left(t\right) &= i^{dc}\left(t\right) + \frac{i^{ac}\left(t\right)}{2} && (4.12)\\ i^{l}\left(t\right) &= i^{dc}\left(t\right) - \frac{i^{ac}\left(t\right)}{2}. && (4.13) \end{aligned}$$

Let us consider the steady-state condition. On the one hand, taking the AC grid voltage:

$$v_{ac}\left(t\right) = \sqrt{2}V_{ac}\cos\left(\omega t\right) \tag{4.14}$$

as the reference, the steady-state behavior of the equivalent AC voltage of the MMC and the AC current are expressed as:

$$\begin{aligned} v_{m}^{ac}\left(t\right) &= \sqrt{2}V_{m}^{ac}\cos\left(\omega t+\delta\right) && (4.15)\\ i^{ac}\left(t\right) &= \sqrt{2}I_{ac}\cos\left(\omega t+\theta\right) && (4.16) \end{aligned}$$

where $V_{m}^{ac}$ and $I_{ac}$ are the *rms* values of the equivalent AC voltage of the MMC and the grid current, $\delta$ the voltage angle, and $\theta$ the phase shift of the current from the grid voltage.

On the other hand, in steady state, the DC components are given by:

$$\begin{aligned} v_{m}^{dc}\left(t\right) &= V_{m}^{dc} && (4.17)\\ i^{dc}\left(t\right) &= \frac{I_{dc}}{3} && (4.18) \end{aligned}$$

where $V_{m}^{dc}$ is the equivalent DC voltage of the MMC, and $I_{dc}$ is the DC grid current which is evenly distributed among the three phase legs in steady state. Accordingly, (4.10) to (4.13) can be rewritten as follows:

$$\begin{aligned} v_{m}^{u}\left(t\right) &= \frac{V_{m}^{dc}}{2} - \sqrt{2}V_{m}^{ac}\cos\left(\omega t+\delta\right) && (4.19)\\ v_{m}^{l}\left(t\right) &= \frac{V_{m}^{dc}}{2} + \sqrt{2}V_{m}^{ac}\cos\left(\omega t+\delta\right) && (4.20)\\ i^{u}\left(t\right) &= \frac{I_{dc}}{3} + \frac{I_{ac}}{\sqrt{2}}\cos\left(\omega t+\theta\right) && (4.21)\\ i^{l}\left(t\right) &= \frac{I_{dc}}{3} - \frac{I_{ac}}{\sqrt{2}}\cos\left(\omega t+\theta\right). && (4.22) \end{aligned}$$

In steady state, it is possible to find the variables in (4.19) to (4.22) as the functions of the operating power and the associated grid voltages. More specifically, those intermediate variables necessary to estimate the steady-state behavior of the capacitor voltage, $\psi = \left\{V_m^{ac}, V_m^{dc}, \delta, I_{ac}, I_{dc}, \theta\right\}$, can be expressed in terms of the input variables $\chi = \{P_{ac}, Q_{ac}, V_{ac}, V_{dc}, \omega\}$, which must be known in steady state.

When the total energy stored inside the MMC is balanced, the DC power $P_{dc}$ is expressed in terms of $P_{ac}$ and the total loss generated in the MMC denoted by $P_{loss}$:

$$P_{dc} = P_{ac} + P_{loss}. \tag{4.23}$$

$P_{loss}$ includes the conduction losses, the switching losses, and the ohmic losses in the inductors [162]. The conduction losses occur in any switching devices in the SMs in conduction. The switching losses are the energy dissipated in each switching action, which strongly depends on the selection of the BCA. In general, the losses in the MMC are insignificant (typically less than 1 % [163]). Since the precise estimation of the losses is not pertinent to the analysis here, those losses are neglected for the sake of simplicity. Thus, the following assumption is made:

$$P_{dc} \overset{hyp}{=} P_{ac}. \tag{4.24}$$

In a three-phase system, the active and reactive power flows into the AC grid is given by:

$$P_{ac} + jQ_{ac} = 3\vec{V}_{ac}\overline{\vec{I}_{ac}} = 3V_{ac}\left(I_{ac}\cos\theta - jI_{ac}\sin\theta\right), \tag{4.25}$$

where the positive sign of the active and reactive power indicates the power is supplied to the AC grid. The amplitude of the current and the power angle are given by:

$$I_{ac} = \frac{\sqrt{P_{ac}^2 + Q_{ac}^2}}{3V_{ac}} \tag{4.26}$$

$$\theta = \begin{cases} \arctan\left(-\dfrac{Q_{ac}}{P_{ac}}\right) & \text{if}\, P_{ac} > 0 \\ \arctan\left(-\dfrac{Q_{ac}}{P_{ac}}\right) + \pi & \text{if}\, P_{ac} < 0 \end{cases}. \tag{4.27}$$

From the voltage drop across the phase reactor, the equivalent AC voltage of the MMC are expressed as functions of the active and reactive power:

$$V_m^{ac} = \sqrt{\left(\frac{X_{eq}^{ac}Q_{ac}}{3V_{ac}} + V_{ac}\right)^2 + \left(\frac{X_{eq}^{ac}P_{ac}}{3V_{ac}}\right)^2} \tag{4.28}$$

$$\delta = \arctan\frac{X_{eq}^{ac}P_{ac}}{X_{eq}^{ac}Q_{ac} + 3V_{ac}^2}. \tag{4.29}$$

The DC side variables are relatively simple. The DC grid current $I_{dc}$ can be derived from the active power $P_{ac}$ and the DC grid voltage $V_{dc}$:

$$I_{dc} = \frac{P_{ac}}{V_{dc}}, \tag{4.30}$$

and the common mode DC voltage is assumed to be:

$$V_m^{dc} = V_{dc}. \tag{4.31}$$

Accordingly, the intermediate variables, $V_m^{ac}$, $V_m^{dc}$, $\delta$, $I_{ac}$, $I_{dc}$, $\theta$, are hereinafter considered as estimable quantities from the operating power and the AC/DC grid voltages. More detailed descriptions about derivation of the above expressions can be found in Appendix B.

### 4.3.2 Capacitor Voltage Ripple Estimation

Let us return to the main issue. Substituting (4.19) to (4.22) into (4.8) and (4.9) yields the steady-state dynamics of the arm energy:

$$\begin{aligned}\frac{dW^u(t)}{dt} = \frac{I_{dc}V_m^{dc}}{6} - \frac{\sqrt{2}I_{dc}V_m^{ac}}{3}\cos(\omega t+\delta) \\ + \frac{I_{ac}V_m^{dc}}{2\sqrt{2}}\cos(\omega t+\theta) - \frac{I_{ac}V_m^{ac}}{2}\left\{\cos(2\omega t+\delta+\theta)+\cos(\theta-\delta)\right\}\end{aligned} \tag{4.32}$$

$$\begin{aligned}\frac{dW^l(t)}{dt} = \frac{I_{dc}V_m^{dc}}{6} + \frac{\sqrt{2}I_{dc}V_m^{ac}}{3}\cos(\omega t+\delta) \\ - \frac{I_{ac}V_m^{dc}}{2\sqrt{2}}\cos(\omega t+\theta) + \frac{I_{ac}V_m^{ac}}{2}\left\{\cos(2\omega t+\delta+\theta)+\cos(\theta-\delta)\right\}.\end{aligned} \tag{4.33}$$

By replacing $V_m^{dc}$ of the first term by (4.31) and using the fact that

$$V_m^{ac}\cos(\theta-\delta) = V_{ac}\cos\theta, \tag{4.34}$$

the previous equations can be rewritten as:

$$\begin{aligned}\frac{dW^u(t)}{dt} = \frac{I_{dc}V_{dc}}{6} - \frac{I_{ac}V_{ac}}{2}\cos\theta - \frac{\sqrt{2}I_{dc}V_m^{ac}}{3}\cos(\omega t+\delta) \\ + \frac{I_{ac}V_m^{dc}}{2\sqrt{2}}\cos(\omega t+\theta) - \frac{I_{ac}V_m^{ac}}{2}\cos(2\omega t+\delta+\theta)\end{aligned} \tag{4.35}$$

$$\begin{aligned}\frac{dW^l(t)}{dt} = \frac{I_{dc}V_{dc}}{6} - \frac{I_{ac}V_{ac}}{2}\cos\theta + \frac{\sqrt{2}I_{dc}V_m^{ac}}{3}\cos(\omega t+\delta) \\ - \frac{I_{ac}V_m^{dc}}{2\sqrt{2}}\cos(\omega t+\theta) - \frac{I_{ac}V_m^{ac}}{2}\cos(2\omega t+\delta+\theta).\end{aligned} \tag{4.36}$$

The first two terms on the right sides of the equations above represent the balance between the AC and DC power. Since we assume that the internal losses are negligible, the sum of those terms must be zero when the energy is stabilized. The remaining terms represent the intrinsic oscillations of the energy. It consists of two fundamental frequency components and a component which oscillates at twice of the fundamental frequency.

The stored energy level in the upper and lower arm can be obtained by the time-integral of (4.35) and (4.36). Before taking the time-integral, the initial timing must be aptly chosen. By assuming the initial time $t_0^u$ and $t_0^l$ such that the sum of the oscillatory components becomes zero for the upper and lower arms, respectively, we can define the initial energy level as the time average value of the stored energy. Let us suppose

$$-\frac{\sqrt{2}I_{dc}V_m^{ac}}{3\omega}\sin\left(\omega t_0^u+\delta\right)+\frac{I_{ac}V_m^{dc}}{2\sqrt{2}\omega}\sin\left(\omega t_0^u+\theta\right)-\frac{I_{ac}V_m^{ac}}{4\omega}\cos\left(2\omega t_0^u+\delta+\theta\right)=0 \tag{4.37}$$

$$\frac{\sqrt{2}I_{dc}V_m^{ac}}{3\omega}\sin\left(\omega t_0^l+\delta\right)-\frac{I_{ac}V_m^{dc}}{2\sqrt{2}\omega}\sin\left(\omega t_0^l+\theta\right)-\frac{I_{ac}V_m^{ac}}{4\omega}\cos\left(2\omega t_0^l+\delta+\theta\right)=0. \tag{4.38}$$

Then denoting the time average of the energy by $W_0^u$ and $W_0^l$, the energy stored in upper and lower arms are given as follows:

$$\begin{aligned} W^u(t) &= \int_{t_0^u}^{t}\frac{dW^u(\tau)}{d\tau}d\tau+W_0^u \\ &= \left[\frac{I_{dc}V_{dc}}{6}-\frac{I_{ac}V_{ac}}{2}\cos\theta\right](t-t_0^u) \\ &\quad+\left[-\frac{\sqrt{2}I_{dc}V_m^{ac}}{3\omega}\sin(\omega t+\delta)+\frac{I_{ac}V_m^{dc}}{2\sqrt{2}\omega}\sin(\omega t+\theta)\right] \\ &\quad+\left[-\frac{I_{ac}V_m^{ac}}{4\omega}\cos(2\omega t+\delta+\theta)\right]+W_0^u \end{aligned} \tag{4.39}$$

$$\begin{aligned} W^l(t) &= \int_{t_0^l}^{t}\frac{dW^l(\tau)}{d\tau}d\tau+W_0^l \\ &= \left[\frac{I_{dc}V_{dc}}{6}-\frac{I_{ac}V_{ac}}{2}\cos\theta\right]\left(t-t_0^l\right) \\ &\quad+\left[\frac{\sqrt{2}I_{dc}V_m^{ac}}{3\omega}\sin(\omega t+\delta)-\frac{I_{ac}V_m^{dc}}{2\sqrt{2}\omega}\sin(\omega t+\theta)\right] \\ &\quad+\left[-\frac{I_{ac}V_m^{ac}}{4\omega}\cos(2\omega t+\delta+\theta)\right]+W_0^l. \end{aligned} \tag{4.40}$$

The first terms represent the AC and DC power balance. The second and third terms represent the oscillatory components of the energy. Each arm energy consists of two fundamental frequency components and a component which oscillates at twice of the fundamental frequency. Thus, the arm energy can be decomposed into the oscillatory component, $\widetilde{W}^{u}(t)$ or $\widetilde{W}^{l}(t)$, and the time average value as:

$$\begin{aligned} W^{u}(t) &= \widetilde{W}^{u}(t) + W_0^{u} \qquad (4.41) \\ W^{l}(t) &= \widetilde{W}^{l}(t) + W_0^{l} \qquad (4.42) \end{aligned}$$

where

$$\widetilde{W}^{u}(t) = -\frac{\sqrt{2} I_{dc} V_m^{ac}}{3\omega} \sin(\omega t + \delta) + \frac{I_{ac} V_m^{dc}}{2\sqrt{2}\omega} \sin(\omega t + \theta) - \frac{I_{ac} V_m^{ac}}{4\omega} \cos(2\omega t + \delta + \theta) \qquad (4.43)$$

$$\widetilde{W}^{l}(t) = +\frac{\sqrt{2} I_{dc} V_m^{ac}}{3\omega} \sin(\omega t + \delta) - \frac{I_{ac} V_m^{dc}}{2\sqrt{2}\omega} \sin(\omega t + \theta) - \frac{I_{ac} V_m^{ac}}{4\omega} \cos(2\omega t + \delta + \theta). \qquad (4.44)$$

When the total energy in the MMC is evenly distributed among all the arms, the time average values must be given by:

$$W_0^{u} = W_0^{l} = \frac{W_{mmc}}{6}. \qquad (4.45)$$

Finally, the total capacitor voltages are derived from the estimated arm energy:

$$\begin{aligned} v_{C\Sigma}^{u}(t) &= \sqrt{\frac{2}{C_\Sigma} W^{u}(t)} \qquad (4.46) \\ v_{C\Sigma}^{l}(t) &= \sqrt{\frac{2}{C_\Sigma} W^{l}(t)}. \qquad (4.47) \end{aligned}$$

In Fig. 4.6, the synthesis of the capacitor voltage estimation procedure is illustrated. Now the steady-state behavior of the total capacitor voltage $v_{C\Sigma}^{u,l}(t)$ are readily estimable according to the input variables $\chi$.

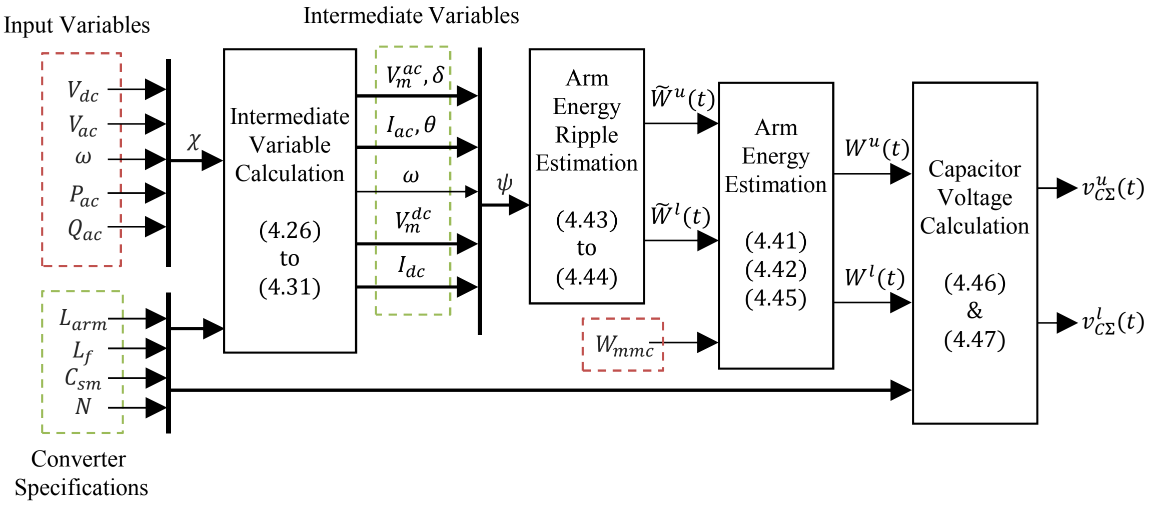

Figure 4.6: Synthesis of capacitor voltage estimation procedure.

### 4.3.3 Verification by Simulation

In this subsection, the derived expressions and the aforementioned capacitor voltage estimation procedure are verified by simulations. A three-phase MMC represented by reduced-order arm average model is implemented in EMTP-RV platform. The MMC is rated at 1000 MW and connected to a DC voltage source ($V_{dc}$ = 640 kV) and an AC voltage source ($V_{ac}$ = 320 kV). The equivalent capacitance of the arm is 32.55 $\mu$F, i.e. the base quantity of the energy stored in an arm is defined as 6.67 MJ. More detailed specifications of the MMC are summarized in Appendix A. The simulation concerns the MMC under inverter operation, providing an active power of 0.7 p.u. and a reactive power of 0.1 p.u. to the AC grid. The total energy in the MMC is maintained at the nominal level. Then, the obtained dynamics of the arm energy as well as the total capacitor voltages are compared with those derived by the analytic expressions.

Fig. 4.7 shows the simulation results. In Fig. 4.7a, estimated waveform of each oscillatory terms, which are defined as:

$$\widetilde{W}^{u}_{\omega 1} = -\frac{\sqrt{2} I_{dc} V^{ac}_{m}}{3\omega} \sin\left(\omega t + \delta\right) \tag{4.48}$$

$$\widetilde{W}^{u}_{\omega 2} = \frac{I_{ac} V^{dc}_{m}}{2\sqrt{2}\omega} \sin\left(\omega t + \theta\right) \tag{4.49}$$

$$\widetilde{W}^{u}_{2\omega} = -\frac{I_{ac} V^{ac}_{m}}{4\omega} \cos\left(2\omega t + \delta + \theta\right), \tag{4.50}$$

and their composition $\widetilde{W}^{u}\left(t\right)$ are depicted. As seen, the waveform of the energy ripple is distorted and is not a sinusoidal wave. In Fig. 4.7b, the measured waveform of the energy in the upper arm of phase $a$ is compared with the one estimated from (4.41) where the oscillatory components are derived from (4.43) as well. As expected, the arm energy oscillates around its average value, and the estimated waveform shown in the dashed line corresponds well to the simulation result. Fig. 4.7c shows the comparison of the total capacitor voltages obtained by the simulation and the ones derived analytically. The estimated waveforms correspond very well to the simulation results. Therefore, it is confirmed that the derived analytic expressions can adequately represent the total capacitor voltage as well as the total energy, and thus they can be used to find the energy limits.

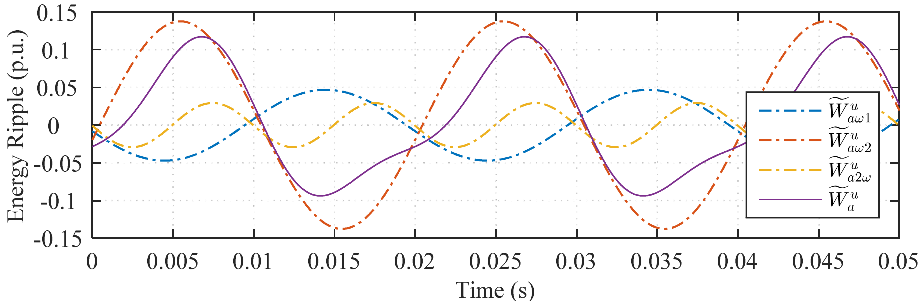

(a) Energy ripple and oscillatory components

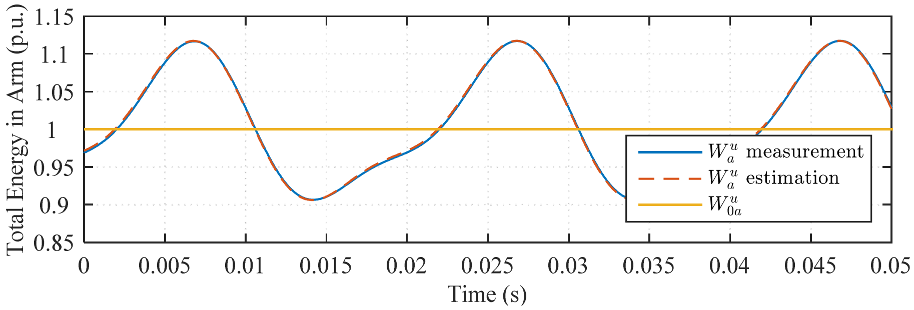

(b) Comparison of the estimation with simulation results: Total energy in arm

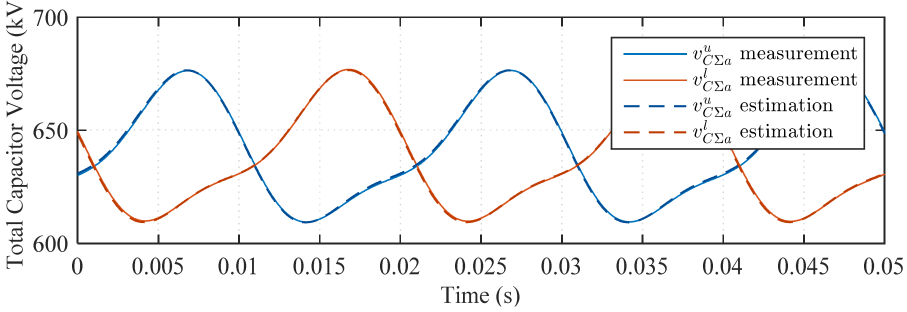

(c) Comparison of the estimation with simulation results: Total capacitor voltage

Figure 4.7: Verification of capacitor voltage ripple estimation.

## 4.4 Analysis on Upper Limit of Energy

The total energy stored inside the MMC must be below the certain level referred to here as $W_{mmc}^{Lim+}$ in order not to violate the rated voltage of the SM capacitor at any instance. This section provides a thorough analysis of the upper limit of the energy. The influence of the power at the operating point as well as the associated grid conditions are also discussed.

### 4.4.1 Derivation of Upper Energy Limit

When the stored energy is evenly distributed among the converter arms, the difference between the upper and lower should be only the phase shift. In such case, exactly the same limit should be assigned to both arms. Thus, only the analysis for the upper arm is provided in the following.

The inequality (4.5) can be rewritten in terms of energy by using (4.1):

$$W^u\left(t\right) \leq \frac{1}{2} C_\Sigma (V_{C\Sigma}^{Max})^2. \tag{4.51}$$

As discussed in the previous section, the arm energy can be decomposed into the oscillatory component and the constant component. Introducing (4.41) to (4.51) yields:

$$\widetilde{W}^u\left(t\right) + W_0^u \leq \frac{1}{2} C_\Sigma (V_{C\Sigma}^{Max})^2. \tag{4.52}$$

In order to ensure the inequality above during the operation, it is necessary to consider the worst condition where the arm energy reaches its maximum peak and the above inequality takes equality at that moment. Under the assumption that the energy is evenly distributed among the arms, the level of the total energy which agrees with this worst case is given by $W_{mmc} = W_{mmc}^{Lim+}$. Then, denoting the timing where the arm energy reaches its peak by $t_p^+$, the problem to be solved is stated as:

$$\widetilde{W}^u\left(t\right) + \frac{W_{mmc}^{Lim+}}{6} \leq \frac{1}{2} C_\Sigma (V_{C\Sigma}^{Max})^2 \tag{4.53}$$

with equality at $t = t_p^+$.

Fig. 4.8 illustrates the relation between the arm energy, total capacitor voltage and the arm current in the worst case condition. The timing which gives the maximum peak of the energy can be found by seeking the condition that the derivative of the energy takes zero. The evolution of the arm energy is given by the power exchanged at the arm. From (4.8), it is expressed by:

$$\left.\frac{dW^u\left(t\right)}{dt}\right|_{t=t_p^+} = i^u(t_p^+) v_m^u(t_p^+) = 0. \tag{4.54}$$

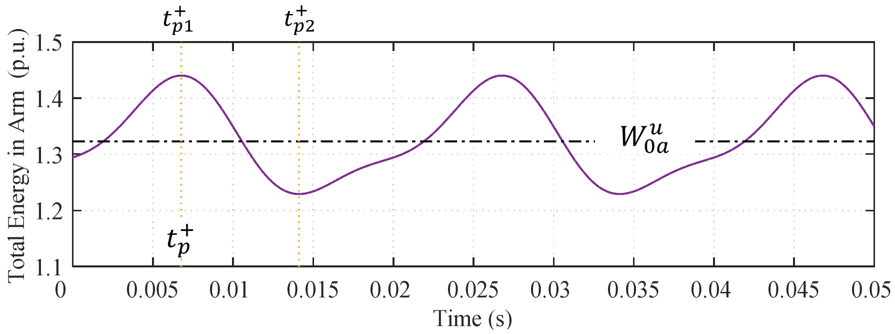

(a) Total energy in arm: $W_a^u$

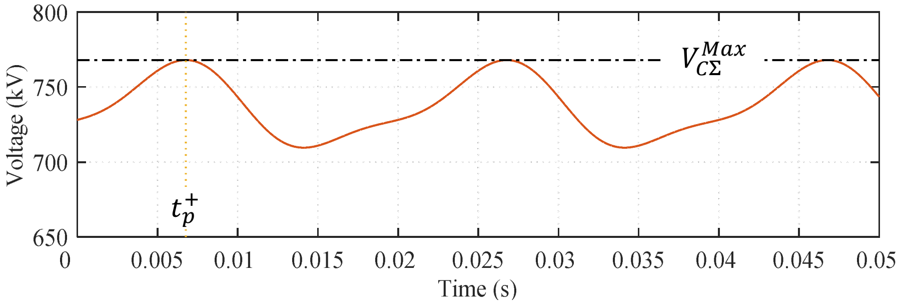

(b) Total capacitor voltage: $v_{C\Sigma}^u$

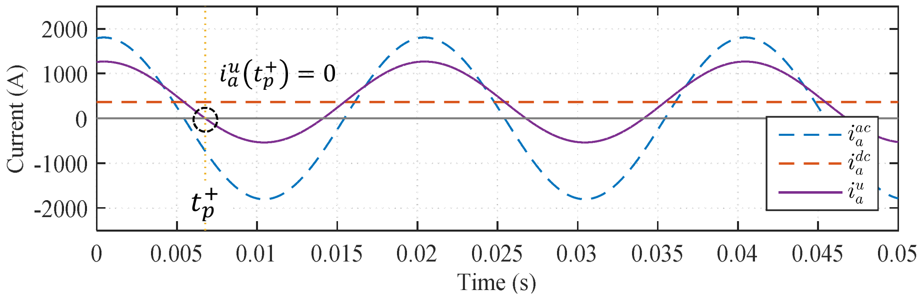

(c) Arm current: $i_a^u$

Figure 4.8: Exemplary illustration of the arm energy, the total capacitor voltage and the arm current at the upper energy limit.

It is obvious that the peak of the energy ripple is achieved either when $i^u(t_p^+)$ or $v_m^u(t_p^+)$ is zero. Since $v_m^u$ only takes a value larger than zero in the half-bridge MMC, we must have $i^u(t_p^+) = 0$. From the steady-state representation of $i_i^u$ given in (4.21), the condition which must hold is given by:

$$i^u(t_p^+) = \frac{I_{dc}}{3} + \frac{I_{ac}}{\sqrt{2}} \cos\left(\omega t_p^+ + \theta\right) = 0. \tag{4.55}$$

Since the inverse function of the cosine takes the range of $[0, \pi]$, solving (4.55) in terms of $t_p^+$ yields two possible solutions:

$$t_{p1}^+ = \frac{1}{\omega}\left\{\arccos\left(-\frac{\sqrt{2}I_{dc}}{3I_{ac}}\right) - \theta\right\} + \frac{2k\pi}{\omega} \tag{4.56}$$

$$t_{p2}^+ = \frac{1}{\omega}\left\{-\arccos\left(-\frac{\sqrt{2}I_{dc}}{3I_{ac}}\right) - \theta\right\} + \frac{2k\pi}{\omega} \tag{4.57}$$

where $k = 0, 1, ..., n$. The first solution corresponds to the case where $\omega t_p^+ + \theta$ is placed in the upper plane of the Cartesian coordinate and the other in the lower plane. When the energy reaches its maximum peak, its second derivative must be negative. Considering that $i_i^u$ takes zero at $t_p^+$, the second derivative of $W^u(t)$ is given by:

$$\begin{aligned} \left.\frac{d^2W^u(t)}{dt^2}\right|_{t=t_p^+} &= \left.\frac{di^u(t)}{dt}\right|_{t=t_p^+} v_m^u(t_p^+) + i^u(t_p^+)\left.\frac{dv_m^u(t)}{dt}\right|_{t=t_p^+} \\ &= -\frac{\omega I_{ac}}{\sqrt{2}} \sin\left(\omega t_p^+ + \theta\right) v_m^u(t_p^+) \leq 0. \end{aligned} \tag{4.58}$$

Recalling that $v_m^u$ can only take positive values, the inequality above can be simplified to:

$$-\frac{\omega I_{ac}}{\sqrt{2}} \sin\left(\omega t_p^+ + \theta\right) \leq 0. \tag{4.59}$$

The required condition can be satisfied only when $\omega t_p^+ + \theta$ is placed in the upper plane of the Cartesian coordinate. Consequently, the timing which satisfies the considered condition is:

$$t_p^+ = \frac{1}{\omega}\left\{\arccos\left(-\frac{\sqrt{2}I_{dc}}{3I_{ac}}\right) - \theta\right\} + \frac{2k\pi}{\omega}. \tag{4.60}$$

Finally, substituting the obtained $t_p^+$ into (4.53) yields the upper limit of the energy:

$$W_{mmc}^{Lim+} = 6\left\{\frac{1}{2}C_\Sigma (V_{C\Sigma}^{Max})^2 - \widetilde{W}^u(t_p^+)\right\} \tag{4.61}$$

where the ripple of the energy can be readily calculated from (4.43). The total energy in the MMC must be always lower than the obtained upper limit $W_{mmc}^{Lim+}$ in order not to exceed the rated voltage of the SM capacitor in steady state.

The value of $V_{C\Sigma}^{Max}$ depends on the converter specification and the SM's rated voltage $V_C^{Max}$. As an example, let us assume that the SM capacitors admit a 20 % voltage rise from its nominal voltage, i.e. $V_C^{Max} = 1.2\, V_C^{Nom}$. Fig. 4.9 shows the upper limit of energy calculated for different operating power. The black circle shows the rated apparent power of the converter. To maintain the maximum peak of the SM voltage below $V_C^{Max}$, the total energy must be always maintained below the obtained surface. It can be observed that a larger power transmission imposes severer constraints on the operating point of the energy. Since the voltage ripple is generated by the instantaneous difference between the DC and AC power exchanged in the arm, a larger power transfer leads to a larger amplitude of the voltage ripple, hence, a higher voltage peak. In such case, the offset level of the SM voltage needs to be set lower in order to secure a larger headroom.

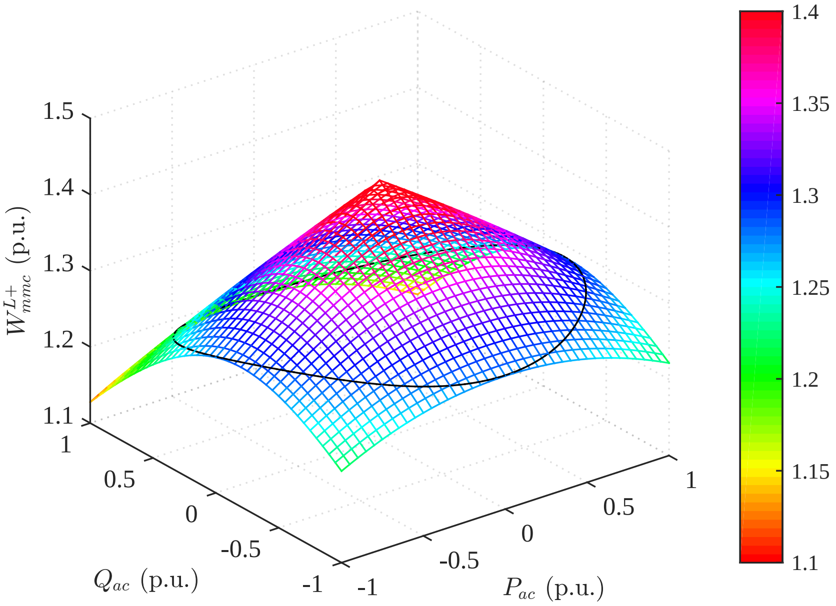

Figure 4.9: Upper limit of total energy against active and reactive power.

### 4.4.2 Sensitivity Analysis on Upper Energy Limit

The provided analysis implies that the upper limit of the energy is influenced by the associated grid conditions and the converter specifications. In practice, the associated grid voltages may not be always fixed at the nominal level. Thus, it is important to understand how the upper energy limit changes with the grid voltages. Moreover, since the SM capacitor size has a major influence on the cost of the converter, clarifying its influence on the limit can provide useful information for the converter dimensioning. Therefore, the following discusses the influences of the DC and AC grid voltages as well as the SM capacitor size on the upper limit of the energy.

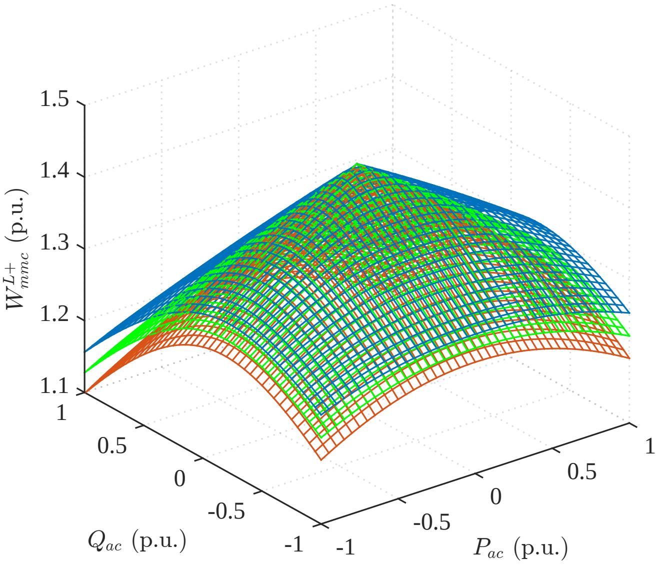

Figure 4.10: Sensitivity study on upper limit of total energy against DC grid voltage (red: $V_{dc} = 1.1$ p.u., green: 1.0 p.u., and blue: 0.9 p.u.).

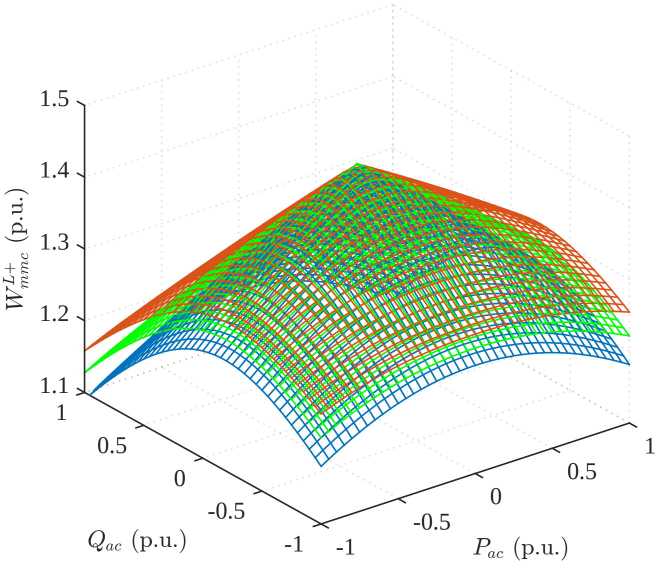

Figure 4.11: Sensitivity study on upper limit of total energy against AC grid voltage (red: $V_{ac} = 1.1$ p.u., green: 1.0 p.u., and blue: 0.9 p.u.).

In Figs. 4.10 and 4.11, the upper limits of the total energy for different DC or AC grid voltages are shown. For both case, ±10 % variation is demonstrated as it is a typical requirement for the operating range of AC grid voltage [61]. Interestingly, a higher DC voltage imposes severer upper limit of the energy, whereas a higher AC voltage loosens this constraint. This can be explained from (4.43). As it can be observed in Fig. 4.7a, the second term of (4.43) dominates the impact on the amplitude of the energy ripple. Thus, it can be said that the peak value of the capacitor voltage is highly influenced by its coefficient, $I_{ac}V_m^{dc}$. In steady state, as (4.31) implies, $V_m^{dc}$ increases in proportion to the DC voltage. On the contrary, as (4.26) indicates, $I_{ac}$ increases inversely proportionally to the AC voltage. For those reasons, the influence of the associated grid voltages are in opposite direction between the DC and AC sides.

Understandably, the amplitude of the capacitor voltage ripple depends on the capacitance value of the SMs. Fig. 4.12 shows the upper limit of the energy calculated for different SM capacitor sizes (increased or decreased by 20 %). Since a smaller capacitor leads to a higher peak of the capacitor voltage ripple, a smaller capacitor imposes severer upper limit of energy. As the capacitor size increases, the influence of the ripple on the upper energy limit becomes smaller; hence, it becomes substantially flatter.

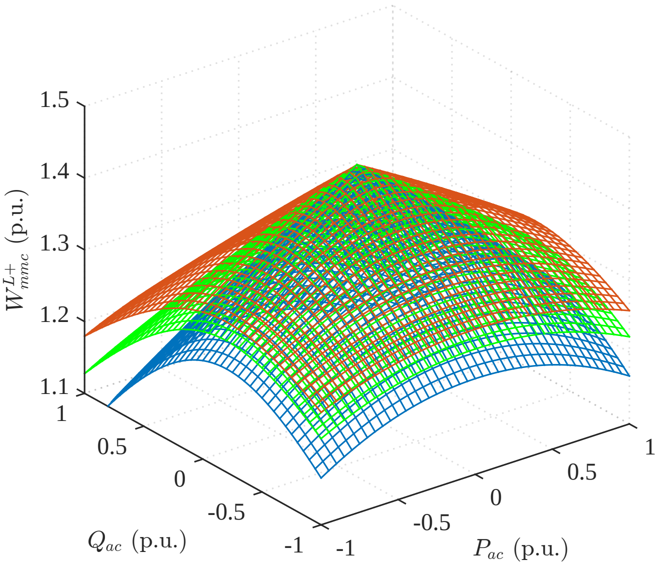

Figure 4.12: Sensitivity study on upper limit of total energy against SM capacitor size (red: $C_{sm} = 15.6$ mF, green: 13.0 mF, and blue: 10.4 mF).

## 4.5 Analysis on Lower Limit of Energy

The capacitor voltages must be always maintained sufficiently high; otherwise, they may not be capable of applying the arm voltages required to deliver the desired power. This section investigates the minimum requirement of the total energy stored in the MMC referred to here as $W_{mmc}^{Lim-}$. The influences of the associated grids condition are analyzed as well.

### 4.5.1 Derivation of Lower Energy Limit

The maximum arm voltage is determined by the available voltage in the arm, i.e. total capacitor voltage $v_{C\Sigma}$. Concerning the decoupling between the DC and AC components in the arm voltages, the required condition of (4.7) can be rewritten respectively as:

$$\frac{v_m^u(t)}{v_{C\Sigma}^u(t)} = \frac{\frac{v_m^{dc}(t)}{2} - v_m^{ac}(t)}{v_{C\Sigma}^u(t)} \leq 1 \tag{4.62}$$

$$\frac{v_m^l(t)}{v_{C\Sigma}^l(t)} = \frac{\frac{v_m^{dc}(t)}{2} + v_m^{ac}(t)}{v_{C\Sigma}^l(t)} \leq 1. \tag{4.63}$$

To satisfy those constraints, the total capacitor voltages of the arms must be higher than the required values of the arm voltages at any instant. Combining (4.19) and (4.20) into (4.62) and (4.63) yields the steady-state representation of the operational constraints:

$$\frac{\frac{V_m^{dc}}{2} - \sqrt{2}V_m^{ac}\cos(\omega t + \delta)}{v_{C\Sigma}^u(t)} \leq 1 \tag{4.64}$$

$$\frac{\frac{V_m^{dc}}{2} + \sqrt{2}V_m^{ac}\cos(\omega t + \delta)}{v_{C\Sigma}^u(t)} \leq 1. \tag{4.65}$$

As it has been already demonstrated, the capacitor voltages contain intrinsic oscillatory components whose amplitudes and phase shifts vary with the transferred power and the associated grid conditions. Furthermore, the sum of these components is no longer a simple sinusoidal waveform, but takes a distorted shape. Therefore, careful attention on the shape of the capacitor voltage ripple is required. Similarly to the previous section, when the stored energy in the upper and lower arms are well balanced in steady state, the exactly same limit should be assigned to both arms; thus, the following analysis is only considering the upper arm.

The instantaneous value of the total capacitor voltage is determined from the energy stored in the arm. Replacing $v_{C\Sigma}^u(t)$ in (4.64) by (4.46) yields the modulation constraint in terms of the energy:

$$\frac{\frac{V_m^{dc}}{2} - \sqrt{2}V_m^{ac}\cos\left(\omega t + \delta\right)}{\sqrt{\frac{2}{C_\Sigma}W^u\left(t\right)}} \leq 1. \tag{4.66}$$

As previously demonstrated, the arm energy contains oscillatory components. Introducing (4.41) and (4.45) into (4.66) leads to an inequality which indicates the requirement on the total energy stored in the MMC:

$$\frac{W_{mmc}}{6} \geq \frac{C_\Sigma}{2}\left(\frac{V_m^{dc}}{2} - \sqrt{2}V_m^{ac}\cos\left(\omega t + \delta\right)\right)^2 - \widetilde{W}^u\left(t\right). \tag{4.67}$$

The internal energy level must be regulated to always satisfy (4.67). However, the existence of the various frequency components in $\widetilde{W}^u\left(t\right)$ makes it difficult to solve the above inequality. Thus, we again consider the worst case where $W_{mmc} = W_{mmc}^{Lim-}$ and the above inequality becomes an equality at the timing denoted by $t_p^-$. Note that the right side of the above inequality is completely independent of the total energy. Thus, once the value of $W_{mmc}^{Lim-}$ is derived, the above inequality can be ensured by simply maintaining the energy level higher than this limit. So, the problem to be solved is expressed by:

$$\frac{W_{mmc}^{Lim-}}{6} \geq \frac{C_\Sigma}{2}\left(\frac{V_m^{dc}}{2} - \sqrt{2}V_m^{ac}\cos\left(\omega t + \delta\right)\right)^2 - \widetilde{W}^u\left(t\right). \tag{4.68}$$

with equality at $t = t_p^-$.

The physical interpretation of the aforementioned worst condition is easier to understand in terms of voltage. Fig. 4.13 illustrates the relation between the arm energy, total capacitor voltage peak and the modulation index in the worst case condition. In such worst case context, the total capacitor voltage must satisfy three conditions. Firstly, $v_m^u\left(t\right)$ and $v_{C\Sigma}^u\left(t\right)$ must be equal to each other at $t = t_p^-$. This leads to that the modulation index reaches one at that instance as we see it in Fig. 4.13c. Secondly, the voltage insertion request and the total capacitor voltage must be tangential at $t_p^-$ which implies their derivatives must be equal. Thirdly, the second derivative of the $v_{C\Sigma}^u\left(t\right)$ must be bigger than that of $v_m^u\left(t\right)$ at $t_p^-$. Hereinafter, the way to derive the timing $t_p^-$ which satisfies all the three conditions is described.

The first condition indicates the equality of (4.68). In terms of voltage, it is simply given by:

$$v_m^u(t_p^-) = v_{C\Sigma}^u(t_p^-). \tag{4.69}$$

The second condition can be expressed by the following formula:

$$\left.\frac{dv_m^u\left(t\right)}{dt}\right|_{t=t_p^-} = \left.\frac{dv_{C\Sigma}^u\left(t\right)}{dt}\right|_{t=t_p^-}. \tag{4.70}$$

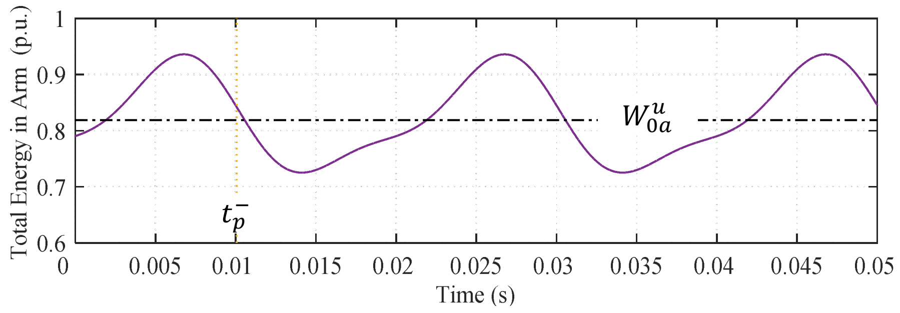

(a) Total energy in arm: $W_a^u$

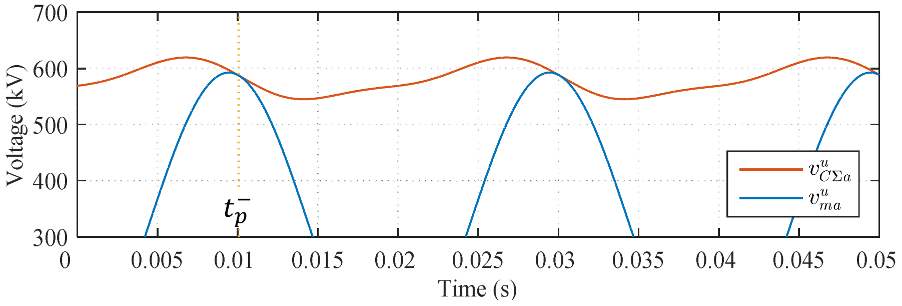

(b) Total capacitor voltage: $v_{C\Sigma}^{u}$.

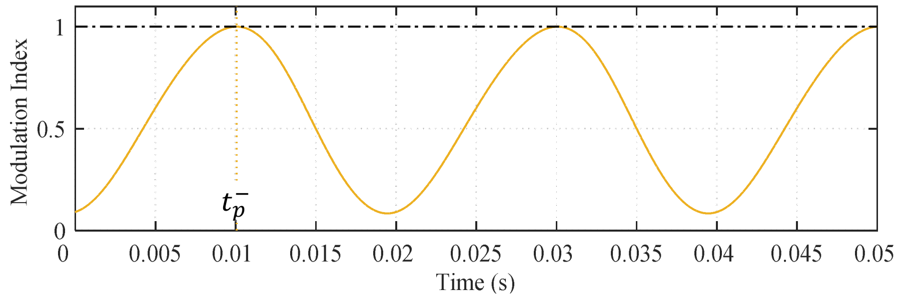

(c) Modulation Index: $m_a^u$

Figure 4.13: Exemplary illustration of the arm energy, the total capacitor voltage peak and the modulation index at the lower energy limit.

The time derivative of the total capacitor voltage can be determined from the equivalent capacitance and the current flows into the capacitor. Thus,

$$\frac{dv^u_{C\Sigma}\left(t\right)}{dt} = \frac{i^u\left(t\right)}{C_\Sigma}. \tag{4.71}$$

Substituting (4.71) into (4.70), the condition which must hold is given as:

$$\left.\frac{dv^u_m\left(t\right)}{dt}\right|_{t=t_p^-} - \frac{i^u(t_p^-)}{C_\Sigma} = 0. \tag{4.72}$$

Now, let us assume that the converter is in the steady-state condition. By substituting the steady-state representation of $v^u_m\left(t\right)$ and $i^u(t)$ given in (4.19) and (4.21) into (4.72), the condition which makes the second condition to hold is given as:

$$\sqrt{2}\omega V^{ac}_m \sin\left(\omega t_p^- + \delta\right) - \frac{\dfrac{I_{dc}}{3} + \dfrac{I_{ac}}{\sqrt{2}}\cos\left(\omega t_p^- + \theta\right)}{C_\Sigma} = 0. \tag{4.73}$$

Then, solving (4.73) in terms of $t_p^-$ leads to two possible solutions:

$$t_{p1}^- = \frac{1}{\omega}\left\{\arcsin\left(\frac{I_{dc}}{3\sqrt{A^2+B^2}}\right) - \phi\right\} + \frac{2k\pi}{\omega} \tag{4.74}$$

$$t_{p2}^- = \frac{1}{\omega}\left\{\pi - \arcsin\left(\frac{I_{dc}}{3\sqrt{A^2+B^2}}\right) - \phi\right\} + \frac{2k\pi}{\omega} \tag{4.75}$$

where

$$\begin{aligned} A &= \sqrt{2}\omega C_\Sigma V^{ac}_m \cos\delta + \frac{I_{ac}}{\sqrt{2}}\sin\theta \\ B &= \sqrt{2}\omega C_\Sigma V^{ac}_m \sin\delta - \frac{I_{ac}}{\sqrt{2}}\cos\theta \\ \phi &= \arctan\frac{B}{A}. \end{aligned}$$

Since the inverse of sine can only take a value within the range of $[-\pi/2, \pi/2]$, the first solution corresponds to the case where $\omega t_p^- + \phi$ is placed in the right plane of the Cartesian coordinate, and the other is in the left plane. To choose the right solution, now the third condition is considered. Taking the second derivatives, the third condition is expressed as follows:

$$\left.\frac{d^2v^u_m\left(t\right)}{dt^2}\right|_{t=t_p^-} \leq \left.\frac{d^2v^u_{C\Sigma}\left(t\right)}{dt^2}\right|_{t=t_p^-}. \tag{4.76}$$

Again, the variables in the above inequality are replaced by their steady-state representation. By substituting (4.19) and (4.71), then replacing $i^u\left(t\right)$ by (4.21), the inequality above becomes:

$$\sqrt{2}\omega^2 V^{ac}_m \cos\left(\omega t_p^- + \delta\right) \leq -\frac{\omega I_{ac}}{\sqrt{2}C_\Sigma}\sin\left(\omega t_p^- + \theta\right). \tag{4.77}$$

Composing two trigonometric functions into one yields:

$$\omega\sqrt{A^2+B^2}\sin\left(\omega t_p^- + \phi + \frac{\pi}{2}\right) \leq 0. \tag{4.78}$$

To satisfy this inequality, the angle of the sinusoidal function must be placed in the lower plain in Cartesian coordinate. Thus, the angle which agrees with the third condition is given by:

$$\pi + \frac{2k\pi}{\omega} \leq \omega t_p^- + \phi + \frac{\pi}{2} \leq 2\pi + \frac{2k\pi}{\omega}. \tag{4.79}$$

By replacing $t_p^-$ by (4.74) and (4.75), two inequalities which indicate the consistency of the previously derived two solutions are derived. For $t_{p1}^-$, the inequality is given as:

$$\pi \leq \arcsin\left(\frac{I_{dc}}{3\sqrt{A^2+B^2}}\right) + \frac{\pi}{2} \leq 2\pi. \tag{4.80}$$

Then, for $t_{p2}^-$:

$$\pi \leq -\arcsin\left(\frac{I_{dc}}{3\sqrt{A^2+B^2}}\right) + \frac{3\pi}{2} \leq 2\pi. \tag{4.81}$$

From the range of the inverse sine function, it is clear that only the second one can be satisfied. As a result, the value of $t_p^-$ which satisfies all the three conditions is given by:

$$t_p^- = \frac{1}{\omega}\left\{\pi - \arcsin\left(\frac{I_{dc}}{3\sqrt{A^2+B^2}}\right) - \phi\right\} + \frac{2k\pi}{\omega} \tag{4.82}$$

Finally, by substituting the obtained $t_p^-$ into (4.68), the minimum limit of the energy which corresponds to the aforementioned worst condition can be derived as:

$$W_{mmc}^{Lim-} = 6\left\{\frac{C_\Sigma}{2}\left(\frac{V_m^{dc}}{2} - \sqrt{2}V_m^{ac}\cos\left(\omega t_p^- + \delta\right)\right)^2 - \widetilde{W}^u\left(t_p^-\right)\right\}. \tag{4.83}$$

As long as the internally stored energy remains higher than the obtained lower limit $W_{mmc}^{Lim-}$, the arm voltages can be synthesized without overmodulation. In Fig. 4.14, the lower limit of the total energy in the MMC is calculated according to (4.83) and plotted against active and reactive power. To maintain the proper operation of the MMC, its internal energy must be maintained higher than the obtained surface. Any violation of this constraint results in overmodulation in the MMC arms. Interestingly, the limit of the total capacitor voltage largely depends on the operating point of reactive power. As observed, the injection of reactive power imposes less severe voltage limit compared to the reactive power consumption.

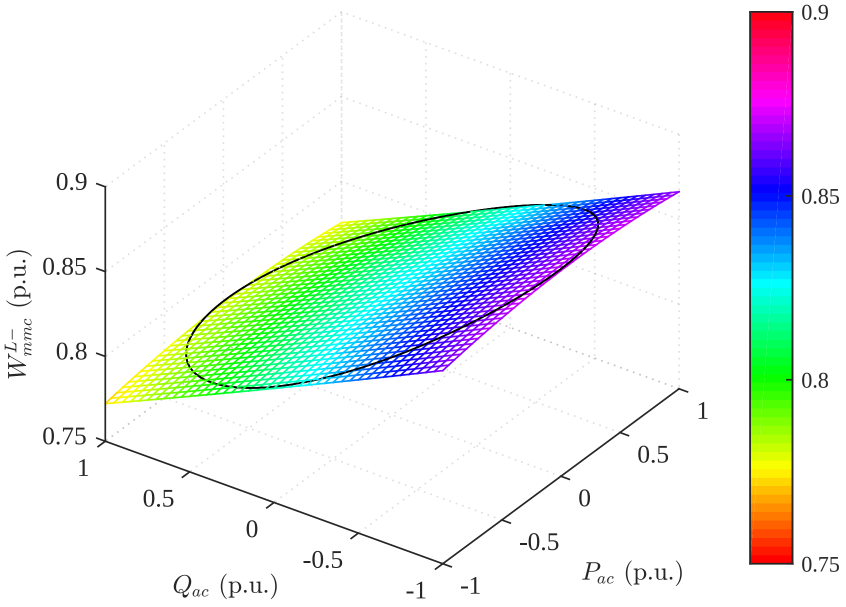

Figure 4.14: Lower limit of total energy against active and reactive power.

### 4.5.2 Sensitivity Analysis on Lower Energy Limit

The lower limit of the total capacitor voltage can be highly influenced by the associated grid conditions. In Fig. 4.15, the lower limits of the total energy for different DC grid voltages are depicted. As it is observed, when the DC grid voltage is increased, the limit of the total energy becomes severer. The higher DC grid voltage demands a larger internal DC voltage on the MMC. As it may be noticed from (4.62), it reduces the margin to generate the internal AC voltage. Therefore, in case of the DC grid voltage rise, it is preferable to increase the total energy level. In contrast, when the DC voltage drop occurs, MMC gains a larger operational margin. This implies that MMC might be capable of damping the DC grid voltage drop by discharging the stored energy in the MMC. In Fig. 4.16, the lower limits of total energy for different AC grid voltage levels are shown. Similar to the previous figure, the increase of the AC grid voltage imposes the MMC to maintain higher total capacitor voltage. In contrast, when the AC grid voltage is decreased, the lower limit of the energy becomes less severe.

In Fig. 4.17, the lower limits of the total energy for different values of capacitance are depicted. Since a larger size of the SM capacitor leads to a smaller magnitude of the capacitor voltage ripple, the surface becomes flatter as $C_{sm}$ increases. Interestingly, the smaller $C_{sm}$ imposes severer limit of the energy when the MMC is operated in inductive mode, but less severe in capacitive operation. Therefore, when the SM capacitors are

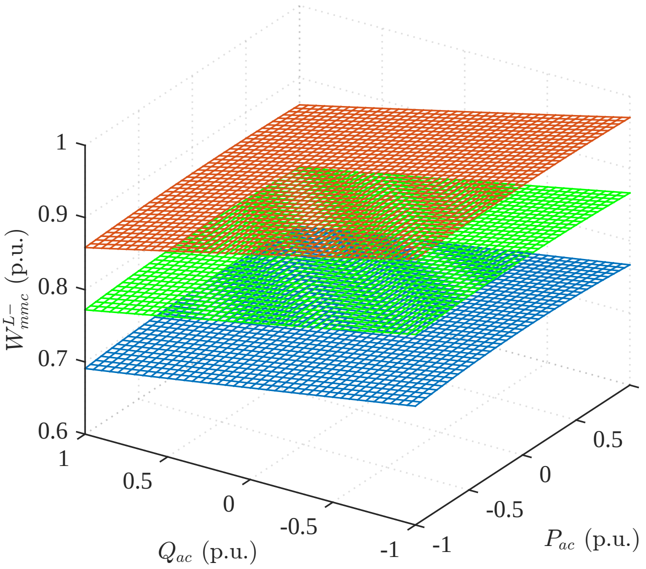

Figure 4.15: Sensitivity study on lower limit of total energy against DC grid voltage (red: $V_{dc} = 1.1$ p.u., green: 1.0 p.u., and blue: 0.9 p.u.).

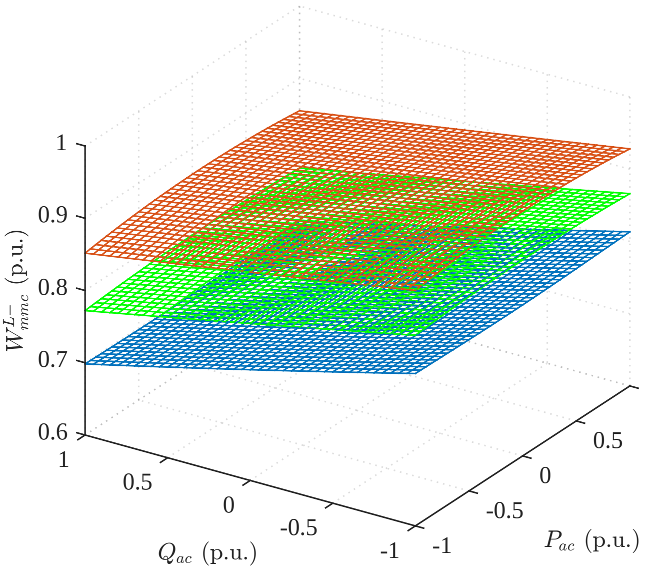

Figure 4.16: Sensitivity study on lower limit of total energy against AC grid voltage (red: $V_{ac} = 1.1$ p.u., green: 1.0 p.u., and blue: 0.9 p.u.).

sized relatively small, the operator must take vigilant attention on the reactive power operation mode of the MMC.

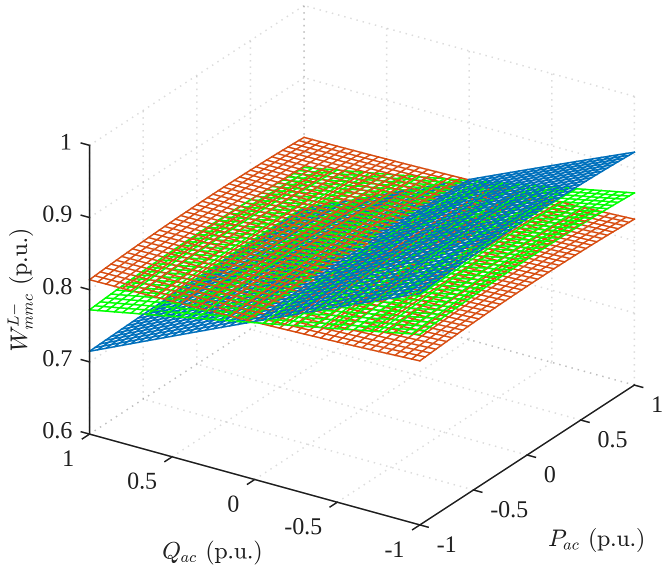

Figure 4.17: Sensitivity study on lower limit of total energy against SM capacitor size (red: $C_{sm} = 15.6$ mF, green: 13.0 mF, and blue: 10.4 mF).

## 4.6 Experimental Confirmation by MMC Mock-up

The theoretical analysis of the energy limits and the derived expressions are tested on a small-scale MMC mock-up. This test bench is part of the SuperGrid Institute real-time simulation platform located in Villeurbanne, France. The specifications of this MMC prototype as well as its control system were examined and developed by Dr. Zama within the work of his Ph.D. (Readers are encouraged to see his dissertation [164] for more details). The MMC prototype is rated at 6 kVA, 400 V DC voltage and 208 line-to-line RMS voltage for AC side. It consists of 10 half-bridge SMs per arm. The MMC is connected to AC and DC power amplifiers: a high bandwidth linear power amplifier *Puissance+ PCU-3X5000-BC* which emulates the AC grid, and a DC power amplifier *CINERGIA*. More detailed specifications of the three-phase MMC mock-up are provided in Appendix A.

The derived expressions are scripted in Matlab language. For the sake of the credibility of this test, only the external input signals (power and energy references) and the specifications of the converter are taken as the inputs of the developed code.

### 4.6.1 Confirmation of Upper Energy Limit

The analysis on the upper limit of the energy provided in Section 4.4 is confirmed by experiments. Initially, the operating power of the MMC prototype, $P_{ac}^*$ and $Q_{ac}^*$, were selected as $-0.7$ p.u. and 0.1 p.u., respectively. According to (4.61) and the converter parameters, the upper limit of the energy $W_{mmc}^{L+}$ at the selected operating power was calculated as 1.305 p.u.. Then whether this energy level satisfies the capacitor voltage constraint given in (4.5) was confirmed on the experimental test. Preliminarily, the internal energy of the MMC mock-up was ramped up until it reached the derived upper energy limit. The same operation was carried out for the active and reactive power. After it reached its steady state, the measured capacitor voltages as well as the converter currents were recorded.

Fig. 4.18 shows the obtained experimental results. To ensure the desired initial conditions for this experimental test, the internal energy level of the MMC and the AC powers in the specified time frame (50 ms) are shown in Fig. 4.18a and 4.18b. As seen, both the energy and power were well stabilized at the desired levels. Fig. 4.18c shows the measured total capacitor voltage in the same time frame and its estimate calculated analytically from the expressions provided in Section 4.3. The experimental results closely corresponds to its estimate. The peak of the total capacitor voltage is confined to the maximum permissible level $V_{C\Sigma}^{Max}$ as expected. Fig. 4.18d shows the measured converter currents. The dashed lines represent their estimated waveforms. The measurement results well coincide with their estimates. The timing $t_p^+$ calculated from (4.60) is in line with the moment the arm current crosses zero, and it well represents the timing that the capacitor voltage reaches its peak. From those experimental results, it can be said that the analysis on the upper limit of the energy provided in Section 4.4 is confirmed.

### 4.6.2 Confirmation of Lower Energy Limit

Next, the analysis on the lower limit of the energy discussed in Section 4.5 is confirmed by test on the MMC mock-up. The same operating conditions of the active and reactive power were selected. From (4.83), the lower energy limit $W_{mmc}^{L-}$ was calculated as 0.847 p.u.. The total energy was ramped down until it reached the calculated lower limit. Once the converter reached steady state, the measured capacitor voltages were recorded.

Fig. 4.19 shows the obtained experimental results. The internal energy level of the MMC and the AC powers are shown in Fig. 4.19a and 4.19b to ensure the presupposed conditions. Fig. 4.19c shows the experimentally obtained total capacitor voltage and its

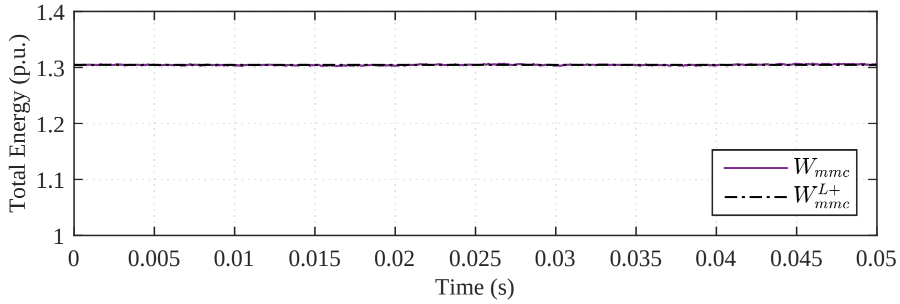

(a) Total energy stored in the MMC

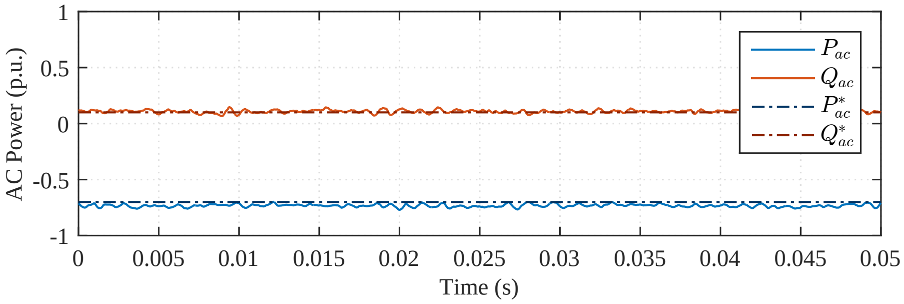

(b) Active and reactive power

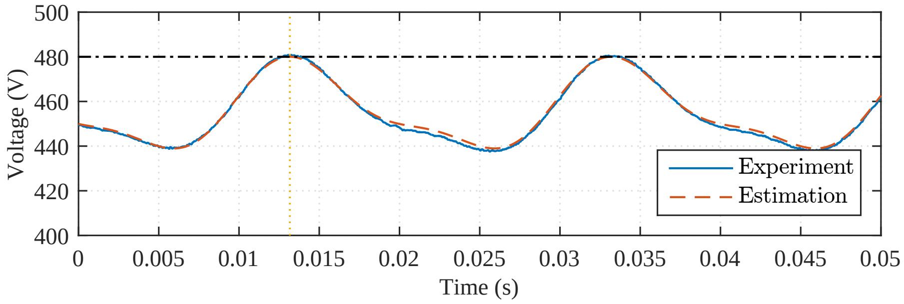

(c) Total capacitor voltage: $V_{C\Sigma a}^{u}$

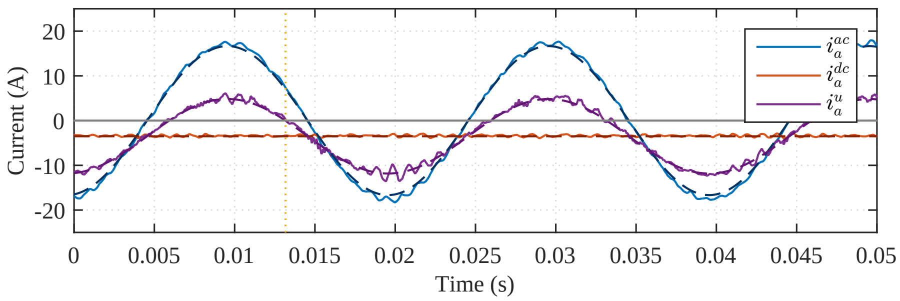

(d) Converter currents: AC current $i_a^{ac}$, DC current $i_a^{dc}$ and arm current $i_a^{u}$

Figure 4.18: Experimental results: Confirmation of upper energy limit estimation.

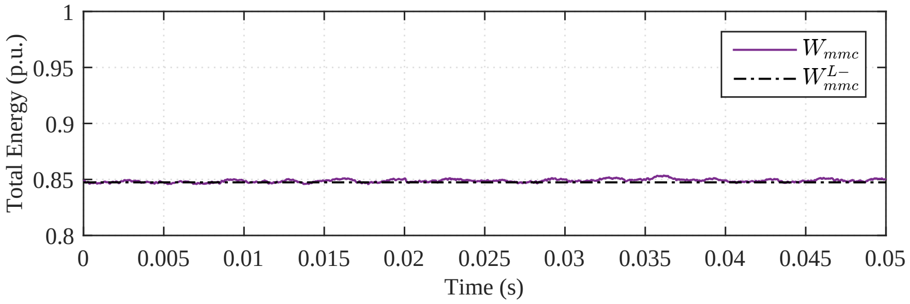

(a) Total energy stored in the MMC

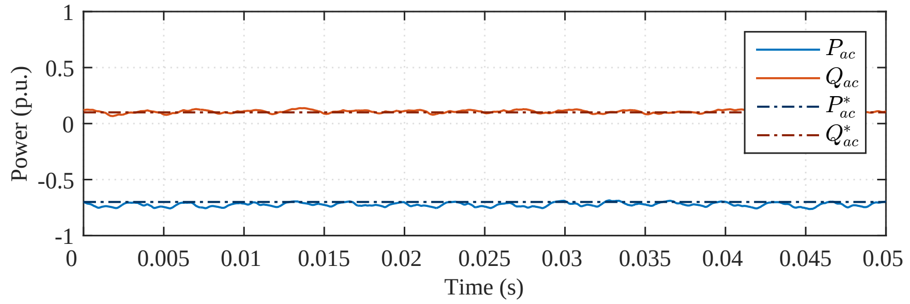

(b) Active and reactive power

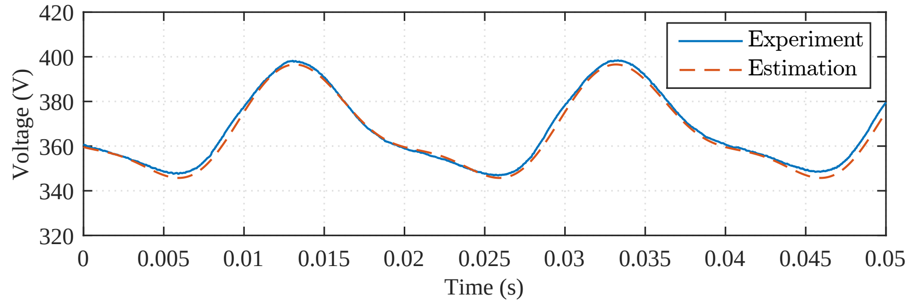

(c) Total capacitor voltage: $V_{C\Sigma a}^{u}$

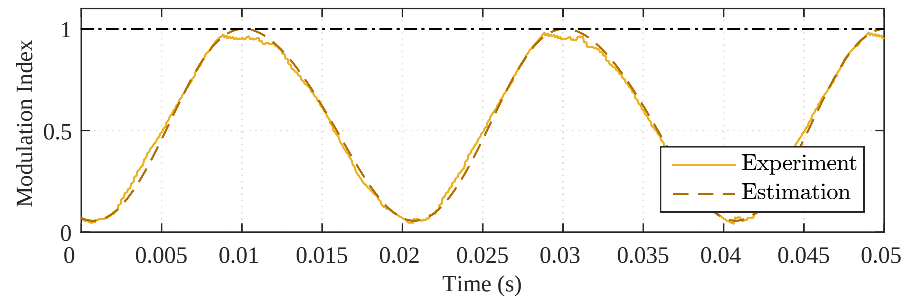

(d) Modulation index: $m_a^u$

Figure 4.19: Experimental results: Confirmation of lower energy limit estimation.

estimate. As observed, there is no significant difference between the experimental result and its estimate. Fig. 4.19d shows the modulation index generated by the converter control. The dashed line represents its analytic estimate. Although small distortions are observed, it shows good correspondence with the experimental result in general. The peak value of the modulation index is always maintained below one. This means the inequality constraint given in (4.7) is satisfied. Therefore, it can be argued that the analysis on the lower limit of the energy is confirmed.

## 4.7 Chapter Conclusion

This chapter provided an analysis on the limitations imposed on the energy stored in the MMC. The upper limit of the energy was defined as the maximum allowable energy that will not violate the maximum admissible voltage of the SMs at its peak, and the lower limit signifies the minimum requirement of the energy which is necessary to ensure the proper function of the MMC without overmodulation. The internal energy pulsations, which appears as the voltage ripple in the arms, are an influencing factor. Firstly, the equations that permit to accurately estimate the voltage ripple according to the converter operating point were derived. Based on the derived expressions, both upper and lower limits of energy were mathematically formulated as functions of the converter operating point. Such analysis enables rigorous parametric studies. The influences of the active and reactive power transfer, the AC and DC grid voltage, and the SM capacitor size on the upper and lower energy limits were analyzed. It revealed that the admissible range of the energy strongly depends on the associated grid conditions and indicated the need for such analysis in the converter dimensioning phase. The derived formulas were confirmed by experimental results using a small-scale MMC mock-up.

The provided analysis can be useful for converter dimensioning and also used for the evaluation of the SM capacitor expenditure. Moreover, one of the evident advantages is that, unlike any existing approaches, the derived formulas can be directly integrated to the converter controller to monitor the available energy reserves in real time.

The theoretical analysis provided in this chapter can bring a new perspective for the MMC control design. As long as the total energy is maintained between the upper and lower limits, the proper function of the converter is ensured. This implies that there is a certain amount of energy available in the MMC and that it can be freely used for specific purposes. In the following chapter, a way to make use of this energy to improve the DC system dynamics will be presented.

# Chapter 5

# Virtual Capacitor Control

## 5.1 Chapter Introduction

The previous chapters revealed that the Modular Multilevel Converter (MMC) is capable of charging and discharging the energy stored in the distributed sub-modules (SMs) as long as the level of the total energy stored in the MMC remains within certain limits. This degree of freedom is not available in the conventional Voltage Source Converters (VSCs) where the DC link capacitors are directly connected to the DC bus. Therefore, it can be said that this controllable internal energy is an important additional degree of freedom for the MMC.

This chapter investigates ways of using this additional degree of freedom. Firstly, a crucial requirement for the DC systems is identified by establishing the analogy between the DC systems and the well-known AC systems. As described with more details later, the DC voltage is a global measure of the energy balance in the DC system. It is revealed that, without explicit control, the DC voltage tends to be inherently volatile against power disturbances compared to the frequency of conventional AC systems. In order to solve this problem, this chapter proposes a novel control method, named *Virtual Capacitor Control*, which enables this additional degree of freedom to be used to attenuate voltage fluctuations of DC systems. With the proposed control, the MMC behaves as if there were a physical capacitor whose size is adjustable. Thus, this control can greatly broaden the operability of the DC systems.

## 5.2 Comparison between AC and DC Systems

Many common features exist between AC and DC systems. However, compared to the AC systems which have been investigated over a hundred years, DC systems are less understood. Explaining the similarities between the AC and DC can help to develop an intuitive comprehension of the DC system. This section describes the AC and DC systems in analogical terms to highlight their similarities and more importantly to identify the crucial difference of the DC system which needs to be treated for its secure operation.

### 5.2.1 Global Variables

In an AC system, the system frequency $f$ or the angular frequency given by $\omega = 2\pi f$ is the common variable throughout the system. It acts as a global measure of the instantaneous balance between the total generation and load of the system. When this balance collapses, the system frequency fluctuates and deviates from the nominal value.

For DC system, the DC voltage $v_{dc}$ can be attributed the same role of the power balance indicator as the frequency in AC systems. In the similar sense that the frequency in AC system reflects the balance between "supply" and "demand" of the power, the DC voltage reflects the balance between the power injected to and withdrawn from the DC system. Note that, unlike the frequency in AC systems, DC voltage is not truly a global variable because of the voltage drops along the conductors. However, according to the practical XLPE cable data sheet [165][1], the typical value of the resistance is 7.3 mΩ/km. This means that, for HVDC transmission rated at ±320 kV and 1000 MW, the voltage drop across 300 km cable is less than 1 % even at the nominal power. Therefore, it can be said that the DC voltages at the cable terminals remain within a very close vicinity in general.

### 5.2.2 System Dynamics

In AC systems, energy is stored in the form of kinetic energy in the rotating mass of synchronous generators. The rotational kinetic energy, denoted by $E_k$, is related to the angular frequency $\omega$ as:

$$E_k = \frac{1}{2}J\omega^2 \tag{5.1}$$

---

[1] XLPE 2400 $m^2$ cross section submarine cable with copper conductor.

where $J$ is the moment of inertia in kgm$^2$. Generally, the so-called inertia constant $H$, defined as the ratio between the stored kinetic energy and the rated power of the power plant, is commonly used in AC systems to compare the inertial effect of the generators with different ratings [70]:

$$H = \frac{\frac{1}{2}J\omega_n^2}{S_b} \tag{5.2}$$

where $S_b$ is the rated apparent power, and $\omega_n$ is the nominal angular frequency. The inertia constant is measured in seconds and can be interpreted as the time that the machine can supply its rated power solely with its stored kinetic energy [166]. The inertia constant typically ranges from 2 to 10 s according to the type of the generating unit [70].

The motion of a single generator is expressed by the well-known swing equation:

$$\frac{d}{dt}E_k = \frac{d\left(\frac{1}{2}J\omega^2\right)}{dt} = P_m - P_e. \tag{5.3}$$

where $P_m$ is the mechanical input power and $P_e$ is the electrical load. Then, rewriting (5.3) in per-unit value ($\bar{x}$) with the above defined inertia constant leads to:

$$\frac{d\bar{\omega}}{dt} = \frac{\bar{P}_m - \bar{P}_e}{2H} \tag{5.4}$$

where

$$\bar{\omega} = \frac{\omega}{\omega_n}. \tag{5.5}$$

Since the frequency is the global variable of the whole AC system, (5.4) can be readily extended to an aggregated mass model [167]:

$$\frac{d\bar{\omega}}{dt} = \frac{\bar{P}_g - \bar{P}_l}{2H_{sys}} \tag{5.6}$$

where $\bar{P}_g$ is the total generated power, $\bar{P}_l$ the total load power, and $H_{sys}$ the inertia constant of the whole system given by:

$$H_{sys} = \frac{\sum_{i=1}^{n} H_i S_{bi}}{\sum_{i=1}^{n} S_{bi}}. \tag{5.7}$$

As (5.6) indicates, when the system is subjected to a sudden power disturbance, e.g. loss of a generator or a large load, the system frequency changes, and its rate of change is characterized by the system inertia constant $H_{sys}$. If this value decreases, the frequency will be less damped, and thus, the rate of change becomes more prominent [168]. The typical value of the system inertia constant of the pan-European grid is around 5 to 6 s [169].

In DC systems, the energy is stored in the form of electrostatic potential energy in the capacitors. Denoting this energy by $E_c$, its relation with the DC voltage is expressed as:

$$E_c = \frac{1}{2} C v_{dc}^2 \tag{5.8}$$

where $C$ is the capacitance. As noticed, it is given in an analogical form by considering the capacitance as the inertia in the AC systems. The concept of inertia constant can be extended to the DC systems with the electrostatic constant $H_c$ defined as the ratio between the stored potential energy and the rated power:

$$H_c = \frac{\frac{1}{2} C v_{dcn}^2}{S_b} \tag{5.9}$$

with $v_{dcn}$ as the nominal DC voltage. According to [81], the typical value of $H_c$ of an MMC is around 40 ms, which is around a hundred times smaller than that of a generator unit in AC system.

Following the same procedure as the case of AC system, the swing equation of an aggregated DC system is obtained in an analogical form:

$$\frac{d\bar{v}_{dc}}{dt} = \frac{\bar{P}_{rec} - \bar{P}_{inv}}{2H_{c\,sys}} \tag{5.10}$$

where $\bar{P}_{rec}$ is the total power injected into the DC system, and $\bar{P}_{inv}$ is the total power withdrawn from the DC system. To the extent of our knowledge, no practical value of the electrostatic constant of DC system is available in literature. However, it can be deduced that it will not be so far from the individual inertia constant, i.e. 40 ms. Thus, it is considerably smaller than the typical value of the bulk AC system. This means that if the same power disturbance occurs in an AC and a DC system of the same scale, the rate of change of the DC voltage is around 100 times more important than that of the frequency.

Table 5.1: Analogy between AC and DC systems.

| | AC System | DC System |
|---|---|---|
| Common variable | Angular frequency<br>$\omega$ | DC voltage<br>$v_{dc}$ |
| Stored energy | Kinetic energy<br>in rotating mass<br>$E_k = \frac{1}{2} J\omega^2$ | Electrostatic energy<br>in capacitor<br>$E_c = \frac{1}{2} C v_{dc}^2$. |
| Inertia or Electrostatic Constant | Generator<br>$H = \frac{E_k}{S_b} = 2 \sim 10$ s | Converter<br>$H_c = \frac{E_c}{S_b} = 40$ ms |
| System Inertia or Electrostatic Constant | pan-European grid<br>$H_{sys} = 5 \sim 6$ s | Plausible Value<br>$H_{c\,sys} \approx 40$ ms |
| Swing Equation<br>(per unit) | $\frac{d\bar{\omega}}{dt} = \frac{\bar{P}_g - \bar{P}_l}{2H_{sys}}$ | $\frac{d\bar{v}_{dc}}{dt} = \frac{\bar{P}_{rec} - \bar{P}_{inv}}{2H_{c\,sys}}$ |

In Table 5.1, the analogy and difference between AC and DC systems are summarized. In short, the stored energy level in the DC system is considerably smaller than that of the AC systems. This means that, without explicit control, the DC system can be extremely volatile against power disturbances compared to the bulk AC power systems [170].

## 5.3 MMC Control to Support HVDC Systems Dynamics

The crucial problem of the DC system is the volatility of the DC voltage originating from the amount of the energy stored in the system being considerably smaller than the conventional AC systems. As demonstrated in previous chapters, the MMC has an additional degree of freedom which is the controllability of the internal energy level. As long as it stays within the admissible range, the MMC can freely exchange the energy with the DC grid without any adverse effect on the AC grid. This additional degree of freedom of the MMC can be used to provide energy contribution to overcome the intrinsic volatility of the DC system.

A reasonable solution to make the MMC contribute to DC voltage dynamics is to regulate the internal energy in conjunction with the variation of the DC voltage. A previous work proposed to directly link the reference level of the energy to the square of the measured DC voltage [171]. However, in that approach, the nominal level of the energy is imposed by the nominal DC voltage, so that both are strictly coupled. This restrains the contribution of the MMC and prevents it from fully exerting its potential.

This section introduces the concept of the novel control strategy, named *Virtual Capacitor Control,* which can overcome the limits of the existing approach and provide greater energy contribution by further exploring the potential of the MMC.

### 5.3.1 Electrical Equivalent Model of MMC

To make this chapter self-contained, the fundamental equations of the MMC are revisited here. The MMC currents of phase $i$ are governed by the two decoupled equations (see Section 3.2):

$$v_{mi}^{ac} - v_i^{ac} = L_{eq,i}^{ac}\frac{di_i^{ac}}{dt} + R_{eq,i}^{ac}i_i^{ac} \tag{5.11}$$

$$v_{dc} - v_{mi}^{dc} = L_{eq,i}^{dc}\frac{di_i^{dc}}{dt} + R_{eq,i}^{dc}i_i^{dc}. \tag{5.12}$$

In balanced condition, the AC equation (5.11) can be written in $dq$ frame:

$$\begin{aligned} v_{md}^{ac} - v_d^{ac} &= L_{eq}^{ac}\frac{di_d^{ac}}{dt} + R_{eq}^{ac} i_d^{ac} - \omega L_{eq}^{ac} i_q^{ac} && (5.13) \\ v_{mq}^{ac} - v_q^{ac} &= L_{eq}^{ac}\frac{di_q^{ac}}{dt} + R_{eq}^{ac} i_q^{ac} + \omega L_{eq}^{ac} i_d^{ac}. && (5.14) \end{aligned}$$

where

$$R_{eq}^{ac} = R_{eq,i}^{ac}, \quad L_{eq}^{ac} = L_{eq,i}^{ac}. \tag{5.15}$$

On the other hand, when the DC grid current $i_{dc}$ is evenly distributed among the phases, the dynamics of those three phase legs can be combined into the single equation:

$$v_{dc} - v_m^{dc} = L_{eq}^{dc}\frac{di_{dc}}{dt} + R_{eq}^{dc} i_{dc} \tag{5.16}$$

with

$$v_m^{dc} = v_{ma}^{dc} = v_{mb}^{dc} = v_{mc}^{dc}, \quad \frac{i_{dc}}{3} = i_a^{dc} = i_b^{dc} = i_c^{dc} \tag{5.17}$$

$$R_{eq}^{dc} = \frac{R_{eq,i}^{dc}}{3}, \quad L_{eq}^{dc} = \frac{L_{eq,i}^{dc}}{3}. \tag{5.18}$$

The MMC control evenly distributes the energy among the six arms under balanced operation. This leads to the introduction of an aggregated capacitance $C_{mmc}$ and an average voltage $\hat{v}_{C\Sigma}$ [114], which are defined as:

$$\begin{aligned} C_{mmc} &= 6C_{\Sigma} && (5.19) \\ \hat{v}_{C\Sigma} &= \frac{1}{3}\sum_{i=a,b,c}\frac{v_{C\Sigma i}^{u} + v_{C\Sigma i}^{l}}{2}. && (5.20) \end{aligned}$$

Then the modulation of AC and DC voltages can be expressed by using $\hat{v}_{C\Sigma}$:

$$v_{md}^{ac} = m_d^{ac}\hat{v}_{C\Sigma}, \quad v_{mq}^{ac} = m_q^{ac}\hat{v}_{C\Sigma}, \quad v_m^{dc} = m_{dc}\hat{v}_{C\Sigma} \tag{5.21}$$

where $m_{dq}^{ac}$ and $m_{dc}$ are the equivalent AC and DC modulation indices.

The evolution of the energy stored inside the MMC is expressed by the instantaneous DC and AC power exchanged between the MMC and the respective grids, denoted by $p_m^{dc}$ and $p_m^{ac}$. Thus,

$$\frac{dW_{mmc}}{dt} = p_m^{dc} - p_m^{ac} \tag{5.22}$$

where $p_m^{dc}$ is expressed by the product of $i_{dc}$ and $v_m^{dc}$:

$$p_m^{dc} = v_m^{dc} i_{dc} = m_{dc}\hat{v}_{C\Sigma} i_{dc}, \tag{5.23}$$

and $p_m^{ac}$ is given by:

$$p_m^{ac} = v_{md}^{ac} i_d^{ac} + v_{mq}^{ac} i_q^{ac} = \left(m_d i_d^{ac} + m_q i_q^{ac}\right)\hat{v}_{C\Sigma}. \tag{5.24}$$

Assuming that the losses in the MMC are negligible leads to $P_{dc} \simeq p_m^{dc}$ and $P_{ac} \simeq p_m^{ac}$ where $P_{dc}$ and $P_{ac}$ are the DC and AC power at the respective grid connection points, i.e. $P_{dc} = v_{dc} i_{dc}$ and $P_{ac} = v_d^{ac} i_d^{ac}$. Thus, (5.22) is rewritten as:

$$\frac{dW_{mmc}}{dt} = \frac{1}{2} C_{mmc} \frac{d\hat{v}_{C\Sigma}^2}{dt} = P_{dc} - P_{ac} = P_w \tag{5.25}$$

where $P_w$ is the mismatch between the DC and AC power.

When the MMC is connected to the DC grid, the power exchanged by the MMC affects the behavior of the DC voltage. If we suppose that $C_{dc}$ represents the aggregated capacitance of the DC system including the capacitive effects of the cables as well as the capacitors installed in the other terminals of non-MMC type converters, the evolution of the DC voltage is expressed as follows:

$$P_l - P_{dc} = P_c = \frac{1}{2} C_{dc} \frac{dv_{dc}^2}{dt} \tag{5.26}$$

where $P_l$ is the power coming from the other stations of the DC grid, and $P_c$ is the power absorbed by the aggregated DC grid capacitor.

According to the aforementioned simplifications, an equivalent circuit model of the MMC with the DC bus is developed as illustrated with its power flow diagram in Fig. 5.1. The circuit related to the reactive power is not presented in the model because it is not relevant to the discussion here.

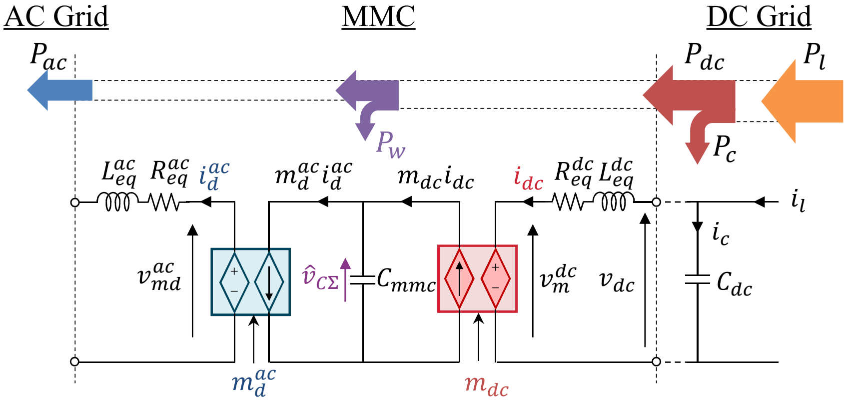

Figure 5.1: Electric equivalent model of MMC with DC bus.

## 5.3.2 Concept of Virtual Capacitor Control

As (5.25) indicates, the change of the internal energy of the MMC is derived from the difference between the DC power input and AC power output. By combining (5.26) and

(5.25), the following equation is obtained:

$$P_l - P_{ac} = P_c + P_w = \frac{1}{2}C_{dc}\frac{dv_{dc}^2}{dt} + \frac{dW_{mmc}}{dt}. \tag{5.27}$$

Here, it is considered that the AC power follows its reference value and that the total energy controller adjusts the DC power to obtain the desired internal energy level. Under the virtual capacitor control, the energy reference is defined by:

$$W_{mmc}^* = \frac{1}{2}k_{vc}C_{mmc}(v_{dc}^2 - v_{dc}^{*2}) + W_{mmc0}^* \tag{5.28}$$

where $v_{dc}^*$ is the set-point of the DC grid voltage, and $W_{mmc0}^*$ is the nominal level of the stored energy. A new coefficient, named *Virtual Capacitor Coefficient* $k_{vc}$, is introduced as an arbitrarily adjustable variable.

Let us suppose that the response speed of the energy controller is fast enough, and so that the energy can properly follow its reference, i.e. $W_{mmc} \approx W_{mmc}^*$. Then, replacing $W_{mmc}$ in (5.27) by (5.28) yields:

$$\begin{aligned} P_l - P_{ac} &= \frac{1}{2}C_{dc}\frac{dv_{dc}^2}{dt} + \frac{1}{2}k_{vc}C_{mmc}\frac{dv_{dc}^2}{dt} \\ &= \frac{1}{2}\left(C_{dc} + C_{vc}\right)\frac{dv_{dc}^2}{dt} \end{aligned} \tag{5.29}$$

where the size of *Virtual Capacitor* $C_{vc}$ is given by:

$$C_{vc} = k_{vc}C_{mmc}. \tag{5.30}$$

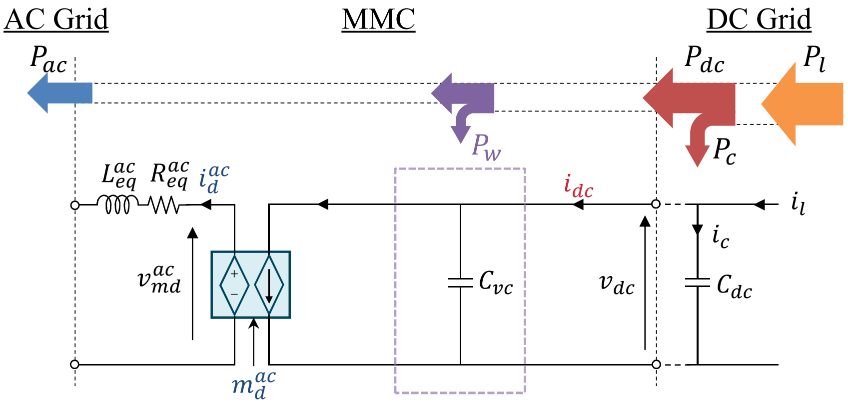

Figure 5.2: Apparent model of MMC with virtual capacitor.

The interpretation of (5.29) is shown in Fig. 5.2. Now the MMC is apparently the same as a conventional VSC, but with an adjustable capacitor $C_{vc}$. This brings a great advantage in terms of the DC grid voltage control. The modeling approaches of the DC system and the DC voltage controller designs widely accepted for the classical VSC based systems, e.g. [145], can now be readily applied to the MMC by considering $C_{vc}$ as a station capacitor.

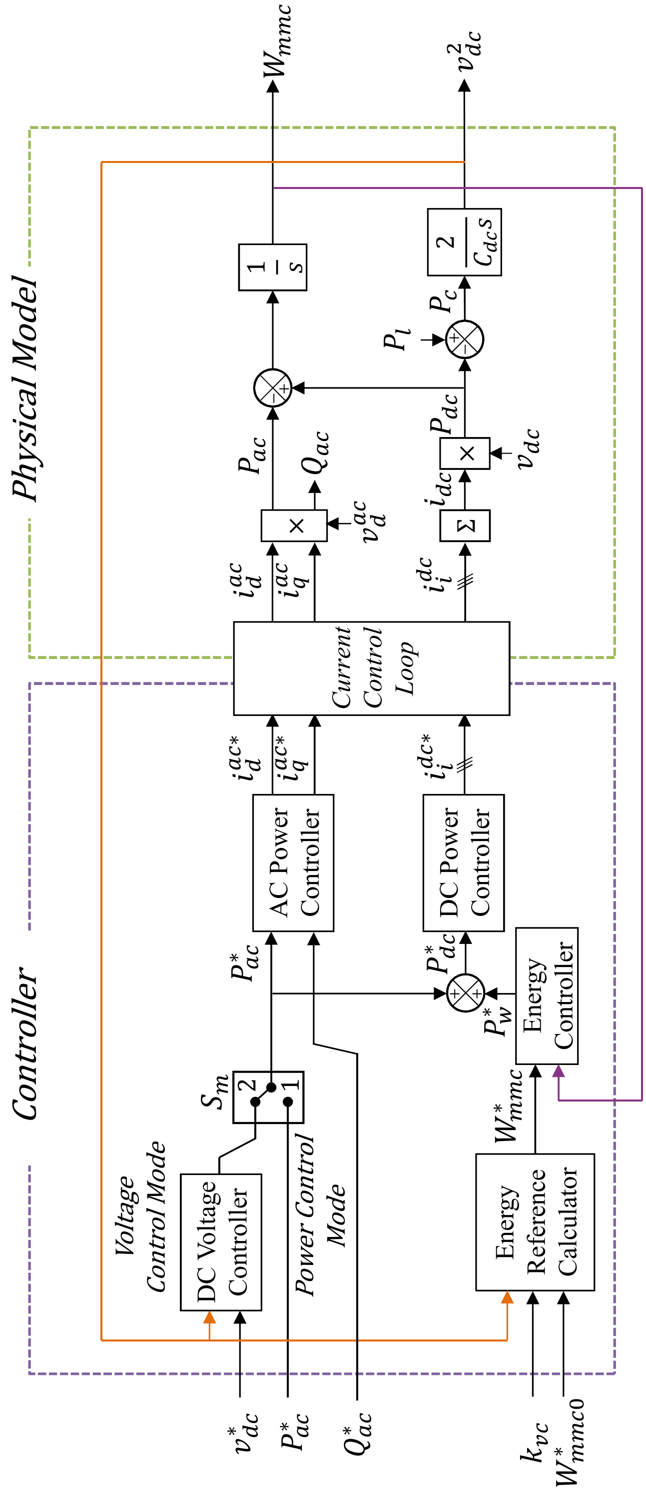

Figure 5.3: Global control architecture of MMC with virtual capacitor control.

Fig. 5.3 shows the global control architecture with the virtual capacitor control. The Energy Reference Calculator dynamically derives the appropriate reference value of the internal energy according to (5.28), while the energy controller makes the energy follow this reference. Any type of controller can be used for the energy controller. However, in order to satisfy the assumption on the energy reference tracking that is necessary to establish (5.29), the response speed of the energy control loop must be sufficiently faster than the dynamics of the DC voltage. The AC power reference is either explicitly given or derived by the DC voltage controller depending on the control mode, which will be discussed in detail in the following section.

## 5.4 Application of Virtual Capacitor Control to HVDC Systems

In this section, the virtual capacitor control is applied to a point-to-point HVDC link, where one converter controls the AC active power while the other one regulates the DC voltage [145]. Firstly, the impact of the virtual capacitor control on the DC voltage dynamics is demonstrated by using an equivalent system model. Then a theoretical analysis is provided to quantify the effectiveness of the proposed control. Later in this section, the feasibility of the virtual capacitor control is verified by simulations of a point-to-point HVDC system using full-order equivalent model (See Section 2.4.3.2) for credibility.

### 5.4.1 DC Voltage Controller Tuning under Virtual Capacitor Control

In this subsection, the converter in DC voltage control mode is considered. During the operation of the DC system, the voltage must be maintained within a certain range (e.g. ±5 % around its nominal value), otherwise a large DC voltage drop may temporarily limit the converter operation and affect the stability of the controlled systems. To evaluate the performance of the virtual capacitor control, the equivalent circuit shown in Fig. 5.4 is used, where $C_{dc}$ represents the sum of the equivalent capacitor of the DC bus and that of the other converter connected to the same DC bus. The ideal power source represents the converter on the other side.

Under the virtual capacitor control, the converter station appears to be equipped with a physical capacitor $C_{vc}$. This results in a simplified closed-loop diagram as depicted

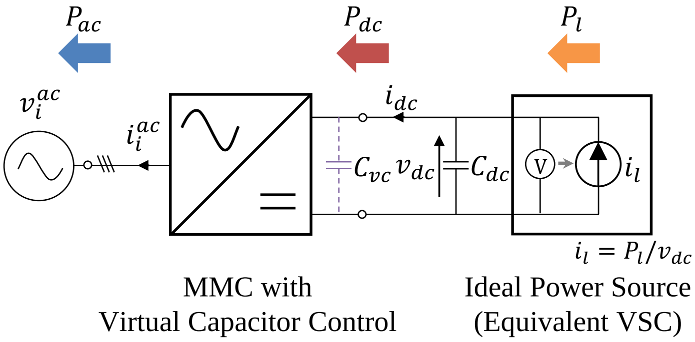

Figure 5.4: Equivalent circuit model of the point-to-point system for evaluation.

in Fig. 5.5, where $C_{eq}$ represents the equivalent capacitance of the whole system, i.e. $C_{eq} = C_{dc} + C_{vc}$. For the DC voltage controller, a proportional-integral $(PI)$ controller which can be defined as $F_v(s) = K_p^{v_{dc}} + K_i^{v_{dc}}/s$ is commonly used. The transfer function between $v_{dc}^2$ and the input $v_{dc}^{2*}$ can be obtained as:

$$\frac{v_{dc}^2}{v_{dc}^{2*}} = \frac{F_v(s)\dfrac{2}{C_{eq}s}}{1 + F_v(s)\dfrac{2}{C_{eq}s}} = \frac{2K_p^{v_{dc}}s + 2K_i^{v_{dc}}}{C_{eq}s^2 + 2K_p^{v_{dc}}s + 2K_i^{v_{dc}}}. \tag{5.31}$$

The controller parameters are tuned to fit the denominator of (5.31) with the second order characteristic polynomial according to the desired response time $T_r$ and the equivalent capacitance of the system, so that $K_p^{v_{dc}} = \zeta\omega_n C_{eq}$ and $K_i^{v_{dc}} = \omega_n^2 C_{eq}/2$ where $\omega_n$ is the natural frequency typically obtained by $\omega_n = 3/T_r$ with the damping ratio $\zeta = 0.707$.

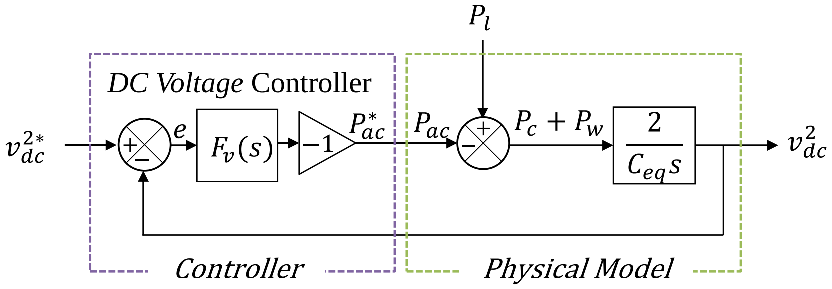

Figure 5.5: Simplified closed-loop for DC voltage control with virtual capacitor control.

### 5.4.2 Simulation of Equivalent HVDC Link

For the evaluation of the virtual capacitor control, the circuit shown in Fig. 5.4 is implemented in EMTP-RV software using the reduced-order arm average model of MMC. The AC grid is modeled as a 400/320 kV Delta-Star transformer and an equivalent three-phase source with a short-circuit power of 10 GVA. The rated power of the MMC is set at 1000 MW, and the rated DC voltage is ±320 kV. The $C_{dc}$ is sized to be identical to the equivalent capacitance of the MMC, i.e. 195.3 $\mu$F. The initial AC power of the MMC as well as the power delivered by the power source is set at 0.2 p.u., and the DC voltage controller is tuned to have 100 ms response time according to the equivalent capacitance of the whole DC system. At $t_0 = 0.6$ s, a 0.5 p.u. step increase of the power injection is imposed by the power source. The simulation is run with $k_{vc} = 0$, 1, 2, 5. The case with $k_{vc} = 0$ represents the reference case where there is no contribution from the internal energy.

In Fig. 5.6, the obtained results are compared. Fig. 5.6a shows the DC voltage. As seen, they show the same dynamics regardless of the value of $k_{vc}$. However, the DC voltage variation becomes smaller as the value of $k_{vc}$ increases. This indicates that the value of $k_{vc}$ is an additional degree of freedom which can greatly affect the DC voltage transient behavior. Since the improvement of the DC voltage transient behavior is accomplished by using the internal energy storage of the MMC, a larger value of $k_{vc}$ results in a higher peak of the energy as seen in Fig. 5.6b. The AC power dynamics is shown in Fig. 5.6c. Its response is always kept the same regardless of the value of $k_{vc}$. This implies that the virtual capacitor control enables to improve the DC voltage dynamics without any adverse effects on the AC system. By contrast, the DC power dynamics changes in accordance with $k_{vc}$. As seen in Fig. 5.6d, the response of the DC power becomes closer to the disturbance as the value of $k_{vc}$ increases, which means a smaller energy absorption by $C_{dc}$ and eventually a smaller variation of the DC voltage.

### 5.4.3 Theoretical Analysis on Peak of MMC Internal Energy

The improvement of the DC voltage transient dynamics is achieved by the reinforcement of the equivalent capacitance of the system by using the internal energy storage of the MMC. However, as discussed in the previous chapter, the internal energy must be maintained within the admissible range in order to avoid overvoltage of the SMs and overmodulation. Therefore, under the proposed control, it is important to ensure that the total energy in the MMC remains within an acceptable range. In the following, a theoretical analysis on the internal energy dynamics is provided to quantify the energy contribution of the MMC under the virtual capacitor control. In particular, the relation between the value of $k_{vc}$ and the peak of the internal energy variation will be shown.

The sum of the energy absorbed by the $C_{dc}$ and the MMC is given by the time integral of (5.29):

$$W_l\left(t\right) = \int_{t_0}^{t_0+t} \left(P_l - P_{ac}\right) d\tau. \tag{5.32}$$

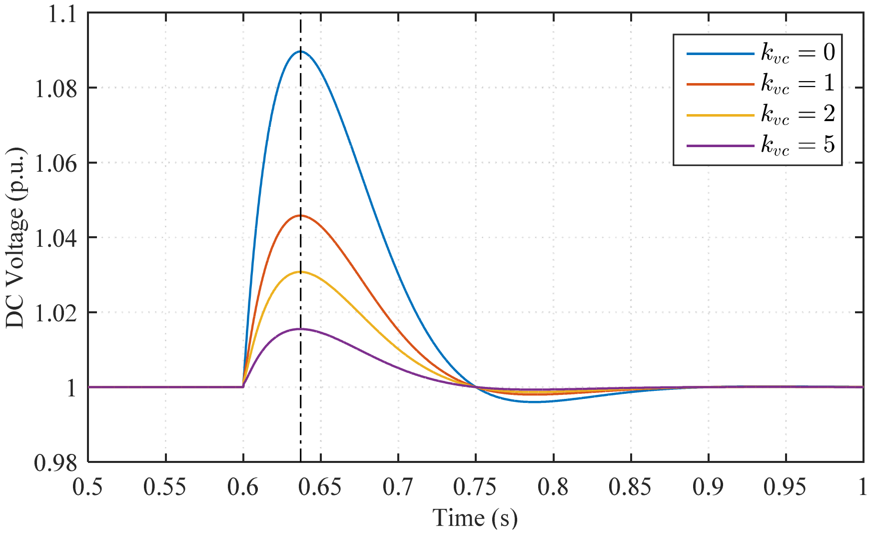

(a) DC voltage

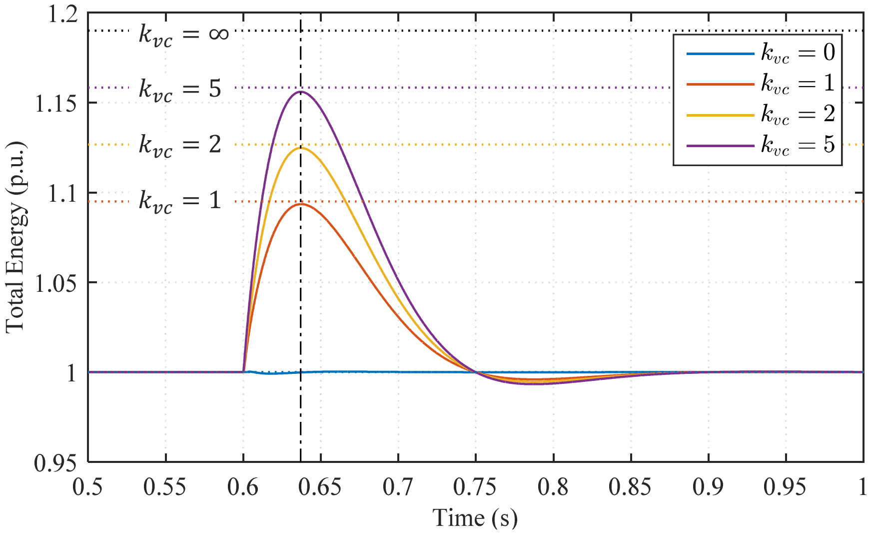

(b) Total energy

Figure 5.6: Simulation results - Comparison with different values of $k_{vc}$.

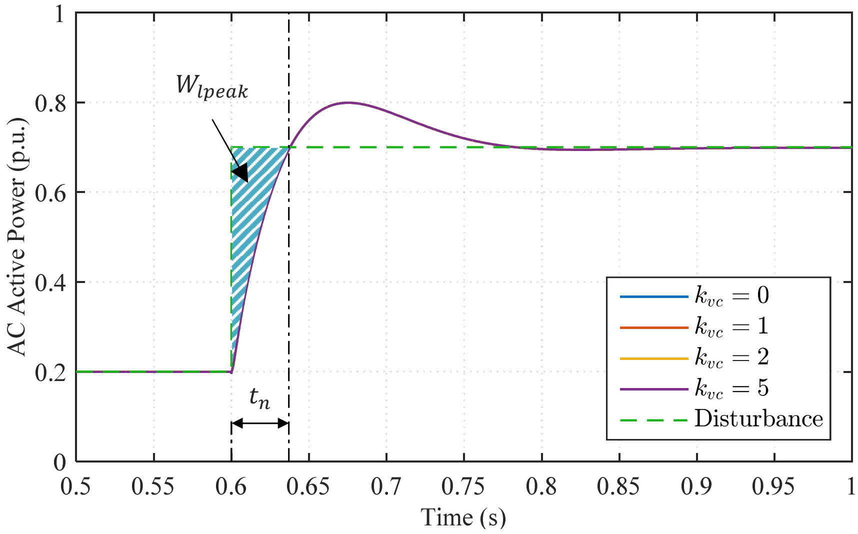

(c) AC active power

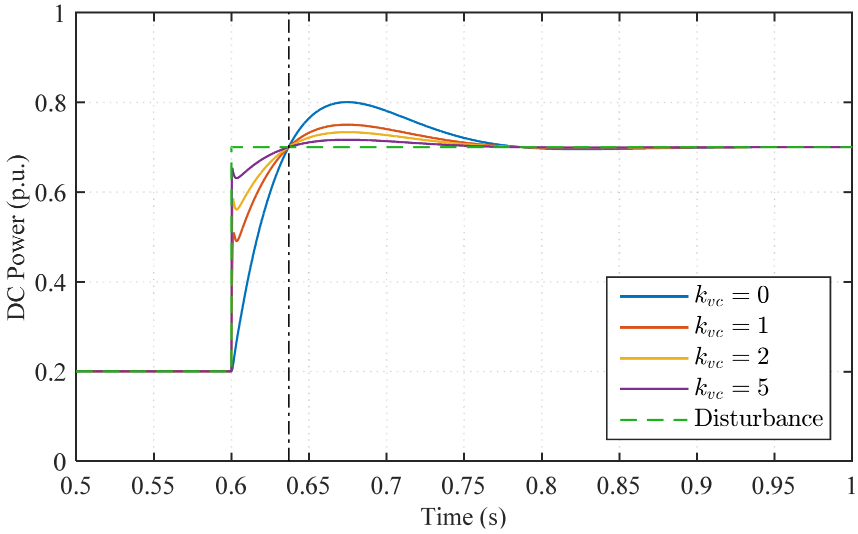

(d) DC power

Figure 5.6: (Continued) Simulation results - Comparison with different values of $k_{vc}$.

As (5.29) implies, if the virtual capacitor control can properly emulate the dynamics of a physical capacitor, $W_l$ is distributed between the $C_{dc}$ and the MMC in proportion to their capacitance. Thus, the variation of the total energy in the MMC should hold:

$$W_{mmc}\left(t\right) = \frac{C_{vc}}{C_{vc} + C_{dc}} W_l\left(t\right) + W^*_{mmc0}. \tag{5.33}$$

In order to estimate the peak of the energy in the MMC, it is necessary to quantify the peak value of the disturbance energy $W_{lpeak} = W_l(t_n)$, which corresponds to the shadowed area shown in Fig. 5.6c, where $t_n$ is the instant that $P_{ac}$ becomes equal to the disturbance for the first time. From Fig. 5.5, the transfer function from the load $P_l$ to the AC power $P_{ac}$ is obtained as:

$$G_{pl}\left(s\right) = \frac{P_{ac}}{P_l} = \frac{2\zeta\omega_n s + \omega_n^2}{s^2 + 2\zeta\omega_n s + \omega_n^2}. \tag{5.34}$$

To simplify the analysis, the pre-contingency steady state $P_{ac0} = P_{l0}$ is assumed, so that $P_l$ and $P_{ac}$ are rewritten as $P_{ac} = P_{ac0} + \Delta P_{ac}$ and $P_l = P_{l0} + \Delta P_l$. Then, the variation of the AC power $\Delta P_{ac}$ against a step disturbance $\Delta P_l$ is derived as:

$$\Delta P_{ac}\left(t\right) = \mathscr{L}^{-1}\{G_{pl}(s)\frac{\Delta P_l}{s}\} = \Delta P_l \left\{1 - e^{-\alpha t}\left(\cos\beta t - \frac{\alpha}{\beta}\sin\beta t\right)\right\} \tag{5.35}$$

where $\alpha = \zeta\omega_n$ and $\beta = \omega_n\sqrt{1-\zeta^2}$. The time $t_n$ that $P_{ac}$ reaches the disturbance for the first time, i.e. $\Delta P_{ac}\left(t_n\right) = \Delta P_l$, is derived from (5.35) as:

$$t_n = \frac{\arctan\frac{\beta}{\alpha}}{\beta}. \tag{5.36}$$

Substituting the derived $t_n$ and (5.35) in (5.32) yields:

$$W_{lpeak} = \int_{t_0}^{t_0+t_n} \Delta P_l e^{-\alpha\tau}\left(\cos\beta\tau - \frac{\alpha}{\beta}\sin\beta\tau\right) d\tau = \frac{\gamma}{\omega_n}\Delta P_l \tag{5.37}$$

where $\gamma = e^{-\frac{\alpha}{\beta}\arctan\frac{\beta}{\alpha}}$. From (5.37) and (5.33), the estimate of the peak value of the total energy in the MMC, $W^{peak}_{mmc}$, is obtained as:

$$W^{peak}_{mmc} = \frac{C_{vc}}{C_{vc} + C_{dc}}\frac{\gamma}{\omega_n}\Delta P_l + W^*_{mmc0}. \tag{5.38}$$

In Fig. 5.6b, the estimated peak values of the total energy calculated from (5.38) for each value of $k_{vc}$ are plotted in dotted lines. As it can be observed, the estimated values are fairly close to the simulation results. Thus, (5.38) is confirmed. According to (5.38), if an infinite value of $k_{vc}$ is assigned, all the disturbance energy will be absorbed by the MMC. The calculated theoretical maximum peak of the energy for the studied case is also plotted in Fig. 5.6b. As seen, even with an infinite value of $k_{vc}$, the internal energy is kept below 1.2 p.u. of its nominal level, which corresponds to a less than 10 % increase of the SM voltage on average.

As discussed in the previous chapter, the proper operation of the MMC is ensured when the energy stored inside the MMC is maintained within the upper and lower limits:

$$W_{mmc}^{Lim-} < W_{mmc} < W_{mmc}^{Lim+}. \tag{5.39}$$

Those energy limits impose the greatest value of $k_{vc}$. Therefore, the operator of the converter must select an appropriate value of $k_{vc}$ according to those limits, the present level of the energy, and maximum possible disturbances. With (5.38) and (5.30), the above inequality is rearranged as follows:

$$W_{mmc}^{Lim-} < \frac{k_{vc}C_{mmc}}{k_{vc}C_{mmc}+C_{dc}}\frac{\gamma}{\omega_n}\Delta P_l + W_{mmc0}^{*} < W_{mmc}^{Lim+}. \tag{5.40}$$

Let us suppose that $\Delta P_l$ is positive. It may be noticed that, if the available headroom of the energy, $W_{mmc}^{Lim+} - W_{mmc0}^{*}$, is larger than the maximum possible energy disturbance $\gamma\Delta P_l/\omega_n$, the peak of the energy variation will not reach the limit regardless of the assigned value of $k_{vc}$. On the other hand, when $\gamma\Delta P_l/\omega_n$ is bigger than the available headroom, the limits of the energy may be violated depending on the assigned value of $k_{vc}$. This is also the case where $\Delta P_l$ is negative. By solving (5.40) in terms of $k_{vc}$, the required conditions to ensure the energy limits are obtained as follows:

$$k_{vc} < \frac{C_{dc}\left(W_{mmc}^{Lim+} - W_{mmc0}^{*}\right)}{C_{mmc}\left\{\frac{\gamma\Delta P_l}{\omega_n} - (W_{mmc}^{Lim+} - W_{mmc0}^{*})\right\}} \quad \text{if}\ \frac{\gamma\Delta P_l}{\omega_n} > W_{mmc}^{Lim+} - W_{mmc0}^{*} \tag{5.41}$$

$$k_{vc} < \frac{C_{dc}\left(W_{mmc0}^{*} - W_{mmc}^{Lim-}\right)}{C_{mmc}\left\{-\frac{\gamma\Delta P_l}{\omega_n} - (W_{mmc0}^{*} - W_{mmc}^{Lim-})\right\}} \quad \text{if}\ \frac{\gamma\Delta P_l}{\omega_n} < W_{mmc}^{Lim-} - W_{mmc0}^{*}. \tag{5.42}$$

As seen, the required condition of $k_{vc}$ is determined not only by the concerned converter itself but also by the proportion of the $C_{mmc}$ to the system capacitance $C_{dc}$. Therefore, the transmission system operator (TSO) must assign an adequate value of $k_{vc}$ to each converter station taking into account its available headroom of the energy and the proportion of the capacitance in the whole system.

### 5.4.4 Simulation of a Point-to-Point HVDC System

To demonstrate the feasibility of the proposed control, simulations of a point-to-point HVDC system, shown in Fig. 5.7, are carried out.

For the sake of credibility, the two MMCs are modeled based on the full-order equivalent model representation (See Section 2.4.3.2) in which each arm is composed of 400 SMs. In this model, the individual SMs are considered separately; thus, the individual

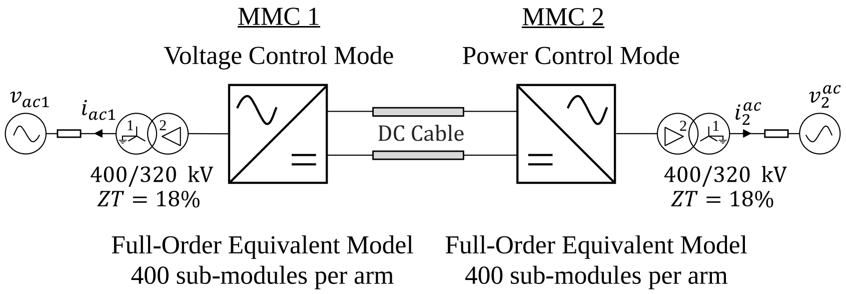

Figure 5.7: Simulation setup (HVDC point-to-point system).

cell-voltage dynamics are conserved, and the discrete voltage steps are reproduced. The standard BCA provided in the EMTP-RV library is implemented. The two MMC stations are connected through 64.5 km DC cables, which are modeled by the Wide Band Cable Model provided in EMTP-RV library [172]. The geometrical and electrical parameters are referred to [173] and shown in below.

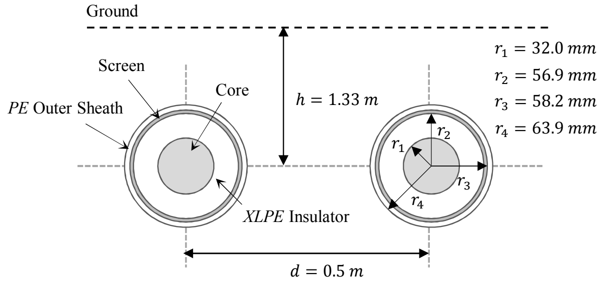

Figure 5.8: Cable cross section.

Table 5.2: DC cable parameters.

| Parameter | Value |
|---|---|
| Resistivity of Core | $1.72e^{-8}\Omega$m |
| Resistivity of Screen | $2.83e^{-8}\Omega$m |
| Insulator relative permittivity | 2.5 |
| Insulator loss factor | 0.0004 |

The initial operating points are given as:

- MMC 1 : $v_{dc1}^{*} = 1.0$ p.u., $Q_{ac1}^{*} = 0.2$ p.u.
- MMC 2 : $P_{ac2}^{*} = 0.5$ p.u., $Q_{ac2}^{*} = 0.2$ p.u.

In order to assess the effectiveness of the proposed control to cope with unexpected disturbances, a series of step changes of active power is generated. The active power reference of MMC 2 is decreased to 0.25 p.u. at $t = 0.6$ s. Then it is increased to 0.75 p.u. at $t = 1.1$ s. Four cases are studied as detailed in Table 5.3; they are classified by the sum of the assigned $k_{vc}$ of each station. For each case, the DC voltage controller of MMC 1 is tuned to maintain 100 ms response time according to the equivalent capacitance of the whole system.

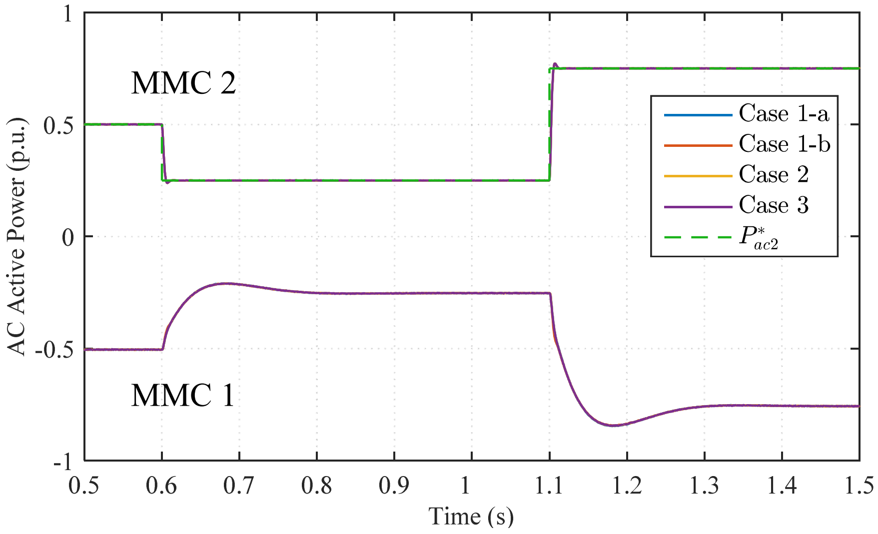

(a) AC active power

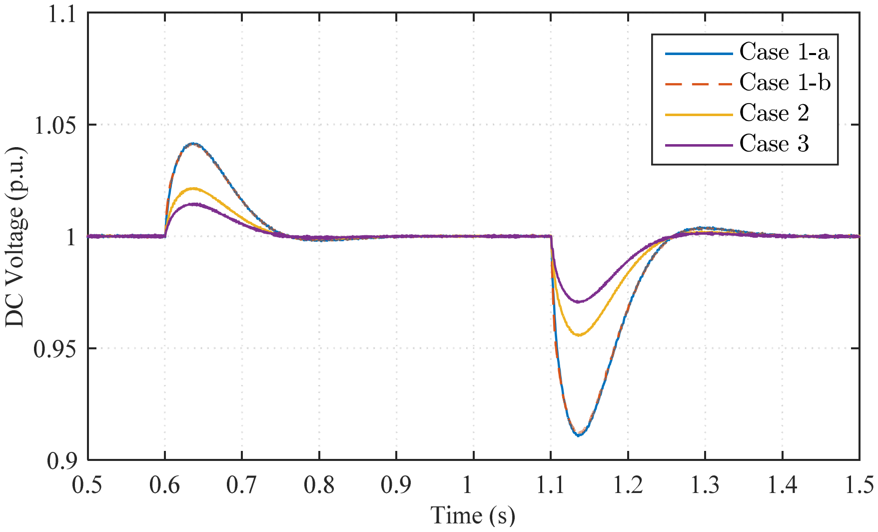

(b) DC voltage - MMC 1

Figure 5.9: Simulation results - HVDC point-to-point system with different values of $k_{vc}$.

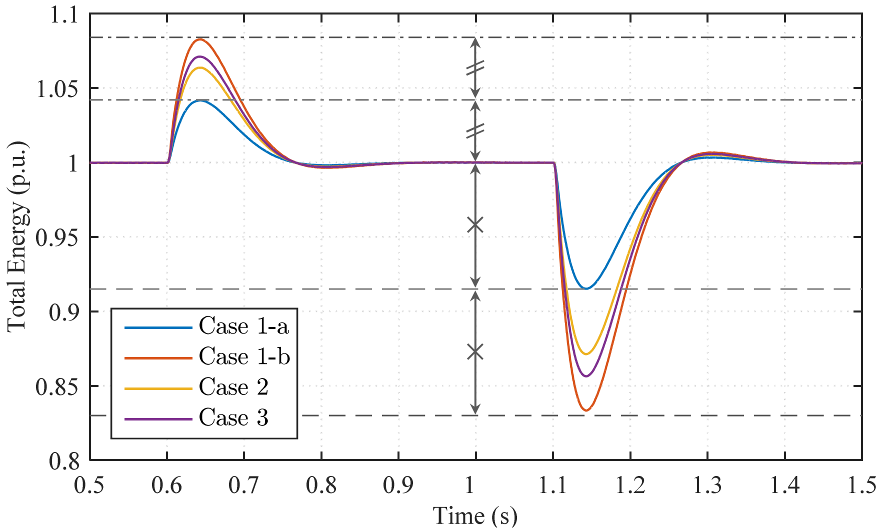

(c) Total energy - MMC 1

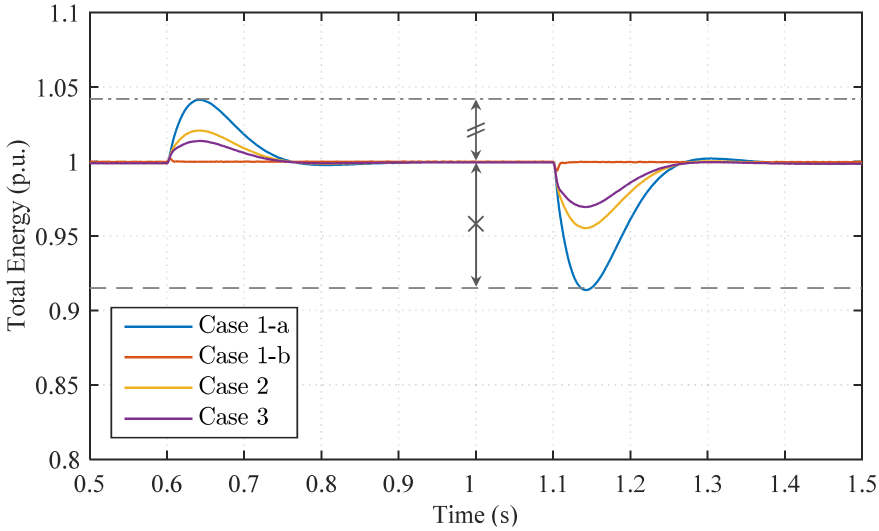

(d) Total energy - MMC 2

Figure 5.9: (Continued) Simulation results - HVDC point-to-point system with different values of $k_{vc}$.

Table 5.3: HVDC point-to-point system simulation studied cases

| Case | $k_{vc1}$ | $k_{vc2}$ | $\Sigma k_{vc}$ |
|---|---|---|---|
| Case 1-a | 0.5 | 0.5 | 1 |
| Case 1-b | 1.0 | 0.0 | 1 |
| Case 2 | 1.5 | 0.5 | 2 |
| Case 3 | 2.5 | 0.5 | 3 |

The obtained results are compared in Fig. 5.9. As seen in Fig. 5.9a, the power controlling station (i.e. MMC 2) appropriately follows the change of the active power reference in any cases, and MMC 1 properly absorbs the excess or deficit of the power to stabilize the DC voltage. For both stations, the AC power does not change with the value of $k_{vc}$. This implies that the introduction of the virtual capacitor control does not have any impact on the AC power in the studied cases. On the other hand, the value of $k_{vc}$ can greatly affect the DC voltage dynamics. In Fig. 5.9b, it can be seen that the DC voltage dynamics are exactly the same between Cases 1-a and 1-b. This is because Cases 1-a and 1-b have apparently the same total capacitance from the DC system point of view. When the total values of $k_{vc}$ is increased (i.e. Case 2 and Case 3), the variation of the DC voltage becomes smaller. Fig. 5.9c and 5.9d show the internal energy level of MMC 1 and MMC 2. In Case 1-a, the same value of $k_{vc}$ is assigned for both stations. Therefore, they provide equal energy contribution. In contrast, in Case 1-b, only MMC 1 contributes while MMC 2 maintains its energy level during the disturbances. Thus, MMC 1 takes the share of the MMC 2, and the peak energy level reaches double as that of Case 1-a.

From the simulations on the detailed point-to-point HVDC system model, the effectiveness of the virtual capacitor control is confirmed. In addition, the obtained results reveal that the energy contribution of each MMC can be arbitrarily adjusted by simply changing its value of $k_{vc}$. The appropriate values of $k_{vc}$ can be determined by the system operator taking into account the constraints on the DC system and the available energy headroom of the MMCs.

### 5.4.5 Comparison with Conventional MMC Control

In order to highlight the advantage of the virtual capacitor control, the proposed control is compared with the conventional MMC control scheme consisting of the same decoupled $dq$-frame AC current controller with the second harmonic Circulating Current Suppression Controller (abbreviated as CCSC henceforth) [127]. The same point-to-point HVDC system model as the previous subsection is used. For the proposed control, the virtual capacitor coefficient of $k_{vc1} = 3$ and $k_{vc2} = 1$ are assigned to the respective stations. For the conventional case, the MMC controller is replaced by the CCSC for both stations. Then, the same disturbance scenario as the previous subsection is imposed.

The obtained simulation results are compared in Fig. 5.10. As seen in Fig. 5.10a, both have approximately the same dynamic responses on the AC side. However, the transient behavior of the DC voltage, shown in Fig. 5.10b, greatly differs in amplitude. This can be explained by the difference in the equivalent capacitance of the DC system. Under the CCSC, the arm capacitor voltages follow the DC bus voltage without explicit control. This is confirmed in Fig. 5.10c and 5.10d, which show the uncontrolled energy variations during the transient. As demonstrated in [174], the MMC under the CCSC provides an implicit energy contribution as an equivalent capacitor $C_{mmc}$. Thus, the equivalent capacitance of the whole DC system in the CCSC case is approximately the same as the case with $\Sigma k_{vc} = 2$, so that it is a half of the case with the virtual capacitor control. As a result, the variation of the DC voltage under the proposed control is reduced by almost half of that of the CCSC.

In Fig. 5.11, the total capacitor voltage in six arms are depicted. As seen, they are effectively balanced in the steady state for both cases. There is a slight energy disparity observed during the transient in the CCSC case, but it is less significant in the proposed control case. Thus, it can be said that the proposed control does not cause unbalance of the arm energy; thus, it provides better uniformity of the energy during the transient.

In Fig. 5.12, the representative SM capacitor voltages for both cases are shown. Note that the horizontal grid lines in the figures indicate ±10 and 20 % of the nominal SM voltage. It can be noticed that there is no significant difference in the peak values of the SM voltages between the proposed control and the CCSC. Therefore, for this given set of parameters, it can be argued that the proposed control has very little effect on the voltage stresses of the SMs.

In Fig. 5.13, all the currents measured under the virtual capacitor control are depicted. All the currents are effectively controlled.

From those results, no particular issue has been identified for the practical application of the proposed control.

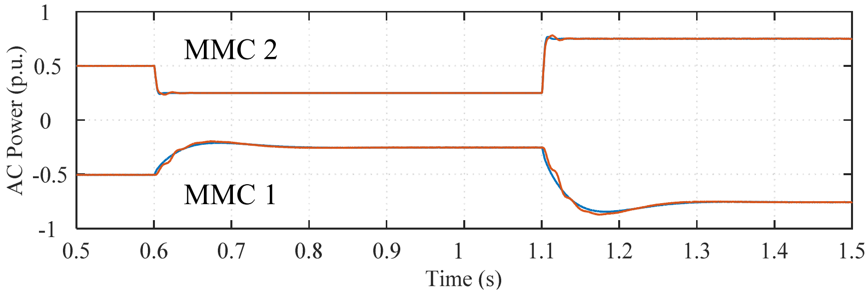

(a) AC active power

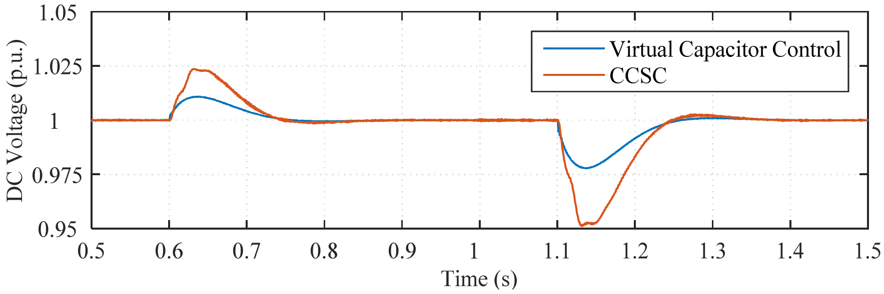

(b) DC voltage - MMC 1

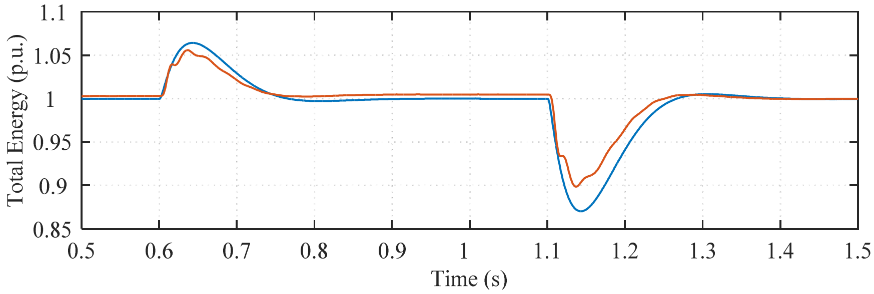

(c) Total energy - MMC 1

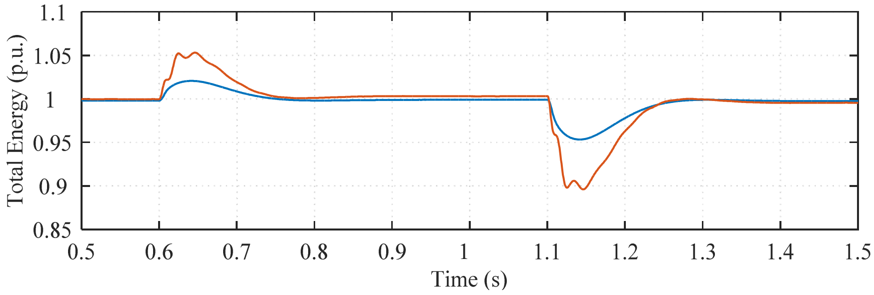

(d) Total energy - MMC 2

Figure 5.10: Comparison of simulation results - blue: Virtual Capacitor Control, red: CCSC.

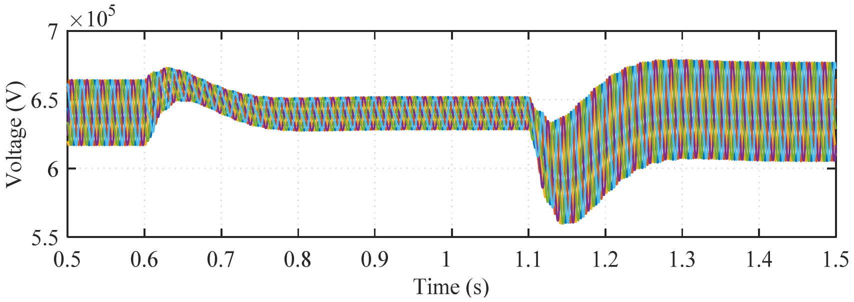

(a) Total capacitor voltage - MMC 1 with proposed control

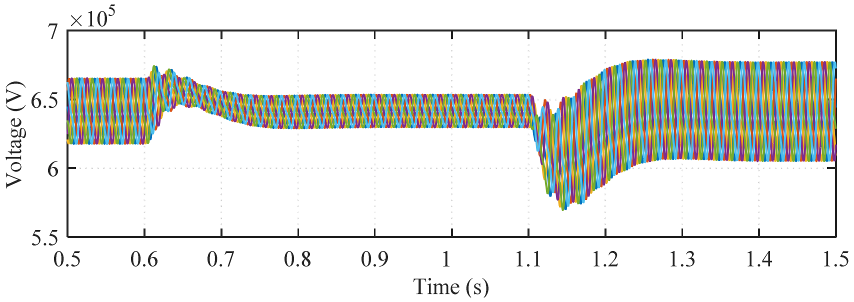

(b) Total capacitor voltage - MMC 1 with CCSC

Figure 5.11: Comparison of arm capacitor voltage - MMC 1.

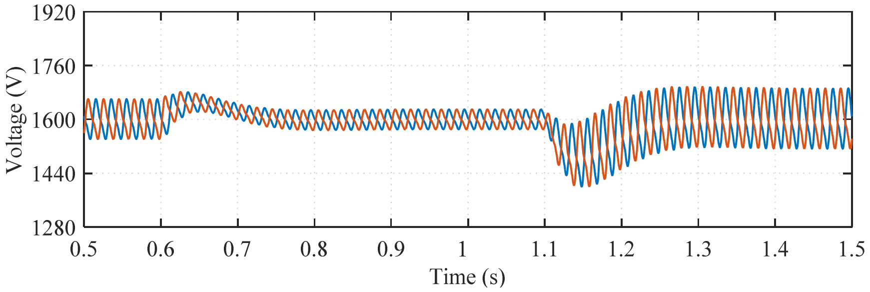

(a) SM capacitor voltage: $v^u_{Ca,1}$and $v^l_{Ca,1}$ with proposed control

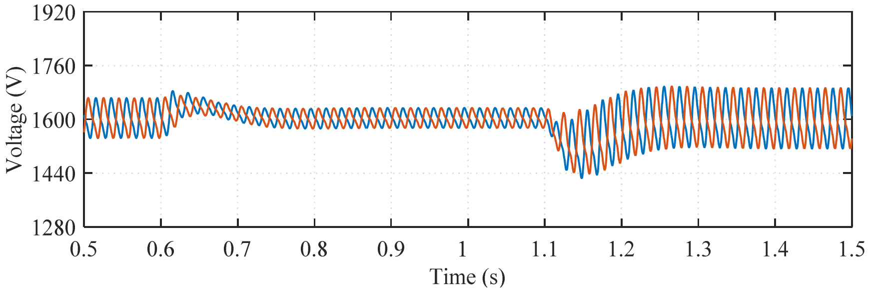

(b) SM capacitor voltage: $v^u_{Ca,1}$and $v^l_{Ca,1}$ with CCSC

Figure 5.12: Comparison of SM capacitor voltage - MMC 1.

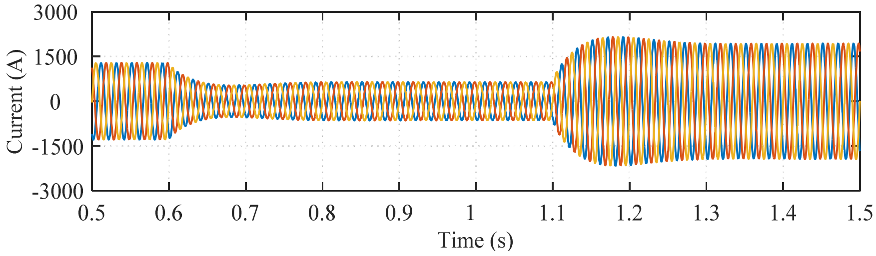

(a) AC grid current

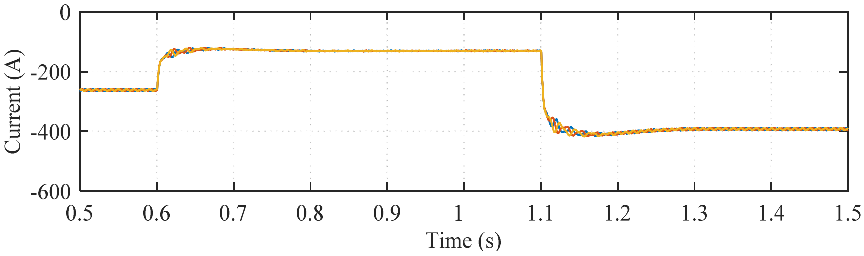

(b) DC common mode current

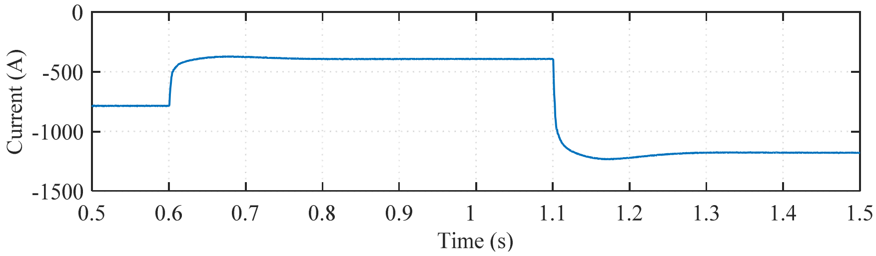

(c) DC grid current

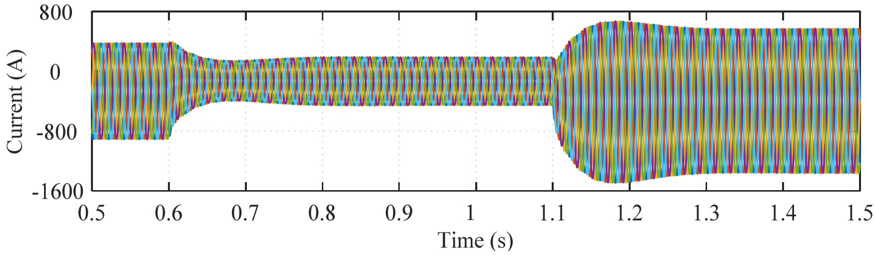

(d) Arm current

Figure 5.13: Current dynamics under the proposed control - MMC 1.

## 5.5 Sizing of Virtual Capacitor

As previously demonstrated, the virtual capacitor control can emulate the behavior of a physical capacitor without any adverse effect on the AC grid. The size of the virtually emulated capacitor does not need to reflect the actual size of the physical capacitor embedded in the MMC; hence, it can be optionally chosen according to the system requirement. This implies that it will bring an additional degree of freedom for the operation of HVDC systems.

In this section, a method to determine the size of this virtual capacitor to limit the peak value of the DC voltage to a desired level is proposed. For the sake of generality, a three-terminal DC grid (see Fig. 5.14), where an onshore converter station collects the power generated by two offshore wind farms, is considered throughout this section. Since the virtual capacitor can be taken into account in the same manner as a physical capacitor, it can be readily integrated to the mathematical model representing the DC voltage dynamics. From the closed-loop DC voltage model analysis, the relation between the peak voltage variation and the virtual capacitor size is clarified, and an expression which determines the required size of the virtual capacitor is derived. The feasibility of the proposed solution is confirmed by EMT simulations.

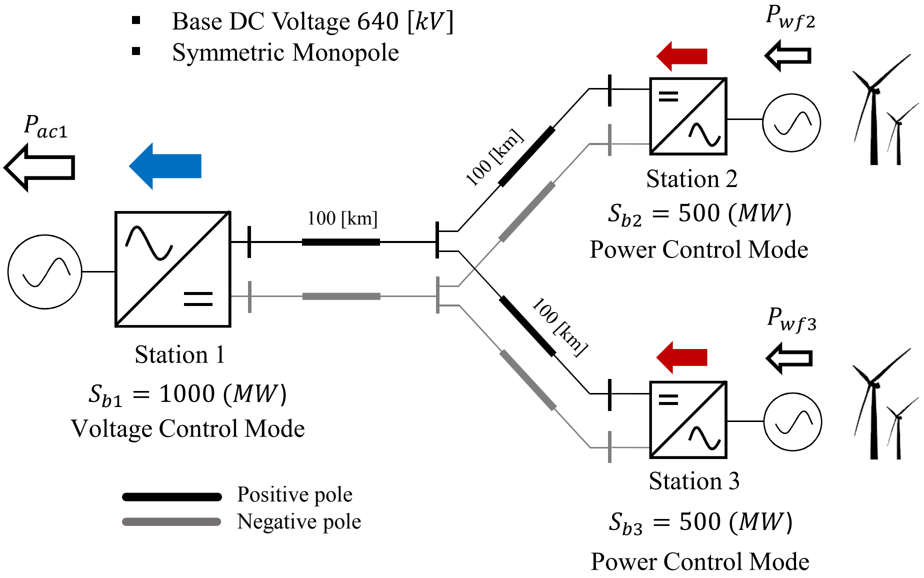

Figure 5.14: 3-terminal HVDC system model.

### 5.5.1 Theoretical Analysis on Peak Variation of DC Voltage

The control methodology of the DC voltage can be roughly categorized into the Master/Slave method and the Voltage Droop method [175]. If we consider the HVDC grid shown in Fig. 5.14, where all the available power generated by offshore wind farms is transferred to an onshore station, the Master/Slave method can be readily applied. The Master/Slave method is an extension of the method adapted for the control of a point-to-point HVDC system [176]. In this method, the master converter station will act as the slack bus taking responsibility to maintain the DC voltage within a certain range by providing or absorbing sufficient power whilst the other (slave) converters control only power [145].

As discussed in Section 5.4.1, the virtual capacitors can be considered as being connected to the DC bus in parallel. For the sake of simplicity, the resistance and inductance of the cables are neglected. Then the equivalent capacitance of the DC grid $C_{eq}$ can be expressed by the sum of the virtual capacitance and the cable capacitance:

$$C_{eq} = \sum_{m}^{N_{st}} C_{vc,m} + \sum_{l}^{N_{cable}} C_{cable,l} \tag{5.43}$$

where $C_{vc,m}$ is the virtual capacitance of $m$th station, and $C_{cable,l}$ is the capacitance of the $l$th cable, $N_{st}$ and $N_{cable}$ are the number of MMC stations and cables, respectively.

Supposing that the dynamics of the inner current loops are negligible, a simplified closed-loop model of the 3-terminal DC grid with the virtual capacitor can be obtained as depicted in Fig. 5.15. Note that the power injected to the AC grid by Station 1 is designated by a positive sign, and the power generated by the wind farms, $P_{wf2}$ and $P_{wf3}$, are designated by positive signs here.

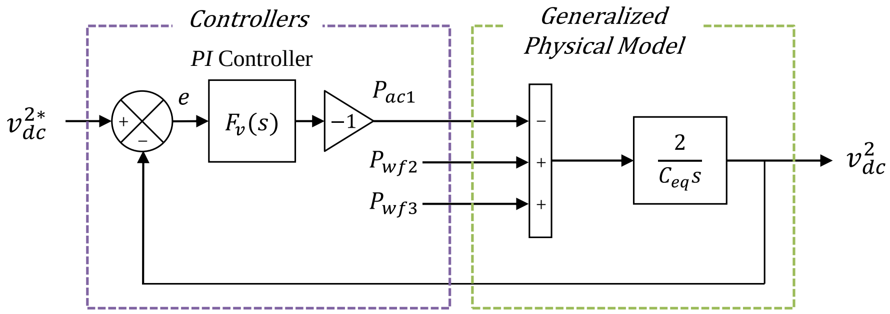

Figure 5.15: Generalized simplified closed-loop model for DC voltage control of 3-terminal DC grid with Virtual Capacitor Control.

During the operation of the DC grid, the voltage must be maintained within a certain range (e.g. ±5 %), otherwise a large DC voltage drop might temporarily limit the converter operation and affect the stability of the controlled systems. Therefore, the poles of the closed-loop system must be placed considering the maximum possible disturbance in the system [177]. From Fig. 5.15, the transfer function from the load disturbance in $P_{wf2}$ or $P_{wf3}$ to the error signal, $e = v_{dc}^{2*} - v_{dc}^2$, is derived as:

$$G_{pe}\left(s\right) = -\frac{\dfrac{2}{C_{eq}s}}{1 + F_v(s)\dfrac{2}{C_{eq}s}}. \tag{5.44}$$

The same *PI* controller as the previous section, i.e. $F_v\left(s\right) = K_p^{v_{dc}} + K_i^{v_{dc}}/s$, is considered. To recall, the gain parameters are tuned according to the desired response time $T_r = 3/\omega_n$ with damping ratio $\zeta = 0.707$ (See Section 5.4.1 for more details on the tuning technique). Then, (5.44) can be rewritten as:

$$G_{pe}\left(s\right) = -\frac{\dfrac{2}{C_{eq}}s}{s^2 + 2\zeta\omega_n s + \omega_n^2}. \tag{5.45}$$

Considering a step disturbance on the wind power generation denoted by $P_{dis}$, the response of the error signal in the time domain becomes:

$$e_d(t) = \mathcal{L}^{-1}\left\{G_{pe}\left(s\right)\frac{P_{dis}}{s}\right\} = -\frac{2P_{dis}}{C_{eq}\beta}e^{-\alpha t}\sin\left(\beta t\right) \tag{5.46}$$

where $\alpha = \zeta\omega_n$ and $\beta = \omega_n\sqrt{1-\zeta^2}$. From the time derivative of (5.46),

$$\frac{de_d(t)}{dt} = -\frac{2P_{dis}}{C_{eq}\omega_n}e^{-\alpha t}\left\{-\frac{\alpha}{\beta}\sin\beta t + \cos\beta t\right\}, \tag{5.47}$$

the timing when the error signal reaches its maximum is calculated as:

$$t_n = \frac{\arctan\dfrac{\beta}{\alpha}}{\beta}, \tag{5.48}$$

Then, substituting (5.48) into (5.46) yields,

$$e_d(t_n) = -\frac{2P_{dis}}{C_{eq}}\frac{\gamma}{\omega_n}, \tag{5.49}$$

with $\gamma = e^{-\frac{\alpha}{\beta}\arctan\frac{\beta}{\alpha}}$. Consequently, the estimate of the peak voltage is derived as:

$$v_{dc\,peak} = \sqrt{\frac{2T_rP_{dis}\gamma}{3C_{eq}} + v_{dc}^{2*}} \tag{5.50}$$

where $\omega_n$ is replaced by $T_r/3$ for convenience.

As the above equation indicates, now the peak value of the DC voltage can be estimated from the size of the disturbance $P_{dis}$, the equivalent system capacitance $C_{eq}$, and the response time of the DC voltage control $T_r$.

### 5.5.2 Confirmation by Simulation

The derived expression (5.50) is confirmed by simulations of the 3-terminal MMC-based DC grid model (see Fig. 5.14). The MMCs are modeled by the full-order equivalent model. Station 1 regulates the DC voltage as the master station while the other stations control the power injection to the DC grid. The DC cables are modeled by the Wide Band Cable Model. The initial operating point is selected as $v_{dc}^{*} = 1$ p.u. and the maximum loading $P_{wf2} = P_{wf3} = 500$ MW. At $t = 1$ s, $P_{wf2}$ is reduced to zero instantly, and the dynamics of the DC voltage are observed. The same simulations are carried out by varying the response time of the DC voltage controller. The identical value of $k_{vc} = 1$ is assigned to all the converter stations. This means that each MMC behaves as if it were associated with a DC link capacitor whose size is equivalent to the converter.

Fig. 5.16 shows the obtained results. In Fig. 5.16a, the DC voltage at Station 1 and the estimated peak values (dashed lines), derived from (5.50) for the respective response time, are shown. The estimated values closely correspond to the simulation results; therefore, the derived analytic expression is verified. However, only the response time around 100 ms is capable of maintaining the DC voltage within the desired range, i.e. $\Delta V_{dc}^{Lim-} = -5$ %. In the conventional manner, there are only two solutions. One is to install a bigger capacitor. However, it requires a great capital cost and may not be economically feasible. Another solution is to reduce the response time of the DC voltage controller. This can be achieved by modifying the control gains. However, as seen in Fig. 5.16b, a faster time response results in a faster propagation of the disturbance to the associated AC grid. Furthermore, a faster response of the DC voltage controller may interact with the inner current control loop and degrade the overall system stability. Thus, the latter solution is not preferred from the viewpoint of the system stability. Fig. 5.16c shows the total energy dynamics. As expected, the total energy stored in the MMC decreases in accordance with the DC voltage variation.

### 5.5.3 Virtual Capacitor Sizing to Respect DC Voltage Limit

As (5.50) implies, the peak voltage level depends on the capacitance of the system. Under the virtual capacitor control, the equivalent capacitance of the system can be adjusted by varying the values of $k_{vc}$. Thus, it brings an alternative solution to restrain the voltage variation. By arranging (5.50), the necessary value of capacitance to limit the voltage deviation above $V_{dc}^{Lim-} = 0.95$ p.u. can be derived as follows:

$$C_{eq}^{*} = \frac{2T_r P_{dis}\gamma}{3\left\{\left(V_{dc}^{Lim-}\right)^2 - 1\right\} v_{dc}^{2*}}. \tag{5.51}$$

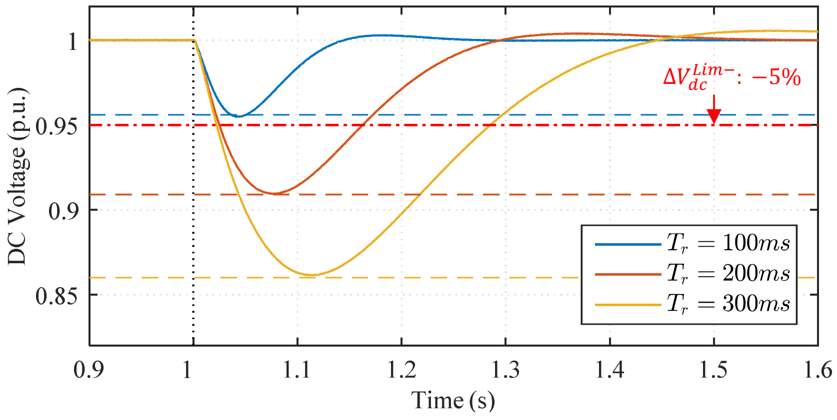

(a) DC voltage at Station 1

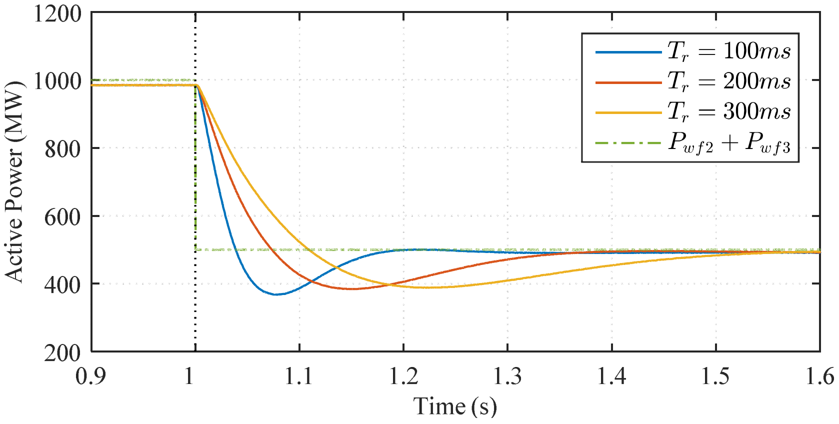

(b) AC active power at Station 1

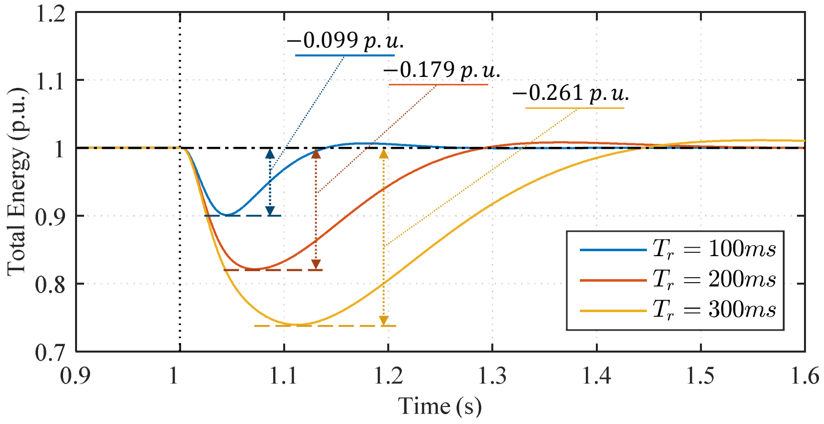

(c) Total energy of Station 1

Figure 5.16: Simulation results - Confirmation of analysis with different response time.

Then, the corresponding values of $k_{vc}$ can be assigned to the stations:

$$C^*_{eq} = \sum_{m}^{N_{st}} k_{vc,m} C_{mmc,m} + \sum_{l}^{N_{cable}} C_{cable,l}. \tag{5.52}$$

According to the given parameters, the value of $k_{vc}$ in case of an identical value for all the stations is calculated and summarized in Table 5.4. Then, the same simulations as the previous section are carried out with the calculated values of $k_{vc}$. The DC voltage controller gains are adapted according to the modified apparent capacitance of the system to maintain the desired response time.

Table 5.4: Required capacitance and virtual capacitor coefficient.

| DC Voltage Controller Response Time $T_r$ (ms) | Required Capacitance $C^*_{eq}$ ($\mu$F) | Total Cable Capacitance $\sum C_{cable}$ ($\mu$F) | Station 1 | Station 2 | Station 3 |
|---|---|---|---|---|---|
| | | | Physical Capacitance $C_{mmc}$ ($\mu$F) | | |
| | | | 195.31 | 97.66 | 97.66 |
| | | | Virtual Capacitance $C_{vc}$ ($\mu$F) | | |
| 100 | 380.6 | 36.3 | 172.2 | 86.1 | 86.1 |
| | | | $k_{vc} = 0.88$ | | |
| 200 | 760.2 | | 362.4 | 181.2 | 181.2 |
| | | | $k_{vc} = 1.86$ | | |
| 300 | 1141.8 | | 552.7 | 276.4 | 276.4 |
| | | | $k_{vc} = 2.83$ | | |

Fig. 5.17 shows the obtained results. As clearly seen in Fig. 5.17a, the voltage peaks now respect the constraints regardless of the response time. In Fig. 5.17b, the AC power dynamics are compared with the previous results (shown by dotted lines). Since the transfer function from the load disturbance to the AC power output of Station 1, i.e. $-F_v(s)G_{pe}(s)$, does not depend on the system capacitance but only on the response time of the controller under this tuning technique, the AC power dynamics remain unchanged. This implies that there is no adverse effect on the AC system. In Fig. 5.17c, the total energy dynamics are depicted. Under the virtual capacitor control, the disturbance energy is distributed among the capacitance of the DC cables and that of the virtual capacitor emulated by the MMCs. This share of the disturbance energy by the MMCs helps to attenuate the DC voltage variations. Concerning the efforts made by the MMC in terms of its internal energy variation, since the capacitance of the DC cables is much smaller than of the MMCs in general, it is possible to significantly attenuate the DC voltage variations at the expense of very small increase of the MMC internal energy variations. Furthermore, under the virtual capacitor control, the nominal level of the total energy can be optionally selected without any interference with the performance of the capacitor emulation. Therefore, by setting it at an appropriate level, the peak energy can be limited to a desired value as observed.

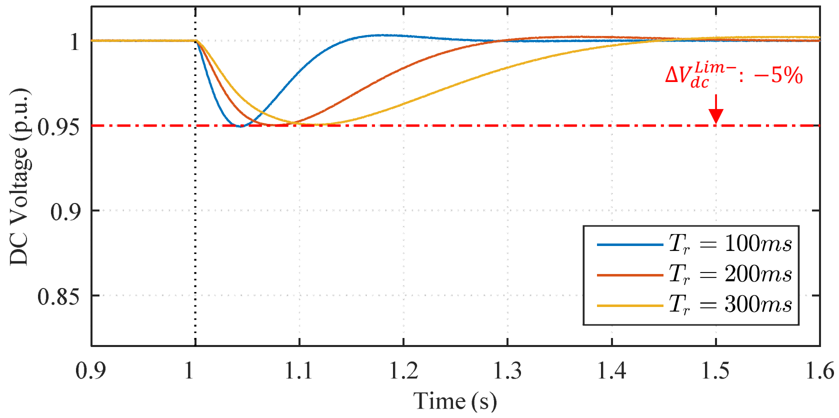

(a) DC voltage at Station 1

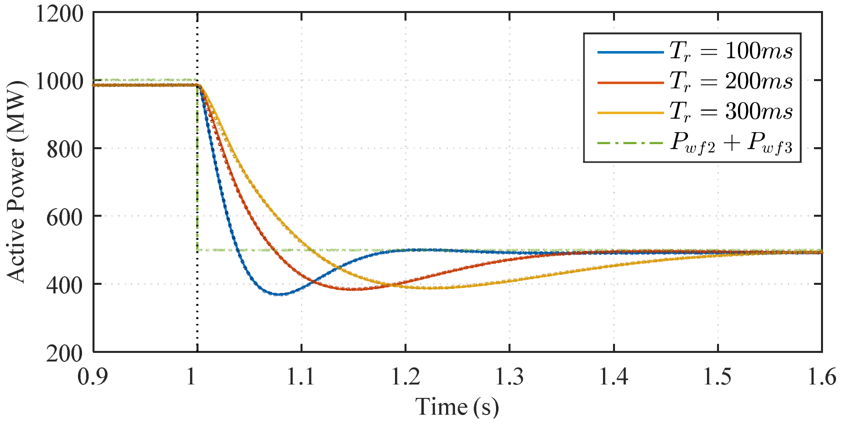

(b) AC active power at Station 1

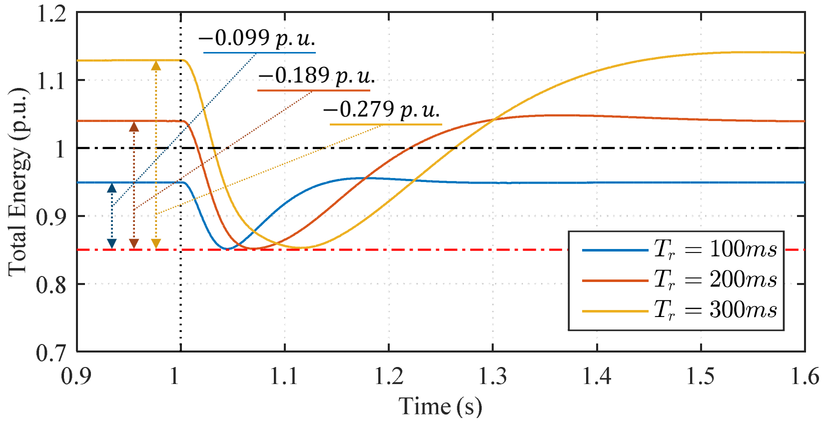

(c) Total energy of Station 1

Figure 5.17: Simulation results - System dynamics under the virtual capacitor control with different response time.

## 5.6 Chapter Conclusion

Firstly, the general dynamics of the DC systems were described in terms of analogies to AC systems. It was revealed that the common variable of the DC systems representing the power balance — the DC voltage — is extremely volatile compared to the frequency in AC systems due to the considerably smaller energy stored in the system. As a solution to this problem, a novel control method for the MMC, named Virtual Capacitor Control, was introduced. This control enables to utilize the energy storage capability of the MMC to enhance the equivalent capacitance of the HVDC system. The proposed virtual capacitor control enables the MMC to behave as if there were an adjustable capacitor on the DC side of the converter. This is realized by the appropriate energy reference calculation which allows regulating the internal energy level in conjunction with the variation of the DC voltage. By simply changing the virtual capacitor coefficient $k_{vc}$, the degree of the contribution by the internal energy can be adjusted. Since the virtual capacitor control simply reproduces the dynamics of a physical capacitor, any practical DC grid voltage control method designed for conventional VSC type converters can be directly applied to the MMCs. Furthermore, the system operator can optionally assign the value of $k_{vc}$ to each MMC station to achieve desired mitigation level of DC voltage fluctuation during the operation. Thus, the proposed control can greatly broaden the operability of the DC systems.

This new degree of freedom brings a solution to maintain the DC voltage within a prescribed range without having an extra capital cost or negative impact on the AC grid. A method to determine the required size of the virtual capacitor was proposed. The analytic expressions and the feasibility of the proposed solution were verified by the EMT simulations of the 3-terminal HVDC grid. The simulation results proved the effectiveness of the proposed solution and extended operability of the DC grid.

# Chapter 6

# Operation of MTDC Grid

## 6.1 Chapter Introduction

Spurred by the remarkable advance of the power electronic converter technology, HVDC transmission has become a both technically and economically attractive option. Despite the large number of HVDC transmission projects around the world, to date, most of HVDC transmission systems comprise only two converter stations, in other words, a point-to-point (PtoP) scheme. If there are more than two VSC converter stations in a DC system, it becomes a multi-terminal DC (MTDC) grid. It is expected that the MTDC grids will bring more reliability and flexibility for power dispatch to conventional power systems. Nonetheless, compared to the vast number of PtoP HVDC link projects, MTDC projects are much less numerous. This may have resulted from the several remaining issues to be solved such as control and protection of MTDC grids.

This chapter first introduces a general overview of the MTDC grid operation and its control hierarchy. There is a common consensus that the Voltage Droop Method is considered as a suitable strategy for voltage regulation in an MTDC grid. The behavior of a droop-controlled MTDC grid against a sudden disturbance is investigated, and the restrictions in the droop parameters selection are identified. Then the virtual capacitor control presented in the previous chapter is applied to the MTDC grid. It is demonstrated that the additional degree brought by this control brings great flexibility to the selection of the droop parameter.

Thereafter, the limitations of the conventional droop approach in regard to the large burden of the power sharing imposed to the converter stations in small MTDC grids are investigated. It is revealed that the desired control action may not be taken when the available headroom of the converter station is insufficient. We thus propose a novel voltage droop control structure which permits different actions depending on the sign of DC voltage deviation caused by the disturbance. A methodology to effectively allocate the reserve capacity taking into account the operating point and the available headroom of each station is also proposed. Its effectiveness and feasibility are confirmed by EMT simulations on a four-terminal MTDC grid model.

## 6.2 Overview of MTDC Grid Operation

As described in the previous chapter, the frequency is a global measure of the balance between the generation and the load in an AC system. When the energy equilibrium collapses, for instance due to a sudden loss of a generation unit, the frequency fluctuates and may result in a massive blackout if an adequate counteraction is not taken. Therefore, although there are small differences in specifications, any AC system contains frequency control services, and most of generation units are supposed to participate in the frequency control [178]. In a similar manner, the imbalance of the power in DC system leads to a variation of the voltage. Therefore, for its secure operation, DC system also requires energy balancing service. As most of the AC systems take a hierarchical structure of frequency control to assure the provision of high-quality power and withstand possible contingencies, the MTDC grid is foreseen to have a similar control structure.

This section provides a general overview of MTDC grid operation. First, the frequency regulation of the conventional AC systems is recalled in order to facilitate the introduction of MTDC grid control. Then, the common consensus on the hierarchical MTDC grid control structure seen in the existing literature is introduced.

### 6.2.1 Control Hierarchy of AC Systems

In AC systems, hierarchical control structure is implemented to maintain the energy balance. Although there are small differences in implementation among Transmission System Operators (TSOs), the general control structure and their roles are practically the same. A very extensive survey is provided in [178] in which the technical features are compared across various existing systems. Also, ENTSO-E has provided a guideline for the requirements for EU-wide load-frequency control and reserve [179]. Fig. 6.1 shows the general control hierarchy of the AC systems. The main roles of the control structure are recalled in the following.

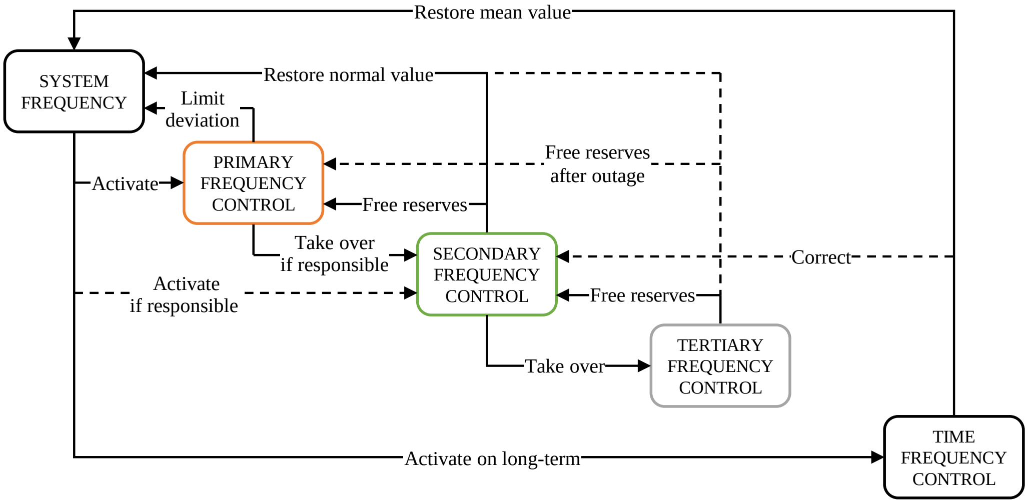

Figure 6.1: Different control actions in AC systems and their linkage [9].

**Primary Frequency Control** Primary frequency control is the first control action taken by the generator units after a deviation of the frequency. Upon detecting this frequency deviation caused by a power disturbance, the speed governor in the generator turbine deviates its power output in proportion to the frequency deviation. The primary frequency control action is realized in a decentralized manner without communication. The stations which participate in the primary frequency control must secure a certain reserve (Frequency Containment Reserve (FCR)). A sufficient amount of the FCR must be secured and kept available in order to perform primary frequency control. The responsibility of the procurement of FCRs is laid on the TSO of the controlled area. The participants of the primary frequency control must guarantee the continuous availability of the FCR and its full deployment when necessary. In case of contingency, the FCR must be deployed in a short period of time (e.g. 30 s) and lasts only a limited time (e.g. 15 to 20 min) [179].

**Secondary Frequency Control** When the primary frequency control is in effect, the frequency deviation caused by a disturbance can be contained within a permissible range. However, it will always leave a certain frequency deviation. The role of the secondary frequency control is to bring the frequency back to the nominal level after a disturbance. The secondary control operates in a centralized manner on a slower time scale. The reestablishment of the system frequency is achieved by activating the reserve power (Frequency Restoration Reserve (FRR)). As the frequency is brought to the nominal value, the power exchanges on the tie-lines between the different zones are also restored to their original values.

**Tertiary Frequency Control** The role of the tertiary frequency control is to guarantee the provision of an adequate FRR and its reallocation. The tertiary frequency control is often manually activated by the system operator. The tertiary frequency control action includes increasing or reducing the output of generators in service, activation of storage as well as load shedding taking into account the economical aspect.

### 6.2.2 Primary Frequency Control of AC system

From the dynamic point of view, the primary frequency control, which is the first action to be taken after the occurrence of a disturbance, plays the most important role in stopping frequency excursion. When a system is subjected to a disturbance and the frequency starts to deviate, the speed governors in the generation units perform automatic action to reestablish the system load and generation balance. The droop of generator $k_f$ is defined as a ratio given in percentage:

$$\bar{k}_f = -\frac{\frac{\Delta f}{f_n}}{\frac{\Delta p}{S_n}} \tag{6.1}$$

where $\Delta f = f - f_n$ is the variation in system frequency with $f_n$ as the nominal frequency, $\Delta p$ is the variation in power generation and $S_n$ is the rated power of the generation unit. Upon detecting the frequency deviation, the generation units change the power output proportionally to the deviation of the system frequency. The value of the droop gains must be agreed by the TSO. Although it depends on the jurisdiction, the typical value of droop is given within a range of 2 $\sim$ 12 % [180]. For example, 2 % of droop means that a 2 % of frequency drop causes an increase of the power output equivalent to the nominal power of the generation unit.

When the system consists of several generator units, the global characteristic of the entire system is expressed by the Network Power Frequency Characteristic $\lambda_f$ [9]. The value of $\lambda_f$ of a synchronous region is given by the quotient of the power deviation $\Delta P_{dis}$ and the steady-state frequency deviation $\Delta F$ after the deployment of the FCR. This value can be estimated from the droop gain of each generator unit and the self-regulation effect of load $D_{load}$:

$$\lambda_f = \frac{\Delta P_{dis}}{\Delta F} = D_{load} + \frac{1}{f_n}\left(\frac{1}{\bar{k}_{f1}}S_{n1} + \frac{1}{\bar{k}_{f2}}S_{n2} + \cdots \frac{1}{\bar{k}_{fN}}S_{nN}\right) \tag{6.2}$$

where $N$ is the number of the generator units. The value of $\lambda_f$ represents the global action of the primary frequency control. According to [9], the minimum requirement of $\lambda_f$ for the pan-European system is 15000 MW/Hz. This corresponds to steady-state frequency deviation of 0.2 Hz after a sudden power deficit of 3000 MW[1], which is the incident equivalent to the tripping of the largest generating facilities in the system.

### 6.2.3 Control Hierarchy of DC Systems

Since only a very few number of MTDC grids exist, one may well assert that there is no standard on the global control structure of MTDC grid today. However, in anticipation of the future development, it is conceivable that the control structure of MTDC grid will be constructed by adopting the well accepted methodology for the conventional AC system [170]. In analogy to the hierarchical AC system control structure, the DC system control can be structured in a cascaded form as Primary, Secondary and Tertiary Control. In the following, their respective objectives are briefly described.

**Primary Voltage Control** The DC voltage balancing control is analogically called primary voltage control. Several control methods have been proposed in literature [181][182]. However, the consensus seems to be the Voltage Droop Method [183][184][185]. As mentioned before, droop control is the method commonly used for load sharing in AC grids. The DC voltage droop method simply adopts this method but with the DC grid voltage as the power balance indicator. Like in AC grids, this method allows several stations to simultaneously contribute to the voltage regulation. When a sudden power imbalance occurs, each droop-embedded converter station regulates the power according to the allocated droop gains. Since the DC grid balance is achieved by several stations, this method exhibits higher reliability; hence it is suitable for multi-terminal HVDC systems [186].

**Secondary Voltage Control** In analogy to the secondary frequency control of AC system, this control level is referred to as the secondary voltage control. One of its important roles is the restoration of the system voltage after being subjected to a disturbance. In [187], several distinct methods are analyzed and evaluated in terms of the voltage restoration capability and deviation from the initial operating power. The proposed methods are based on the redefinition of the set-points of the droop controller. The restoration of the inter-regional power exchange is another role of this control. This role can be achieved by the centralized controller reestablishing the inter-exchanged power on the tie-lines [188].

**Tertiary Voltage Control** The tertiary control in DC system is based on Optimal Power Flow (OPF) algorithms taking into consideration the interaction between AC and

---

[1] It is calculated assuming that the effect of self-regulation of the load is absent.

DC grids, market, losses, security, etc. This control may be automatically or manually activated [170].

### 6.2.4 Primary Voltage Control of DC system

Upon detecting the DC voltage deviation, the droop controller embedded in each converter changes the power set-point proportionally to the locally measured DC voltage deviation. The droop gain $\bar{k}_v$ is commonly defined by the ratio given in percentage:

$$\bar{k}_v = -\frac{\frac{\Delta v_{dc}}{v_{dc\,n}}}{\frac{\Delta p}{S_n}} \tag{6.3}$$

where $\Delta v_{dc} = v_{dc} - v_{dc}^*$ is the variation in the voltage with $v_{dc}^*$ as the DC voltage set-point, $v_{dc\,n}$ the nominal DC voltage, $\Delta p$ the variation in power output, and $S_n$ the rated power of the converter. To keep consistency with the principles of AC systems, the power injected into the DC grid is henceforth designated by a positive sign. In case of a sudden disturbance, the droop-embedded converter stations provide the counter action according to the DC voltage deviation. The DC voltage will reach a new steady state if the converters are able to properly compensate for the excess or deficit of power before the DC voltage exceeds the allowable limits.

Whereas the AC grid has the frequency as a common signal for all generators, the DC grid has no such common signal locally available to all converters due to the voltage drops on the conductors. Using communication to establish a common voltage signal across the DC grid is proposed in [189]. However, as mentioned in [190], this introduces the risk of communication failure. To maintain the autonomous regulation of each converter, it is rather preferred not to rely on communication between the power electronic converters of which very fast control is required.

In literature, some alternatives to the voltage droop control can be found. One is the current-based droop control [191]. The main advantage of this approach is the linear voltage current control characteristic, which is contrary to the nonlinear voltage-power relation with the power-based droop control [181]. In the current-based droop control, the droop gains can be interpreted as resistance in unit of Ω. Thus, it is more intuitive from a physical perspective. On the other hand, power-based droop is more intuitive from a power system perspective because power is the common unit of commodity in electricity market. In general, both approaches are almost identical as long as the DC voltage is controlled within the vicinity of the nominal level. Thus, to keep the analogy with the AC system, this thesis focuses on the power-based droop control.

Similar to the AC grid, the Network Power Voltage Characteristic $\lambda_v$ can be defined as the quotient of the power disturbance $\Delta P_{dis}$ and the steady-state voltage deviation $\Delta V_{dc}$ after the action of droop. Since there is no self-regulating load in DC systems, this value can be estimated from the droop gains assigned to $N$ converters:

$$\lambda_v = \frac{\Delta P_{dis}}{\Delta V_{dc}} \simeq \frac{1}{v_{dc\,n}} \left( \frac{1}{\bar{k}_{v1}} S_{n1} + \frac{1}{\bar{k}_{v2}} S_{n2} + \cdots \frac{1}{\bar{k}_{vN}} S_{nN} \right). \tag{6.4}$$

Note that, unlike the network power frequency characteristic of AC systems, the network power voltage characteristic only allows to grasp the approximate behavior of the voltage because of the voltage drop across the conductors. Yet in a high-voltage DC grid, the voltage drop across the cable is small compared to the voltage level; thus, it can sufficiently represent the general behavior of an MTDC grid.

For the sake of simplicity, a new variable named droop constant $g$ is introduced.

$$g = -\frac{\Delta p}{\Delta v_{dc}} \tag{6.5}$$

The value $g$ is given in W/V; hence, the dependency on the converter rating is avoided. The value of $g$ signifies the amount of the power contribution per 1 V of voltage variation. In this sense, as the value of $g$ becomes larger, more contribution is provided by the station. The stations which do not participate in the droop control can be represented by a zero value of $g$. With the newly introduced $g$, (6.4) can be rewritten in the much simpler form:

$$\lambda_v = g_1 + g_2 + \cdots g_N = \sum_{i=1}^{N} g_i. \tag{6.6}$$

The typical structure of the voltage droop controller using the droop constant $g$ is shown in Fig. 6.2. Upon seeing the deviation of the DC voltage from the reference, the instantaneous power deviation $\Delta p$ is generated by multiplying $\Delta v_{dc}$ by $g$. The converter power reference $P^*_{ac}$ is derived by summing the set-point $P^*$ and $\Delta p$, and then it is sent to the subordinate power controller.

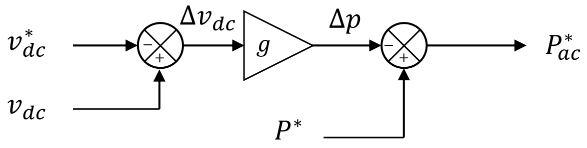

Figure 6.2: Voltage droop controller.

## 6.3 Static and Dynamic Behavior of Droop-Controlled MTDC Grid

In this section, the general behavior of a droop-controlled MTDC grid is analyzed in terms of both static and dynamic aspects by using the four-terminal DC grid shown in Fig. 6.3. The rated DC voltage of the grid is 640 kV. The three stations (Stations 1, 2 and 3) are assumed to be connected to strong AC grids, and Stations 4 is considered as the wind farm converter station that transfers a constant power. The stations are sized identically with the same nominal power of 1000 MW. Taking this value as the maximum possible disturbance and the supposing the maximum allowable DC voltage deviation is ±10 % (±64 kV), the necessary value of the network power voltage characteristic $\lambda_v = 15.625$ MW/kV is calculated provisionally. The stations except Stations 4 contribute to the voltage droop control regulation according to the assigned droop parameters given in Table 6.1.

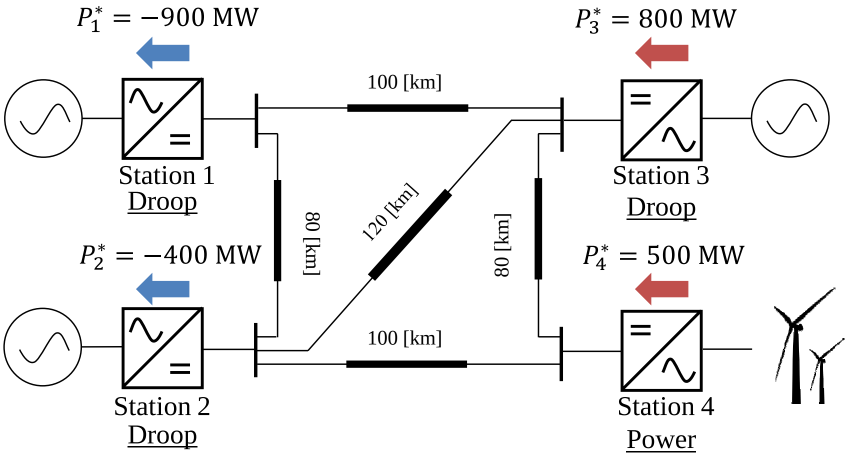

Figure 6.3: 4 terminal MTDC grid.

Table 6.1: Droop parameters.

| Station | Station 1 | Station 2 | Station3 | Station 4 | Network voltage power characteristic $\lambda_v$ (MW/kV) |
|---|---|---|---|---|---|
| Droop Gain $k_v$ (%) | 30 | 30 | 30 | Inf | 15.625 |
| Droop Constant $g$ (MW/kV) | 5.2083 | 5.2083 | 5.2083 | 0 | |

### 6.3.1 Static Behavior of Droop-Controlled MTDC Grid

In this subsection, the behavior of the droop-controlled MTDC grid is analyzed from a static point of view. In steady state, the analytic description of the droop control is given by:

$$P_{ac} = P^{*} - g\left(V_{dc} - v_{dc}^{*}\right) \tag{6.7}$$

where $V_{dc}$ is the steady-state voltage. For the sake of simplicity, the voltage drops on the cables are neglected, hence, it is assumed that the same voltage $V_{dc}$ is locally available for all the stations. Given that the same voltage set-point $v_{dc}^{*} = 640$ kV is assigned to all the stations, the droop characteristics of the four stations can be expressed as follows:

$$\begin{aligned} P_{ac1} &= P_1^{*} - g_1(V_{dc} - v_{dc}^{*}) \\ P_{ac2} &= P_2^{*} - g_2(V_{dc} - v_{dc}^{*}) \\ P_{ac3} &= P_3^{*} - g_3(V_{dc} - v_{dc}^{*}) \\ P_{ac4} &= P_4^{*}. \end{aligned} \tag{6.8}$$

With the given parameters, the droop characteristics of the four stations are plotted in Fig. 6.4. In accordance with the power conversion, the right plane corresponds to the rectifying operation and the left plane corresponds to the inverting. For the sake of visibility, the DC voltage is shown in per-unit with 1 p.u. corresponding to 640 kV.

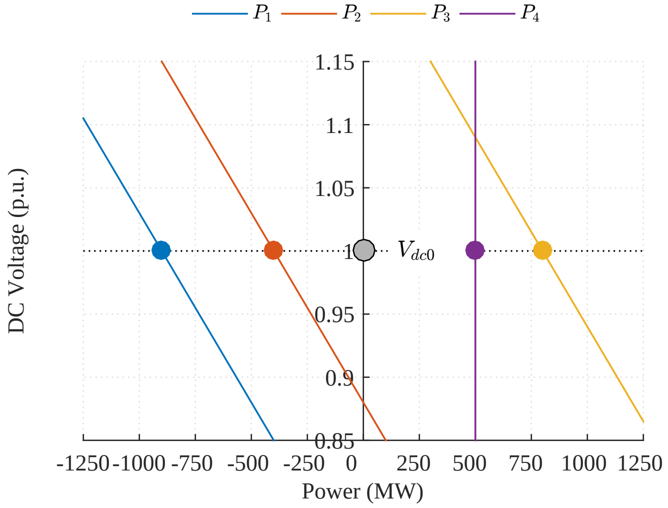

Figure 6.4: Droop characteristic of each converter station.

Summing (6.8) for the four converter stations yields the following equation:

$$\sum_{m=1}^{4} P_{ac\,m} = -(V_{dc} - v_{dc}^{*}) \sum_{m=1}^{4} g_m + \sum_{m=1}^{4} P_m^{*}. \tag{6.9}$$

When the losses in the grid are neglected, the sum of the powers must be equal to zero in steady state, i.e. $\sum_{m=1}^{4} P_{ac\,m} = 0$. Thus, (6.9) can be rewritten as:

$$V_{dc} = \frac{\sum_{m=1}^{4} P_m^*}{\sum_{m=1}^{4} g_m} + v_{dc}^*. \tag{6.10}$$

Then, using the definition of the network power voltage characteristic, (6.11) can be rearranged as follows:

$$V_{dc} = \frac{\sum_{m=1}^{4} P_k^*}{\lambda_v} + v_{dc}^*. \tag{6.11}$$

If the set-points of power are set to be zero in sum, i.e. $\sum_{m=1}^{4} P_k^* = 0$, the desired operating DC voltage can be achieved, i.e. $V_{dc0} = v_{dc}^*$. Then, the operating points of power are determined by the intersections of the horizontal line drawn from the operating voltage and the individual droop characteristics (see Fig. 6.4).

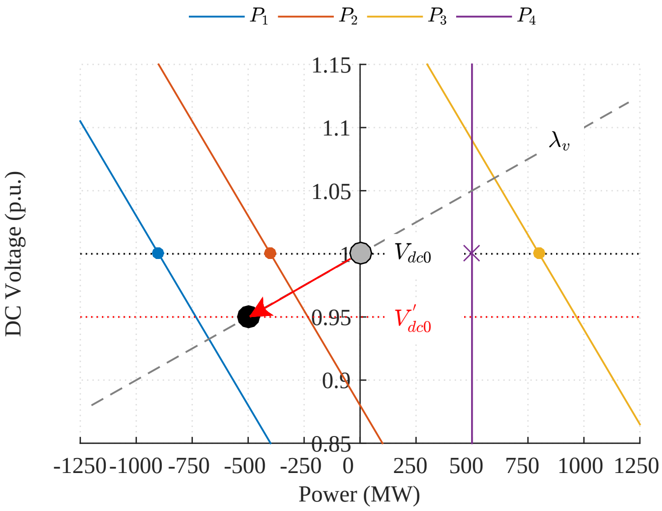

Figure 6.5: Determination of post-contingency DC voltage from system power voltage characteristic.

When this balance is disrupted by some reason, e.g. by variations of wind generation or a converter outage, the system voltage deviates from the initial point. Denoting the power disturbance from the original balanced set-point by $\Delta P_{dis}$, the post-contingency steady-state voltage $V_{dc}^{'}$ is derived by:

$$V_{dc}^{'} = \frac{\Delta P_{dis}}{\lambda_v} + V_{dc0} \tag{6.12}$$

and the deviation of the DC voltage is:

$$\Delta V_{dc} = \frac{\Delta P_{dis}}{\lambda_v}. \tag{6.13}$$

Let up suppose a sudden loss of Station 4, i.e. $\Delta P_{dis} = -P_4^*$. The post-contingency steady-state voltage is simply obtained from the network power voltage characteristic and the size of power disturbance. As confirmed in Fig. 6.5, the post-contingency steady-state voltage is derived by shifting $-500$ MW from the initial DC voltage along the network power voltage characteristic.

Fig. 6.6 illustrate the post-contingency operating power. The contribution of power of each station is displayed by the colored area. The steady-state power deviation of the station $m$ is deduced from (6.13) and (6.5):

$$\Delta P_m = -g_m \frac{\Delta P_{dis}}{\lambda_v}. \tag{6.14}$$

Thus, the post-contingency steady-state power is given by:

$$P'_{ac\,m} = P^*_m - g_m \frac{\Delta P_{dis}}{\lambda_v}. \tag{6.15}$$

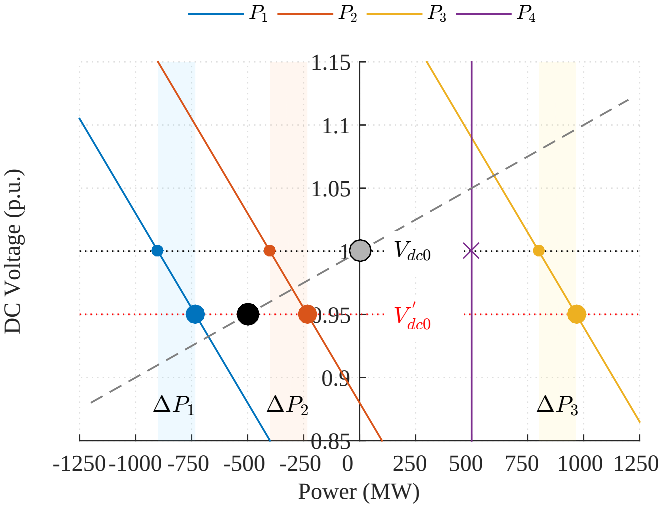

Figure 6.6: Post-contingency operating points of the converters.

## 6.3.2 Dynamic Behavior of Droop-Controlled MTDC Grid

The dynamic behavior of a droop-controlled VSC-based MTDC grid was thoroughly investigated by Rault in [192]. It was revealed that the general dynamics of the droop-controlled MTDC grid can be represented by a first-order transfer function which is characterized by the droop parameters and the equivalent capacitance of the system under certain assumptions. However, the provided analysis was based on conventional 2-level VSCs. Therefore, some adaptations must be needed to apply the proposed concept to the MMC-based MTDC grid. The following recalls the analytical approach proposed in [192] while introducing some adaptation techniques necessary for the MMC-based MTDC grid.

In DC systems, energy is stored in the form of electrostatic potential in capacitors. If we neglect the resistance and inductance of the DC cables, a DC cable can be considered as an equivalent capacitor $C_{cable}$. The capacitance of the converter stations also needs to be taken into account because they take a large portion of the overall capacitance of the system. A conventional 2-level VSC is normally installed with a large DC link capacitor [193]. However, such a component is avoided in the MMC scheme for the purpose of modular realization [86]. Ignoring such a difference between the conventional VSC and the MMC may lead to an improper understanding of the system and unexpected DC voltage dynamics. The virtual capacitor control proposed in the previous chapter can greatly facilitate to compensate this gap. Under this control, the MMC appears associated with a capacitance whose size is given by $C_{vc} = k_{vc}C_{mmc}$, where $k_{vc}$ is the virtual capacitor coefficient, and $C_{mmc}$ is the equivalent capacitance of the MMC. Therefore, it permits to consider the MMC as if it were a classical VSC by considering $C_{vc}$ as the station capacitor. Consequently, the DC grid can be simplified into an equivalent capacitor $C_{eq}$ which is the sum of the cable capacitors and the capacitors of the MMC stations:

$$C_{eq} = \sum_{m=1}^{N_{st}} C_{vc,m} + \sum_{l=1}^{N_{cable}} C_{cable,l} \tag{6.16}$$

where $C_{vc,m}$ is the virtual capacitance of the $m$th MMC, $C_{cable,l}$ is the capacitance of the $l$th cable, $N_{st}$ and $N_{cable}$ are the number of MMC stations and cables, respectively.

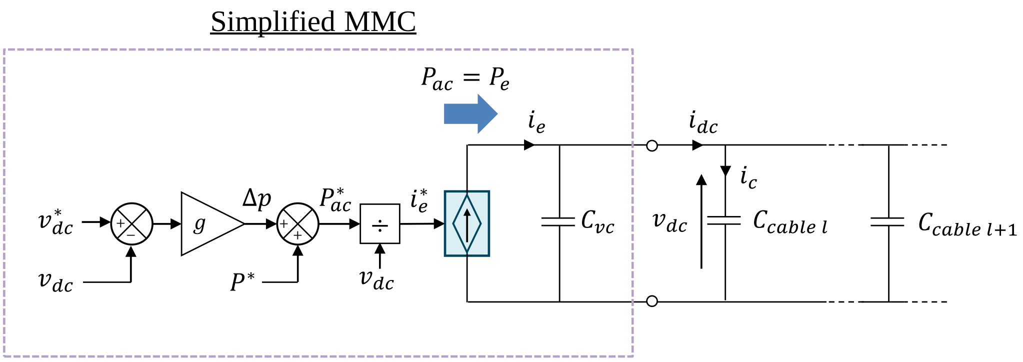

Figure 6.7: Simplified MMC model for analysis purpose.

The influence of the droop controller with the DC voltage dynamics is described using the simplified MMC model introduced in [174]. The model depicted in Fig. 6.7 displays only the essential parts pertinent to the DC voltage dynamics. Sufficiently fast dynamics of the power control are assumed, i.e. the assumption $P_{ac}^* \overset{hyp}{=} P_{ac}$ is made. The parts related to the reactive power control are not presented. Under the virtual capacitor control, the energy stored inside the MMC can be considered as a capacitor connected to the DC terminal. In this sense, the power exchanged with the AC grid contributes to the increase or decrease of the energy stored in the whole DC grid. For convenience, this

AC power is represented by its equivalent $P_e$. Accordingly, an intermediate equivalent DC current $i_e$ is defined as $i_e = P_e/v_{dc}$.

The dynamics of the DC grid voltage $v_{dc}$ is now characterized by the equivalent currents injected to the single capacitor $C_{eq}$:

$$v_{dc} = \frac{1}{C_{eq}} \int_0^t \sum_{m=1}^{N_{st}} i_{e,m} d\tau + V_{dc0} \tag{6.17}$$

Then, this equation is linearized around the operation point denoted by capital letters with subscript 0. Denoting the small variations by $\Delta$, the small-signal representation of the DC voltage dynamics is obtained as:

$$\Delta v_{dc} = \frac{1}{C_{eq}} \int_0^t \sum_{m=1}^{N_{st}} \frac{\Delta p_{ac,m} - \Delta v_{dc} I_{e0,k}}{V_{dc0}} d\tau. \tag{6.18}$$

When the cable losses are neglected, the sum of the infeed currents must be zero at a stable condition. Thus,

$$\sum_{m=1}^{N_{st}} I_{e0,m} = 0. \tag{6.19}$$

As a consequence, the block diagram of the simplified four-terminal DC grid model is obtained as illustrated in Fig. 6.8.

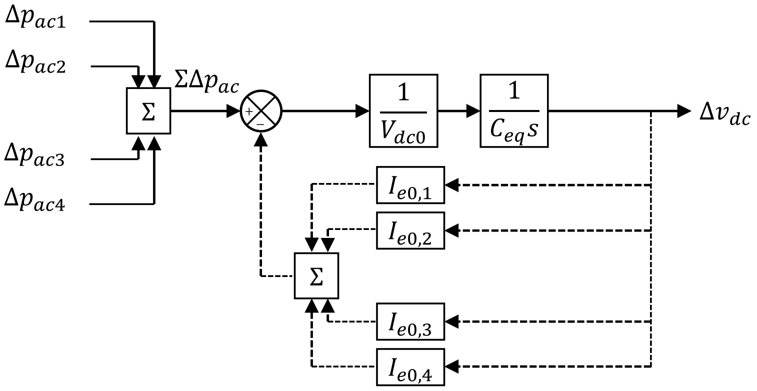

Figure 6.8: Block diagram of the simplified four-terminal DC grid model.

Then integrating the droop controllers to this model yields the simplified droop-controlled DC grid model shown in Fig. 6.9. From the obtained model, the first-order transfer function from $\Delta p_4$ to $\Delta v_{dc}$ is derived as:

$$\Delta v_{dc} = \frac{\frac{1}{g_1 + g_2 + g_3}}{1 + \frac{V_{dc0} C_{eq}}{g_1 + g_2 + g_3} s} \Delta p_4^*. \tag{6.20}$$

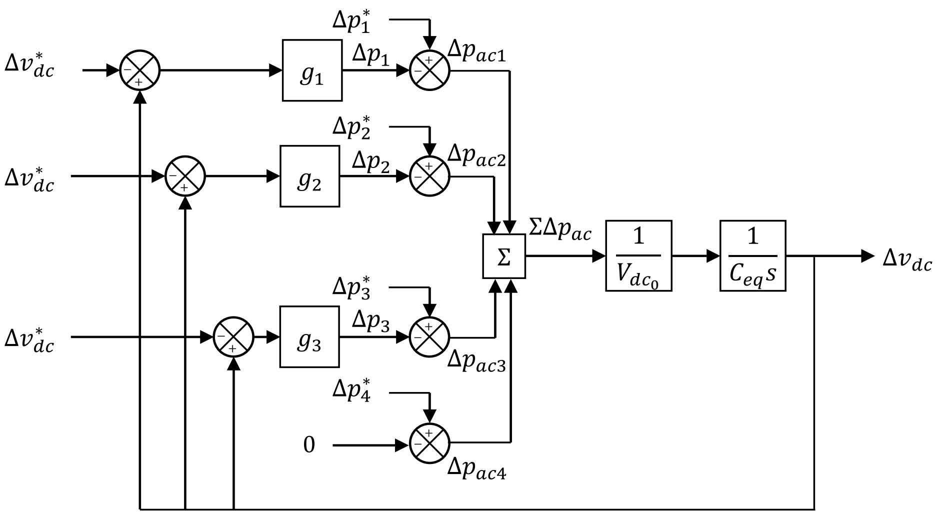

Figure 6.9: Small-signal droop-controlled four-terminal DC grid model.

The obtained formula is generalized using the network power voltage characteristic as:

$$\Delta v_{dc} = \frac{\dfrac{1}{\lambda_v}}{1 + \dfrac{V_{dc0}C_{eq}}{\lambda_v}s}\Delta P_{dis}. \tag{6.21}$$

The numerator of (6.21) describes the post-contingency steady-state variation. As expected, it corresponds to (6.13). The denominator characterizes the DC voltage dynamics, and its time constant $\tau_v$ is given by:

$$\tau_v = \frac{V_{dc0}C_{eq}}{\lambda_v}. \tag{6.22}$$

The response time $t_r$, which is defined as the time that the DC voltage reaches 95 % of the post-contingency steady-state value when subjected to a step disturbance, is given by:

$$t_r = 3\tau_v = \frac{3V_{dc0}C_{eq}}{\lambda_v}. \tag{6.23}$$

Finally, by combining (6.21) and (6.7), the dynamics of the power sharing is expressed by:

$$\Delta p_k = -\frac{\dfrac{g_k}{\lambda_v}}{1 + \dfrac{V_{dc0}C_{eq}}{\lambda_v}s}\Delta P_{dis} \tag{6.24}$$

in which the numerator corresponds to the expression derived in (6.14).

### 6.3.3 Confirmation by Simulation

In this subsection, the analysis on the general behavior of the droop-controlled MTDC grid is confirmed using the four-terminal MTDC grid model (see Fig. 6.3). The total length of the DC cables is 480 km. The equivalent cable capacitance is calculated to be 58.1 $\mu$F in total. The equivalent capacitance of each MMC is sized as 195.3 $\mu$F. The droop parameters in Table 6.1 are assigned to the converter stations, so that the network power voltage characteristic is $\lambda_v = 15.625$ MW/kV. A sudden loss of power injection through Station 4 is used as the study case, i.e. $\Delta P_{dis} = -500$ MW. If we assume the pre-contingency voltage being at the nominal voltage $V_{dc0} = 640$ kV, the post-contingency steady-state voltage can be readily estimated from (6.12). The analytical simplification approach of the MMC-based MTDC grid dynamics described in the previous subsection is based on the assumption that the virtually emulated capacitors can be taken into account as if they were physical ones. Taking the case where the same virtual capacitor coefficient $k_{vc} = 1$ is assigned to all the stations as an example, the response time of the system is calculated from (6.23). The power sharing burden as well as the post-contingency steady-state power of each station are calculated from (6.15). The estimated values are summarized in Table 6.2 and 6.3.

Table 6.2: Estimated values of DC voltage and response time.

| | Post-Contingency voltage $V_{dc}^{'}$ (p.u.) | Total cable capacitance $\sum C_{cable}$ ($\mu$F) | Total virtual capacitance $\sum C_{vc}$ ($\mu$F) | Response time (ms) |
|---|---|---|---|---|
| $k_{vc} = 1$ | 0.950 | 58.1 | 781.2 | 103.1 |

Table 6.3: Power sharing burden and post-contingency steady-state power.

| Station | Station 1 | Station 2 | Station3 | Station 4 |
|---|---|---|---|---|
| Power set-point (MW) | -900 | -400 | 800 | 500 |
| Power sharing burden $\Delta P$ (MW) | 166.7 | 166.7 | 166.7 | 0 |
| Post-contingency power $P^{'}$ (MW) | 733.3 | 233.3 | 966.7 | 0 |

In order to check whether the estimated values correspond to the actual values, time domain simulations are carried out. The aforementioned four-terminal MTDC grid is implemented in EMTP-RV platform. All the converter stations are designed based on the reduced-order average model of MMC. The cables are modeled by the Wide Band model provided in EMTP-RV library. Due to the existence of the cable resistance, the sum of injected powers is not exactly equal to the extracted power. Therefore, the pre-contingency operating power is re-calculated assuming that the losses are compensated by the Station 1. The coefficient $k_{vc} = 1$ is assigned for all the stations. At $t = 1.0$ s, the AC power of Station 4 is reduced to zero instantly. Then, the dynamic response of the DC voltage as well as the power contribution of the stations are observed.

In Fig. 6.10, the obtained results are shown. Fig. 6.10a depicts the DC voltage at each station terminal. As observed, the DC voltages show the expected first-order response and converge to the close vicinity of the estimated post-contingency voltage level. The time to reach the 95 % of steady-state value matches well the estimated response time. For the purpose of comparison, the voltage at Station 1 when $k_{vc} = 0$ is assigned to all the stations is plotted in dashed line. Although it converges to the same steady-state voltage level after the contingency regardless of the value of $k_{vc}$, its transient dynamics greatly differs from the case with $k_{vc} = 1$. The rate of change of voltage (ROCOV) is considerably greater in the case with $k_{vc} = 0$, and it results in exceeding the estimated voltage level over roughly 20 %. In Fig. 6.10b, the AC power of the four stations are depicted. The dashed lines with corresponding colors show the results obtained with $k_{vc} = 0$. After the loss of Station 4, the remaining stations adjust their power to compensate for the deficit as expected. The power converges to the estimated value regardless of the virtual capacitor coefficient. However, there are clear differences in transient. In the case with $k_{vc} = 0$, its fast ROCOV leads to the drastic change of power at each station and results in exceeding the estimated values. On the other hand, when the MMCs provide the virtual capacitor contribution, the impacts of the disturbance are effectively damped, and the AC power converges to the estimated value without overshoot.

In short, it is confirmed that both the steady-state analysis and the simplified dynamics model represented by the first-order transfer function correspond well to the EMT simulation results of the MMC-based MTDC grid under the virtual capacitor control. Compared to the case where MMCs do not provide capacitive contribution, the proposed virtual capacitor control can greatly improve the dynamic behavior of the MTDC grid. Moreover, it permits to predict the maximum value of the DC voltage deviation as well as the variation of the power with very simple expressions.

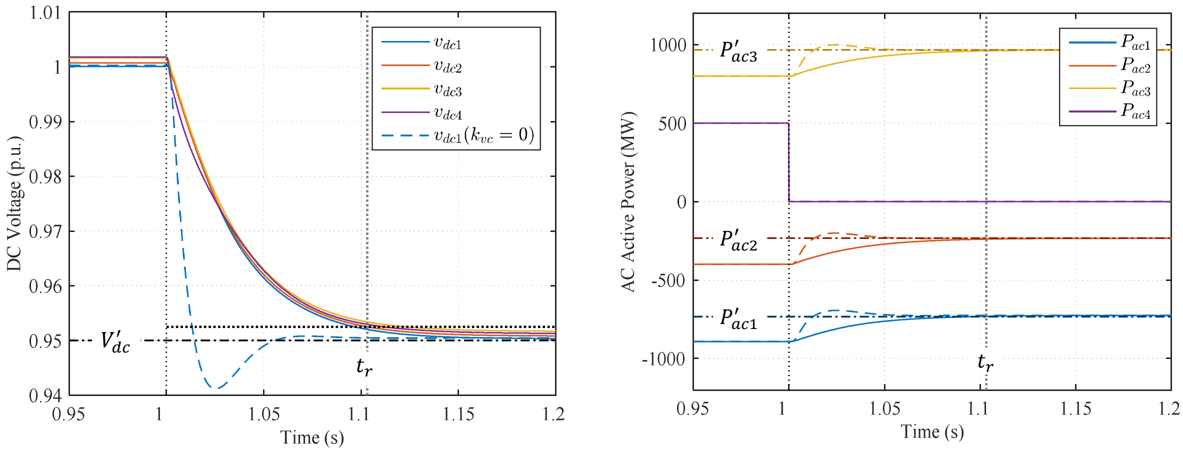

(a) DC voltage

(b) AC active power

Figure 6.10: Simulation results: Verification of analysis on droop-controlled MTDC grid behavior.

## 6.4 Coordinated Tuning of Droop Parameters and Virtual Capacitor Coefficient

For the conventional operation of MTDC grid, the droop constants are the only parameter that the system operator can change in order to satisfy the static and dynamic specifications on the voltage profile. However, with the virtual capacitor control, the virtual capacitor coefficient of the converter can be considered as another adjustable parameter. The aim of this section is to explore the advantage brought by this additional degree of freedom. First, the influences of these two adjustable parameters are demonstrated separately. Then a method to select the virtual capacitor coefficient in accordance with the droop parameters are presented.

### 6.4.1 Impacts of Droop Parameters

In order to further understand the influence of the droop parameters, time-domain simulations of the same four-terminal DC grid model with different sets of droop parameters are carried out. Three cases are examined as summarized in Table 6.4. Case 1 corresponds to the reference case where an identical droop constant $g = 5.2083$ MW/kV is assigned to Station 1, 2 and 3, so that $\lambda_{v0} = 15.625$ MW/kV. In Case 2 and 3, the droop parameters are adjusted to have twice and thrice larger value of network power voltage characteristics. For all the three cases, the virtual capacitor coefficient $k_{vc} = 1$ is assigned to all the stations. In the same manner as Subsection 6.3.3, a sudden cease of Station 4 is imposed at $t = 1.0$ s.

Table 6.4: Droop parameters.

| | | Station 1 | Station 2 | Station3 | Station 4 | Network Power Voltage Characteristic $\lambda_v$ (MW/kV) |
|---|---|---|---|---|---|---|
| Droop Constant $g$ (MW/kV) | Case 1 | 5.2083 | 5.2083 | 5.2083 | 0 | 15.625 |
| | Case 2 | 10.417 | 10.417 | 10.417 | 0 | 31.250 |
| | Case 3 | 15.625 | 15.625 | 15.625 | 0 | 46.875 |

In Fig. 6.11, the obtained results are compared. Fig. 6.11a shows the DC voltages after being subjected to the disturbance. As observed, the deviation of the DC voltage decreases as the value of $\lambda_v$ increases. In exchange, the system dynamics becomes faster inversely proportionally to $\lambda_v$. The obtained results correspond well to the estimated post-contingency steady-state voltage and the response time summarized in Table 6.5. In Fig. 6.11b, the AC active power dynamics are compared. As seen, all three droop-embedded stations effectively adjust their operating power. To highlight the differences, the AC power at Station 3 is enlarged in Fig. 6.11c. The post-contingency operating power converges to the estimated value regardless of the value of $\lambda_v$. In Case 1, the AC power reaches the steady-state without overshoot, whereas small overshoots are observed in Case 2 and 3.

Table 6.5: Estimated post-contingency DC voltage and the response time.

| | Response Time $t_r$ (ms) | Post-Contingency Voltage $V_{dc}^{'}$ (p.u.) |
|---|---|---|
| Case 1 | 103.1 | 0.950 |
| Case 2 | 51.6 | 0.975 |
| Case 3 | 34.4 | 0.983 |

In Fig. 6.11d, the total energy at Station 3 is displayed. According to (5.28), the post-contingency level of the energy $W_{mmc}^{'}$ is expressed by:

$$W_{mmc}^{'} = \frac{1}{2} C_{mmc} k_{vc} (V_{dc}^{'2} - V_{dc0}^{2}) + W_{mmc0}^{*}. \tag{6.25}$$

This implies that the deviation of the energy increases as the deviation of the DC voltage increases. Thus, it is important to maintain the DC voltage within a certain range in terms of the security of the MMC components.

Indeed, in order to maintain the DC voltage within a very close vicinity of the nominal level, a large value of $\lambda_v$ is required. However, as the frequency-response analysis in [184] suggests, a large value of $\lambda_v$ tends to excite high frequency modes and can threaten the stability of the whole system. Thus, it can be said that the DC voltage deviation and the system stability are a trader-off. An appropriate set of droop parameters must be selected to respect the requirements on both the DC voltage deviation and the system dynamics.

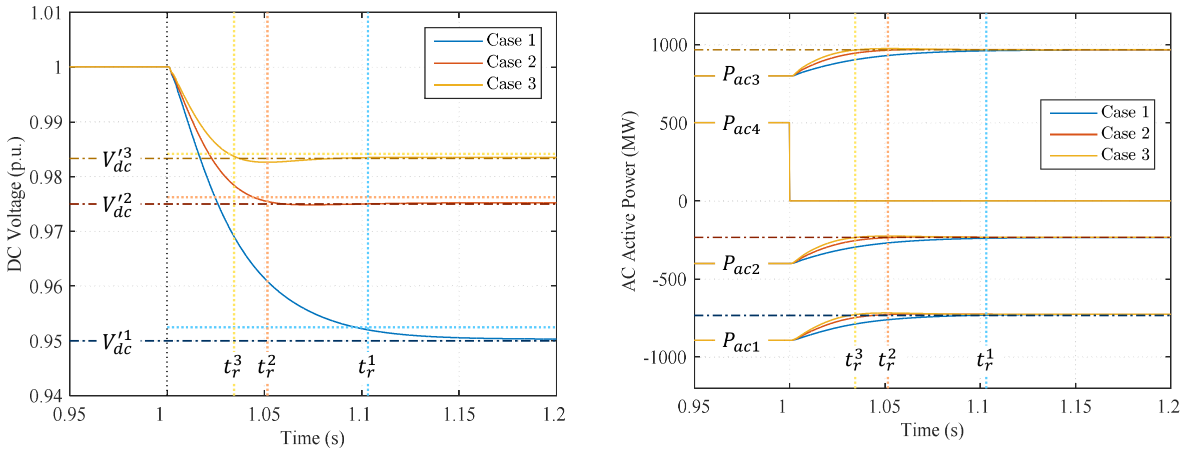

(a) DC voltage at Station 1

(b) AC active power

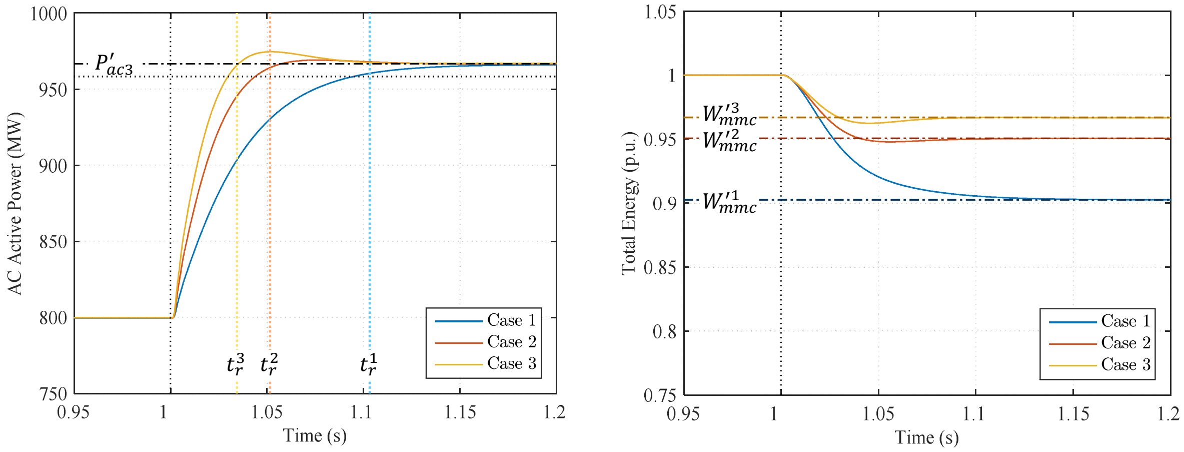

(c) AC active power at Station 3

(d) Total energy at Station 3

Figure 6.11: Simulation results: impact of droop parameter.

### 6.4.2 Impact of Virtual Capacitor Coefficient

In this subsection, the influence of the virtual capacitor coefficient is demonstrated by using the same four-terminal DC grid model. In order to maintain the DC voltage within a close vicinity of the nominal level, a large value of the network power voltage characteristic is required. However, this may lead to an excessively fast dynamics and cause unwanted overshoot in voltage and power, given the trade-off relation, shown in previous simulations, between the DC voltage deviation and the response time of the system. As (6.23) indicates, the main cause of such restriction lies in the relatively small capacitance of the system. In the conventional manner, the equivalent capacitance of the system is normally fixed once the construction of the system is completed. Physically installing additional capacitors can be a technically possible solution, but it is difficult due to the very high cost of the high-voltage capacitors. The virtual capacitor control can offer a feasible solution to this problem. Under this control, the apparent capacitance of the system can be virtually augmented by simply adjusting the virtual capacitor coefficient without any additional expenditure.

This time, an identical droop constant $g = 15.625$ MW/kV, which corresponds to the Case 3 of the previous simulation, is used. Then the simulations of the same disturbance scenario as the previous subsection are carried out with different virtual inertia coefficients as detailed in Table 6.6.

Table 6.6: Simulation parameter: capacitance.

| | Total cable capacitance $\sum C_{cable}$ ($\mu$F) | Total virtual capacitance $\sum C_{vc}$ ($\mu$F) | Network voltage power characteristic $\lambda_v$ (MW/kV) | Response time $t_r$ (ms) |
|---|---|---|---|---|
| $k_{vc} = 1$ | 36.3 | 781.2 | 46.875 | 34.4 |
| $k_{vc} = 2$ | | 1562 | | 66.4 |
| $k_{vc} = 5$ | | 3906 | | 162.4 |

In Fig. 6.12, the obtained results are depicted. As seen in Fig. 6.12a, the DC voltage converges to the same level regardless of the virtual capacitor coefficient. However, their transient dynamics are different from each other. As expected, the dynamics of the DC voltage become slower as the value of $k_{vc}$ increases. This means that the DC voltage becomes better damped. In Fig. 6.11b the AC active power dynamics are compared, and the enlarged detail of the AC active power at Station 3 is shown in Fig. 6.12c. The post-contingency power converges to the theoretical values regardless of the value of $k_{vc}$. Like the DC voltage, the dynamics of the AC power becomes more damped as the value of $k_{vc}$ increases. In Fig. 6.12d, the total energy at Station 3 is compared. As observed, a larger value of $k_{vc}$ leads to a larger deviation of the energy level because the improved dynamics of the system is achieved at the expense of the internally stored energy in the MMC. In order to avoid violating the constraints on the energy discussed in Chapter 4, $k_{vc}$ must be carefully chosen according to the available headroom and the maximum possible variation of the DC voltage.

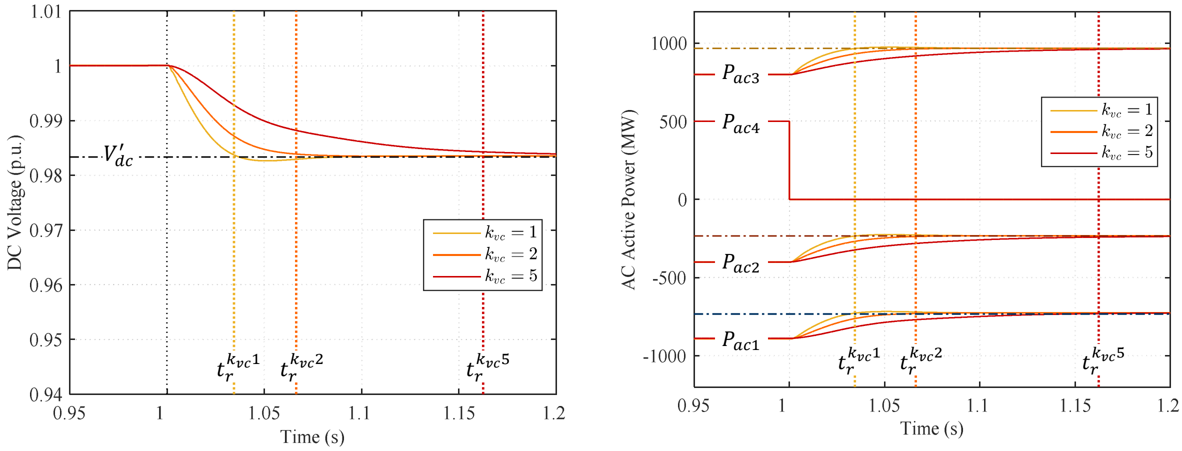

(a) DC voltage at Station 1

(b) AC active power

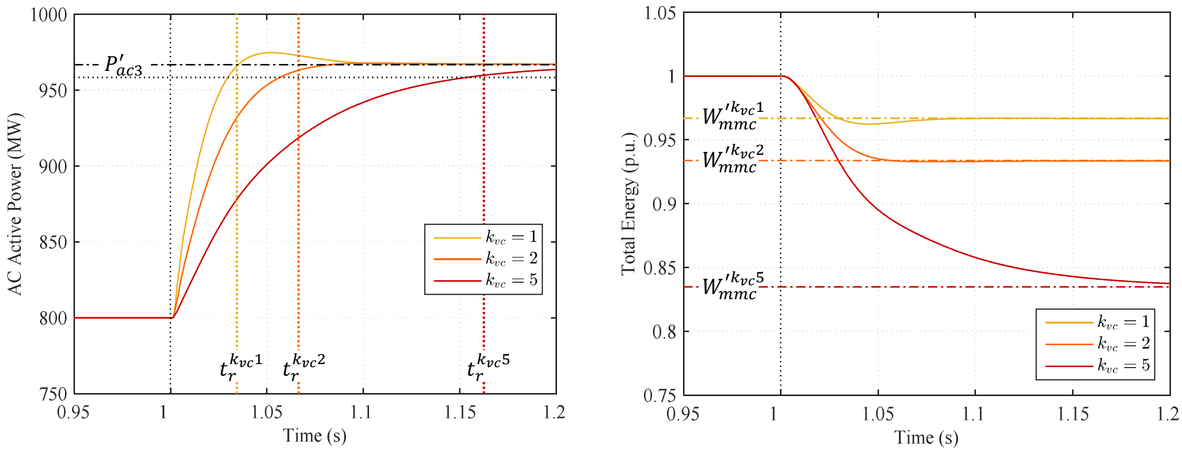

(c) AC active power at Station 3

(d) Total energy at Station 3

Figure 6.12: Simulation results: fixed droop parameter with different virtual capacitor coefficient.

### 6.4.3 Adjustment of Virtual Capacitor Coefficient in Accordance with Droop Parameter

As demonstrated in the previous two subsections, the steady-state DC voltage deviation for a given size of disturbance is uniquely determined by the value of $\lambda_v$, but the dynamics of the system is determined not only by the value of $\lambda_v$ but also by the equivalent capacitance of the system. The degree of the freedom introduced by the virtual capacitor control can bring a great flexibility to satisfy the requirements on the steady-state DC voltage deviation and the dynamics of the system at the same time. In the following, a methodology to select the virtual capacitor coefficient in accordance with the droop parameter is discussed.

According to (6.23), the response time of the system is determined by the ratio of the equivalent capacitance of the system $C_{eq}$ to the value of $\lambda_v$. Thus, by keeping this ratio constant, it is possible to keep the same response time of the system. Rearranging (6.23) with (6.16) yields:

$$\sum_{m=1}^{N_{st}} C_{vc,m} = \frac{t_r^* \lambda_v}{3V_{dc0}} - \sum_{l=1}^{N_{cable}} C_{cable,l} \tag{6.26}$$

where $t_r^*$ is the desired response time. By adjusting apparent capacitance of the MMCs to satisfy the above equation, the system dynamics can be maintained regardless of the value of $\lambda_v$.

To demonstrate the proposed approach, EMT simulations are carried out. The same four-terminal DC grid model is considered. To highlight the advantage of the proposed methodology, the same set of droop parameters in Section 6.4.1 is used. To recall, Case 1 corresponds to the reference case with $\lambda_{v0} = 15.625$ MW/kV. In Case 2 and 3, the twice and thrice larger $\lambda_v$ are assigned. Let us take Case 1 as a reference case where the response time of the system is calculated as $t_r^* = 103.1$ ms. In order to maintain the same response time, the appropriate values of $k_{vc}$ are assigned as detailed in Table. 6.7.

Table 6.7: Simulation parameter: droop parameters and virtual capacitor coefficient.

| | | Station 1 | Station 2 | Station3 | Station 4 | Network voltage power characteristic $\lambda_v$ (MW/kV) |
|---|---|---|---|---|---|---|
| Case 1 | $g$ (MW/kV) | 5.2083 | 5.2083 | 5.2083 | 0 | 15.625 |
| | $k_{vc}$ | 1.00 | 1.00 | 1.00 | 1.00 | — |
| Case 2 | $g$ (MW/kV) | 10.417 | 10.417 | 10.417 | 0 | 31.250 |
| | $k_{vc}$ | 2.07 | 2.07 | 2.07 | 2.07 | — |
| Case 3 | $g$ (MW/kV) | 15.625 | 15.625 | 15.625 | 0 | 46.875 |
| | $k_{vc}$ | 3.15 | 3.15 | 3.15 | 3.15 | — |

In Fig. 6.13, the obtained results are shown. As observed in Fig. 6.13a, the variation of the DC voltages are effectively decreased as the value of $\lambda_v$ increases. However, unlike the results shown in Fig. 6.11, all the three cases have the same response time. In Fig. 6.13b, the AC active power dynamics are compared, and in Fig. 6.13c, the enlarged AC power dynamics at Station 3 are shown. As observed, the AC power shows the same dynamics for all the cases. This means that the improved voltage profile is achieved without any adverse effects on the AC systems. Fig. 6.13d shows the total energy stored in the MMC at Station 3. For comparison, the dashed lines show the results obtained in Section 6.4.1. As seen, the variation of the energy increases compared to the previous cases. However, no significant difference is observed among the cases in the end. This implies that the improved voltage profile is achieved at the expense of a very small increase of the MMC internal energy variations. As confirmed in the simulation results, the additional degree of freedom brought by the virtual capacitor control can greatly extend the flexibility on the droop parameter selection, and makes it possible to significantly improve the voltage profile without any adverse effect on the AC grids.

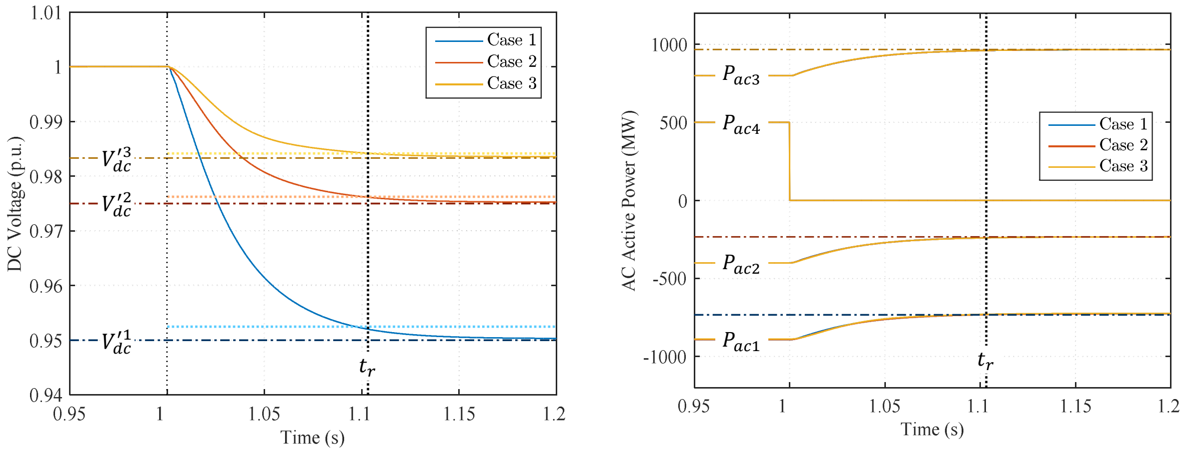

(a) DC voltage at Station 1

(b) AC active power

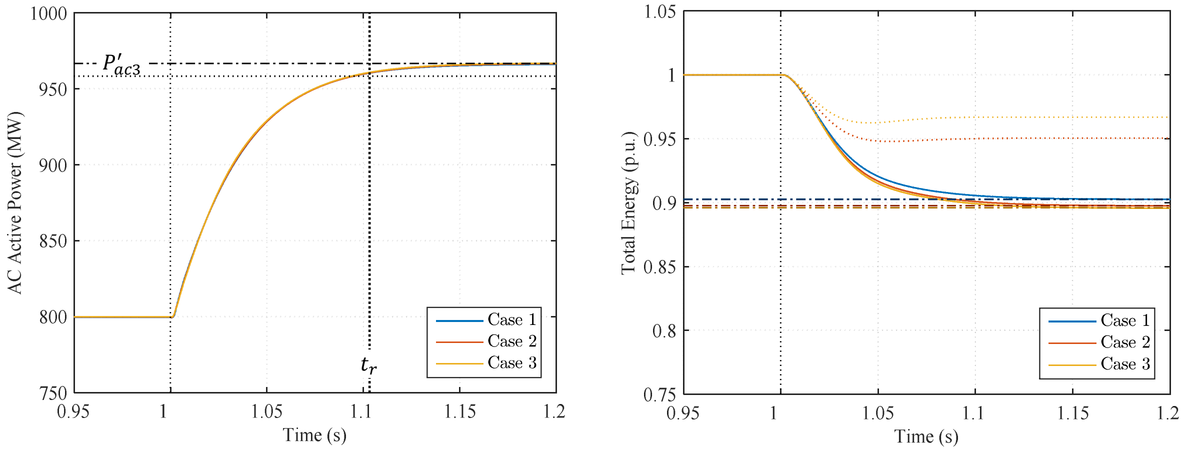

(c) AC active power at Station 3

(d) Total energy at Station 3

Figure 6.13: Simulation results: fixed response time with different network voltage power characteristic and virtual capacitor coefficient.

## 6.5 Variable Voltage Droop

Although the voltage droop method seems to be an effective strategy for the primary voltage control of an MTDC grid, there are still some issues to be solved. One of the notable differences between the DC systems and the conventional AC power systems is the number of the stations comprising the system. In continental AC systems such as the pan-European AC grid, hundreds of generators are running synchronously in the interconnected AC system. Thus, a sudden imbalance of the power is sparsely shared among them. On the other hand, it is anticipated that the construction of an MTDC will start with a relatively small number of stations, then expand by interconnecting the developed systems as suggested by the history pursued by the AC grid [59]. Therefore, it is easily imagined that an early stage of MTDC grid should comprise a relatively small number of converter stations. A particular issue of such a small MTDC grid is the large share of the reserve capacity required of each converter station. In the ENTSO-E proposal on the AC system, the share of the reserve capacity provided by a primary frequency control participating unit is recommended to be less than 5 % of the total reserve capacity required for the system (Article 45-5-a-I [179]). However, for a small MTDC grid, an imbalance of the power needs to be shared by a small number of stations. Thus, a burden of power imposed by the sudden loss of a station likely becomes considerably larger than what is normally required of the generators in the AC systems. It can be intuitively imagined that such a large power sharing may result in an overloading of the converters. Since overloading can cause severe damage on the converter, the control signal must be saturated when it reaches its allowable limit. Thus, for the secure operation, the droop-embedded stations are compelled to spare a relatively large headroom of power, i.e. the difference between the rated power capacity and actual loading. However, securing a large headroom of power can hinder the economically optimal operation of the entire MTDC grid.

In this section, those particular issues which must be tackled in the MTDC grid are discussed. Firstly, the impact of the restriction imposed by the available headroom is analyzed. Thereafter, a methodology to effectively employ the available headroom capacity is proposed. In the end, the effectiveness of the proposed methodology is confirmed by simulations.

### 6.5.1 Problems on Conventional Voltage Droop Approach

In this subsection, the particular issues that can be the obstacles for the conventional droop-based primary voltage control are explained. Then the limitations of the conventional droop control are clarified by means of a comprehensive analysis.

#### 6.5.1.1 Impact of Loss of a Droop-Embedded Station

So far, only the loss of a non-droop station has been considered. However, the loss of a droop-embedded station can cause a much severer impact on the system. When one of the droop-embedded stations is lost, this station can no longer give a contribution to the primary voltage control; thus, it imposes greater burdens on the remaining stations.

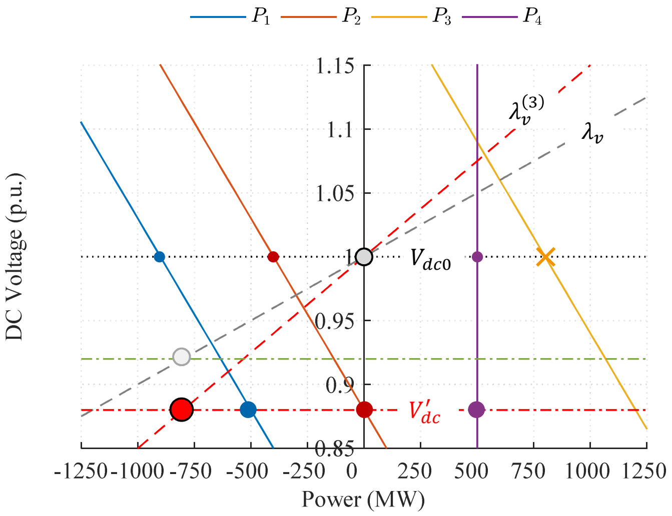

Figure 6.14: Post-contingency steady-state voltage in case of loss of Station 3.

Based on the droop characteristics shown in Fig. 6.4, the influence of the loss of Station 3 on the network power voltage characteristic is illustrated in Fig. 6.14. When a sudden disturbance occurs, i.e. $\Delta P_{dis} = -P_3 = -800$ MW, the imbalance of the power leads to a decline of the DC voltage. With the initial network power voltage characteristic $\lambda_v = 15.625$ MW/kV, the estimated DC voltage deviation calculated from (6.5) is $-51.2$ kV which corresponds to 8 % of voltage drop. However, since the Station 3 can no longer contribute to the droop control after its outage, the deficit of power needs to be compensated for by the remaining two stations. Therefore, the actual network power voltage characteristic becomes smaller than the initial value. The actual network power voltage characteristic in case of loss of $k_{\text{th}}$ station can be expressed as:

$$\lambda_v^{(k)} = \sum_{m=1,\, m\neq k}^{N_{st}} g_m. \tag{6.27}$$

Thus, in case of loss of droop-station $k$, (6.12) and (6.13) no longer hold, and they should be revised as:

$$\Delta V_{dc} = -\frac{P_k^*}{\lambda_v^{(k)}} \tag{6.28}$$

$$V_{dc}' = -\frac{P_k^*}{\lambda_v^{(k)}} + V_{dc0}. \tag{6.29}$$

As a consequence of the smaller value of $\lambda_v$, the deviation of the DC voltage becomes more significant. The influence of the loss of droop station is not limited only to the DC voltage. Due to the reduced number of stations that can contribute to the primary voltage control, the share of the power burdens imposed on the remaining stations becomes larger. For those reasons, particular attention must be paid to the loss of a droop-embedded station in a relatively small MTDC grid. And thus, the selection of the droop parameter must take into account the impact of the loss of droop-embedded stations.

#### 6.5.1.2 Impact of Available Power Transfer Capability

In practice, the converters are often operated close to their rated power. This means that the degree of the power contribution to the primary voltage control is restricted by their maximum power transfer capability. As mentioned before, the power sharing burden imposed to the converters in a small MTDC grid is likely much greater than that of generators in bulk AC systems. When the available headroom is insufficient, the contribution to the primary voltage control must be suspended before resulting in an overloading of the converter.

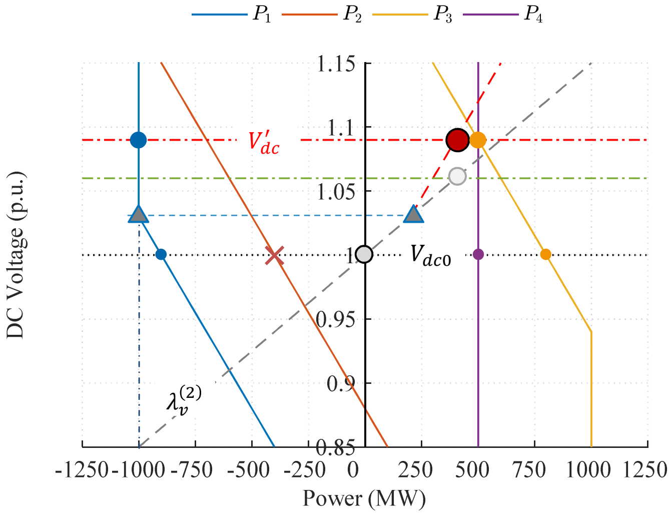

Figure 6.15: Droop characteristic considering the limitations of the power.

Using the same parameters of the four-terminal DC grid previously introduced, the influence of the maximum power limit of the converter is explained in the following. Fig.

6.15 illustrates the droop characteristics of the stations taking the maximum loading of ±1000 MW into consideration. Let us consider a sudden loss of Station 2. The DC voltage increases due to the excessive power injection, and the remaining droop-embedded stations eventually adjust their power along with their droop characteristics. When the DC voltage increases to a certain level, Station 1 reaches its maximum power limit. This station can no longer increase its contribution of power, hence, it turns into a constant power mode. If the equilibrium of the power is not yet achieved, the remaining excessive power must be compensated for by the remaining droop-embedded station, i.e. Station 3. Consequently, the deviation of the DC voltage becomes further greater than what is initially expected.

#### 6.5.1.3 Limitations of Conventional Voltage Droop Approach

As described earlier in this section, the loss of a droop-embedded station can result in a larger DC voltage deviation than expected. Moreover, the voltage deviation can become more significant if one or more stations reach the maximum power transfer capability as a consequent of power sharing before the DC voltage reaches the post-contingency steady-state. However, the impact of a converter outage as well as the severity of the power sharing burden on each station may differ depending on the operating power of the stations. This part aims to clarify the boundaries where the conventional droop approach becomes no longer effective by means of a comprehensive analysis.

The methodology is shown in Fig. 6.16. It intends to systematically evaluate the maximum DC voltage deviation presumed to occur taking into account the impact of each converter outage and the availability of the headroom power transfer capacity for different pre-contingency power flow conditions of the system. If we consider the same four-terminal DC grid model and assume that the offshore wind farm station injects a constant power, the possible operating power of the rest of three stations can be approximated by a three-dimensional plane. Assuming that the power comes from Station 4 is at its nominal power, the possible operating power of the system can be expressed as follows:

$$\begin{aligned} -1000 \leq \;& P_1 \; \leq 1000 \\ -1000 \leq \;& P_2 \; \leq 1000 \\ -1000 \leq \;& P_3 \; \leq 1000 \\ & P_4 \; = \; 1000 \end{aligned} \tag{6.30}$$

where all the power are given in MW, and the set-points of the power are restrained by:

$$P_1 + P_2 + P_3 + P_4 = 0. \tag{6.31}$$

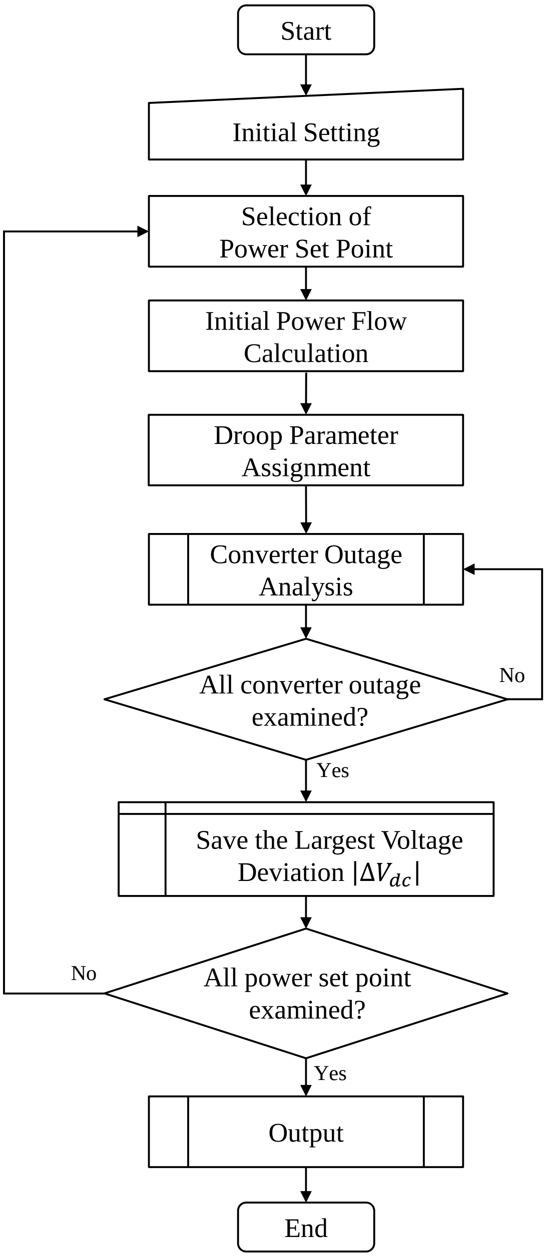

Figure 6.16: Flowchart of methodology for evaluation of DC voltage deviation.

First, the DC grid topology, the converter rating and the cable specifications are set as the inputs. A possible set-point of power which satisfies (6.30) and (6.31) is selected. The pre-contingency condition are determined by the generic DC power flow calculation algorithm based on the Newton Raphson method [194]. Then, the uniform droop constants provided in Table 6.1 are assigned to Station 1, 2 and 3. It should be noted that, conventionally, the corresponding value of the network power voltage characteristic is expected to maintain the DC voltage within ±10 % (±64 kV) in case of the maximum possible disturbance ±1000 MW equivalent to the rated power of a station.

For the selected operating point, the deviation of the DC voltage from the pre-contingency level is evaluated for each converter outage. The saturation of the droop characteristics caused by the maximum power transfer capability imposes strong non-linearity, and it makes the anticipated system behavior expressed by the simple expressions no longer valid. In order to determine the precise impact of converter outages taking into account the availability of the headroom of power transfer capacity, a modified power flow calculation algorithm is developed referencing [195]. This algorithm based on the superposition principle enables to estimate the post-contingency steady state of the MTDC grid taking into account the maximum loading capability of the converters and the change of their control mode. No restriction on the power exchange with the associated AC systems is considered, so the droop-embedded stations are assumed to be capable of providing power contribution until they reach their rated power transfer capacity. Irrespective of the sign of the DC voltage deviation, the maximum voltage deviation caused by any converter outage at that power operating point is recorded. The whole procedure is repeated for all operating points in the 3-dimensional interval defined by (6.30) and discretized with a step of 20 MW.

Fig. 6.17 shows the obtained result. The possible operating point of power is given as a triangle. The vertices of the triangle signify that all the converters operate at the maximum power transfer capability. Naturally, the available headroom of power becomes smaller as the operating point gets closer to a vertex of the triangle. As observed, the deviation of the DC voltage is maintained within ±10 % only around the central part, which means that the voltage constraints are respected only if all the stations are in lightly loaded operation. As the operating power gets closer to a vertex, the maximum deviation of the DC voltage increases and far exceeds ±10 %. At the vertices, the deviation of the DC voltage reaches ±30 %, which is surely unacceptable in terms of the security of the overall system.

As the obtained result clearly suggests, the conventional droop cannot ensure securing the voltage within the desired range for all the operating conditions. The main cause of this is that the conventional approach of the droop parameter selection directly adapts

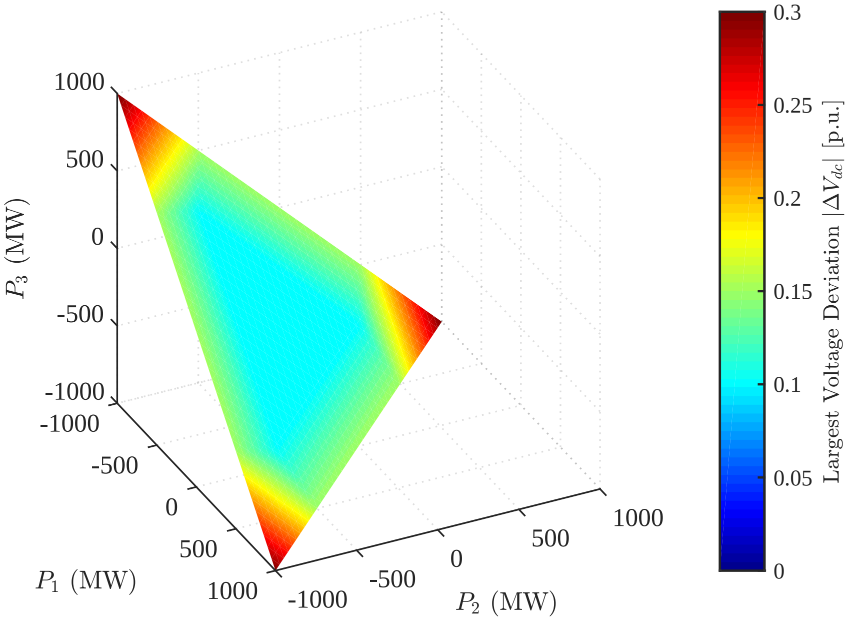

Figure 6.17: Maximum DC voltage deviation among each converter outage with uniform droop constant.

the practice used in AC systems without considering the particular issues of a small MTDC grid. In order to solve this problem, a new approach with respect to the control design and parameter selection is required.

## 6.5.2 Flexible Selection of Droop Parameters

The analysis provided earlier revealed that the conventional voltage droop control is not capable of maintaining the DC voltage within a secured range for any possible converter outages. As a possible solution, we propose a methodology that allows more flexibility on the selection of the droop parameters and choosing the right values according to the available headroom of the converter stations. In the following, the proposed approach is described.

### 6.5.2.1 Non-uniform Droop Constant

As it may be noticed in (6.14), a deficit (or excess) of power $\Delta P_{dis}$ is compensated for by the droop-embedded stations according to the relative ratio of the individual droop constant $g_m$ to the network power voltage characteristic $\lambda_v$. Under the conventional approach where an identical droop parameter is assigned to all the stations, the burden of power sharing is allocated uniformly regardless of the available headroom. In order to optionally allocate the power sharing burden to each station, the droop parameters must be assigned in a non-uniform manner [196].

The flexible selection of droop constant allows to modify the degree of power contribution of each station in case of contingency. The contribution of power of $m$th station upon the loss of $k$th station can be expressed by:

$$\Delta P_m \quad = \quad \frac{g_m}{\sum_{m=1,\, m\neq k}^{N_{st}} g_m} P_k^*. \tag{6.32}$$

It is noteworthy to state that allowing non-uniform droop parameters does not change the principle of the voltage droop method and the general behavior of the overall system. The post-contingency steady-state voltage can still be estimated by (6.29), and the DC voltage dynamics is governed by the network power voltage characteristic. Thus, although the non-uniform droop parameter allows assigning power sharing burden according to the availability of the headroom, the selection of the individual droop constraints still requires careful attention to ensure the security of the DC voltage deviation and the overall dynamics of the system.

#### 6.5.2.2 Over and Under Droop Constant

In general, the primary frequency control in AC systems considers only the generation units. On the other hand, VSC type converters can employ bi-directional power transfer. A converter in the rectifying mode injects power like a generator in AC system, and similarly an inverting mode converter withdraws power like a load. The conventional voltage droop control treats both in the same way. However, in regard to the availability of headroom power transfer capacity, its implication is not the same for the rectifying stations and the inverting stations.

Fig. 6.18 illustrates the relation between the direction of the disturbance and the operating mode of the converter station. Only two representative stations are displayed: the one shown on the right side of the figure is in rectifying mode (Station $r$), and the other shown on the left side is in inverter mode (Station $i$). When there is a sudden loss of a third station which was rectifying power, the imbalance between the injected and extracted powers results in a fall of the DC voltage. Station $r$ must increase its power injection to compensate for the deficit of power. However, since this station was already injecting a large amount of power, the amount of power injection this station can increase is limited by its rated power transfer capacity. In contrast, the converter in inverting mode can contribute a much larger power than the rectifying station because decreasing the inverting power leads to moving its operating power away from its maximum transfer capability. This implies that the available headroom of the power transfer capacity of

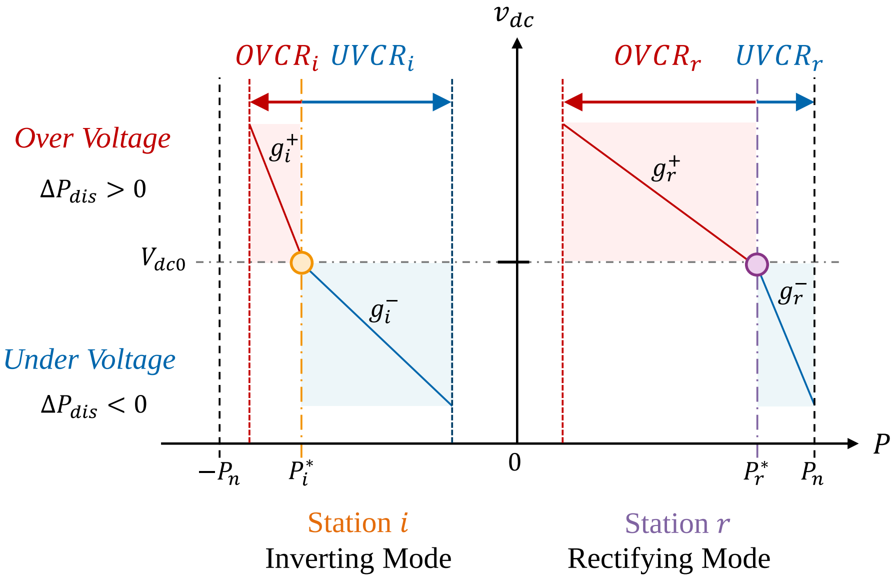

Figure 6.18: Concept of over- and under- voltage droop.

the droop-embedded stations differs depending on the present operating condition and the direction of the disturbance. For convenience, the reserve capacity secured by the converter for the primary voltage control is defined as the Voltage Containment Reserve (VCR) in analogy to the definition of the FCR in AC system. Regardless of the control mode of the converter, the VCR to be effectuated in case of DC voltage drop is defined as the Under-Voltage Containment Reserve (UVCR). It is naturally thought that the amount of the UVCR which the inverting station can offer by reducing the inverted power must be considerably larger than that of the rectifying station. The same principle also applies to the Over-Voltage Containment Reserve (OVCR) for the case where the DC voltage rises. The degree of the power contribution that rectifying stations can offer must be considerably larger than inverting station in over-voltage.

To make effective use of the available OVCR and UVCR which greatly differ according to the operating mode of converter, it is reasonable to handle them in a separated manner. For this purpose, Over- and Under- Voltage Droop Constant, $g^+$ and $g^-$ are introduced.

$$\Delta p = \begin{cases} -g^+ \Delta v_{dc} & \text{for} \quad \Delta v_{dc} > 0 \\ -g^- \Delta v_{dc} & \text{for} \quad \Delta v_{dc} < 0 \end{cases} \tag{6.33}$$

As the value of either the over- or under- voltage droop increases, the contribution of the power against the voltage deviation becomes larger. Thus, a larger value of $g^+$ can be assigned to the stations which is rectifying larger power, while a larger value of $g^-$ can be assigned to the stations inverting larger power. In this way, the OVCR and UVCR can be effectively employed according to the availability of the headroom. This greatly increases the flexibility on the primary voltage control of the MTDC grid. A similar example is found in the AC system in New Zealand, where the FCR for over frequency is referred to as "Over-Frequency Reserve" and the FCR for under frequency as "Instantaneous Reserve" [197]. This fact backs up the importance of handling the directions of the disturbance in a separated manner in relatively small systems.

### 6.5.3 Selection of Variable Droop Parameters

The aforementioned non-uniform droop concept and the independent over/under droop concept bring a great flexibility to the primary voltage control. However, selecting an appropriate set of the droop parameters that respects all the system constraints still remains a problem. Thus, the following proposes a methodology to select an appropriate set of the droop parameters. Thereafter, the proposed method is evaluated by an analytical approach.

#### 6.5.3.1 Requirement on Over and Under Voltage Containing Reserve

In an AC system, the overall amount of the FCR is determined with respect to the size of the reference incident [9]. Such approach can be effective only if the system comprises a large number of stations and the reserves are assigned sparsely among them. However, in a relatively small MTDC grid, the procurement of the reserve must be done in much more elaborate manner.

The reserve of the individual stations must be secured within their power transfer capability. In addition, fully deploying the available headroom capacity may not be allowed under certain circumstances, e.g. if the station is connected to a relatively weak AC grid. In such case, the reserve capacity may be further restricted. The maximum amount of the reserve which the station can secure, defined as Procurable Over- and Under-VCRs (POVCR and PUVCR), can be expressed as:

$$\begin{aligned} POVCR_m &= \max\Big( -P_{n,m} - P_m^*, \;\; POVCR_m^{AC} \Big) && (6.34) \\ PUVCR_m &= \min\Big( P_{n,m} - P_m^*, \;\; PUVCR_m^{AC} \Big) && (6.35) \end{aligned}$$

where $P_{n,m}$ is the rated power transfer capacity of the $m$th converter station (assumed to be the same for rectifying and inverting mode), and $POVCR_m^{AC}$ and $PUVCR_m^{AC}$ are the maximum amount of the reserve that the associated AC grid can provide. Then the Over- and Under-VCRs of the $m$th station must be secured under the constraints:

$$\begin{aligned} POVCR_m \leq OVCR_m &\leq 0. && (6.36) \\ 0 \leq UVCR_m &\leq PUVCR_m. && (6.37) \end{aligned}$$

In case of loss of the $k$th station in the MTDC grid, the resulting excess or deficit of power needs to be compensated for by the remaining stations. The secured reserve capacity must be larger than the size of the disturbance, otherwise the system will not be capable of fully compensating for the excess or deficit of power. With the notion of the Over- and Under-VCRs, the conditions that the secured reserves must satisfy can be expressed by the two inequalities:

$$\sum_{m=1,\, m\neq k}^{N_{st}} OVCR_m \leq P_k^* \qquad \text{if} \quad P_k^* \leq 0 \tag{6.38}$$

$$\sum_{m=1,\, m\neq k}^{N_{st}} UVCR_m \geq P_k^* \qquad \text{if} \quad P_k^* \geq 0. \tag{6.39}$$

As seen, (6.38) uniquely concerns the outage of each inverting station ($P_k^* \leq 0$). In contrast, (6.39) concerns only the rectifying stations ($P_k^* \geq 0$). A sufficient amount of OVCR must be available at the loss of each inverting station, and in the same way for UVCR with each rectifying station. Note that the above constraints do not intend to determine the unique set of the reserves of the individual converter stations but indicate the essential requirements for the primary voltage control of MTDC grids.

In practice, the procurement of the reserve capacity may have to reflect various factors including the ancillary market of the associated AC grids because the actual supply sources of the reserves deployed by the converters are the generators and the controllable loads in the AC grids. In such case, an optimization problem can be formulated that takes into account the relative cost of the reserve procurement. By adapting the reserve market design for AC systems discussed in [198], we define the optimization functions as:

$$\begin{aligned} \min \quad & \sum_{m=1}^{N_{st}} -\psi_m^{OVCR} OVCR_m && (6.40) \\ \text{subject to} \quad & (6.36)\ (6.38) \\ \min \quad & \sum_{m=1}^{N_{st}} \psi_m^{UVCR} UVCR_m && (6.41) \\ \text{subject to} \quad & (6.37)\ (6.39) \end{aligned}$$

where $\psi_m^{OVCR}$ and $\psi_m^{UVCR}$ are weighting factors accounting for the procurement cost of the reserves.

Using the same four-terminal MTDC grid, the set of OVCR and UVCR are calculated according to (6.40) and (6.41). In order to prioritize the available headroom capacity along with the operation mode, different weighting factors are assigned. No restrictions on the AC grids are considered, i.e. $POVCR_m$ and $PUVCR_m$ are defined not to exceed the rated power transfer capacity of ±1000 MW. When some of stations have the same weighting factor, an unique solution may not be found. In such case, the reserves are evenly allocated among them. The calculated set of OVCR and UVCR are summarized in Table 6.8.

Table 6.8: Example of OVCR and UVCR for four stations.

| Station | Station 1 | Station 2 | Station3 | Station 4 |
|---|---|---|---|---|
| Rated Power (MW) | 1000 | 1000 | 1000 | 1000 |
| Power Set-point (MW) | -900 | -400 | 800 | 500 |
| Weighting Factor OVCR | 1 | 1 | 3 | $\infty$ |
| Weighting Factor UVCR | 3 | 3 | 1 | $\infty$ |
| OVCR (MW) | -100 | -600 | -300 | 0 |
| UVCR (MW) | 400 | 400 | 0 | 0 |

In Fig. 6.19, the available OVCR and UVCR of the system are compared with the power to be compensated for upon each converter outage. As observed, a sufficient amount of the reserve capacity is always available to fully compensate for the excess or deficit of power at any converter outage. Now the remaining issue is how to effectively provide the power contribution within the allocated reserves while respecting the DC voltage constraints.

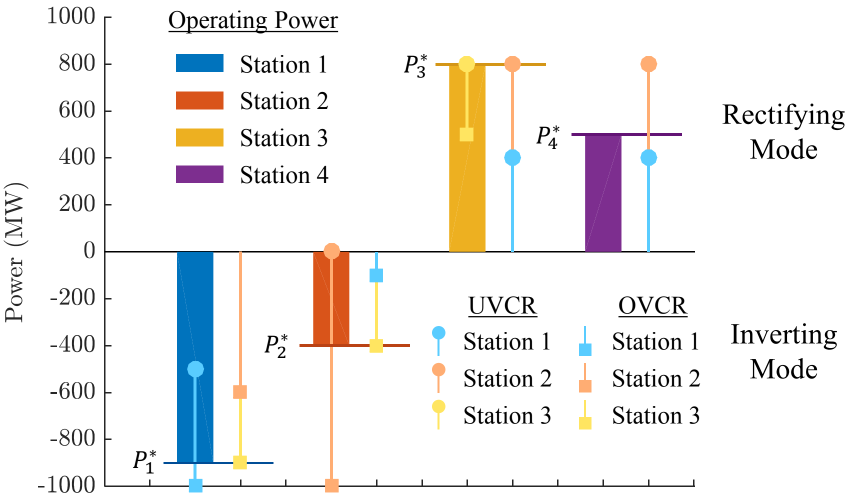

Figure 6.19: Available OVCR and UVCR in each converter outage.

#### 6.5.3.2 Selection of Droop Parameters

In order to adequately provide the power contribution according to the procured reserve capacity of each station, an appropriate set of droop parameters must be selected. The following proposes the methodology to select the right values of the droop parameters according to the allocated reserve capacities.

Let us consider that the DC voltage must be maintained within a certain range between $V_{dc}^{Lim+}$ and $V_{dc}^{Lim-}$. The allocated reserves must be fully deployed before the voltage exceeds those limits. Denoting the limits of the upper and lower voltage deviation from the nominal voltage by $\Delta V_{dc}^{Lim+}$ and $\Delta V_{dc}^{Lim-}$, the appropriate droop constants are simply determined from the definitions of the over- and under-voltage droop (6.33) as follows:

$$g_m^+ = -\frac{OVCR_m}{\Delta V_{dc}^{Lim+}} \tag{6.42}$$

$$g_m^- = -\frac{UVCR_m}{\Delta V_{dc}^{Lim-}}. \tag{6.43}$$

With the aggregated OVCR and UVCR, the network power voltage characteristics for over- and under-voltage are expressed by:

$$\lambda_v^+ = -\frac{\sum_{m=1,}^{N_m} OVCR_m}{\Delta V_{dc}^{Lim+}} \tag{6.44}$$

$$\lambda_v^- = -\frac{\sum_{m=1,}^{N_m} UVCR_m}{\Delta V_{dc}^{Lim-}}. \tag{6.45}$$

Under the proposed droop parameter selection method, the network power voltage characteristic is indirectly determined by the total reserve capacity. Understandably, unnecessary procurement of the reserves may not be preferred in terms of cost. Since an excessively large value of the network power voltage characteristic can degrade the overall stability of the system, procuring minimum required reserves is advantageous from both economic and stability aspects.

Once the allocated reserve capacity and the desired voltage range are determined, the right values of over- and under-voltage droop constants can be easily calculated according to (6.42) and (6.43). Taking the DC voltage limits of ±10 % as an example, the over- and under-voltage droop constants are calculated according to the allocated reserves given in Table 6.8. The calculated droop constants are summarized in Table 6.9 and the droop characteristics are plotted in Fig. 6.20. As seen, the droop characteristics reach the allocated reserves at the DC voltage limits.

Table 6.9: Calculated droop parameters for the allocated reserves.

| Station | Station 1 | Station 2 | Station3 | Station 4 | Network Power Voltage Characteristic $\lambda_v$ (MW/kV) |
|---|---|---|---|---|---|
| Over Voltage Droop Constant $g^+$ (MW/kV) | 1.563 | 9.375 | 4.688 | 0 | 15.625 |
| Under Voltage Droop Constant $g^-$ (MW/kV) | 6.250 | 6.250 | 0 | 0 | 12.500 |

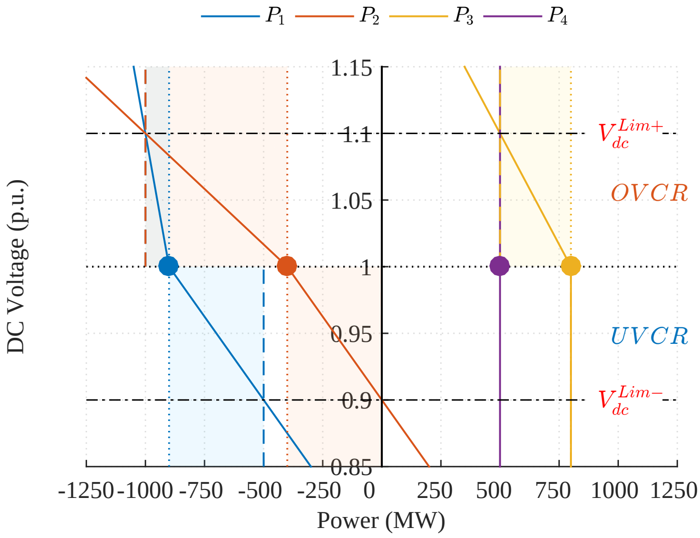

Figure 6.20: Calculated droop characteristics for four stations.

Now the same analysis in Section 6.5.1.3 is carried out with the flexible droop concept and the proposed droop parameter selection methodology. For each operating point of power, the OVCRs and UVCRs are preliminary determined by the optimization problem (6.40) and (6.41). In order to compare the results on the same basis, the total amount of OVCRs and UVCRs are constrained to be ±1000 MW. Then the over- and under-voltage droop parameters are calculated from (6.42) and (6.43) according to the assigned reserve capacity. In this way, the same value of network power voltage characteristic $\lambda_v = 15.625$ MW/kV as in Section 6.5.1.3 is obtained.

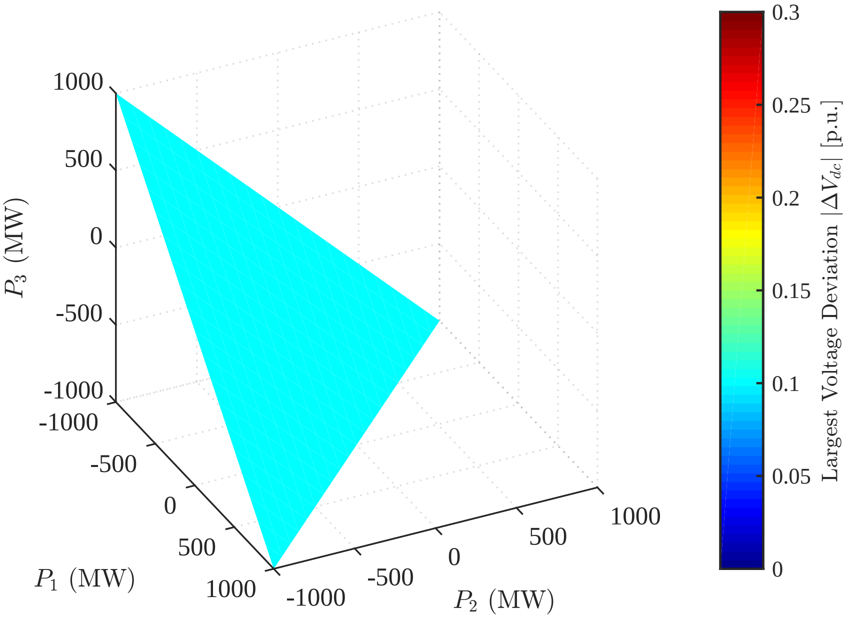

Figure 6.21: Maximum DC voltage deviation in case of each converter outage with variable droop constant.

Fig. 6.21 depicts the resulting maximum DC voltage deviation under the proposed methodology. Unlike the case under the conventional uniform droop (see Fig. 6.17), the DC voltage deviation is maintained within ±10 % at any operating point. This is clear evidence that allowing flexibility on the droop parameters selection has a great advantage in regard to the security of the system. Under the proposed methodology, it is no longer necessary to restrict the operating power in order to secure a sufficient headroom. Thus, it can be said that the proposed variable droop selection methodology can greatly extend the operability of power of the MTDC grid without compromising the security of the system.

### 6.5.4 Application of the Proposed Solution

This subsection describes the implementation of the proposed methodology and the structure of the overall MTDC grid control framework. Then, the effectiveness of the proposed control system is confirmed by time-domain simulations.

#### 6.5.4.1 Secondary Control Structure

The proposed methodology is based on the appropriate procurement of the reserve capacity in accordance with the operating set-points of power and the selection of the droop parameters. Whenever the power flow condition of the system changes either deliberately or due to a disturbance, the impact of the loss of each converter outage and the available reserve capacity of the system will change. The present setting of the droop parameters and the available reserve capacity of the system may no longer satisfy the system constraints. Thus, they need to be reevaluated and, if necessary, a new set of droop parameters must be calculated and dispatched. Such tasks cannot be done locally and need to be handled by the centralized controller. Given that, it is reasonable to attributed those roles to the higher control hierarchy, i.e. secondary voltage control.

Fig. 6.22 illustrates the conceptual scheme of the proposed secondary controller. In addition to the original tasks of the secondary control, namely the reestablishment of the voltage profile and redispatching of the power set-points after a contingency, the proposed controller comprises two additional control blocks in order to allocate the reserves in accordance with the availability and calculate an appropriate set of droop parameters. Since the voltage reestablishment and power flow redispatching are discussed in detail in [187][188][199] and are not within the scope of this thesis, further description on them is omitted. When the set-points of power are changed by following the new references provided by the tertiary voltage control, or due to a sudden increase of wind power generation, or due to the redispatching after a contingency, the available OVCRs and UVCRs are rechecked according to (6.38) and (6.39). Then, if necessary, an appropriate sets of the reserves are allocated to the stations within their procurable capacity. According to the allocated OVCRs and UVCRs, a new set of the over- and under-voltage droop parameters are calculated by (6.42) and (6.43). Then, they are dispatched to the individual converter stations through the central regulator and the communication interface in a coordinated manner.

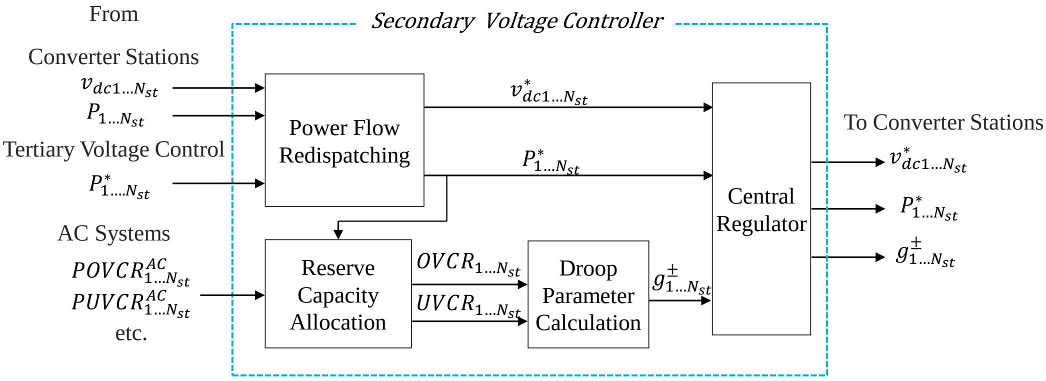

Figure 6.22: General structure of the proposed secondary controller.

### 6.5.4.2 Confirmation by Simulation

Finally, the proposed methodology of droop parameter selection is tested by time-domain simulations. The same four-terminal MTDC grid is implemented in EMTP-RV platform. Two load conditions summarized in Table 6.10 are considered. The light load condition represents the case where each converter has a sufficient headroom capacity. In contrast, in the heavy load condition, the stations have limited headroom capacity. To begin with, the conventional uniform droop parameters are examined for both load conditions to clarify the problems of the conventional approach. Thereafter, the proposed methodology is applied to the same MTDC grid model.

Table 6.10: Two load conditions.

| Station | Station 1 | Station 2 | Station3 | Station 4 |
|---|---|---|---|---|
| Light Load Condition (MW) | -500 | -500 | 500 | 500 |
| Heavy Load Condition (MW) | -900 | -700 | 850 | 750 |

**Light Load Condition** Table 6.11 shows the set-points of the power and the assigned reserve capacity at the light load condition. In order to keep the coherence with the subsequent simulations, the reserves are evenly allocated over Station 1, 2 and 3 to make their sum equal to ±1000 MW. The conventional uniform droop constants are assigned as summarized in Table 6.12. Then the transient dynamics at each converter outage is examined.

Table 6.11: Operating power and VCR at the light load condition.

| Station | Station 1 | Station 2 | Station3 | Station 4 | Total VCR (MV) |
|---|---|---|---|---|---|
| Power Set-point (MW) | -500 | -500 | 500 | 500 | — |
| OVCR (MW) | -333 | -333 | -333 | 0 | -1000 |
| UVCR (MW) | 333 | 333 | 333 | 0 | 1000 |

Table 6.12: Droop parameters under the conventional approach.

| Station | Station 1 | Station 2 | Station3 | Station 4 | $\lambda_v$ |
|---|---|---|---|---|---|
| Over Voltage Droop Constant $g^+$(MW/kV) | 5.2083 | 5.2083 | 5.2083 | 0 | 15.625 |
| Under Voltage Droop Constant $g^-$(MW/kV) | 5.2083 | 5.2083 | 5.2083 | 0 | 15.625 |

Fig. 6.23 shows the DC voltage dynamics. The deviation of the voltage in the cases of outage of Stations 1, 2 and 3 is larger than the case of Station 4 due to the smaller number of the remaining droop-embedded stations. The DC voltages are maintained within the given range in all the cases. In Fig. 6.24, the AC active power dynamics are depicted. Similarly, the loss of a droop-embedded station imposes a larger burden on the remaining stations. Yet, the power contributions are effectuated within the assigned reserve capacity. The obtained results confirm the analysis in Section 6.5.1.3, that is, the conventional uniform droop approach can be still effective when the operating power of the stations are far from its rated capacity and the available headroom capacities suffice for evenly assigning the reserves to the stations.

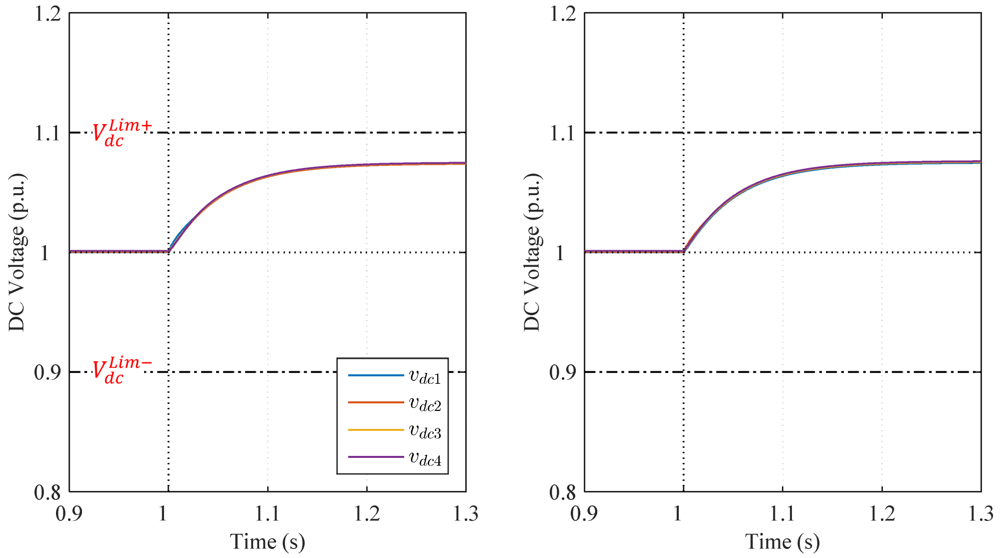

(a) Loss of Station 1 (b) Loss of Station 2

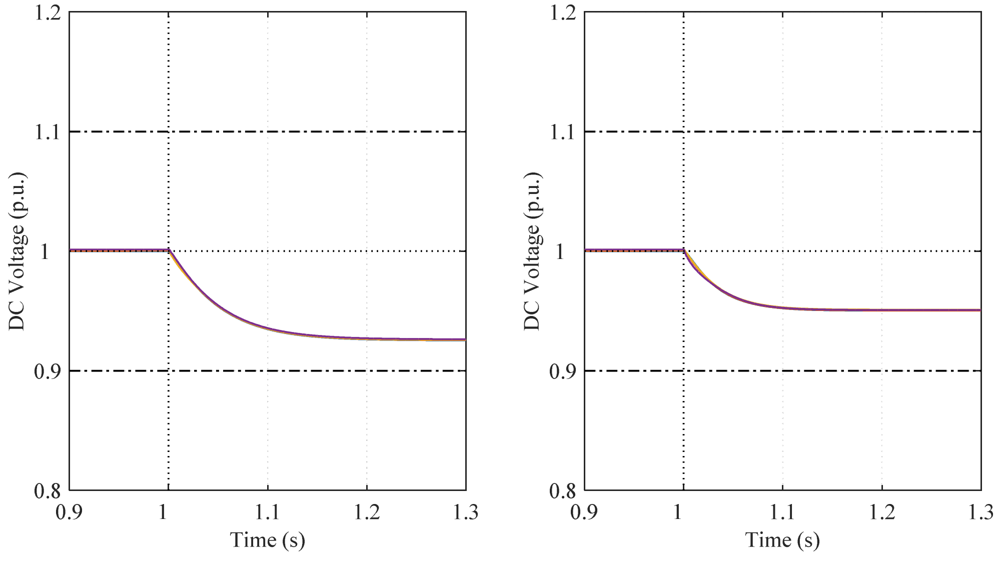

(c) Loss of Station 3 (d) Loss of Station 4

Figure 6.23: DC voltage transient in case of each converter outage at the light load condition.

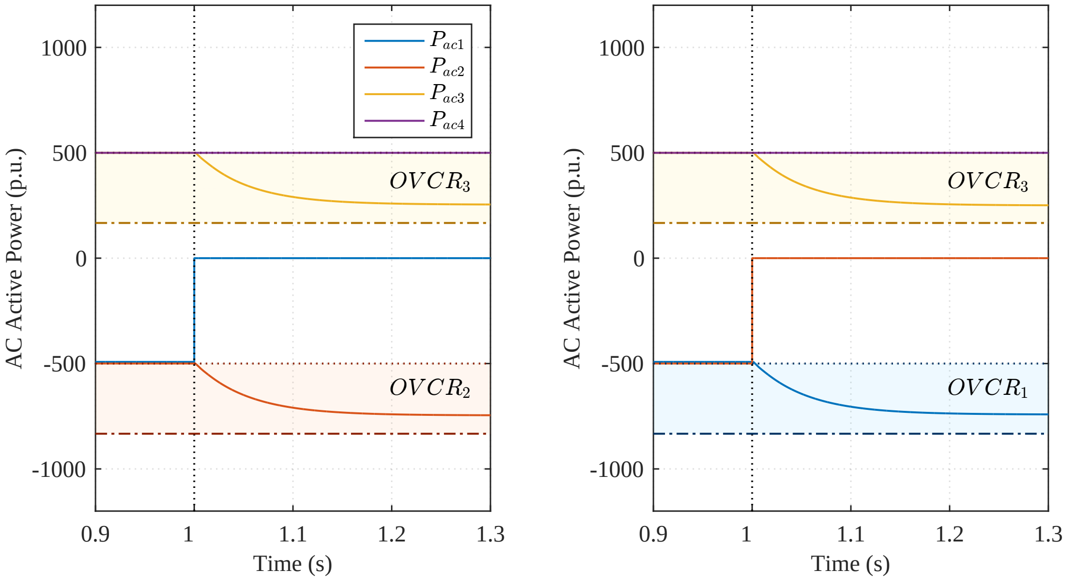

(a) Loss of Station 1

(b) Loss of Station 2

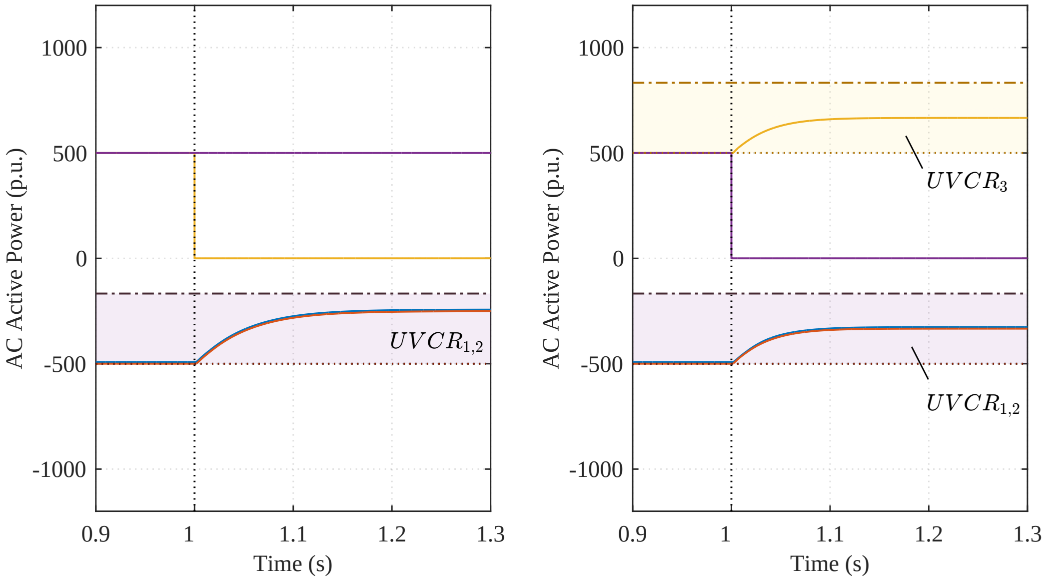

(c) Loss of Station 3

(d) Loss of Station 4

Figure 6.24: AC power transient in case of each converter outage at the light load condition.

**Heavy Load Condition** Now let us suppose that the new power references are given by the tertiary control. With this new power set-point (see heavy load condition in Table 6.10), all the stations will be heavily loaded; thus, the impact of the converter outage are presumed to be larger. Moreover, due to their heavy load rate, the available headroom capacities are reduced.

Even though the operating power flow and loading condition are changed significantly, the conventional approach does not change the droop parameters. Thus, keeping the same droop parameters, each converter outage under the heavy load condition is examined, and the DC voltage dynamics and the AC active power are observed.

Fig. 6.25 shows the DC voltage dynamics when subjected to each converter outage. As clearly seen, the DC voltage largely exceeds the desired voltage limits in the cases of the loss of Stations 1, 2, and 3. The reason for such large voltage deviations can be found in Fig. 6.26 which shows the AC active power after each converter outage. As observed in the cases of loss of Stations 1, 2, and 4, the loss of the station results in the saturation of the power at the remaining stations before the DC voltage reaches a new steady state. The saturated station can no longer provide power contribution; hence, it results in leaving the responsibility of stopping the voltage deviation to the remaining stations which eventually leads to a smaller network power voltage characteristic of the system. Consequently, a larger voltage deviation occurs. As clearly demonstrated, the conventional approach cannot ensure the secure operation of the MTDC grid in the heavy load condition.

Table 6.13: Operating power and VCR at the heavy load condition.

| Station | Station 1 | Station 2 | Station3 | Station 4 | Total VCR (MV) |
|---|---|---|---|---|---|
| Power Set-point (MW) | -900 | -700 | 850 | 750 | — |
| Weighting Factor OVCR | 1 | 1 | 3 | $\infty$ | — |
| Weighting Factor UVCR | 3 | 3 | 1 | $\infty$ | — |
| OVCR (MW) | -100 | -300 | -600 | 0 | -1000 |
| UVCR (MW) | 425 | 425 | 150 | 0 | 1000 |

Now the proposed methodology and the centralized secondary control structure are applied. Under the proposed methodology, the OVCRs and UVCRs are reevaluated and a new set of droop parameters are calculated when the operating power changes. For the heavy load condition, the OVCRs and UVCRs are calculated according to (6.40) and (6.41) as summarized in Table 6.13. In order to compare the results on the same basis, the total amount of OVCRs and UVCRs are constrained to be ±1000 MW. As noticed, the OVCRs and UVCRs are allocated within their rated power transfer capacity. According to the allocated reserves, the droop constants are determined as summarized in Table

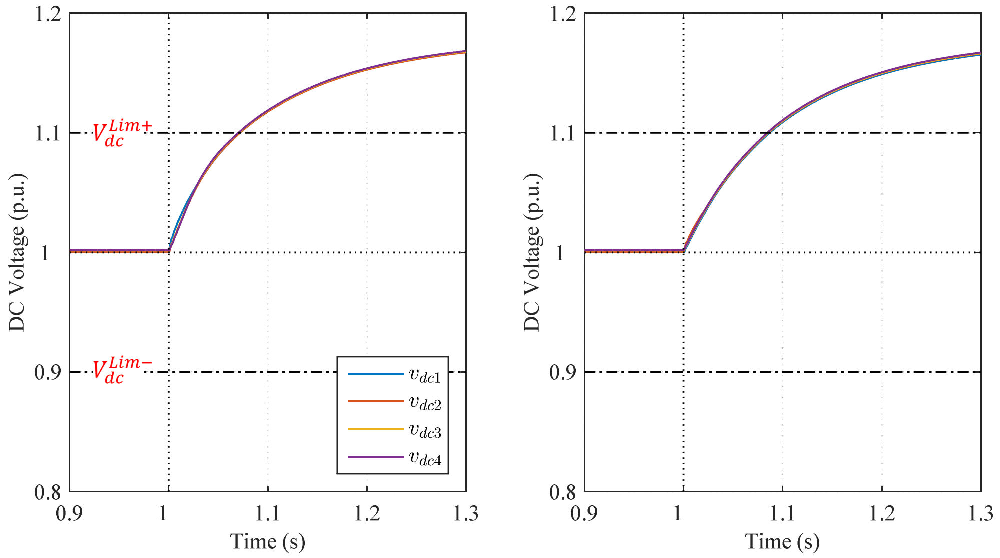

(a) Loss of Station 1 (b) Loss of Station 2

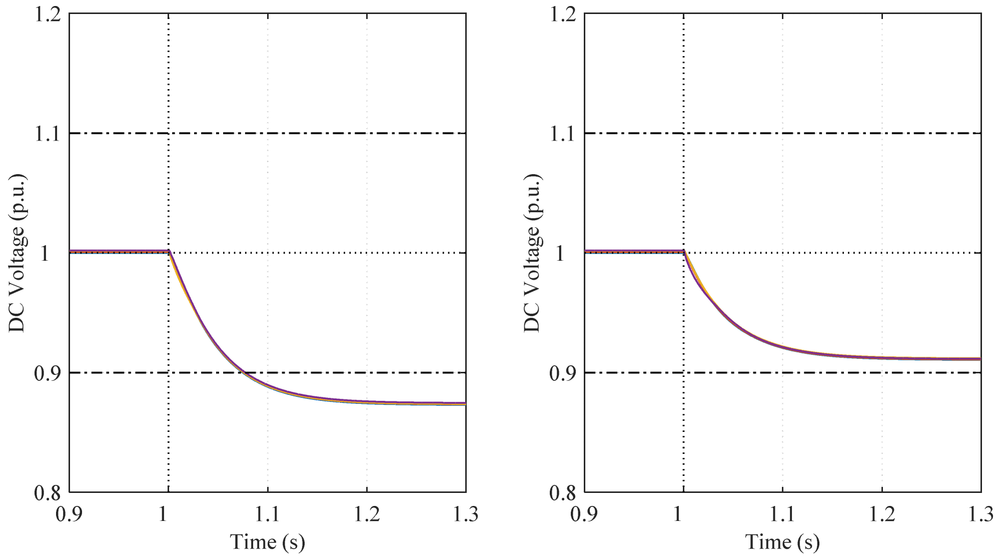

(c) Loss of Station 3 (d) Loss of Station 4

Figure 6.25: DC voltage transient in case of each converter outage under conventional solution at the heavy load condition.

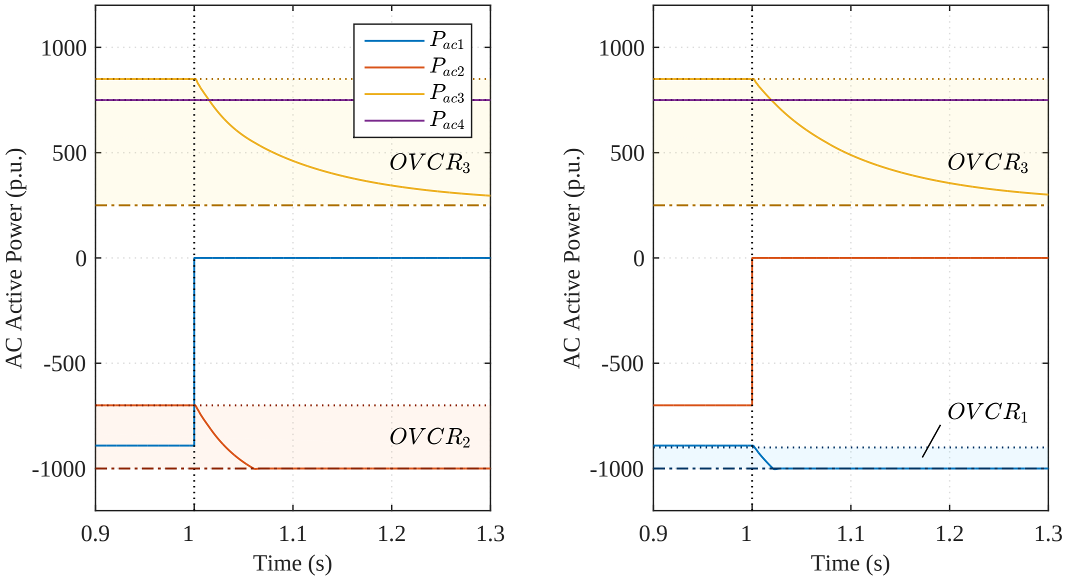

(a) Loss of Station 1 (b) Loss of Station 2

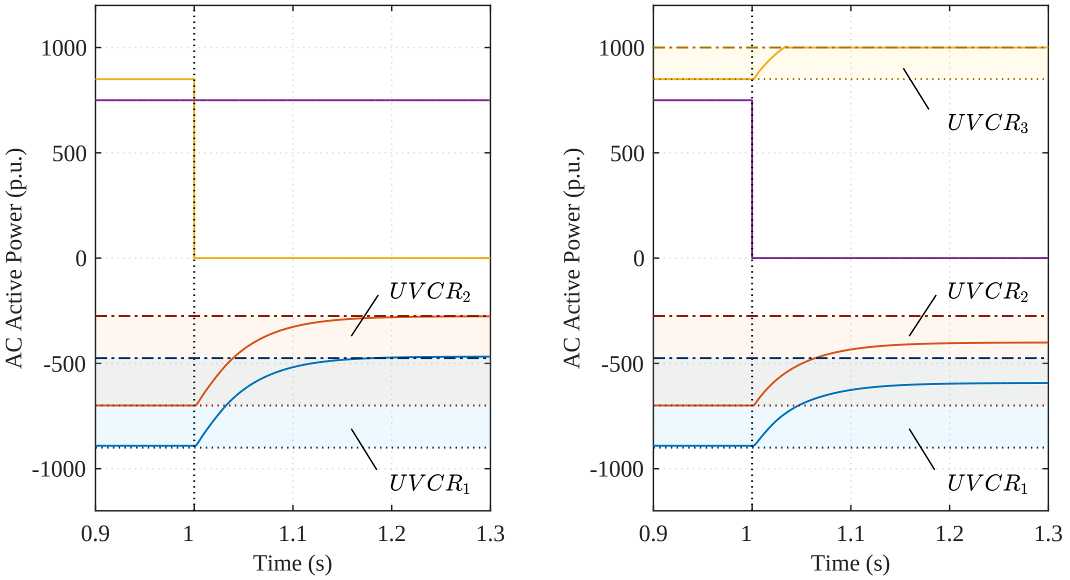

(c) Loss of Station 3 (d) Loss of Station 4

Figure 6.26: AC power transient in case of each converter outage under conventional solution at the heavy load condition.

6.14. Note that the network power voltage characteristic is the same as the previous simulation. Thus, the calculated droop constants differ from the conventional case but have the same sum. The calculated droop parameters are assigned to the stations. Then the DC voltage and AC active power dynamics after being subjected to each converter outage are examined.

Table 6.14: Droop parameters calculated according to the allocated reserves.

| Station | Station 1 | Station 2 | Station3 | Station 4 | $\lambda_v$ |
|---|---|---|---|---|---|
| Over Voltage Droop Constant $g^+$(MW/kV) | 1.5625 | 4.6875 | 9.3750 | 0 | 15.625 |
| Under Voltage Droop Constant $g^-$(MW/kV) | 6.6406 | 6.6406 | 2.3438 | 0 | 15.625 |

In Fig. 6.27, the obtained simulation results are shown. As clearly seen, the DC voltage is maintained within the desired limits for any cases. In Fig. 6.28, the AC active powers are depicted. Unlike the case with the conventional approach, no saturation is observed. The assigned reserves are effectively deployed without any overloading of the converters. It is noteworthy to state that there is no difference in terms of the post-contingency steady-state power between the conventional case and the proposed methodology. Despite the same conditions of the network power voltage characteristic and post-contingency steady-state power, the voltage profiles after the contingency are greatly improved under the proposed methodology. This fact emphasizes the effectiveness of flexible selection of droop parameters in MTDC grid.

From those results, the effectiveness of the proposed methodology of the droop parameter selection and the secondary control structure is confirmed. The obtained results clearly show the advantage of the proposed methodology in terms of the security of the overall system. The flexibility brought by the variable droop concept enables to adequately allocate the reserve capacities, and the suitable droop parameters are readily determined without any complex calculation. The proposed methodology is applicable to any MTDC grids even with larger number of rectifying and inverting stations. Thus, it can be a suitable method for the future supergrid.

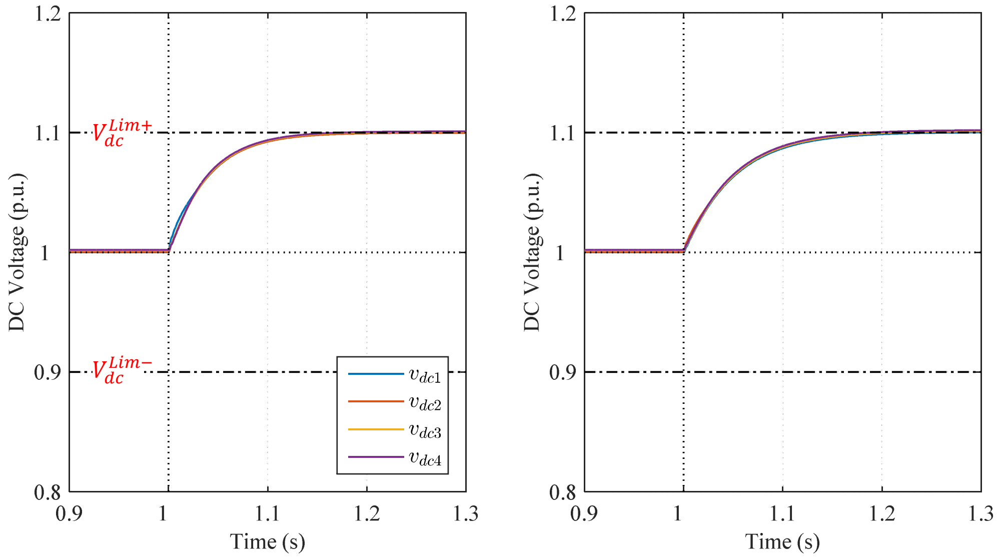

(a) Loss of Station 1

(b) Loss of Station 2

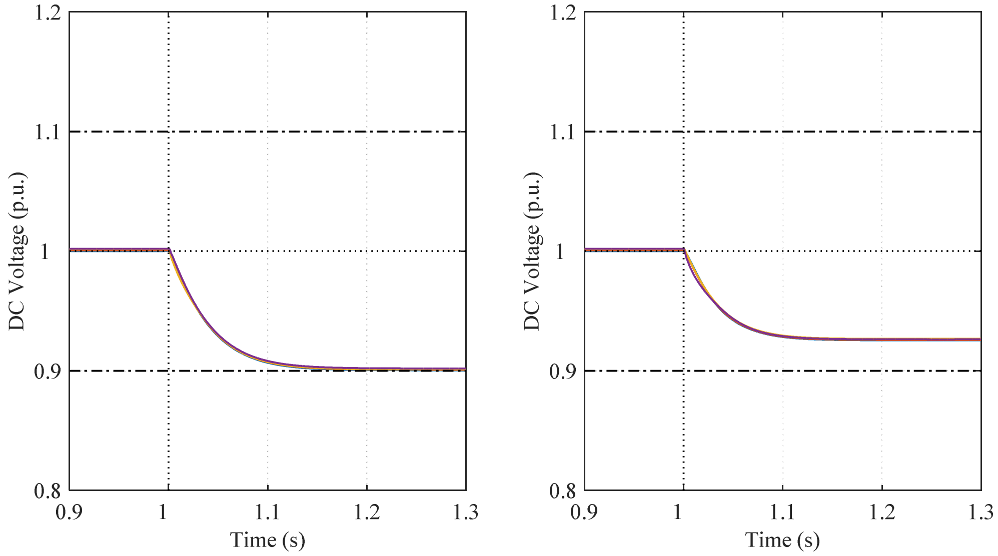

(c) Loss of Station 3

(d) Loss of Station 4

Figure 6.27: DC voltage transient in case of each converter outage under proposed solution at the heavy load condition.

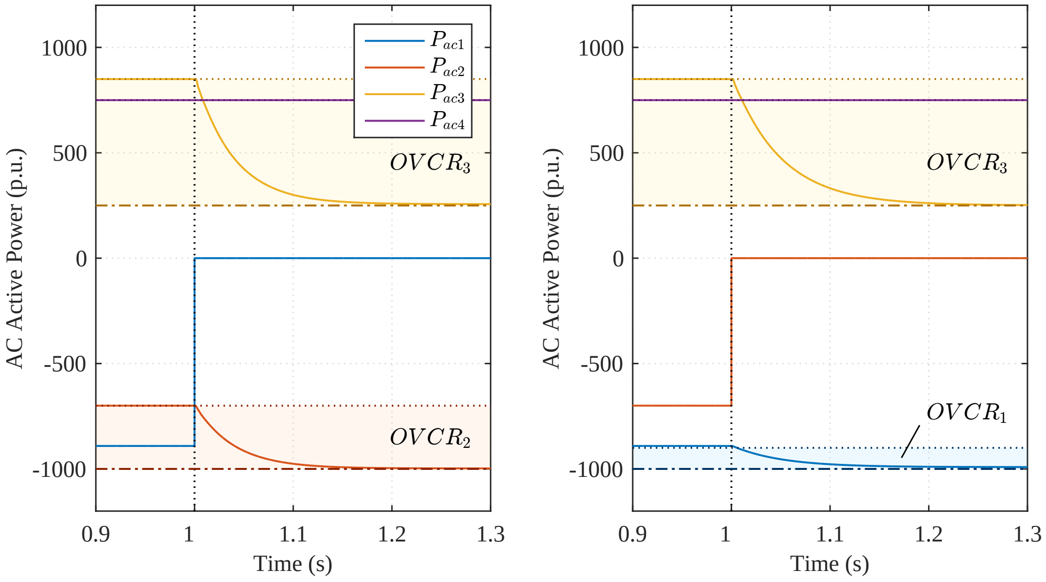

(a) Loss of Station 1 (b) Loss of Station 2

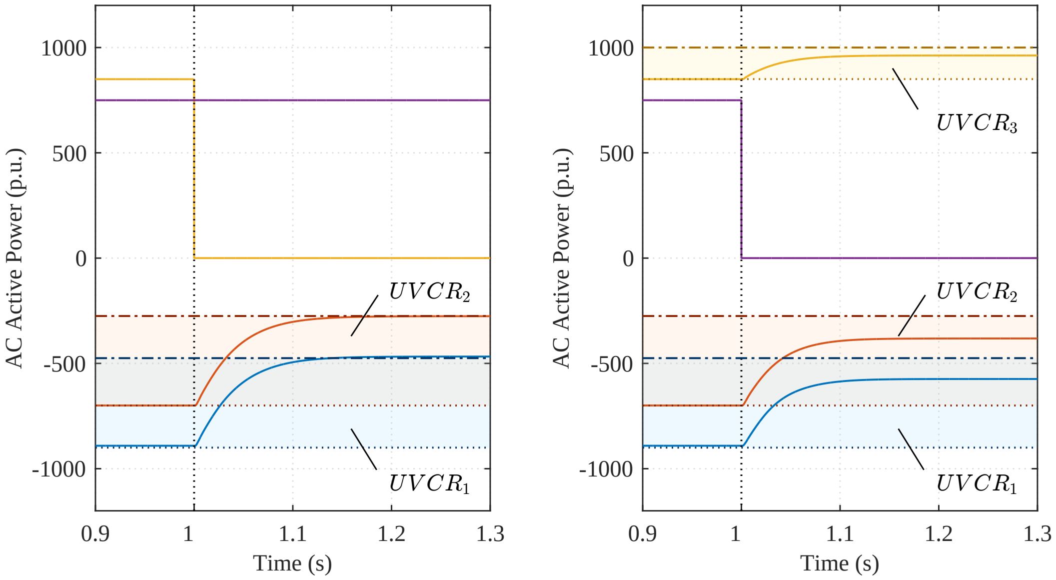

(c) Loss of Station 3 (d) Loss of Station 4

Figure 6.28: AC power transient in case of each converter outage under proposed solution at the heavy load condition.

## 6.6 Chapter Conclusion

This chapter first gave a general overview of the MTDC grid operation and its hierarchical control architecture with analogy to the well-known AC grids. For the primary voltage control which takes the first action to stop the DC voltage variation in case of contingency, the consensus is to use the voltage droop method. This is like the frequency control in the AC system but with the DC grid voltage as the power balance indicator. The influence of the droop parameters on the system behavior was analyzed from both static and dynamic aspects, and it was confirmed that the dynamics of the DC voltage can be represented by the first-order transfer function characterized by the network power voltage characteristic and the equivalent capacitance of the system.

For the conventional operation of MTDC grid, the droop parameters are the only parameter that the system operator can change in order to satisfy the static and dynamic specifications on the voltage profile; thus, it can be said that the selection of the droop parameter is relatively restrictive and may require compromise. To overcome this restriction, the virtual capacitor control introduced in the previous chapter was applied to the MTDC grid. With the additional degree of freedom brought by this control, the compromise between the steady-state voltage deviation and the system dynamics is no longer needed. Thus, it can greatly extend the flexibility of the MTDC grid control.

Finally, the particular issues which must be taken into account in relatively small DC grids and the limitations on the conventional uniform droop approach were investigated. It was revealed that the conventional droop approach can ensure the security of the system only if all the stations secures a sufficient headroom of power transfer capacity. This implies that the conventional droop approach can impede the economically optimal operation of the MTDC grid. As a solution to this problem, we proposed a novel methodology that enables efficient allocation of the reserve capacity to the individual stations according to their available headroom capacity. The distinctive feature of the proposed solution is the structure of the droop control which permits to provide different actions in the over-voltage and under-voltage. In accordance with the operating set-points of power, the required over- and under-voltage reserve capacities to cope with any possible converter outage are calculated separately. In this way, the appropriate droop parameters that allow the converter stations to efficiently deploy the allocated reserves can be readily determined without a complex algorithm. The effectiveness of the proposed approach was demonstrated by a comprehensive analysis, and its feasibility was confirmed by EMT simulations on the four-terminal MTDC grid model.

# Chapter 7

# Conclusions and Future Work

This chapter summarizes the major findings and conclusions of the thesis and presents possible future work.

## 7.1 Conclusions

In response to the continuous rise of the overall energy consumption and the growing concern on sustainable development, policymakers and all relevant actors are seeking today alternatives to the limited and polluting conventional fossil energy resources. The abundantly available renewable energy resources, such as wind, solar, biomass, geothermal, etc. are considered as promising alternatives, and they are expected to supersede the conventional fossil-based power plants in the generation fleet in upcoming decades. Nonetheless, accommodating the geographically dispersed renewable resources, which are likely located at remote places unfavorable to grid integration, and handling their intermittent nature have already imposed unprecedented stress on the existing power transmission systems. A fundamental upgrade of the existing transmission system by more efficient and flexible means than the traditional AC technology is required. HVDC transmission is considered as a good candidate, and numerous projects have been launched during the past decades. The HVDC transmission has become a technically and economically attractive solution thanks to the remarkable advancement of the converter technology, represented by the state-of-the-art Modular Multilevel Converter (MMC). Due to its various remarkable advantages over conventional converter topologies, the MMC is deemed as the standard technology and used in many of the recent projects. In line with the growing number of HVDC applications, the concept of connecting several HVDC stations to form a Multi-Terminal DC (MTDC) grid arose. It is expected to bring more flexibility of power dispatching and reliability of power supply by serving as an additional bulk power overlay grid.

However, incorporating several converters, which may be developed by different manufacturers with their own topologies, parameters, and control algorithms, to form such an MTDC grid and operating them in a coordinated manner pose a number of challenging tasks, notably, an adequate modeling of the converters, a deep understanding of the system dynamics and the maturing of the control and operation strategy. The main contributions of this thesis are the modeling and detailed analysis of the internal dynamics of the MMC, the development of its novel control scheme that permits to improve the HVDC system voltage dynamics, and the investigation and development of MTDC grid control strategy.

In Chapter 3, the basic design of the high-level control was presented. The internal current dynamics of the MMC was studied, and its analytical model was developed. The inner controller which governs the AC and DC currents was then developed by inverting the causality relation between the converter arm voltages and the currents to be controlled. The outer controller was designed by regarding its dynamics sufficiently slower than the subordinate inner control loop. One of the challenges in this control level was to regulate the energy stored in the six converter arms. By an adequate change of variables, those six state variables were transformed into another set of six variables: the total energy stored inside the MMC and five other variables which represent the dispersion of the energy among the arms. From the developed energetic model, the two types of total energy controllers were developed, and their distinct differences were demonstrated by simulations. It was shown that the MMC possesses an inherent feature — controllability of the internally stored energy — which enables it to act as an energy storage buffer by exchanging energy with the associated grid without affecting the other side of the converter.

In Chapter 4, a thorough analysis on the limitations imposed on the energy stored in the MMC was provided. The upper limit of the energy was defined as the maximum allowable energy that will not violate the maximum admissible voltage of the SMs at its peak, and the lower limit signifies the minimum requirement of the energy which is necessary to ensure the proper function of the MMC without overmodulation. The internal energy pulsations, which appear as the voltage ripples in the arms, were analyzed. Then both upper and lower limits of energy were mathematically formulated as functions of the converter operating point, and they were confirmed by experimental results using a small-scale MMC mock-up. In addition, sensitivity analysis on the influence of the active and reactive power transfer, the AC and DC grid voltage, and the SM capacitor size on the upper and lower energy limits were provided.

In Chapter 5, the general dynamics of the DC systems were described by analogy with the AC systems. It was revealed that the DC voltage is extremely volatile compared to the frequency in AC systems due to the considerably smaller energy stored in the DC system. As a solution to this problem, a novel control method for MMC, named Virtual Capacitor Control, was proposed. This control enables to utilize the energy storage capability of the MMC to enhance the equivalent capacitance of the HVDC system. Its feasibility was demonstrated and confirmed by simulations of a detailed HVDC link model on EMTP-RV software. The proposed virtual capacitor control enables the MMC to behave as if there were an adjustable capacitor on the DC side of the converter. This is realized by the appropriate energy reference calculation which allows regulating the internal energy level in conjunction with the variation of the DC voltage. By simply changing the virtual capacitor coefficient $k_{vc}$, the degree of the contribution by the internal energy can be adjusted. This additional degree of freedom can greatly broaden the operability of the DC systems, making it possible to maintain the DC voltage within a prescribed range without having an extra capital cost or negative impact on the AC grid.

In Chapter 6, the general overview of the MTDC grid operation and its hierarchical control architecture was first introduced by analogy with the well-known AC grids. The influence of the droop parameters on the system behavior was analyzed from both static and dynamic aspects. The virtual capacitor control was applied to the MTDC grid. It was demonstrated that the additional degree of freedom brought by this control enables to greatly extend the flexibility of the MTDC grid control. Thereafter, the particular issues which must be taken into account in relatively small DC grids and the limitations on the conventional uniform droop were investigated. It was revealed that the conventional droop approach can ensure the security of the system only if all the stations secure a sufficient headroom of power transfer capacity, which can impede the economically optimal operation of the MTDC grid. As a solution to this problem, a novel methodology that enables efficient allocation of the reserve capacity to the individual stations according to their available headroom capacity was proposed. The distinctive feature of the proposed solution is the structure of the droop control which permits to provide different actions in the over-voltage and under-voltage. The effectiveness of the proposed approach was demonstrated by a comprehensive analysis. And its feasibility was confirmed by EMT simulations on a four-terminal MTDC grid model.

## 7.2 Future Work

The following is a list of the possible future research topics:

- In practice, handling a phase-to-ground fault or any asymmetric conditions in the AC grid is an important requirement for the control of HVDC converter. Modeling the MMC in positive and negative sequences and elaborating the controller design to prevent propagating the disturbance to the DC grid needs to be addressed.
- Using advanced control theory is an attractive solution to improve the performance of the converter. Integrating the analysis on the energy limits into the control optimization criteria is an interesting application.
- The provided analysis on the energy limits concerned only the half-bridge sub-module topology. The future work in this respect encompass the extension of the provided study to different sub-module topologies, such as full-bridge, double clamped, etc.
- Interaction between the HVDC system and the interfaced AC grid is an interesting topic. In light of this, assessment of the impact of the virtual capacitor control in frequency domain using more complex AC grid models is a possible future work.
- Confirming the proposed variable droop concept by using real-time simulation platform should be addressed.

# Bibliography

[1] U.S. Energy Information Administration, “International Energy Outlook 2016,” Tech. Rep., 2016. [Online]. Available: www.eia.gov/forecasts/ieo/pdf/0484(2016).pdf

[2] OECD, “Electricity generation,” 2016. [Online]. Available: https://data.oecd.org/energy/electricity-generation.htm

[3] Enerdata, “Global Energy Statical Yearbook 2017,” 2017. [Online]. Available: https://yearbook.enerdata.net/electricity/world-electricity-production-statistics.html

[4] ENTSO-E, “Ten Year Network Development Plan 2014,” 2014.

[5] SIEMENS AG, “High voltage direct current transmission,” Tech. Rep., 2011.

[6] M. Barnes and A. Beddard, “Voltage source converter HVDC links - The state of the art and issues going forward,” *Energy Procedia*, vol. 24, pp. 108–122, 2012.

[7] J. Rodriguez, J.-S. Lai, and F. Z. Peng, “Multilevel inverters a survvey of topologies, controls and applications,” *IEEE Trans. Ind. Electron.*, vol. 49, no. 4, pp. 724–738, 2002.

[8] H. Saad, S. Dennetiere, J. Mahseredjian, P. Delarue, X. Guillaud, J. Peralta, and S. Nguefeu, “Modular Multilevel Converter Models for Electromagnetic Transients,” *IEEE Trans. Power Deliv.*, vol. 29, no. 3, pp. 1481–1489, 2014.

[9] ENTSO-E, “Continental Europe Operation Handbook P1 - Policy 1: Load-Frequency Control and Performance,” Tech. Rep. Cc, 2009. [Online]. Available: https://www.entsoe.eu/fileadmin/user_upload/_library/publications/entsoe/Operation_Handbook/Policy_1_final.pdf

[10] ABB, “Insulated-gate bipolar transistors (IGBT) and diode dies.” [Online]. Available: http://new.abb.com/semiconductors/insulated-gate-bipolar-transistors-(igbt)-and-diode-dies

[11] Infeneon, “Infeneon.com.” [Online]. Available: http://www.infineon.com/

[12] S. Debnath, J. Qin, B. Bahrani, M. Saeedifard, and P. Barbosa, “Operation, Control, and Applications of the Modular Multilevel Converter: A Review,” *IEEE Trans. Power Electron.*, vol. 30, no. 1, pp. 37–53, 2015.

[13] J. Qin, M. Saeedifard, A. Rockhill, and R. Zhou, “Hybrid design of modular multilevel converters for HVDC systems based on various submodule circuits,” *IEEE Trans. Power Deliv.*, vol. 30, no. 1, pp. 385–394, 2015.

[14] W. Li, “Real-time simulation of CDSM modular multilevel converter for HIL test applications,” in *IECON 2016 - 42nd Annu. Conf. IEEE Ind. Electron. Soc.*, 2016, pp. 2372–2377.

[15] OECD, “List of OECD Member countries - Ratification of the Convention on the OECD.” [Online]. Available: http://www.oecd.org/about/membersandpartners/list-oecd-member-countries.htm

[16] National Development and Reform Commission (NDRC), “13th Renewable Energy Development Five Year Plan (2016-2020),” 2016. [Online]. Available: http://zfxxgk.nea.gov.cn/auto87/201612/t20161216_2358.htm

[17] Australian Government Department of the Environment and Energy, “The Renewable Energy Target (RET) scheme,” 2015. [Online]. Available: http://www.environment.gov.au/climate-change/renewable-energy-target-scheme

[18] European Commission, “Energy 2020 A strategy for competitive, sustainable and secure energy,” 2010. [Online]. Available: http://eur-lex.europa.eu/legal-content/EN/TXT/?qid=1409650806265&uri=CELEX:52010DC0639

[19] ——, “A policy framework for climate and energy in the period from 2020 to 2030,” 2014. [Online]. Available: http://eur-lex.europa.eu/legal-content/EN/ALL/?uri=CELEX:52014DC0015

[20] European Environmental Agency, “Trends and projections in Europe 2015: Tracking progress towards Europe’s Climate and energy targets,” Tech. Rep. 4/2015, 2015. [Online]. Available: https://www.eea.europa.eu

[21] European Commission, “A Roadmap for moving to a competitive low carbon economy in 2050,” 2011. [Online]. Available: http://eur-lex.europa.eu/legal-content/EN/ALL/?uri=CELEX:52011DC0112

[22] European Environmental Agency, “Renewable energy in Europe - recent growth and knock-on effects,” Tech. Rep. 4/2016, 2016. [Online]. Available: http://www.eea.europa.eu/publications/renewable-energy-in-europe-2016/download

[23] ENTSO-E, “TYNDP 2016 Scenario Development Report,” 2015.

[24] ——, “Ten Year Network Development Plan 2016,” 2016.

[25] European Commission, “Energy Union Package,” 2015.

[26] N. Flourentzou, V. Agelidis, and G. Demetriades, “VSC-Based HVDC Power Transmission Systems: An Overview,” *IEEE Trans. Power Electron.*, vol. 24, no. 3, pp. 592–602, 2009.

[27] K. Bell, D. Cirio, a. M. Denis, L. He, C. C. Liu, G. Migliavacca, C. Moreira, and P. Panciatici, “Economic and technical criteria for designing future off-shore HVDC grids,” in *2010 IEEE PES Innov. Smart Grid Technol. Conf. Eur. (ISGT Eur.*, oct 2010, pp. 1–8.

[28] WindEurope, “Unleashing Europe’s offshore wind potential - A new resource assessment,” 2017.

[29] T. Ackermann and N. Negra, “Evaluation of Electrical Transmission Concepts for Large Offshore Windfarms,” in *Offshore Wind Conf. Expo.*, Copenhagen, 2005, pp. 1–10.

[30] C. S. Schifreen and W. C. Marble, “Charging Current Limitations in Operation or High-Voltage Cable Lines,” *Trans. Am. Inst. Electr. Eng. Part III Power Appar. Syst.*, vol. 75, no. 3, pp. 803–817, 1956.

[31] M. P. Bahrman, “HVDC Transmission Overview,” *Transm. Distrib. Conf. Expo.*, pp. 1–7, 2008.

[32] D. Van Hertem, M. Ghandhari, and M. Delimar, “Technical limitations towards a SuperGrid-A European prospective,” *Energy Conf. Exhib. (EnergyCon), 2010 IEEE Int.*, pp. 302–309, 2010.

[33] Cigré, “HVDC Connection of Offshore Wind Power Plants,” WG B4.55, Tech. Rep. May, 2015.

[34] ——, “HVDC Grid Feasibility Study,” WG B4-52, Tech. Rep. April, 2013.

[35] M. Haeusler, G. Schlayer, and G. Fitterer, “Converting AC power lines to DC for higher transmission ratings,” *ABB Rev.*, no. 3, pp. 4–11, 1997.

[36] J. Lundkvist, I. Gutman, and L. Weimers, “Feasibility study for converting 380 kV AC lines to hybrid AC/DC lines,” in *EPRI’s High-Voltage Direct Curr. Flex. AC Transm. Syst. Conf.*, 2009, p. 11.

[37] B. Sander, J. Lundquist, I. Gutman, C. Neumann, B. Rusek, and K. H. Weck, “Conversion of AC multi-circuit lines to AC-DC hybrid lines with respect to the environmental impact,” in *Cigré Sess. Paris*, vol. B2, no. 105, 2014, pp. 36–47.

[38] P. L. Francos, S. S. Verdugo, and S. Guyomarch, “New French-Spanish VSC link,” in *Cigré Sess. 2012*, Paris, France, 2012.

[39] RTE, “L’Interconnexion Electrique France - Angleterre : Une Renovation au Service de la Fiabilite,” 2012.

[40] J. Dorn and M. Pohl, “Transformation of the Energy System in Germany - Enhancement of System Stability by Integration of innovative Multilevel HVDC in the AC Grid,” in *Int. ETG-Congress 2013; Symp. 1 Secur. Crit. Infrastructures Today*, 2013, pp. 1–6.

[41] O. Peake, “The History of High Voltage Direct Current Transmission,” in *3rd Australas. Eng. Herit. Conf. 2009*, vol. 8, no. 1, 2009, pp. 1–8.

[42] ABB, “The early HVDC development: The key challenge in the HVDC technique,” Tech. Rep., 2005. [Online]. Available: http://www.abb.com/hvdc

[43] ——, “Special Report 60 years of HVDC,” Tech. Rep. ABB Review, 2014.

[44] D. Tiku, “dc Power Transmission: Mercury-Arc to Thyristor HVdc Valves [History],” *IEEE power energy magzine*, vol. 12, no. 2, pp. 76–96, 2014.

[45] J. F. Graham, T. Holmgren, P. Fischer, and N. Shore, “The Rio Madeira HVDC System - Design aspects of Bipole 1 and the connector to Acre-Rondônia Sweden,” in *Cigré Sess.*, 2012, pp. 1–10.

[46] S. P. Teeuwsen and R. Rössel, “Dynamic performance of the 1000 MW BritNed HVDC interconnector project,” *IEEE PES Gen. Meet. PES 2010*, pp. 1–8, 2010.

[47] U. Axelsson, A. Holm, C. Liljegren, K. Eriksson, and L. Weimers, “Gotland HVDC light transmission-world’s first commercial small scale dc transmission,” in *CIRED Conf.*, 1999.

[48] C. Du, M. H. J. Bollen, E. Agneholm, and A. Sannino, “A New Control Strategy of a VSC; HVDC System for High-Quality Supply of Industrial Plants,” *Power Deliv. IEEE Trans.*, vol. 22, no. 4, pp. 2386–2394, 2007.

[49] R. Marquardt, “Current rectification circuit for voltage source inverters with separate energy stores replaces phase blocks with energy storing capacitors,” DE Patent 10 103 031, January 24, 2001.

[50] B. D. Gemmell, J. Dorn, D. Retzmann, and D. Soerangr, “Prospects of multilevel VSC Technologies for power transmission,” in *Transm. Distrib. Expo. Conf. 2008 IEEE PES Powering Towar. Futur. PIMS 2008*, 2008, pp. 1–16.

[51] J. Peralta, H. Saad, S. Dennetiere, J. Mahseredjian, and S. Nguefeu, “Detailed and averaged models for a 401-level MMC-HVDC system,” *IEEE Trans. Power Deliv.*, vol. 27, no. 3, pp. 1501–1508, 2012.

[52] I. M. de Alegría, J. L. Martín, I. Kortabarria, J. Andreu, and P. I. Ereño., “Transmission alternatives for offshore electrical power,” *Renew. Sustain. Energy Rev.*, vol. 13, no. 5, pp. 1027–1038, 2009.

[53] O. Gomis-Bellmunt, J. Liang, J. Ekanayake, R. King, and N. Jenkins, “Topologies of multiterminal HVDC-VSC transmission for large offshore wind farms,” *Electr. Power Syst. Res.*, vol. 81, no. 2, pp. 271–281, 2011.

[54] K. Meng, W. Zhang, Y. Li, Z. Y. Dong, Z. Xu, K. P. Wong, and Y. Zheng, “Hierarchical SCOPF Considering Wind Energy Integration through Multi-Terminal VSC-HVDC Grids,” *IEEE Trans. Power Syst.*, vol. Early Acce, pp. 1–1, 2017.

[55] K. Bell, L. Xu, and T. Houghton, “Considerations in design of an offshore network,” in *Cigré Sess.*, 2014, pp. 1–2.

[56] D. Van Hertem, O. Gomis-bellmunt, and J. Liang, *HVDC grids: for offshore and supergrid of the future.* Wiley-IEEE Press, 2016.

[57] N. Ahmed, S. Norrga, H.-P. Nee, A. Haider, D. Van Hertem, L. Zhang, and L. Harnefors, “HVDC SuperGrids with modular multilevel converters The power transmission backbone of the future,” in *Int. Multi-Conference Syst. Sygnals Devices*, 2012, pp. 1–7.

[58] N. Ahmed, A. Haider, D. Van Hertem, L. Zhang, and H.-P. Nee, “Prospects and challenges of future HVDC SuperGrids with modular multilevel converters,” *Proc. 2011 14th Eur. Conf. Power Electron. Appl.*, pp. 1–10, 2011.

[59] D. Van Hertem and M. Ghandhari, “Multi-terminal VSC HVDC for the European supergrid: Obstacles,” *Renew. Sustain. Energy Rev.*, vol. 14, no. 9, pp. 3156–3163, 2010.

[60] V. Akhmatov, M. Callavik, C. M. Franck, S. E. Rye, T. Ahndorf, M. K. Bucher, H. Muller, F. Schettler, and R. Wiget, “Technical guidelines and prestandardization work for first HVDC Grids,” *IEEE Trans. Power Deliv.*, vol. 29, no. 1, pp. 327–335, 2014.

[61] European Commission, “COMMISSION REGULATION (EU) 2016/1447 of 26 August 2016 establishing a network code on requirements for grid connection of high voltage direct current systems and direct current-connected power park modules,” 2016. [Online]. Available: http://eur-lex.europa.eu/eli/reg/2016/1447/oj

[62] E. Kontos, S. Member, R. T. Pinto, and S. Member, “Impact of HVDC Transmission System Topology on Multiterminal DC Network Faults,” *IEEE Trans. Power Deliv.*, vol. 30, no. 2, pp. 844–852, 2015.

[63] W. A. Patterson, “The Eel River HVDC scheme - A 320 MW asynchronous interconnection between the New Brunswick Electric Power Commission and Hydro-Québec employing thyristor valves,” *Can. Electr. Eng. J.*, vol. 2, no. 1, pp. 9–16, 1977.

[64] R. Rudervall, J. Chapentier, and Raghuveer Sharma, “High voltage direct current (HVDC) transmission systems technology review paper,” in *Energy Week*, 2000, pp. 1–19.

[65] SIEMENS AG, “First 800-kV high-voltage direct-current link in China now fully operational,” Tech. Rep., 2010.

[66] N. Mohan, T. M. Undeland, and W. P. Robbins, *Power Electronics.* John Wiley & Sons, Inc., 2003.

[67] B. K. Bose, *Modern Power Electronics and AC Drives.* Prentice-Hall, Inc., 2002.

[68] ABB, “Power Semiconductors Product catalog 2017,” 2017. [Online]. Available: https://library.e.abb.com/public/067a2dbc2c6140b4a616639cf70b615f/ABB_PC_2017_Final_web.pdf

[69] R. Rendina, G. Pazienza, R. Niccolai, B. Jansson, W. Lovison, and F. Alvarez, “SAPEI HVDC converters,” in *AEIT HVDC Work.*, 2008, pp. 1–10.

[70] P. Kundur, *Power System Stability and Control.* McGraw-Hill, Inc., 1994.

[71] R. Brandt, P. Kuffel, and P. Thomas, “Lower churchill project - Multi-terminal HVdc feasibility studies,” in *IEEE PES Gen. Meet.*, 2010, pp. 1–9.

[72] M. P. Bahrman, “HVDC Transmission Overview,” in *2008 IEEE/PES Transm. Distrib. Conf. Expo.*, 2007, pp. 1–7.

[73] D. R. L. Sellick and M. Akerberg, “Comparison of HVDC Light (VSC) and HVDC Classic (LCC) Site Aspects, for a 500MW 400kV HVDC Transmission Scheme,” *IET ACDC 2012 Conf.*, no. Lcc, pp. 1–6, 2012.

[74] C. Blake and C. Bull, “IGBT or MOSFET : Choose Wisely,” Tech. Rep., 2006.

[75] M. Takei, T. Naito, and K. Ueno, “Reverse blocking IGBT for matrix converter with ultra-thin wafer technology,” *IEE Proceedings-Circuits, Devices Syst.*, vol. 151, no. 3, pp. 243–247, 2004.

[76] H. Wang and K.-w. Ma, “IGBT technology for future high-power VSC-HVDC applications,” in *12th IET Int. Conf. AC DC Power Transm. (ACDC 2016)*, 2016, pp. 1–6.

[77] B. R. Andersen, “VSC Transmission Tutorial,” in *CIGRE Study Comm. B4 Meet.*, 2005, pp. 1–22.

[78] Cigré, “VSC Transmission,” Wg B4.37, Tech. Rep., 2005.

[79] B. Jacobson, Y. Jiang-Hafner, P. Rey, G. Asplund, M. Jeroense, A. Gustafsson, and M. Bergkvist, “HVDC with Voltage Source Converters and Extruded Cables for Up To +/-300 kV and 1000 MW,” *CIGRE B4-105 Colloq.*, 2006.

[80] M. Bahrman and P.-E. Bjorklund, “The New Black Start: System Restoration with Help from Voltage-Sourced Converters,” *Power Energy Mag. IEEE*, no. february, pp. 44–53, 2014.

[81] B. Jacobson, P. Karlsson, G. Asplund, L. Harnefors, and T. Jonsson, “VSC-HVDC transmission with cascaded two-level converters,” in *Cigré Sess.*, 2010.

[82] L. G. Franquelo, J. Rodríguez, J. I. Leon, S. Kouro, R. Portillo, and M. A. M. Prats, “The Age of Multilevel Converters Arrives,” *IEEE Ind. Electron. Mag.*, vol. 2, no. 2, pp. 28–39, 2008.

[83] A. Nabae, I. Takahashi, and H. Akagi, “A New Neutral-Point-Clamped PWM Inverter,” *IEEE Trans. Ind. Appl.*, vol. IA-17, no. 5, pp. 518–523, 1981.

[84] S. Kouro, M. Malinowski, K. Gopakumar, J. Pou, L. Franquelo, B. W. B. Wu, J. Rodriguez, M. Perez, and J. Leon, “Recent Advances and Industrial Applications of Multilevel Converters,” *IEEE Trans. Ind. Electron.*, vol. 57, no. 8, pp. 2553–2580, 2010.

[85] M. Saeedifard, R. Iravani, and J. Pou, “Analysis and control of DC-capacitor-voltage-drift phenomenon of a passive front-end five-level converter,” *IEEE Trans. Ind. Electron.*, vol. 54, no. 6, pp. 3255–3266, 2007.

[86] A. Lesnicar and R. Marquardt, “An innovative modular multilevel converter topology suitable for a wide power range,” in *Power Tech Conf. Proceedings, 2003 IEEE Bol.*, vol. 3, 2003, pp. 272–277.

[87] R. Marquardt, “Modular Multilevel Converter: An universal concept for HVDC-Networks and extended DC-bus-applications,” *2010 Int. Power Electron. Conf. - ECCE Asia -, IPEC 2010*, pp. 502–507, 2010.

[88] C. Oates, “Modular Multilevel Converter Design for VSC HVDC Applications,” *IEEE J. Emerg. Sel. Top. Power Electron.*, vol. 3, no. 2, pp. 505–515, 2015.

[89] S. Rohner, S. Bernet, M. Hiller, and R. Sommer, “Modelling, simulation and analysis of a Modular Multilevel Converter for medium voltage applications,” *Ind. Technol. (ICIT), 2010 IEEE Int. Conf.*, pp. 775–782, 2010.

[90] Q. Tu, Z. Xu, H. Huang, J. Zhang, T. Qingrui, X. Zheng, H. Hongyang, and Z. Jing, “Parameter design principle of the arm inductor in modular multilevel converter based HVDC,” *Power Syst. Technol. (POWERCON), 2010 Int. Conf.*, pp. 1–6, 2010.

[91] J. Dorn, P. L. Seta, F. Schettler, J. Stankewitz, M. Berge, R. T. Pinto, K. Uecker, M. Walz, K. Vennemann, B. Rusek, J. Reisbeck, and C. Butterer, “Full-Bridge VSC: an essential enabler of the transition to an energy system dominated by renewable sources,” in *2016 IEEE Power Energy Soc. Gen. Meet.*, 2016.

[92] C. Karawita, D. Suriyaarachchi, and M. Mohaddes, “A Controlled DC Fault Clearance Mechanism for Full-Bridge MMC VSC Converters,” in *Cigré Sess.*, Lund, Sweeden, 2015, pp. 1–8.

[93] D. Schmitt, Y. Wang, T. Weyh, and R. Marquardt, “DC-side fault current management in extended multiterminal-HVDC-grids,” in *Int. Multi-Conference Syst. Signals Devices, SSD 2012 - Summ. Proc.*, no. Lcc, 2012, pp. 1–5.

[94] X. Yu, Y. Wei, and Q. Jiang, “STATCOM Operation Scheme of the CDSM-MMC during a Pole-to-Pole DC Fault,” *IEEE Trans. Power Deliv.*, vol. 31, no. 3, pp. 1150–1159, 2016.

[95] A. Nami, L. Wang, F. Dijkhuizen, and A. Shukla, “Five level cross connected cell for cascaded converters,” *2013 15th Eur. Conf. Power Electron. Appl. EPE 2013*, 2013.

[96] E. Spahic, F. Schettler, D. Varma, and J. Dorn, “Impact of the DC technology on transmission grids,” in *11th IET Int. Conf. AC DC Power Transm.*, 2015, pp. 1–7.

[97] T. Modeer, H.-P. Nee, and S. Norrga, “Loss Comparison of Different Sub-Module Implementations for Modular Multilevel Converters in HVDC Applications,” in *Proc. 2011 14th Eur. Conf. Power Electron. Appl.*, no. January 2011, 2011.

[98] H. Dommel, “Digital Computer Solution of Electromagnetic Transients in Single- and Multiphase Networks,” *IEEE Trans. Power Appar. Syst.*, vol. PAS-88, no. 4, pp. 388–399, 1969.

[99] J. Xu, S. Member, C. Zhao, and W. Liu, “Accelerated Model of Modular Multilevel Converters in PSCAD / EMTDC,” *IEEE Trans. Power Deliv.*, vol. 28, no. 1, pp. 129–136, 2013.

[100] U. N. Gnanarathna, A. M. Gole, and R. P. Jayasinghe, “Efficient modeling of modular multilevel HVDC converters (MMC) on electromagnetic transient simulation programs,” *IEEE Trans. Power Deliv.*, vol. 26, no. 1, pp. 316–324, 2011.

[101] H. Saad, J. Peralta, S. Dennetiere, J. Mahseredjian, J. Jatskevich, J. a. Martinez, A. Davoudi, M. Saeedifard, V. Sood, X. Wang, J. Cano, and A. Mehrizi-Sani, “Dynamic averaged and simplified models for mmc-based hvdc transmission systems,” *IEEE Trans. Power Deliv.*, vol. 28, no. 3, pp. 1723–1730, 2013.

[102] A. Beddard, M. Barnes, and R. Preece, “Comparison of Detailed Modeling Techniques for MMC Employed on VSC-HVDC Schemes,” *IEEE Trans. Power Deliv.*, vol. 30, no. 2, pp. 579–589, 2015.

[103] F. B. Ajaei and R. Iravani, “Enhanced Equivalent Model of the Modular Multilevel Converter,” *IEEE Trans. Power Deliv.*, vol. 30, no. 2, p. 8040, 2015.

[104] A. Beddard, C. Sheridan, M. Barnes, and T. Green, “Improved Accuracy Average Value Models of Modular Multilevel Converters,” *IEEE Trans. Power Deliv.*, vol. PP, no. 99, p. 1, 2016.

[105] Cigré, “Guide for the Development of Models for HVDC Converters in a HVDC Grid,” Wg B4.57, Tech. Rep., 2014.

[106] A. Strollo, “A new IGBT circuit model for SPICE simulation,” in *IEEE Power Electron. Spec. Conf.*, vol. 1, 1997, pp. 133–138.

[107] H. Slhi and C. Christopoulos, “Generalised TLM switch model for power electronics applications,” *IEE Proceedings-Science, Meas. Technol.*, vol. 145, no. 3, pp. 101–104, 1998.

[108] H. Saad, K. Jacobs, W. Lin, and D. Jovcic, “Modelling of MMC including half-bridge and Full-bridge submodules for EMT study,” in *19th Power Syst. Comput. Conf. PSCC 2016*, 2016, pp. 1–7.

[109] A. Antonopoulos, L. Angquist, and H.-P. Nee, “On dynamics and voltage control of the Modular Multilevel Converter,” *2009 13th Eur. Conf. Power Electron. Appl. (EPE’13 ECCE-Europe)*, 2009.

[110] S. P. Teeuwsen, “Simplified dynamic model of a voltage-sourced converter with modular multilevel converter design,” *2009 IEEE/PES Power Syst. Conf. Expo. PSCE 2009*, pp. 1–6, 2009.

[111] D. Jovcic and A. Jamshidifar, “Phasor Model of Modular Multilevel Converter With Circulating Current Suppression Control,” *IEEE Trans. Power Deliv.*, vol. 30, no. 4, pp. 1889–1897, 2015.

[112] H. Ouquelle, L. A. Dessaint, and S. Casoria, “An average value model-based design of a deadbeat controller for VSC-HVDC transmission link,” *2009 IEEE Power Energy Soc. Gen. Meet. PES ’09*, pp. 1–6, 2009.

[113] N. T. Trinh, M. Zeller, K. Wuerflinger, and I. Erlich, “Generic Model of MMC-VSC-HVDC for Interaction Study with AC Power System,” *IEEE Trans. Power Syst.*, vol. 31, no. 1, pp. 27–34, 2016.

[114] J. Freytes, L. Papangelis, H. Saad, P. Rault, T. V. Cutsem, and X. Guillaud, “On the modeling of MMC for use in large scale dynamic simulations,” in *2016 Power Syst. Comput. Conf.*, 2016.

[115] D. Siemaszko, A. Antonopoulos, K. Ilves, M. Vasiladiotis, L. Ängquist, and H. P. Nee, “Evaluation of control and modulation methods for modular multilevel converters,” *2010 Int. Power Electron. Conf. - ECCE Asia -, IPEC 2010*, pp. 746–753, 2010.

[116] G. Bergna, J. A. Suul, and S. D’Arco, “State-space modelling of modular multilevel converters for constant variables in steady-state,” in *2016 IEEE 17th Work. Control Model. Power Electron. COMPEL 2016*, 2016.

[117] M. Hagiwara and H. Akagi, “Control and Experiment of Pulsewidth-Modulated Modular Multilevel Converters,” *IEEE Trans. Power Electron.*, vol. 24, no. 7, pp. 1737–1746, 2009.

[118] S. Kouro, R. Bernal, H. Miranda, C. a. Silva, and J. Rodríguez, “High-performance torque and flux control for multilevel inverter fed induction motors,” *IEEE Trans. Power Electr.*, vol. 22 (6), no. 6, pp. 2116–2123, 2007.

[119] J. Beerten, G. Bergna, S. D’Arco, and J. A. Suul, “Comparison of small-signal dynamics in MMC and two-level VSC HVDC transmission schemes,” in *2016 IEEE Int. Energy Conf. ENERGYCON 2016*, 2016.

[120] C. Oates, “Observer based monitoring and control of submodules in modular multilevel converter,” WO Patent Application 2015 082 698 A1, December 5, 2013.

[121] L. Angquist, A. Antonopoulos, D. Siemaszko, K. Ilves, M. Vasiladiotis, and H.-P. Nee, “Open-loop control of modular multilevel converters using estimation of stored energy,” *IEEE Trans. Ind. Appl.*, vol. 47, no. 6, pp. 2516–2524, 2011.

[122] Y. Deng, K. H. Teo, C. Duan, T. Habetler, and R. Harley, “A Fast and Generalized Space Vector Modulation Scheme for Multilevel Inverters,” *IEEE Trans. Power Electron.*, vol. 29, no. 10, pp. 5204–5217, 2014.

[123] S. Fan, K. Zhang, J. Xiong, and Y. Xue, "An Improved Control System for Modular Multilevel Converters with New Modulation Strategy and Voltage Balancing Control," *IEEE Trans. Power Electron.*, vol. PP, no. 99, pp. 1–1, 2014.

[124] G. S. Konstantinou, M. Ciobotaru, and V. G. Agelidis, "Selective harmonic elimination pulse-width modulation of modular multilevel converters," *IET Power Electron.*, vol. 6, no. 1, pp. 96–107, 2013.

[125] Q. Tu, S. Member, and Z. Xu, "Impact of Sampling Frequency on Harmonic Distortion for Modular Multilevel Converter," *IEEE Trans. Power Deliv.*, vol. 26, no. 1, pp. 298–306, 2011.

[126] A. Zama, S. Ait Mansour, D. Frey, A. Benchaib, S. Bacha, B. Luscan, and L. Blum, "A Comparative Assessment of Different Balancing Control Algorithms for Modular Multilevel Converter (MMC)," in *2016 18th Eur. Conf. Power Electron. Appl. (EPE'16 ECCE Eur.*, no. Mmc, 2016, pp. 1–10.

[127] Q. Tu, S. Member, Z. Xu, L. Xu, and S. Member, "Reduced Switching-Frequency Modulation and Circulating Current Suppression for Modular Multilevel Converters," *IEEE Trans. Power Deliv.*, vol. 26, no. 3, pp. 2009–2017, 2011.

[128] F. Martinez-rodrigo, S. D. Pablo, and L. C. H.-d. Lucas, "Current control of a modular multilevel converter for HVDC applications," *Renew. Energy*, vol. 83, pp. 318–331, 2015.

[129] M. Hagiwara, R. Maeda, and H. Akagi, "Control and analysis of the modular multilevel cascade converter based on double-star chopper-cells (MMCC-DSCC)," *IEEE Trans. Power Electron.*, vol. 26, no. 6, pp. 1649–1658, 2011.

[130] S. Li, X. Wang, Z. Yao, T. Li, and Z. Peng, "Circulating current suppressing strategy for MMC-HVDC based on nonideal proportional resonant controllers under unbalanced grid conditions," *IEEE Trans. Power Electron.*, vol. 30, no. 1, pp. 387–397, 2015.

[131] L. He, K. Zhang, J. Xiong, and S. Fan, "A Repetitive Control Scheme for Harmonic Suppression of Circulating Current in Modular Multilevel Converters," *IEEE Tran. Power Electron*, vol. 30, no. 1, pp. 471–481, 2015.

[132] M. Zhang, S. Member, L. Huang, and W. Yao, "Circulating Harmonic Current Elimination of a CPS-PWM-Based Modular Multilevel Converter With a Plug-In Repetitive Controller," *IEEE Trans. Power Electron.*, vol. 29, no. 4, pp. 2083–2097, 2014.

[133] P. Münch, D. Görges, M. Izák, and S. Liu, "Integrated current control, energy control and energy balancing of Modular Multilevel Converters," in *IECON 2010 - 36th Annu. Conf. IEEE Ind. Electron. Soc.*, 2010, pp. 150–155.

[134] M. Vatani, M. Hovd, and M. Saeedifard, "Control of the Modular Multilevel Converter Based on a Discrete-Time Bilinear Model using the Sum of Squares Decomposition Method," *IEEE Trans. Power Deliv.*, vol. PP, no. 99, pp. 1–1, 2015.

[135] S. Yang, S. M. Ieee, P. Wang, S. M. Ieee, Y. Tang, and M. Ieee, "Feedback Linearization Based Current Control Strategy for Modular Multilevel Converters," *IEEE Trans. Power Electron.*, vol. PP, no. 99, 2017.

[136] B. Riar, T. Geyer, and U. Madawala, "Model Predictive Direct Current Control of Modular Multilevel Converters: Modelling, Analysis and Experimental Evaluation," *IEEE Trans. Power Electron.*, vol. PP, no. 1, pp. 1–1, 2014.

[137] A. Dekka, B. Wu, V. Yaramasu, and N. Zargari, "Model Predictive Control with Common-Mode Voltage Injection for Modular Multilevel Converter," *IEEE Trans. Power Electron.*, vol. 8993, no. c, pp. 1–1, 2016.

[138] Z. Gong, S. Member, P. Dai, and X. Yuan, "Design and Experimental Evaluation of Fast Model Predictive Control for Modular Multilevel Converters," *IEEE Trans. Ind. Electron.*, vol. 63, no. 6, pp. 3845–3856, 2016.

[139] J. Bocker, B. Freudenberg, A. The, and S. Dieckerhoff, "Experimental Comparison of Model Predictive Control and Cascaded Control of the Modular Multilevel Converter," *IEEE Trans. Power Electron.*, vol. 30, no. 1, pp. 422–430, 2015.

[140] H. Barnklau, A. Gensior, and J. Rudolph, "A Model-Based Control Scheme for Modular Multilevel Converters," *IEEE Trans. Ind. Electron.*, vol. 60, no. 12, pp. 5359–5375, 2013.

[141] H. Fehr, A. Gensior, and M. Marcus, "Analysis and Trajectory Tracking Control of a Modular Multilevel Converter," *IEEE Trans. Power Electron.*, vol. 30, no. 1, pp. 398–407, 2015.

[142] J. Kolb, F. Kammerer, M. Gommeringer, and M. Braun, "Cascaded control system of the modular multilevel converter for feeding variable-speed drives," *IEEE Trans. Power Electron.*, vol. 30, no. 1, pp. 349–357, 2015.

[143] S. Wenig, F. Rojas, K. Schonleber, M. Suriyah, and T. Leibfried, "Simulation Framework for DC Grid Control and ACDC Interaction Studies Based on Modular Multilevel Converters," *IEEE Trans. Power Deliv.*, vol. 31, no. 2, pp. 780–788, 2016.

[144] P. J. Barrre, A. Bouscayrol, P. Delarue, E. Dumetz, F. Giraud, J. P. Hautier, X. Kestelyn, B. Lemaire-Semail, and E. Semail, “Inversion-based control of electromechanical systems using causal graphical descriptions,” in *IECON 2006 - 32nd Annu. Conf. IEEE Ind. Electron.*, 2006, pp. 5276–5281.

[145] S. Cole, J. Beerten, and R. Belmans, “Generalized dynamic VSC MTDC model for power system stability studies,” *IEEE Trans. Power Syst.*, vol. 25, no. 3, pp. 1655–1662, 2010.

[146] T. M. Haileselassie, M. Molinas, and T. Undeland, “Multi-Terminal VSC-HVDC System for Integration of Offshore Wind Farms and Green Electrification of Platforms in the North Sea,” in *Nord. Work. Power Ind. Electron. (NORPIE 2008)*, 2008, pp. 1–8.

[147] G. Bergna, E. Berne, P. Egrot, P. Lefranc, A. Arzande, J. C. Vannier, and M. Molinas, “An energy-based controller for HVDC modular multilevel converter in decoupled double synchronous reference frame for voltage oscillation reduction,” *IEEE Trans. Ind. Electron.*, vol. 60, no. 6, pp. 2360–2371, 2013.

[148] W. Wenyuan, A. Beddard, M. Barnes, O. Marjanovic, W. Wang, A. Beddard, M. Barnes, and O. Marjanovic, “Analysis of Active Power Control for VSC-HVDC,” *IEEE Trans. Power Deliv.*, vol. 29, no. 4, pp. 1978–1988, 2014.

[149] W. Yang, Q. Song, and W. Liu, “Decoupled Control of Modular Multilevel Converter Based on Intermediate Controllable Voltages,” *IEEE Trans. Ind. Electron.*, vol. 63, no. 8, pp. 4695–4706, 2016.

[150] S. Samimi, F. Gruson, P. Delarue, and X. Guillaud, “Synthesis of different types of energy based controllers for a Modular Multilevel Converter integrated in an HVDC link,” in *11th IET Int. Conf. AC DC Power Transm.*, 2015, pp. 1–7.

[151] A. Ferreira, C. Collados, O. Gomis-Bellmunt, and M. Teixido, “Modular multilevel converter electrical circuit model for HVdc applications,” *2015 17th Eur. Conf. Power Electron. Appl. (EPE’15 ECCE-Europe)*, pp. 1–10, 2015.

[152] K. Shinoda, J. Freytes, A. Benchaib, J. Dai, H. Saad, and X. Guillaud, “Energy Difference Controllers for MMC without DC Current Perturbation,” in *2nd Int. Conf. HVDC*, 2016, pp. 717–722.

[153] M. M. C. Merlin and T. C. Green, “Cell capacitor sizing in multilevel converters: cases of the modular multilevel converter and alternate arm converter,” *IET Power Electron.*, vol. 8, no. 3, pp. 350–360, 2015.

[154] R. Marquardt, A. Lesnicar, and J. Hildinger, “Modulares Stromrichterkonzept für Netzkupplungsanwendungen bei hohen Spannungen,” *ETG Fachtagung*, 2002.

[155] H. Bärnklau, A. Gensior, and S. Bernet, "Submodule capacitor dimensioning for modular multilevel converters," *IEEE Trans. Ind. Appl.*, vol. 50, no. 3, pp. 1915–1923, 2014.

[156] K. Ilves, S. Norrga, L. Harnefors, and H.-P. Nee, "On Energy Storage Requirements in Modular Multilevel Converters," *IEEE Trans. Power Electron.*, vol. 29, no. 1, pp. 77–88, 2014.

[157] S. P. Engel and R. W. D. Doncker, "Control of the Modular Multi-Level Converter for minimized cell capacitance," *Proc. 2011 14th Eur. Conf. Power Electron. Appl.*, pp. 1–10, 2011.

[158] H. Kim, S. Kim, Y.-H. H. Chung, D.-W. W. Yoo, C.-K. K. Kim, and K. Hur, "Operating Region of Modular Multilevel Converter for HVDC with Controlled Second-Order Harmonic Circulating Current: Elaborating P-Q Capability," *IEEE Trans. Power Deliv.*, vol. 31, no. 2, pp. 1–1, 2016.

[159] X. Li, Q. Song, W. Liu, S. Xu, Z. Zhu, and X. Li, "Performance Analysis and Optimization of Circulating Current Control for Modular Multilevel Converter," *IEEE Trans. Ind. Electron.*, vol. 63, no. 2, pp. 716–727, 2016.

[160] G. Bergna, E. Berne, P. Egrot, P. Lefranc, J. Vannier, and A. Arzand, "A generalized power control approach in ABC frame for Modular Multilevel Converters based on mathematical optimization," *IEEE Trans. Power Deliv.*, vol. 29, no. 1, pp. 386–394, 2014.

[161] Electronicon Kondensatoren GmbH, "PEC APPLICATION NOTES," Tech. Rep., 2013.

[162] S. Rodrigues, A. Papadopoulos, E. Kontos, T. Todorcevic, and P. Bauer, "Steady-State Loss Model of Half-Bridge Modular Multilevel Converters," *IEEE Trans. Ind. Appl.*, vol. 52, no. 3, pp. 2415–2425, 2016.

[163] P. S. Jones and C. C. Davidson, "Calculation of power losses for MMC-based VSC HVDC stations," *2013 15th Eur. Conf. Power Electron. Appl. EPE 2013*, pp. 1–10, 2013.

[164] A. Zama, "Modeling and Control of Modular Multilevel Converters (MMCs) for HVDC applications," Ph.D. dissertation, Université Grenoble Alpes, 2017.

[165] ABB, "HVDC Light It's time to connect," Tech. Rep., 2013. [Online]. Available: http://new.abb.com/docs/default-source/ewea-doc/hvdc-light.pdf?sfvrsn=2

[166] A. Ulbig, T. S. Borsche, and G. Andersson, "Impact of low rotational inertia on power system stability and operation," *IFAC World Congr.*, vol. 47, no. 3, pp. 7290–7297, 2014.

[167] P. Tielens and D. Van Hertem, "The relevance of inertia in power systems," *Renew. Sustain. Energy Rev.*, vol. 55, pp. 999–1009, 2016.

[168] M. Imhof and G. Andersson, "Power System Stability Control using Voltage Source Converter Based HVDC in Power Systems with a High Penetration of Renewables," in *2014 Power Syst. Comput. Conf.*, 2014, pp. 1–7.

[169] UCTE, "Operation Handbook," 2004.

[170] R. H. Renner and D. Van Hertem, "Potential of using DC voltage restoration reserve for HVDC grids," *Electr. Power Syst. Res.*, vol. 134, pp. 167–175, 2016.

[171] S. Samimi, F. Gruson, P. Delarue, F. Colas, M. M. Belhaouane, and X. Guillaud, "MMC Stored Energy Participation to the dc Bus Voltage Control in an HVDC Link," *IEEE Trans. Power Deliv.*, vol. 31, no. 4, pp. 1710–1718, 2016.

[172] I. Kocar, J. Mahseredjian, and G. Olivier, "Weighting method for transient analysis of underground cables," *IEEE Trans. Power Deliv.*, vol. 23, no. 3, pp. 1629–1635, 2008.

[173] D. Loume, M. N. Tuan, A. Bertinato, and B. Raison, "DC cable modelling and High Voltage Direct Current grid grounding system," *9th Int. Conf. Insul. Power Cables*, pp. 1–6, 2015.

[174] J. Freytes, P. Rault, F. Colas, F. Gruson, and X. Guillaud, "Dynamic impact of MMC controllers on DC voltage droop controlled MTDC grids," in *2016 18th Eur. Conf. Power Electron. Appl. (EPE'16 ECCE-Europe)*, 2016, pp. 1–10.

[175] J. Beerten, S. Cole, and R. Belmans, "Modeling of multi-terminal vsc hvdc systems with distributed dc voltage control," *IEEE Trans. Power Syst.*, vol. 29, no. 1, pp. 34–42, 2014.

[176] C. Barker and R. Whitehouse, "Autonomous converter control in a multi-terminal HVDC system," in *9th IET Int. Conf. AC DC Power Transm. (ACDC 2010)*, 2010, pp. 1–5.

[177] L. Zhang, L. Harnefors, and H. P. Nee, "Interconnection of two very weak AC systems by VSC-HVDC links using power-synchronization control," *IEEE Trans. Power Syst.*, vol. 26, no. 1, pp. 344–355, 2011.

[178] Y. G. Rebours, D. S. Kirschen, M. Trotignon, and S. Rossignol, "A Survey of Frequency and Voltage Control Ancillary Services-Part I: Technical Features," *IEEE Trans. Power Syst.*, vol. 22, no. 1, pp. 350–357, 2007.

[179] ENTSO-E, "Network Code on Load-Frequency Control and Reserves," ENTSO-E, Tech. Rep., 2013. [Online]. Available: http://networkcodes.entsoe.eu/wp-content/uploads/2013/08/130628-NC_LFCR-Issue1.pdf

[180] European Commission, "COMMISSION REGULATION (EU) 2016/631 of 14 April 2016 establishing a network code on requirements for grid connection of generators," 2016. [Online]. Available: http://eur-lex.europa.eu/legal-content/EN/TXT/?uri=OJ:JOL_2016_112_R_0001

[181] T. K. Vrana, J. Beerten, R. Belmans, and O. B. Fosso, "A classification of DC node voltage control methods for HVDC grids," *Electr. Power Syst. Res.*, vol. 103, pp. 137–144, 2013.

[182] F. Thams, R. Eriksson, and M. Molinas, "Interaction of Droop Control Structures and Its Inherent Effect on the Power Transfer Limits in Multiterminal VSC-HVDC," *IEEE Trans. Power Deliv.*, vol. 32, no. 1, pp. 182–192, 2017.

[183] T. M. Haileselassie and K. Uhlen, "Impact of DC line voltage drops on power flow of MTDC using droop control," *IEEE Trans. Power Syst.*, vol. 27, no. 3, pp. 1441–1449, 2012.

[184] E. Prieto-Araujo, F. D. Bianchi, A. Junyent-Ferré, and O. Gomis-Bellmunt, "Methodology for droop control dynamic analysis of multiterminal VSC-HVDC grids for offshore wind farms," *IEEE Trans. Power Deliv.*, vol. 26, no. 4, pp. 2476–2485, 2011.

[185] J. Beerten, D. Van Hertem, and R. Belmans, "VSC MTDC systems with a distributed DC voltage control - A power flow approach," *2011 IEEE Trondheim PowerTech*, pp. 1–6, 2011.

[186] K. Rouzbehi, A. Miranian, J. I. Candela, A. Luna, and P. Rodriguez, "A generalized voltage droop strategy for control of multiterminal DC grids," *IEEE Trans. Ind. Appl.*, vol. 51, no. 1, pp. 607–618, 2015.

[187] J. Beerten and D. Van Hertem, "Analysis of power redispatch schemes for HVDC grid secondary voltage control," *IEEE Power Energy Soc. Gen. Meet.*, vol. 2015-Septe, no. 3, 2015.

[188] A. Egea-Alvarez, J. Beerten, D. Van Hertem, and O. Gomis-Bellmunt, "Hierarchical power control of multiterminal HVDC grids," *Electr. Power Syst. Res.*, vol. 121, pp. 207–215, 2015.

[189] B. Berggren, R. R. Majumder, C. Sao, and K. Linden, "Method and control device for controlling power flow within a dc power transmission network," WO Patent 2012 000 549, 06 30, 2010.

[190] B. Berggren, K. Lindén, and R. Majumder, "DC Grid Control Through the Pilot Voltage Droop Concept - Methods for Establishing Droop Constants," *IEEE Trans. Power Syst.*, vol. 30, no. 5, pp. 2312–2320, 2015.

[191] O. Gomis-Bellmunt, J. Liang, J. Ekanayake, and N. Jenkins, "Voltage-current characteristics of multiterminal HVDC-VSC for offshore wind farms," *Electr. Power Syst. Res.*, vol. 81, no. 2, pp. 440–450, 2011.

[192] R. Pierre, "Dynamic Modeling and Control of Multi-Terminal HVDC Grids," Ph.D. dissertation, L'Ecole Centrale de Lille, 2014.

[193] L. Xu, B. Andersen, P. Cartwright, and P. Horton, "Topologies for VSC transmission," *Power Eng. J.*, vol. 16, no. 3, pp. 142–150, 2002.

[194] W. Wang and M. Barnes, "Power flow algorithms for multi-terminal VSC-HVDC with droop control," *IEEE Trans. Power Syst.*, vol. 29, no. 4, pp. 1721–1730, 2014.

[195] L. Xiao, Z. Xu, T. An, and Z. Bian, "Improved Analytical Model for the Study of Steady State Performance of Droop-controlled VSC-MTDC Systems," *IEEE Trans. Power Syst.*, pp. 1–, 2016.

[196] J. Beerten, R. Eriksson, and R. Belmans, "Influence of DC voltage droop settings on AC system stability," in *10th IET Int. Conf. AC DC Power Transm. (ACDC 2012)*, 2012, pp. 13–13.

[197] Transpower, "Ancillary Services," 2016. [Online]. Available: http://www.systemoperator.co.nz/market/ancillary-services

[198] D. Gan and E. Litvinov, "Energy and reserve market designs with explicit consideration to lost opportunity costs," *IEEE Trans. Power Syst.*, vol. 18, no. 1, pp. 53–59, 2003.

[199] K. Rouzbehi, A. Miranian, A. Luna, and P. Rodriguez, "DC Voltage Control and Power Sharing in Multiterminal DC Grids Based on Optimal DC Power Flow and Voltage-Droop Strategy," *Emerg. Sel. Top. Power Electron. IEEE J.*, vol. 2, no. 4, pp. 1171–1180, 2014.

# Appendix A

# Simulation Parameters

The simulation parameters used throughout the thesis are detailed in Table. A.1 and A.2.

Table A.1: Specifications of the 1000 MVA MMC simulation model: Grid parameters.

| Parameter | | Value |
|---|---|---|
| DC grid voltage | $V_{dc}$ | 640 kV |
| AC grid voltage | $V_{ac}$ | 320 VLLrms |
| AC grid frequency | $f$ | 50 Hz |

Table A.2: Specifications of the 1000 MVA MMC simulation model: Converter parameters.

| Parameter | | Value | |
|---|---|---|---|
| Rated power | $S_n$ | 1000 MVA | |
| SM per arm | $N$ | 400 /arm | |
| SM capacitance | $C_{sm}$ | 13.02 mF | |
| Total capacitance of an arm | $C_{\Sigma}$ | 32.55 $\mu$F | |
| Aggregated capacitance of MMC | $C_{mmc}$ | 195.3 $\mu$F | |
| Electrostatic constant | $H_c$ | 40 ms | |
| Arm inductance | $L_{arm}$ | 48.9 mH | 0.15 p.u. |
| Arm resistance | $R_{arm}$ | 0.4 $\Omega$ | 0.0039 p.u. |
| AC filter inductance | $L_f$ | 58.7 mH | 0.18 p.u. |
| AC filter resistance | $R_f$ | 0.102 $\Omega$ | 0.001 p.u. |

The specifications of the small-scale MMC prototype are summarized in Table. A.3 and A.4[1].

Table A.3: Specifications of the experimental setup : Grid parameters.

| Parameter | | Value |
|---|---|---|
| DC grid voltage | $V_{dc}$ | 400 V |
| AC grid voltage | $V_{ac}$ | 208 VLLrms |
| AC grid frequency | $f$ | 50 Hz |

Table A.4: Specifications of the small-scale MMC prototype: Converter parameters.

| Parameter | | Value | |
|---|---|---|---|
| Rated power | $S_n$ | 6 kVA | |
| SM per arm | $N$ | 10 /arm | |
| SM capacitance | $C_{sm}$ | 4.21 mF | |
| Total capacitance of an arm | $C_\Sigma$ | 421 $\mu$F | |
| Aggregated capacitance of MMC | $C_{mmc}$ | 2.526 $\mu$F | |
| Electrostatic constant | $H_c$ | 34.1 ms | |
| Arm inductance | $L_{arm}$ | 6 mH | 0.26 p.u. |
| Arm resistance | $R_{arm}$ | 35.8 m$\Omega$ | 0.0049 p.u. |
| AC filter inductance | $L_f$ | 5 mH | 0.22 p.u. |
| AC filter resistance | $R_f$ | 26 m$\Omega$ | 0.0036 p.u. |

---

[1] The value of SM capacitance given in the table is the effective value identified in a preliminary experiment; and thus, a slight difference from the data-sheet provided by the manufacturer can be found.

# Appendix B

# Derivation of Intermediate Variables of MMC in Steady State

The following describes the way to express the modulated AC/DC voltage and currents

$$\psi = \left\{ V_m^{ac},\, V_m^{dc},\, \delta,\, I_{ac},\, I_{dc},\, \theta \right\} \tag{B.1}$$

as the functions of the input variables

$$\chi = \left\{ P_{ac},\, Q_{ac},\, V_{ac},\, V_{dc},\, \omega \right\}.$$

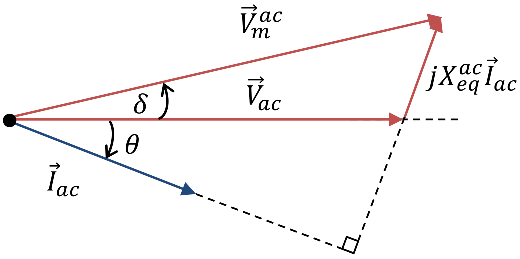

Figure B.1: Phasor diagram of corresponding circuit.

The desired AC power transfer of the MMC is achieved by regulating the equivalent AC voltage $v_m^{ac}$. The AC side grid connection can be represented by the vector diagram shown in Fig. B.1. Taking the AC grid voltage as the reference, the equivalent AC voltage of the MMC is expressed in the vectorial form as follows:

$$\vec{V}_m^{ac} = V_m^{ac} \cos\delta + jV_m^{ac} \sin\delta \tag{B.2}$$

$$\vec{V}_{ac} = V_{ac}. \tag{B.3}$$

The AC current flows into the AC grid is defined as:

$$\vec{I}_{ac} = I_{ac} \cos\theta + jI_{ac} \sin\theta. \tag{B.4}$$

In a three-phase system, the active and reactive power injected into the AC grid is given by:

$$P_{ac} + jQ_{ac} = 3\vec{V}_{ac}\overline{\vec{I}_{ac}} = 3V_{ac}\left(I_{ac}\cos\theta - jI_{ac}\sin\theta\right), \tag{B.5}$$

where the positive sign of the active and reactive power indicates the power is supplied to the AC grid. The amplitude of the current and the power angle are given by:

$$I_{ac} = \frac{\sqrt{P_{ac}^2 + Q_{ac}^2}}{3V_{ac}} \tag{B.6}$$

$$\theta = \begin{cases} \arctan\left(-\frac{Q_{ac}}{P_{ac}}\right) & \text{if } P_{ac} > 0 \\ \arctan\left(-\frac{Q_{ac}}{P_{ac}}\right) + \pi & \text{if } P_{ac} < 0 \end{cases}. \tag{B.7}$$

From the voltage drop across the phase reactor, the equivalent AC voltage of the MMC are expressed as functions of the active and reactive power:

$$V_m^{ac}\cos\delta = -X_{eq}^{ac}I_{ac}\sin\theta + V_{ac} = \frac{X_{eq}^{ac}Q_{ac}}{3V_{ac}} + V_{ac} \tag{B.8}$$

$$V_m^{ac}\sin\delta = X_{eq}^{ac}I_{ac}\cos\theta = \frac{X_{eq}^{ac}P_{ac}}{3V_{ac}} \tag{B.9}$$

$$V_m^{ac} = \sqrt{\left(\frac{X_{eq}^{ac}Q_{ac}}{3V_{ac}} + V_{ac}\right)^2 + \left(\frac{X_{eq}^{ac}P_{ac}}{3V_{ac}}\right)^2} \tag{B.10}$$

$$\delta = \arctan\frac{X_{eq}^{ac}P_{ac}}{X_{eq}^{ac}Q_{ac} + 3V_{ac}^2}. \tag{B.11}$$

The DC side variables are relatively simple. The DC grid current $I_{dc}$ can be derived from the active power $P_{ac}$ and the DC grid voltage $V_{dc}$:

$$I_{dc} = \frac{P_{ac}}{V_{dc}}, \tag{B.12}$$

and the common mode DC voltage is assumed to be:

$$V_m^{dc} = V_{dc}. \tag{B.13}$$

According to the analysis above, all the variables necessary to estimate the steady-state behavior of the capacitor voltage are given in terms of the operating power and the AC/DC grid voltages.

# Control and Energy Management of MMC-based Multi-Terminal HVDC Grids

**Abstract**: The scope of this thesis includes control and management of the Modular Multilevel Converter (MMC)-based Multi-Terminal Direct Current (MTDC). At first, our focus is paid on the internally stored energy, which is the important additional degree of freedom brought by the complex topology of MMC. In order to draw out the utmost of this additional degree of freedom, an in-depth analysis of the limits of this internally stored energy is carried out, and they are mathematically formulated. Then, this degree of freedom of the MMC is used to provide a completely new solution to improve the DC voltage dynamics. A novel control strategy, named Virtual Capacitor Control, is proposed. Under this control, the MMC behaves as if there were a physical capacitor whose size is adjustable. Thus, it is possible to virtually increase the equivalent capacitance of the DC grid to mitigate the DC voltage fluctuations in MTDC systems. Finally, the scope is extended to a MMC-based MTDC grid. One of the crucial challenges for such system is to cope with a sudden loss of a converter station which may lead to a great variation of the system voltage. The voltage droop method is commonly used for this purpose. The analysis shows that the desired control action may not be exerted when the available headroom of the converter stations are insufficient. We thus propose a novel voltage droop control structure which permits to provide different actions depending on the sign of DC voltage deviation caused by the disturbance of system voltage as well as an algorithm that determines the droop parameters taking into account the operating point and the available headroom of each station.

**Keywords**: Modular Multilevel Converters (MMCs), High-voltage direct current (HVDC) transmission, Multi-Terminal DC (MTDC) grid, Converter control, Energy management, Primary voltage control, Voltage droop control, Modeling

# Contrôle et Opération des Réseaux HVDC Multi-Terminaux à base de Convertisseurs MMC

**Résumé**: Cette thèse porte sur la commande de réseaux multi-terminaux à courant continu (MTDC) basés sur des convertisseurs multiniveaux modulaires (MMCs). Tout d'abord, notre attention se focalise sur l'énergie stockée à l'intereur du MMC qui constitue un degré de liberté additionnel apporté par sa topologie complexe. Afin d'en tirer le meilleur parti, les limites de l'énergie interne sont formulées mathématiquement. Ensuite, afin de améliorer la dynamique de la tension DC, l'utilisation de ce nouveau degré de liberté s'avère d'une grande importance. Par conséquent, une nouvelle stratégie de commande, nommée «Virtual Capacitor Control», est proposée. Cette nouvelle stratégie de commande permet au MMC de se comporter comme s'il existait un condensateur physique dont la taille est réglable aux bornes, contribuant ainsi à l'atténuation des fluctuations de la tension DC. Enfin, la portée de l'étude est étendue au réseau MTDC. L'un des défis majeurs pour un tel système est de faire face à une perte soudaine d'une station de convertisseur qui peut entraîner une grande variation de la tension du système. A cet effet, la méthode de statisme de tension est la plus couramment utilisée. Cependant, l'analyse montre que l'action de contrôle souhaitée risque de ne pas être réalisée lorsque la marge disponible de réserve de puissance du convertisseur est insuffisante. Nous proposons donc une nouvelle structure de commande de la tension qui permet de fournir de différentes actions en fonction du signe de l'écart de la tension suite à une perturbation, associée à un algorithme qui détermine les paramètres de statisme en tenant compte du point de fonctionnement et de la réserve disponible à chaque station.

**Mots-clefs**: Convertisseurs modulaires multiniveaux (MMCs), Transmission à haute tension courant continu (HVDC), Réseaux multi-terminaux DC (MTDC), Commande de convertisseur, Gestion de l'énergie, Réglage primaire de tension, Modélisation